University of Cape Town

PhD Thesis

Aspects of Quantum States of Matter

Author:
Ruach Pillay Slayen

Supervisor:
Prof J Murugan
Prof J Shock

A thesis submitted in fulfillment of the requirements for the degree of PhD

in the

Laboratory for Quantum Gravity and Strings
Mathematics and Applied Mathematics
Faculty of Science

February 12, 2024

Abstract

In this thesis we explore two aspects of the spectra of low-dimensional quantum systems with potential relevance for modern condensed matter and holography. We begin with a study of two-dimensional systems in magnetic fields whose spectra exhibit Landau level structure. We then study disordered quantum field theories whose spectra exhibit the correlations characteristic of quantum chaotic/integrable systems.

In Part I, we review established results concerning the eigenstates and spectra of spin-0 and spin-1/2 quantum fields confined to two-dimensional planes and spheres, in homogeneous magnetic field configurations. We then study a novel variation of Haldane's spherical monopole system called the *spherical dipole system*. We review and expand on the results for the single-particle Hilbert space and spectra for the spin-0 case, then extend these to the spin-1/2 case. The latter is relevant for the study of experimentally realisable systems such as C_{60} fullerine. We find that in the strong-field limit, the spectrum exhibits a Landau level structure, which is explained by the tendency of a strong dipole field to localise the particles at the poles of the sphere. The spin-1/2 system features a new (approximately) zero-energy lowest Landau level for certain values of the angular momentum quantum number relative to the dipole strength.

In Part II, we give an overview of random matrix theory and its relation to the study of quantum chaos via spectral statistics, with a focus on the spectral form factor (SFF) as a diagnostic of chaos. After reviewing a $0+1$ dimensional, disordered quantum field theory called the Sachdev-Ye-Kitaev (SYK) model and its chaos properties, we study a novel variation of the model: the *gauged complex SYK_2 model*. This model describes N complex fermions with a disordered quadratic interaction term (the SYK_2 model) coupled to a one-dimensional external gauge field, where the introduction of the external gauge field is equivalent to a twisting of the boundary conditions of the fermions. We probe the large N chaos properties of this model from the perspective of the SFF. We find that the gauge field does not affect the integrability of the original SYK_2 model, but nonetheless gives rise to notable effects on the slope-dip-ramp structure of the SFF. Namely, by tuning the gauge field, one may control both the decay of the early time slope as well as the explicit timescale needed for the appearance of zero modes. These zero modes are responsible for an exponential ramp of the SFF, which is conjectured to be a feature of all non-interacting, disordered systems. While the timescale governing their appearance takes a fixed finite value in the ungauged model, in our model it may be made arbitrarily small.

Declaration of Authorship

The content of this thesis is partially based on collaborations with a number of individuals: Jeff Murugan, Jonathan P. Shock and Hendrik J.R. Van Zyl (University of Cape Town).

The list below identifies section of this thesis which are partially based on the listed publications or preprints.

Chapters 3 and 4:
J. Murugan, J. P. Shock and R. P. Slayen, *Remarks on fermions in a dipole magnetic field*, JHEP **10**, 082 (2021) [arXiv:2107.10076].

Chapters 9 and 10, Appendices E and F:
J. Murugan, R. P. Slayen and H.J.R. Van Zyl, *A Study of the SYK_2 Model with Twisted Boundary Conditions* (2023), [arXiv:2307.01099][1]

I, Ruach Pillay Slayen, declare that this thesis titled, *Quantum States of Matter* and the work presented in it are my own. I confirm that:

- This work was done wholly while in candidature for a research degree at the University of Cape Town.
- Where I have consulted the published work of others, this is always clearly attributed.
- Where I have quoted from the work of others, the source is always given. With the exception of such quotations, this thesis is entirely my own work.

Signed: _____

Date: _____

[1] Please note that edits have since been made to the results reported in this paper (as it stands at the time of submission). This thesis contains the correct results.

Acknowledgements

Thanks to my supervisors, Jeff Murugan and Jonathan Shock, for the academic guidance and for the support and understanding during the times when the non-academic aspects of life were most challenging. And to Jeff for the opportunity to spend a month at the Abdus Salam International Center for Theoretical Physics in Trieste, Italy.

Thanks to all of the past, present and honourary members of QGaSLab, for the discussions and camaraderie: Zayd, Thato, Atiq, Mpho, Jaco, Toma, Shruti, Nitin, Dima, Cameron and Surajit.

Thank you to the Shuttleworth Postgraduate Scholarship Programme for funding my studies, and to the National Institute for Theoretical and Computational Sciences and Amanda Weltman for the additional support.

To my brothers Asher and Ntokozo and my cousin Jyestha, who went through the throes of thesis writing alongside me. To Leila and Nishal, for opening up your home, and for always being there. To Micaela, for your understanding, patience and care, especially during the final push. To Luthando and Marlo, for your support and company during the COVID years. To Brian, for your advice and encouragement from afar. To La'eeqa and Lungi, for the good times since moving back home. I could write another thesis expressing my gratitude to and love for you all.

But most of all, thank you to my parents, Thikam and Mike: for your patience, loving care and unwavering support throughout my entire academic journey, particularly during the final year of this PhD. For the great coffee and the chicken pulau that kept me going. I could not have done it without you.

Contents

Part I

Two-Dimensional Quantum States in Magnetic Fields

Chapter 1

Introduction to Part I

The first part of this thesis will be concerned with the simple set up of electrons, confined to a two-dimensional surface, in the presence of a strong magnetic field. Despite their simplicity, such systems a) have provided the backdrop to some of the most surprising and interesting phenomena in physics [1], b) constitute an active field of research today, c) are of fundamental significance as examples of quantum mechanical effects at the macroscopic scale [2], d) have fascinating links to the mathematical study of topology and e) have applications to technological research into topological insulators/superconductors and quantum computing. The phenomena arising in the study of these systems are referred to collectively as the *quantum Hall effect* (QHE). To motivate our study of such systems, we begin with an overview of the QHE [8].

The classical Hall effect was discovered by Edwin Hall in 1879[1], who studied an electrical conductor in which current flows perpendicular to an applied magnetic field normal to the surface. The Lorentz force from the applied field acts on the current carrying electrons, which accumulate on one side of the conductor. The Hall effect then refers to the resulting potential difference transverse to the direction of the current I_x. This potential difference is called the *Hall voltage* $V_H = \rho_{xy} I_x$, where ρ_{xy} is the *Hall resistivity*.

[1] While the classical Hall effect can be explained using basic classical electromagnetic theory, its experimental discovery eighteen years prior to the discovery of the electron is noteworthy.

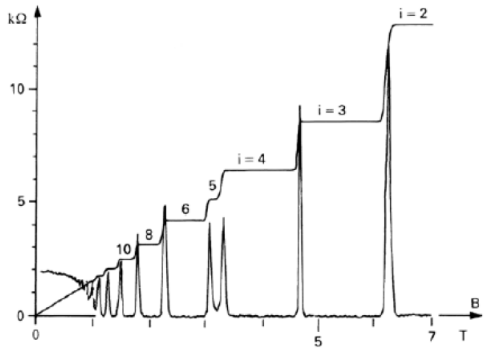

Figure 1.1: Resistivities in the integer quantum Hall effect [1].

A century later, using very strong applied magnetic fields at very low temperatures, the first experiments exploring the quantum regime of the Hall effect were performed [3]. The Hall resistivity was now found to take precisely quantised values $\rho_{xy} = \frac{2\pi\hbar}{e^2}\frac{1}{\nu}$, where ν is an integer (see Fig. 1.1). As a function of magnetic field strength, ρ_{xy} exhibits a series of increasing plateaux at the quantised values, separated by sharp jumps; this result was termed the integer quantum Hall effect (IQHE). These plateaux of the IQHE are readily explained: electron-electron interactions can be ignored, and a standard quantum mechanical treatment reveals that the electrons in the conductor occupy highly degenerate energy eigenstates. These are the famous *Landau levels*, which form the theoretical basis of the QHE in all its guises, and which will play a starring role in the first part of this thesis. Interestingly, the precise quantisation of the IQHE is deeply related to the imprecise physics of disorder: impurities in the sample localise electron states, which are then unable to carry current, giving rise to the quantisation of the Hall resistivity [1].

When these experiments were repeated using samples with less disorder[2], new resistivity plateaux were observed at values corresponding to rational, not integer ν [4]. This result is known as the fractional quantum Hall effect (FQHE). To explain the FQHE, interactions between electrons must be taken into account, resulting in a tougher but far richer problem, the study of which has yielded many advances in physics[3]. The building blocks of the theory of the FQHE are the so-called Laughlin

[2]Disorder here refers to the presence of symmetry-breaking impurities, contained to some degree in all experimental samples. These are generally modelled by a random potential, see Section 6.4.3.

[3]These include the discovery of exotic states of quantum matter called *anyons* [5], practical applications of the notion of topological order [11] and its associated ideas including the non-Abelian Berry phase [14], edge excitations [15], topological entanglement entropy [12], ground state degeneracy [13], as well as the successful application of Chern-Simons theories [51, 6, 7, 9, 10].

states [16] which are eigenstates of the planar system of a two-dimensional electron gas in the presence of a perpendicular magnetic field. In order to localise the states within a finite area[4], an external confining potential must then be introduced on the infinite plane. Such a potential breaks translational invariance and introduces boundary effects, such as edge modes.

To circumvent this issue, in 1983 Haldane considered a geometrical variation of the planar system, the so-called *Haldane sphere*[5] [31], where the charged particles are confined to the surface of a sphere with a magnetic monopole at its center. While considered unphysical due to the magnetic monopole, the spherical system is ideal for investigating the bulk physics of the Landau problem: the system replicates many of the key features of its planar counterpart such as a constant, perpendicular magnetic field through its surface, while being more amenable to numerical simulation and the thermodynamic limit than the latter due to its finite surface area [58].

Haldane's innovation has since been extended to the study of QHE states on a huge variety of curved and flat, compact and non-compact two-dimensional manifolds[6]. Despite being mostly theoretical (thus far), these studies have actually contributed to our understanding of experimentally observable states[7], highlighting the importance of geometry, as opposed to topology, in our understanding of the QHE [21, 22, 23]. However, regardless of the particular geometry considered, studies of two-dimensional quantum states in magnetic fields have tended to treat only constant, perpendicular (to the surface on which the particles are constrained) field figurations. Little attention has been given to quantum states in *inhomogeneous* magnetic fields: field configurations in which the flux density is not constant across the surface. Studies of compact surfaces have generally assumed small variations over a large constant background [20]; studies of planar systems have either assumed the same [34], or have considered only highly constrained variations, such as fields which are monotonic functions of radial distance[8] [33].

[4]For the purposes of, for example, numerical study.

[5]Which was, however, first considered in the 1930s by Dirac and others [24, 25].

[6]See the prescriptions for IQHE [18] and FQHE [20] states on surfaces such as cylinders [19], tori [17] and higher genus Riemann surfaces [13].

[7]The study of lowest Landau level states on curved surfaces turn out to uncover universal features of the QHE inaccessible to calculations in flat space. For example, in [20] low energy transport coefficients of the QHE were described as the response of the ground state to changes in scalar curvature.

[8]In this case, the Landau level degeneracy is lifted. This is readily understood by noting that eigenstates of the magnetic Schrödinger operator $H = (-i\boldsymbol{\nabla} - \boldsymbol{A})^2$ are labelled by angular momentum quantum number m and Landau level number n, with states with larger m values located further away from the origin. Consequently, eigenstates encountering a monotonically decreasing

The case which will be of interest to us in the first part of this thesis is a novel variation of Haldane's spherical monopole system: the *spherical dipole system*. It is obtained by simply replacing the magnetic monopole at the centre of the Haldane sphere with a magnetic dipole. This system differs from the Haldane sphere in that it involves a magnetic field configuration which is: a) physically realisable, b) inhomogeneous, and c) has vanishing net magnetic flux through the spherical surface. As we have seen, a key feature of two-dimensional electronic matter in a homogeneous magnetic field configuration is the existence of highly degenerate *Landau levels*, which then serve as the conceptual building blocks of the QHE. The primary question we sought to answer in our research was then: *would the spherical dipole system exhibit a Landau level structure?*

We initially postulated the spherical dipole system as a toy model for studying quantum matter in astrophysical settings such as the ultra-dense atmospheres encountered in neutron stars. These are spherical systems in which an incredibly strong dipole field is present, offering the possibility of probing condensed matter in sustained magnetic fields orders of magnitude stronger than anything produced terrestrially, and seeking for the possibility of astrophysical signatures of topological quantum matter. However, modelling such systems as a two-dimensional sphere is clearly a huge simplification.

On the other hand, as the ability of experimentalists to grow two-dimensional graphene surfaces expands, a genuine two-dimensional spherical dipole system could be physically realisable in the not-so-distant future. While the Haldane sphere, with its unphysical monopole field, could never be built in the lab, such systems could present an empirical opportunity to test some of the theoretical predictions for various aspects of the quantum Hall effect on compact geometries. The study of spin-1/2 particles on the dipole sphere is of particular interest in the phenomenology of other compact configurations such as a C_{60} fullerene enclosing a magnetic dipole, or one of its larger allotropic cousins like C_{540}, fullerite. With this in mind, we begin our study of two-dimensional systems in the presence of magnetic fields.

(increasing) magnetic field will exhibit a decreasing (increasing) set of eigenvalues $E_{m,n}$ as a function of m within a given Landau level. For the lowest ($n = 0$) Landau level, this can be proven exactly [33] while for $n > 0$, one must be satisfied with a perturbative treatment.

Chapter 2

Two-Dimensional Quantum States in Perpendicular Fields

In this chapter we review established results concerning the eigenstates and spectra of spin-0 and spin-1/2 quantum fields confined to two-dimensional surfaces in the presence of magnetic fields. In particular, we will be concerned with the plane and the sphere, and we will consider magnetic field configurations which are everywhere perpendicular to these surfaces. The methods and results reviewed here will serve as a starting point to our analysis of the spherical dipole system in Chapter 3.

2.1 The Planar System

In this section we consider a system of non-interacting charged particles moving in the plane in a perpendicular uniform magnetic field of strength $\boldsymbol{B} = \boldsymbol{\nabla} \times \boldsymbol{A}$, where all quantities in bold are two-dimensional vectors. We will work in symmetric gauge

$$\boldsymbol{A} = \frac{B}{2}(-y, x), \tag{2.1}$$

which preserves rotational symmetry, ensuring that angular momentum will be a good quantum number. The magnetic field is then given by $\boldsymbol{B} = B\hat{\boldsymbol{z}}$.

2.1.1 Spin-0 Particles

Following the treatment in [52], the Hamiltonian for a spin-0 particle of unit mass is given by

$$H_0 = \frac{1}{2}(-i\boldsymbol{\nabla} - \mathbf{A})^2 \,. \tag{2.2}$$

where we have set $\hbar = e = 1$. We will work in complex coordinates

$$z = \sqrt{B/2}(x^1 + ix^2)\,, \tag{2.3}$$
$$\bar{z} = \sqrt{B/2}(x^1 - ix^2)\,. \tag{2.4}$$

where we have rescaled by $\sqrt{B/2}$ for convenience.

Analytic Approach

The Hamiltonian (2.2) can be written

$$H_0 = B\Big(-\partial\bar{\partial} - \frac{1}{2}(z\partial - \bar{z}\bar{\partial}) + \frac{1}{4}z\bar{z}\Big)\,, \tag{2.5}$$

with holormorphic and anti-holomorphic derivatives given respectively by

$$\partial \equiv \frac{\partial}{\partial z} = \sqrt{2/B}(\partial_1 - i\partial_2)\,, \tag{2.6}$$
$$\bar{\partial} \equiv \frac{\partial}{\partial \bar{z}} = \sqrt{2/B}(\partial_1 + i\partial_2)\,. \tag{2.7}$$

Introducing energy eigenstates $H_0\psi = E\psi$, we define the *reduced eigenstates* [26] via

$$\psi \equiv e^{-|z|^2/2}\hat{\psi}. \tag{2.8}$$

We will identify $\hat{\psi}$ with elements of the Hilbert space, while the factor $e^{-|z|^2/2}$ will appear in the measure of the Hilbert space inner product

$$\langle f|g\rangle \equiv \int \frac{dzd\bar{z}}{2\pi i} e^{-|z|^2}\overline{f}g. \tag{2.9}$$

Each operator A which acts on eigenstates as $A\psi = a\psi$ has an associated Hilbert space operator

$$\hat{A} \equiv e^{|z|^2/2} A e^{-|z|^2/2}\,, \tag{2.10}$$

which acts on the reduced states to return the same eigenavalue: $\hat{A}\hat{\psi} = a\hat{\psi}$. The Hilbert space Hamiltonian operator (2.5) is then

$$\hat{H}_0 = B\Big(-\partial\bar{\partial} + \bar{z}\bar{\partial} + \frac{1}{2}\Big)\,. \tag{2.11}$$

The ground states of $\hat{H}$ are just holomorphic wavefunctions $f(z)$ satisfying $\bar{\partial}f(z) = 0$, all with ground state energy $B/2$. The corresponding full states are given by

$$\psi_{\rm LLL} = e^{-|z|^2/2} f(z)\,. \tag{2.12}$$

We have found infinitely many degenerate ground state eigenfunctions. These constitute what is known as the *lowest Landau level*, henceforth referred to as the LLL.

The standard planar angular momentum operator for a spin-0 particle, given in polar coordinates by $J = -i\partial_\phi$, becomes

$$J_0 = z\partial - \bar{z}\bar{\partial} = \hat{J}_0, \tag{2.13}$$

which of course satisfies $[J_0, H_0] = 0$ due to rotational symmetry. We can then choose a general angular momentum eigenstate

$$\hat{\psi} = z^m P(|z|^2)\,, \tag{2.14}$$

where single valuedness requires $m \in \mathbb{Z}$, as our ansatz for the energy eigenstates. We obtain the following differential equation for P

$$\hat{H}_0\hat{\psi} = E\hat{\psi} \quad \Rightarrow \quad B\Big(-\partial\bar{\partial} + \bar{z}\bar{\partial} + \frac{1}{2}\Big)z^m P = Ez^m P\,. \tag{2.15}$$

Changing variables to $r = |z|^2$, we obtain

$$r\frac{d^2P}{dr^2} + (m+1-r)\frac{dP}{dr} + \Big(\frac{E}{B} - \frac{1}{2}\Big)P = 0\,. \tag{2.16}$$

which is a differential equation of Laguerre form

$$xf'' + (m+1-x)f' + nf = 0\,. \tag{2.17}$$

Its solutions are given by the *generalised Laguerre polynomials*

$$L_n^m(x) \equiv \frac{1}{n!}e^x x^{-m}\frac{d^n}{dx^n}(e^{-x}x^{n+m}) \tag{2.18}$$

$$= \sum_{j=0}^{n}\frac{(-1)^j}{j!}\binom{n+m}{n-j}x^j\,, \tag{2.19}$$

which are defined for $n \in \mathbb{Z}$, $n \geq 0$ and $j \geq -n$. Comparing (2.17) with (2.16), restoring the exponential measure factor using (2.8) and the B dependence by rescaling $z \to \sqrt{B/2}z$ as well as all factors of $e, \hbar, m$, we obtain the full eigenstates

$$\begin{aligned}
\psi_n^m(z,\bar{z}) &= \mathcal{N}\left(\frac{z}{\sqrt{2}l}\right)^m L_n^m\left(\frac{|z|^2}{2l^2}\right)e^{-|z|^2/4l^2} \\
E_{B,n} &= \hbar\omega_B\Big(n+\frac{1}{2}\Big) \\
n &= 0, 1, 2, ... \\
m &= -n, -n+1, ...
\end{aligned} \tag{2.20}$$

where we have defined the *magnetic length* $l \equiv \sqrt{\hbar/eB}$ and the *cyclotron frequency* $\omega_B = \frac{eB}{m}$. The choice of normalisation constant

$$\mathcal{N} = \sqrt{\frac{n!}{(n+m)!}}\,. \tag{2.21}$$

ensures that the wavefunctions (2.20) are orthonormal with respect to both quantum numbers

$$\left\langle \hat{\psi}_n^m \middle| \hat{\psi}_{n'}^{m'} \right\rangle = \delta_{n,n'}\delta_{m,m'}\,. \tag{2.22}$$

The $n = 0$ case corresponds to our LLL states (2.14), while the rest of the spectrum is composed of evenly spaced energy levels labelled by the positive integer n, each infinitely degenerate with respect to m. These highly degenerate energy levels are the famous *Landau levels* and are a vital feature of the physics of charged particles on two-dimensional surfaces in constant perpendicular magnetic fields.

We may may plot the eigenstates (2.20) most easily in polar coordinates $z = re^{i\phi}$, by defining

$$\psi_n^m(z,\bar{z}) = \rho_n^m(B;r)e^{im\phi}, \tag{2.23}$$

where

$$\rho_n^m(B;r) = \mathcal{N}(B/2)^{m/2}r^m L_n^m\left(Br^2/2\right)e^{-Br^2/4}, \tag{2.24}$$

is the radial part of the eigenstate (with $\hbar = e = 1$).

In each Landau level the lowest angular momentum $m = 0$ state is localised at the origin, while as m increases, the states become localised at larger values of r. The decay of the states around the region of localisation is faster for larger field strength B, meaning that the effect of a stronger field strength is to more sharply localise the particle (radially) on the plane (see Fig. 2.1). Higher energy states have more nodes and are less spatially localised than their counterparts with the same m in lower Landau levels, as we would expect (see Fig. 2.2).

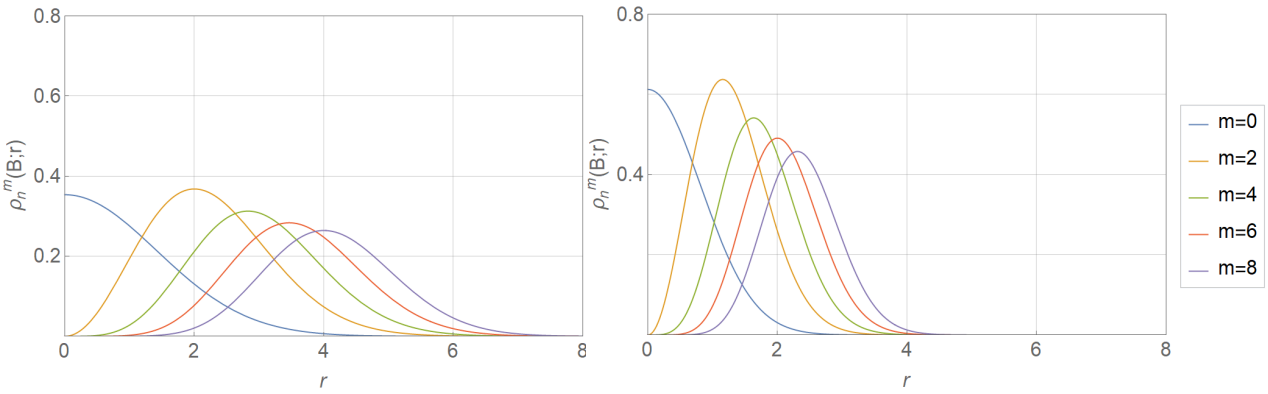

(a) $B = 1$ (b) $B = 3$

Figure 2.1: Radial part of the eigenstates, $\rho_n^m(B;r)$, for $n = 0$ (the lowest Landau level) and various m. As the angular momentum m increases the states are localised further from the origin. Note that all states are more sharply localised in a stronger field (a) than a weaker one (b).

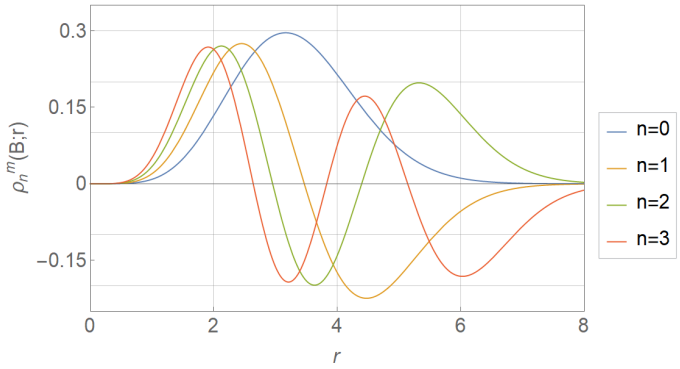

Figure 2.2: Radial part of the eigenstates, $\rho_n^m(B;r)$, in various Landau levels n for $B = 1$ and $m = 5$. Note that with increasing n the increasingly energetic states become less localised.

Algebraic Approach

We briefly introduce a set of operators which allow for an alternative, algebraic derivation of the above results. They will be crucial for our treatment of the spin-1/2 problem in Section 2.1.2.

We begin by defining

$$a^\dagger = l\Big(\partial - \frac{1}{2l^2}\bar{z}\Big)\,, \quad a = -l\Big(\bar{\partial} + \frac{1}{2l^2}z\Big)\,. \tag{2.25}$$

These operators are adjoints of each other with respect to the standard inner product and satisfy the commutation relations

$$[a, a^\dagger] = 1\,. \tag{2.26}$$

We may then rewrite our Hamiltonian (2.5) (rescaling $z \to \sqrt{B/2}z$ and restoring $e, \hbar, m$ dependence) as

$$H_0 = \hbar\omega_B\left(a^\dagger a + \frac{1}{2}\right). \tag{2.27}$$

We immediately identify a ($a^\dagger$) as the energy lowering (raising) operators of the system. Using this form of the Hamiltonian, the commutation relations (2.26) and the relations

$$[J_0, a^\dagger] = -a^\dagger\,, \qquad [J_0, a] = a\,, \tag{2.28}$$

we see that the operators (2.25) act on our eigenstates states as

$$a^\dagger\psi_n^m = \sqrt{n+1}\psi_{n+1}^{m-1}\,, \qquad a\psi_n^m = \sqrt{n}\psi_{n-1}^{m+1}\,, \tag{2.29}$$

simultaneously lowering (raising) angular momentum and raising (lowering) energy. Consider now the operators

$$b^\dagger = -l\Big(\bar{\partial} - \frac{1}{2l^2}z\Big)\,, \quad b = l\Big(\partial + \frac{1}{2l^2}\bar{z}\Big)\,. \tag{2.30}$$

These commute with both a and $a^\dagger$ and therefore H, and satisfy the further commutation relations

$$[b, b^\dagger] = 1\,, \qquad [J_0, b^\dagger] = b^\dagger\,, \qquad [J_0, b] = -b, \tag{2.31}$$

These relations allow us to identify b ($b^\dagger$) as raising (lowering) operators of angular momentum which leave energy invariant. They act on states in the following way

$$b^\dagger\psi_n^m = \sqrt{m+n+1}\psi_n^{m+1}\,, \qquad b\psi_n^m = \sqrt{m+n}\psi_n^{m-1}\,. \tag{2.32}$$

Using these relations together with (2.29) allows us to rewrite the angular momentum operator (2.13) as

$$J_0 = \hbar(b^\dagger b - a^\dagger a). \tag{2.33}$$

Requiring that ground states are annihilated by a immediately gives a differential equation from which we recover the LLL states (2.12) with energy $\hbar\omega_B/2$. The spectrum as well as all higher energy states may then be constructed via algebraic operator methods [52], reproducing the full result (2.20).

2.1.2 Spin-1/2 Particle

The Hamiltonian we will be considering for describing spin-1/2 particles in (perpendicular, constant) magnetic fields is given by

$$H = v\boldsymbol{\sigma}\cdot\boldsymbol{\Pi} = v\begin{pmatrix} 0 & \Pi_1 - i\Pi_2 \\ \Pi_1 + i\Pi_2 & 0 \end{pmatrix}, \tag{2.34}$$

where $\Pi_i = -i\hbar\partial_i - eA_i$ and v is the Fermi velocity. Such Hamiltonians are relevant for the study of planar graphene [50] and describes massless spin-1/2 fermions confined to a two-dimensional plane. Working again in symmetric gauge (2.1), and changing to complex coordinates

$$\begin{aligned} z &= \frac{1}{\sqrt{2}}\left(x^1 + ix^2\right), \qquad \partial = \frac{1}{\sqrt{2}}\left(\partial_1 - i\partial_2\right), \\ \bar{z} &= \frac{1}{\sqrt{2}}\left(x^1 - ix^2\right), \qquad \bar{\partial} = \frac{1}{\sqrt{2}}\left(\partial_1 + i\partial_2\right). \end{aligned} \tag{2.35}$$

we can rewrite (2.34) as

$$H = \frac{\sqrt{2}v\hbar}{il}\begin{pmatrix} 0 & a^\dagger \\ -a & 0 \end{pmatrix}, \tag{2.36}$$

in terms of the ladder operators (A.1). For the spin-1/2 problem, the total angular momentum operator is given by

$$J = J_0 + \frac{\hbar}{2}\sigma_3, \tag{2.37}$$

in which the orbital angular momentum J_0 familiar from the spin-0 problem is multiplied by an implicit 2×2 identity matrix, and is now supplemented by the spin angular momentum operator appropriate for 2-component spinors. While neither the spin nor orbital parts of J commute with the spin-1/2 Hamiltonian (2.36),

$$[H, J_0] = \hbar\begin{pmatrix} 0 & a^\dagger \\ a & 0 \end{pmatrix}, \qquad [H, \hbar\sigma_3/2] = -\hbar\begin{pmatrix} 0 & a^\dagger \\ a & 0 \end{pmatrix}, \tag{2.38}$$

their sum J evidently does. We therefore look for simultaneous energy and total momentum eigenstates of H. By simply considering the actions (2.29) of the raising/lowering operators appearing in H, we can write down the spinor solutions to Schrödinger's equation $H\Psi = E_n\Psi$ in terms of the spin-0 solutions ψ_n^m as

$$\begin{aligned} \Psi_n^m(z,\bar{z}) &= \begin{pmatrix} i\psi_n^m(z,\bar{z}) \\ \psi_{n-1}^{m+1}(z,\bar{z}) \end{pmatrix} \\ E_n &= v\sqrt{2\hbar eBn} \\ n &= 1, 2, 3, ... \\ m &= -n, -n+1, ... \end{aligned} \tag{2.39}$$

with an additional zero mode solution corresponding to the $n = 0$ case given by

$$\begin{aligned} \Psi_0^m(z,\bar{z}) &= \begin{pmatrix} \psi_0^m(z,\bar{z}) \\ 0 \end{pmatrix} \\ E_0 &= 0 \\ m &= 0, 1, 2, ... \end{aligned} \tag{2.40}$$

While our spinor solutions do not have a well defined spin or orbital angular momentum, they are eigenstates of the total angular momentum operator

$$J\Psi_n^m = (m + 1/2)\Psi_n^m \,, \tag{2.41}$$

as we would expect given the rotational symmetry of the physics, preserved by our decision to work in symmetric gauge.

Comparing to the spin-0 case, we note that these spinor solutions also exhibit the characteristic Landau level structure of energy levels which are highly degenerate with respect to angular momentum. However, the energy levels are no longer evenly spaced, going as $\sqrt{n}$. We also see the existence of degenerate zero modes with nonzero total angular momentum m. That the energies in the spin-0 problem go as the square of the energies in the spin-1/2 problem can be understood by noting that

$$H_{1/2}^2 \sim \begin{pmatrix} a^\dagger a & 0 \\ 0 & aa^\dagger \end{pmatrix} = \begin{pmatrix} H_0 - 1/2 & 0 \\ 0 & H_0 + 1/2 \end{pmatrix} , \tag{2.42}$$

which also accounts for how the ground state energy shift of $1/2$ in the spin-0 problem disappeared, giving rise to zero modes in the spin-$1/2$ problem.

Discrepancy with the Literature

Our solutions (2.39) differ from the solution given in the literature [20, 49, 50], in which the azimuthal angular momentum quantum number m of both components of the solution are equal. Such solutions are eigenstates of orbital angular momentum $J_0 = i\hbar\partial_\phi$, which contradicts the fact that J_0 does not commute with the Hamiltonian. They are also not eigenstates of total angular momentum $J = i\hbar\partial_\phi + \hbar\sigma_3/2$, which we would expect them to be as this is the conserved quantity following from the rotational symmetry of the problem. It would appear that the authors have not taken into account the fact that the operators a ($a^\dagger$) which appear in the Hamiltonian not only raise (lower) energy n, but also lower (raise) angular momentum m (2.29). See Appendix A for the details of the comparison between our solutions and those in the literature.

2.2 The Spherical System

We now turn our attention to spherical systems, which brings us a step closer to the spherical dipole system of interest. We again restrict our consideration to homogeneous field configurations, which then forces us to consider a magnetic monopole at the center of the sphere on which our particle is confined: the Haldane sphere. Such systems require a slighly more sophisticated version of the algebraic operator methods used for the planar cases, but as we shall see the general structure of the problem generalises nicely.

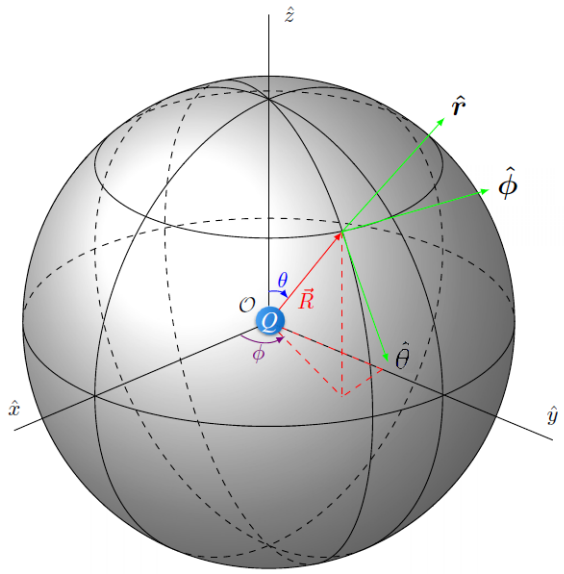

Figure 2.3: The spherical coordinate system for a sphere of radius R, with unit vectors (2.43) plotted in green. A magnetic charge of strength Q is shown at the origin. Image taken from [50].

Before we begin, we introduce the spherical coordinate unit vectors (see Fig. 2.3), given in Cartesian coordinates by

$$\hat{\boldsymbol{r}} = \begin{pmatrix} \cos\phi\sin\theta \\ \sin\phi\sin\theta \\ \cos\theta \end{pmatrix}, \quad \hat{\boldsymbol{\theta}} = \begin{pmatrix} \cos\phi\cos\theta \\ \sin\phi\cos\theta \\ -\sin\theta \end{pmatrix}, \quad \hat{\boldsymbol{\phi}} = \begin{pmatrix} -\sin\phi \\ \cos\theta \\ 0 \end{pmatrix}. \tag{2.43}$$

The cross products are given by

$$\hat{\boldsymbol{r}} \times \hat{\boldsymbol{\theta}} = \hat{\boldsymbol{\phi}}, \quad \hat{\boldsymbol{\theta}} \times \hat{\boldsymbol{\phi}} = \hat{\boldsymbol{r}}, \quad \hat{\boldsymbol{\phi}} \times \hat{\boldsymbol{r}} = \hat{\boldsymbol{\theta}}, \tag{2.44}$$

while the derivatives are

$$\begin{aligned}
&\frac{\partial\hat{\boldsymbol{r}}}{\partial\theta}=\hat{\boldsymbol{\theta}}, \quad \frac{\partial\hat{\boldsymbol{\theta}}}{\partial\theta}=-\hat{\boldsymbol{r}}, \quad \frac{\partial\hat{\boldsymbol{\phi}}}{\partial\theta}=0,\\
&\frac{\partial\hat{\boldsymbol{r}}}{\partial\phi}=\sin\theta\hat{\boldsymbol{\phi}}, \quad \frac{\partial\hat{\boldsymbol{\theta}}}{\partial\phi}=\cos\theta\hat{\boldsymbol{\phi}}, \quad \frac{\partial\hat{\boldsymbol{\phi}}}{\partial\phi}=-\sin\theta\hat{\boldsymbol{r}}-\cos\theta\hat{\boldsymbol{\theta}}.
\end{aligned} \tag{2.45}$$

2.2.1 Spin-0 Particles

Following [32], we look for eigenstates and eigenvectors of the Hamiltonian describing a spin-0 particle with mass M, given by the kinetic energy

$$H=\frac{\hbar^2}{2MR^2}|\boldsymbol{\Lambda}|^2, \tag{2.46}$$

where

$$\boldsymbol{\Lambda}=R\hat{\boldsymbol{r}}\times\Big(-i\boldsymbol{\nabla}+\frac{e}{\hbar}\boldsymbol{A}\Big) \tag{2.47}$$

is the canonical momentum tangent of the particle confined to the surface of the sphere of radius $r=R$. Bold quantities denote two-dimensional vectors. We consider a monopole potential

$$\boldsymbol{A}=-\frac{\hbar Q}{eR}\cot\theta\hat{\boldsymbol{\theta}}, \tag{2.48}$$

where Q is the *monopole strength*, which corresponds to a radial magnetic field

$$\boldsymbol{B}=\frac{\hbar Q}{eR^2}\hat{\boldsymbol{r}}, \tag{2.49}$$

at every point on the sphere (see Fig. 2.4). The total flux through the surface of the sphere is given by

$$4\pi R^2|B|=\frac{4\pi\hbar Q}{e}, \tag{2.50}$$

from which it follows that our Hamiltonian can be rewritten as

$$H=\frac{\omega_B}{2Q}|\boldsymbol{\Lambda}|^2, \tag{2.51}$$

where $\omega_B=\frac{eB}{M}$.

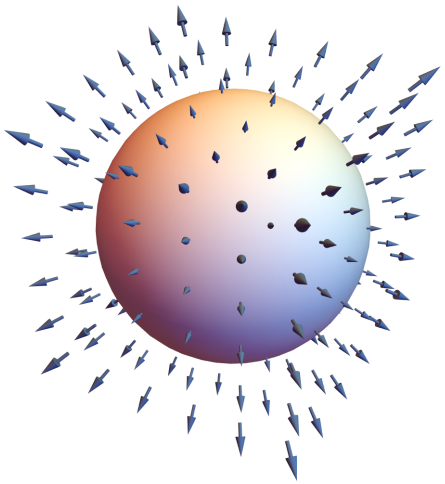

Figure 2.4: The Haldane sphere. The magnetic monopole of strength Q at the center of the sphere of radius R produces a radial magnetic field $\boldsymbol{B} = \frac{\hbar Q}{eR^2}\hat{\boldsymbol{r}}$, illustrated here as a vector field.

In spherical coordinates, we have

$$\begin{aligned}\boldsymbol{\Lambda} &= R\hat{\boldsymbol{r}} \times \left[-i\Big(\hat{\boldsymbol{\theta}}\frac{\partial}{\partial\theta} + \hat{\boldsymbol{\phi}}\frac{1}{\sin\theta}\frac{\partial}{\partial\phi}\Big) - Q\cot\theta\hat{\boldsymbol{\theta}}\right] \\ &= -i\Big(\hat{\boldsymbol{\phi}}\frac{\partial}{\partial\theta} - \hat{\boldsymbol{\theta}}\frac{1}{\sin\theta}\frac{\partial}{\partial\phi}\Big) + Q\cot\theta\hat{\boldsymbol{\theta}}. \end{aligned} \tag{2.52}$$

Some algebra then yields

$$|\boldsymbol{\Lambda}|^2 = -\frac{1}{\sin\theta}\frac{\partial}{\partial\theta}\sin\theta\frac{\partial}{\partial\theta} + \Big(Q\cot\theta + \frac{i}{\sin\theta}\frac{\partial}{\partial\phi}\Big)^2. \tag{2.53}$$

Using (2.45) it can be easily verified that

$$\hat{\boldsymbol{r}}\cdot\boldsymbol{\Lambda} = \boldsymbol{\Lambda}\cdot\hat{\boldsymbol{r}} = 0, \tag{2.54}$$

so the canonical angular momentum has no radial component. Using (2.43, 2.45) we can verify the following commutators

$$[\Lambda_i, \Lambda_j] = i\epsilon_{ijk}(\Lambda_k - Q\hat{r}_k), \tag{2.55}$$

$$[\Lambda_i, \hat{r}_j] = i\epsilon_{ijk}\hat{r}_k, \tag{2.56}$$

where the indices i, j, k refer to the Cartesian components of the vectors they index. Note that (2.55) is not the correct commutator algebra for an angular momentum operator. We rectify this by defining the operator

$$\boldsymbol{L} = \boldsymbol{\Lambda} + Q\hat{\boldsymbol{r}}, \tag{2.57}$$

which is the correct angular momentum operator for the system since

$$\begin{aligned}[L_i, L_j] &= [\Lambda_i + Q\hat{r}_i, \Lambda_j + Q\hat{r}_j] \\ &= [\Lambda_i, \Lambda_j] + Q[\Lambda_i, \hat{r}_j] + Q[\hat{r}_i, \Lambda_j] \\ &= i\epsilon_{ijk}(\Lambda_k - Q\hat{r}_k) + iQ\epsilon_{ijk}\hat{r}_k + iQ\epsilon_{ijk}\hat{r}_k \\ &= i\epsilon_{ijk}(\Lambda_k + Q\hat{r}_k) \\ &= i\epsilon_{ijk}L_k, \end{aligned} \tag{2.58}$$

where we have used (2.55) and (2.56). This is nothing but the $SU(2)$ commutator algebra of angular momentum, so $\boldsymbol{L}$ is indeed the angular momentum operator as advertised. It differs from the canonical angular momentum Λ in that it has a constant radial component

$$\hat{\boldsymbol{r}} \cdot \boldsymbol{L} = \boldsymbol{L} \cdot \hat{\boldsymbol{r}} = Q. \tag{2.59}$$

We can then construct angular momentum raising and lowering operators in the usual way. Explicitly, we find

$$L_z = -i\frac{\partial}{\partial\phi}, \tag{2.60}$$

$$L_\pm \equiv L_x \pm iL_y = e^{\pm i\phi}\Big[\pm\frac{\partial}{\partial\theta} + i\cot\theta\frac{\partial}{\partial\phi} + \frac{Q}{\sin\theta}\Big], \tag{2.61}$$

which can be shown to obey the usual commutation relations

$$[L_z, L_\pm] = \pm L_z. \tag{2.62}$$

Crucially, the angular momentum operator $\boldsymbol{L}$ can be shown to satisfy the commutation relations

$$[L_i, \hat{r}_j] = i\epsilon_{ijk}\hat{r}_k, \qquad [L_i, \Lambda_j] = i\epsilon_{ijk}\Lambda_k. \tag{2.63}$$

Note that our Hamiltonian commutes with the angular momentum operator $\boldsymbol{L}$ since

$$\begin{aligned} H \sim |\boldsymbol{\Lambda}|^2 &= |\boldsymbol{L} - Q\hat{\boldsymbol{r}}|^2 \\ &= L^2 - Q(\hat{\boldsymbol{r}} \cdot \boldsymbol{L} + \boldsymbol{L} \cdot \hat{\boldsymbol{r}}) + Q^2 \\ &= L^2 - Q^2, \end{aligned} \tag{2.64}$$

where in the third equality we have used (2.59). It follows that we can choose eigenfunctions Y_{Qlm} which simultaneously diagonalise H, L^2 and L_z, and use the $L_\pm$ ladder operators to move between them. Such eigenfunctions are called *monopole harmonics*

[53, 27], and are given by

$$\begin{aligned} Y_{Qlm}(\theta,\phi) &= \mathcal{N}_{Qlm} 2^{-m} (1-\cos\theta)^{\frac{m-Q}{2}} (1+\cos\theta)^{\frac{m+Q}{2}} P_{l-m}^{m-Q,m+Q}(\cos\theta) e^{im\phi}, \\ &\equiv \Theta_{Qlm}(\theta) e^{im\phi} \\ m &= -l, -l+1, ..., l \\ l &= Q, Q+1, Q+2, ... \end{aligned} \tag{2.65}$$

where

$$\mathcal{N}_{Qlm} = \sqrt{\frac{(2l+1)}{4\pi} \frac{(l-m)!}{(l-Q)!} \frac{(l+m)!}{(l+Q)!}} \tag{2.66}$$

is a normalisation constant, and the Jacobi polynomials $P_n^{\alpha,\beta}(x)$ are given by

$$\begin{aligned} P_n^{\alpha,\beta}(x) &= \frac{(-1)^n}{2^n n!} (1-x)^{-\alpha} (1+x)^{-\beta} \frac{d^n}{dx^n} \left[(1-x)^{n+\alpha} (1+x)^{n+\beta} \right] \\ &= \frac{1}{2^n} \sum_{s=0}^{n} \binom{n+\alpha}{s} \binom{n+\beta}{n-s} (x-1)^{n-s} (x+1)^s. \end{aligned} \tag{2.67}$$

See Appendix B for a full derivation of the monopole harmonics. We plot a representative selection in Fig. 2.5, plotting only the ϕ independent, polar part of the monopole harmonics, $\Theta_{Qlm}(\theta)$.

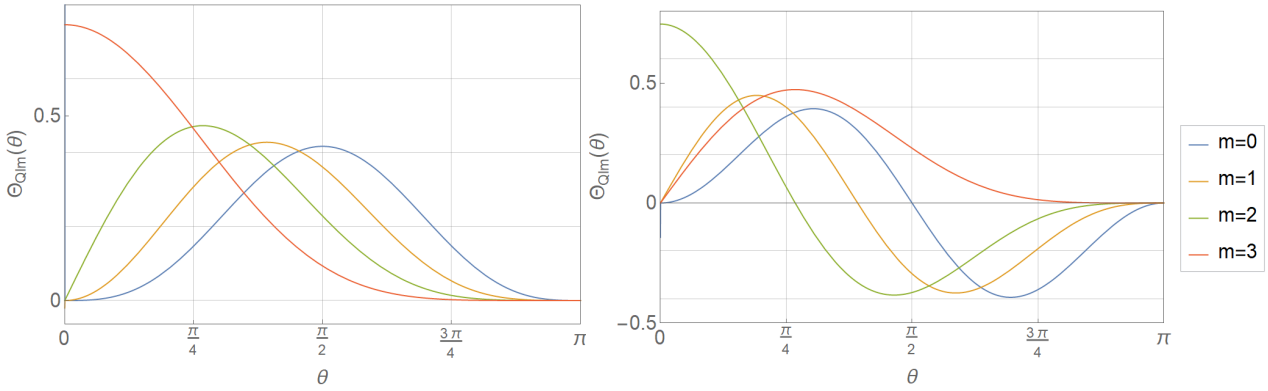

(a) $Q = 3,\ l = 3$ (b) $Q = 2,\ l = 3$

Figure 2.5: Polar part of the monopole harmonics, $\Theta_{Qlm}(\theta)$. The $m = 0$ state is always symmetric about the equator, and states with larger m are localised nearer to the north pole. Negative m states may be obtained from positive m states by reflection about the equator: $\Theta_{Q,l,-m}(\theta) = \Theta_{Q,l,m}(\pi - \theta)$.

In the form (2.65) we note that the monopole harmonics reduce to the usual spherical harmonics when $Q = 0$, as we would expect in the absence of any magnetic field.

They satisfy

$$L_z Y_{Qlm} = m Y_{Qlm}, \tag{2.68}$$
$$L^2 Y_{Qlm} = l(l+1) Y_{Qlm}. \tag{2.69}$$

Since the allowed values of the angular momentum l begin at $l = Q$ and increase in integer steps, we may define the integer Landau level index n via the identification $l = Q + n$. It follows that

$$\begin{aligned} H Y_{Qlm} &= \frac{\omega_B}{2Q}(L^2 - Q^2) Y_{Qlm} \\ &= \frac{\omega_B}{2Q}\left((Q+n)(Q+n+1) - Q^2\right) Y_{Qlm}, \end{aligned} \tag{2.70}$$

so the energy eigenvalues are given by

$$E_{nQ} = \omega_B \left(n + \frac{1}{2} + \frac{n(n+1)}{2Q} \right) Y_{Qlm}. \tag{2.71}$$

Note that the monopole harmonics (2.65) may be written in another useful form, by first using using the definition of the Jacobi polynomials (2.67) to write

$$\begin{aligned} Y_{Qlm} =& \mathcal{N}_{Qlm} 2^{-m} (1-x)^{\frac{m-Q}{2}} (1+x)^{\frac{m+Q}{2}} e^{im\phi} \\ & \sum_{s=0}^{l-m} (-1)^{l-m-s} \binom{l-Q}{s} \binom{l+Q}{l-m-s} (1-x)^{l-Q-s} (1+x)^s. \end{aligned} \tag{2.72}$$

We then follow Haldane [31] and define the spinor variables

$$u = \cos(\theta/2) e^{i\phi/2}, \qquad v = \sin(\theta/2) e^{-i\phi/2}, \tag{2.73}$$

so that

$$x = u^* u - v^* v, \qquad 1 - x = 2\sin^2(\theta/2), \qquad 1 + x = 2\cos^2(\theta/2). \tag{2.74}$$

The monopole harmonics can then be written

$$\mathcal{Y}_{Qnm} = \mathcal{N}_{Q,Q+n,m} (-1)^{Q+n-m} v^{Q-m} u^{Q+m} \sum_{s=0}^{Q+n-m} (-1)^s \binom{n}{s} \binom{2Q+n}{Q+n-m-s} (\bar{v}v)^{n-s} (\bar{u}u)^s, \tag{2.75}$$

where in order to make explicit the dependence on the Landu level index n, we have defined

$$\mathcal{Y}_{Qnm} \equiv Y_{Q,Q+n,m} = Y_{Qlm}. \tag{2.76}$$

In the lowest Landau level, where $l = Q$, we have the LLL states given by

$$\mathcal{Y}_{Q0m} \sim v^{Q-m} u^{Q+m}. \tag{2.77}$$

In the n^{th} Landau level however, where $l = Q + n$, we require the conjugate variables $\bar{u}, \bar{v}$ to describe states. If we treat all four variables as independent, then our angular momentum operators for general Landau levels can be represented by

$$L_+ = u\frac{\partial}{\partial v} - \bar{v}\frac{\partial}{\partial \bar{u}}, \tag{2.78}$$

$$L_- = v\frac{\partial}{\partial u} - \bar{u}\frac{\partial}{\partial \bar{v}}, \tag{2.79}$$

$$L_z = \frac{1}{2}\left(u\frac{\partial}{\partial u} - v\frac{\partial}{\partial v} - \bar{u}\frac{\partial}{\partial \bar{u}} + \bar{v}\frac{\partial}{\partial \bar{v}}\right). \tag{2.80}$$

These operators move us between degenerate states of different angular momenta within a given Landau level, much like the $b, b^\dagger$ operators (2.30) in the planar case. We now follow [58] in defining a set of ladder operators analogous to the planar $a, a^\dagger$ operators (A.1), which move us between Landau levels. These *cyclotron angular momentum* operators are defined as

$$S_+ = u\frac{\partial}{\partial \bar{v}} - v\frac{\partial}{\partial \bar{u}}, \tag{2.81}$$

$$S_- = \bar{v}\frac{\partial}{\partial u} - \bar{u}\frac{\partial}{\partial v}, \tag{2.82}$$

$$S_z = \frac{1}{2}\left(u\frac{\partial}{\partial u} + v\frac{\partial}{\partial v} - \bar{u}\frac{\partial}{\partial \bar{u}} - \bar{v}\frac{\partial}{\partial \bar{v}}\right). \tag{2.83}$$

The components $S_x = (S_+ + S_-)/2$, $S_y = (S_+ - S_-)/2i$ and S_z can be shown to also satisfy an $SU(2)$ angular momentum algebra, and to commute with our original angular momentum operators L_i,

$$[S_i, S_j] = i\epsilon_{ijk} S_k, \qquad [S_i, L_j] = 0. \tag{2.84}$$

It can be verified that

$$\boldsymbol{L}^2 = \boldsymbol{S}^2 = S(S+1), \tag{2.85}$$

where we have defined the operator

$$S = \frac{1}{2}\left(u\frac{\partial}{\partial u} + v\frac{\partial}{\partial v} + \bar{u}\frac{\partial}{\partial \bar{u}} + \bar{v}\frac{\partial}{\partial \bar{v}}\right). \tag{2.86}$$

The action of the various operators on the monopole harmonics is given by

$$S^2\mathcal{Y}_{Qnm} = (Q+n)(Q+n+1)\mathcal{Y}_{Qnm}, \tag{2.87}$$
$$S_\pm\mathcal{Y}_{Qnm} = \sqrt{(Q+n)(Q+n+1)-Q(Q\pm 1)}\,\mathcal{Y}_{Q\pm1,n\mp1,m}, \tag{2.88}$$
$$S_z\mathcal{Y}_{Qnm} = Q\mathcal{Y}_{Qnm}. \tag{2.89}$$

Note that the total angular momentum $l = Q + n$, which appears in the eigenvalues $l(l+1)$ of both S^2 and L^2, is left invariant by the action of all of these operators. Note also that from (2.89) we see that the physical Hilbert space for a monopole of strength Q is limited to states with S_z eigenvalue Q.

We may use the new operators to get another view of our Hamiltonian. It follows from (2.85) that

$$\begin{aligned}|\mathbf{\Lambda}|^2 &= |\boldsymbol{L} - Q\hat{\boldsymbol{r}}|^2\\ &= L^2 - Q^2\\ &= S^2 - (S_z)^2\\ &= \frac{1}{2}(S_+S_- + S_-S_+),\end{aligned} \tag{2.90}$$

where in the second line we have assumed that the Hamiltonian is acting on physical eigenstates for which we can replace Q with S_z. Now, using the standard relation $[S_+, S_-] = 2S_z$, we can write

$$\begin{aligned}H &= \frac{\omega_B}{2Q}|\mathbf{\Lambda}|^2\\ &= \frac{\omega_B}{2Q}(S_-S_+ + S_z)\\ &= \omega_B\Big(\frac{1}{2Q}S_-S_+ + \frac{1}{2}\Big),\end{aligned} \tag{2.91}$$

where we have again assumed that S_z and Q are interchangeable since we are acting on physical states. Note the similarity with our expression for the planar Hamiltonian in (2.27). Clearly our LLL states (2.77), which are annihilated by S_+ (2.81) are eigenstates of this Hamiltonian with eigenvalue $\omega_B/2$. By comparison with the eigenvalue equation for H (2.70) we note the relation

$$S_-S_+\mathcal{Y}_{Qnm} = \left(2Qn + n(n+1)\right)\mathcal{Y}_{Qnm}. \tag{2.92}$$

As a final comment, recall that the physical Hilbert space for a monopole of strength Q is limited to states with S_z eigenvalue Q. On the other hand, from (2.88) we see

that while $S_\pm$ does move us between Landau levels n as advertised, it also shifts the value of Q in such a way as to keep $l = Q + n$ constant, thus taking us out of the Hilbert space for the strength Q monopole. Using $S_\pm$ as genuine ladder operators, from which to construct the full Hilbert space out of the LLL states (2.77) then requires some care. The appropriate prescription [58] is given by

$$\mathcal{Y}_{Qnm} = S_-^n \mathcal{Y}_{Q+n,0,m}. \tag{2.93}$$

2.2.2 Spin-1/2 Particles

Having treated at length the Schrödinger problem, we turn now to the case of a spin-1/2 particle confined to the sphere in the presence of the same monopole field. Following [42] we start with the standard Dirac Hamiltonian in two dimensions (in units of $c = 1$),

$$H = v\hat{\boldsymbol{n}} \cdot \left[\Big(-i\hbar\boldsymbol{\nabla} + e\boldsymbol{A} \Big) \times \boldsymbol{\sigma} \right], \tag{2.94}$$

where $\hat{\boldsymbol{n}}$, the unit normal to the surface, in this case is simply $\hat{\boldsymbol{n}} = \hat{\boldsymbol{r}}$ and $\boldsymbol{\sigma} = (\sigma^x, \sigma^y, \sigma^z)^T$ is a vector of Pauli matrices. In spherical coordinates, the gradient operator is

$$\boldsymbol{\nabla} = \frac{1}{R}\left(\hat{\boldsymbol{\theta}}\partial_\theta + \hat{\boldsymbol{\phi}}\frac{\partial_\phi}{\sin\theta} \right). \tag{2.95}$$

This in turn means that the Dirac operator $-i\hbar\boldsymbol{\nabla}$ is not Hermitian with respect to the natural inner product between two states on the sphere

$$\langle\psi|\varphi\rangle \equiv R^2 \int d\theta d\phi \sin\theta \overline{\psi}\varphi, \tag{2.96}$$

since

$$\langle\psi|\partial_\theta\varphi\rangle = R^2 \int d\theta d\phi \sin\theta \overline{\psi}\partial_\theta\varphi = -R^2 \int d\theta d\phi \sin\theta (\cot\theta\overline{\psi} + \partial_\theta\overline{\psi})\varphi,$$

implies that $\partial_\theta^\dagger = -(\partial_\theta + \cot\theta)$. Similarly, $\partial_\phi^\dagger = -\partial_\phi$. To rectify this, we need to replace this operator in (2.94) with the manifestly Hermitian combination

$$\begin{aligned} \frac{\hbar}{2}(-i\boldsymbol{\nabla} + (-i\boldsymbol{\nabla})^\dagger) &= -\frac{i\hbar}{2R}\left(\hat{\boldsymbol{\theta}}\partial_\theta + \hat{\boldsymbol{\phi}}\frac{\partial_\phi}{\sin\theta} \right) + \frac{i\hbar}{2R}\left(-\hat{\boldsymbol{\theta}}(\partial_\theta + \cot\theta) - \hat{\boldsymbol{\phi}}\frac{\partial_\phi}{\sin\theta} \right) \\ &= -\frac{i\hbar}{R}\left(\hat{\boldsymbol{\theta}}\partial_\theta + \hat{\boldsymbol{\phi}}\frac{\partial_\phi}{\sin\theta} + \frac{\hat{\boldsymbol{\theta}}}{2}\cot\theta \right). \end{aligned} \tag{2.97}$$

We now restrict our attention to a particular class of gauge field configurations which will encapsulate both cases of interest to us, given by

$$\boldsymbol{A} = A(\theta)\hat{\boldsymbol{\phi}}. \tag{2.98}$$

Note that these are symmetric under azimuthal rotations. Using $\boldsymbol{\sigma} = \hat{\theta}\sigma_x + \hat{\phi}\sigma_y + \hat{r}\sigma_z$, the Hamiltonian, (2.94), then becomes

$$\begin{aligned} H &= -\frac{i\hbar v}{R}\hat{\boldsymbol{r}}\cdot\left[\hat{\boldsymbol{\theta}}\Big(\partial_\theta + \frac{1}{2}\cot\theta\Big)\times\boldsymbol{\sigma} + \hat{\boldsymbol{\phi}}\Big(\frac{\partial_\phi}{\sin\theta} + i\frac{eR}{\hbar}A(\theta)\Big)\times\boldsymbol{\sigma}\right] \\ &= -\frac{i\hbar v}{R}\left[\Big(\partial_\theta + \frac{1}{2}\cot\theta\Big)\sigma_y - \Big(\frac{\partial_\phi}{\sin\theta} + i\frac{eR}{\hbar}A(\theta)\Big)\sigma_x\right], \end{aligned}$$

writing this in explicit matrix form, we may now write out the eigenvalue problem for the Dirac operator

$$\frac{\hbar v}{R}\begin{pmatrix} 0 & -\partial_\theta + \frac{i\partial_\phi}{\sin\theta} - \frac{1}{2}\cot\theta - \frac{eR}{\hbar}A(\theta) \\ \partial_\theta + \frac{i\partial_\phi}{\sin\theta} + \frac{1}{2}\cot\theta - \frac{eR}{\hbar}A(\theta) & 0 \end{pmatrix}\Psi = E\Psi. \tag{2.99}$$

We now follow [50] and consider the specific magnetic field configuration of a monopole located at the centre of the sphere, with potential

$$A(\theta) = -\frac{B}{\hbar}R\cot\theta, \tag{2.100}$$

The separable ansatz $\Psi = \frac{1}{\sqrt{\sin\theta}}\Phi(\theta)$, puts the eigenvalue problem (2.99) into the form

$$H\Phi = v\sqrt{\tfrac{eB}{Q}}\begin{pmatrix} 0 & H_+ \\ H_- & 0 \end{pmatrix}\Phi = E\Phi, \tag{2.101}$$

with

$$H_\pm \equiv \mp\partial_\theta + \frac{i\partial_\phi}{\sin\theta} + Q\cot\theta. \tag{2.102}$$

where we have defined (with $c = 1$)

$$Q = eBR^2/\hbar^2, \tag{2.103}$$

which is proportional, up to a convenient factor of $1/\hbar$, to the flux through the sphere in units of the flux quantum $\phi_0 = 2\pi\hbar/e$. In terms of spinor variables (2.73), our

partial derivatives are

$$\partial_\theta = \frac{\partial u}{\partial\theta}\frac{\partial}{\partial u} + \frac{\partial v}{\partial\theta}\frac{\partial}{\partial v} + \frac{\partial \bar{u}}{\partial\theta}\frac{\partial}{\partial \bar{u}} + \frac{\partial \bar{v}}{\partial\theta}\frac{\partial}{\partial \bar{v}} = \frac{1}{2}\bigg(- \bar{v}\frac{\partial}{\partial u} + \bar{u}\frac{\partial}{\partial v} - v\frac{\partial}{\partial \bar{u}} + u\frac{\partial}{\partial \bar{v}}\bigg), \tag{2.104}$$

$$\partial_\phi = \frac{\partial u}{\partial\phi}\frac{\partial}{\partial u} + \frac{\partial v}{\partial\phi}\frac{\partial}{\partial v} + \frac{\partial \bar{u}}{\partial\phi}\frac{\partial}{\partial \bar{u}} + \frac{\partial \bar{v}}{\partial\phi}\frac{\partial}{\partial \bar{v}} = \frac{i}{2}\bigg(u\frac{\partial}{\partial u} - v\frac{\partial}{\partial v} - \bar{u}\frac{\partial}{\partial \bar{u}} + \bar{v}\frac{\partial}{\partial \bar{v}}\bigg). \tag{2.105}$$

We note that we can use the cyclotron angular momentum operators from the spin-0 system (2.81) and (2.82) to write

$$\frac{\partial}{\partial\theta} = (S_+ - S_-)/2 = iS_y. \tag{2.106}$$

With the intention of writing $H_\pm$ fully in terms of the S operators, we next consider the operator

$$\frac{i\partial_\phi}{\sin\theta} + Q\cot\theta = -\frac{1}{2\sin\theta}\bigg(u\frac{\partial}{\partial u} - v\frac{\partial}{\partial v} - \bar{u}\frac{\partial}{\partial \bar{u}} + \bar{v}\frac{\partial}{\partial \bar{v}}\bigg) + \cot\theta S_z, \tag{2.107}$$

where we have used the fact that we may substitute the operator S_z in place of its eigenvalue Q. Making further use of the spinor variable relations (2.73) as well as some trigonometric identities, one may show [50] that this can be written

$$\begin{aligned}\frac{i\partial_\phi}{\sin\theta} + Q\cot\theta &= \frac{1}{2}\bigg(-\bar{v}\frac{\partial}{\partial u} + \bar{u}\frac{\partial}{\partial v} + v\frac{\partial}{\partial \bar{u}} - u\frac{\partial}{\partial \bar{v}}\bigg) \\ &= -\frac{1}{2}(S_+ + S_-) = -S_x.\end{aligned} \tag{2.108}$$

It follows that our operators (2.102) are simply

$$H_\pm = -S_x \mp iS_y = -S_\pm. \tag{2.109}$$

The square of our Hamiltonian H is then given by the diagonal matrix

$$H^2 = \begin{pmatrix} S_+S_- & 0 \\ 0 & S_-S_+ \end{pmatrix} = \begin{pmatrix} S_-S_+ + 2S_z & 0 \\ 0 & S_-S_+ \end{pmatrix}. \tag{2.110}$$

Since clearly $[H^2, H] = 0$, we may simultaneously diagonalise both H^2 and H to find their common eigenfunctions. To this end, and recalling (2.92), we know that

$$S_-S_+\mathcal{Y}_{Qnm} = (2Qn + n(n+1))\,\mathcal{Y}_{Qnm}, \tag{2.111}$$

$$(S_-S_+ + 2S_3)\mathcal{Y}_{Q'n'm} = (2Q'(n'+1) + n'(n'+1))\,\mathcal{Y}_{Q'n'm}. \tag{2.112}$$

We have thus found the eigenfunctions of H^2 (2.110) and thus H, provided that we equate the coefficients on the right hand side to ensure that both spinor components yield the same eigenvalue. This enforces $n' = n - 1$ and $Q' = Q + 1$, so up to normalisation our eigenvalue problem (2.101) has $n \neq 0$ solutions

$$\Phi_n = \begin{pmatrix} \mathcal{Y}_{Q+1,n-1,m} \\ \mathcal{Y}_{Qnm} \end{pmatrix}. \tag{2.113}$$

as well as the zero mode solution

$$\Phi_0 = \begin{pmatrix} 0 \\ \mathcal{Y}_{Q0m} \end{pmatrix}. \tag{2.114}$$

Substituting into (2.101) we verify our solutions

$$\begin{aligned} v\sqrt{\tfrac{eB}{Q}} \begin{pmatrix} 0 & S_+ \\ S_- & 0 \end{pmatrix} \Phi &= v\sqrt{\tfrac{eB}{Q}} \sqrt{(Q+n)(Q+n+1) - Q(Q+1)}\Phi \\ &\equiv E_{nQ}\Phi, \end{aligned} \tag{2.115}$$

where we have used (2.88) for the action of $S_\pm$. Simplifying the right hand side, we then obtain an expression for the energy eigenvalues of the system

$$E_{nQ} = v\sqrt{eB\left[2n + \frac{n(n+1)}{Q}\right]}. \tag{2.116}$$

We have again found our spinor solutions to exhibit a Landau level structure, with energy levels that depend on the Landau level index quantum number n (or equivalently for fixed Q, the total angular momentum $l = Q + n$) but are highly degenerate with respect to the azimuthal angular momentum quantum number m. As in the planar system, where we found that the spin-1/2 energy eigenvalues were proportional to the square root of the spin-0 energy eigenvalues shifted by the constant factor of 1/2, by comparison with (2.71) we see that the same holds true here. Likewise, we have a zero mode with vanishing energy when $n = 0$, in which case the first spinor component of our solution vanishes. In the planar limit $R \to \infty$ in which $Q \to \infty$ (see (2.103)), we indeed recover the planar result for the spectrum (2.39) $E_n = v\sqrt{2\hbar eBn}$.

Note that for our spin-1/2 planar solutions (2.39), when $n \neq 0$, the electron is partially in Landau level (LL) n and LL $n-1$, and does not have a well defined *orbital* angular momentum m (the spinor components have different values of m). In the spin-1/2 spherical solution (2.113) on the other hand, while the electron also sits partially in both LL n and LL $n-1$ for $n \neq 0$, the *total* angular momentum $l = Q+n$ is the same

for both spinor components. This is because the component in LL $n-1$ experiences a monopole strength of $Q+1$, while the component in LL n experiences a monopole strength of Q. The quantum number m, which now labels the *azimuthal* component of the total angular momentum, is also constant for both spinor components.

Chapter 3

The Spherical Dipole System

In this chapter, we again consider a quantum particle confined to the surface of a sphere in the presence of a magnetic field, but this time we depart from the homogeneous field configurations considered in Chapter 2, in favour of an inhomogeneous, *dipole* magnetic field. The results presented here are a continuation of the results reported by the candidate and collaborators in [30]. We begin by presenting the spin-0 system and expanding upon the analysis given in [30]. We then substantially extend these results to treat a spin-1/2 particle. The latter is of particular relevance to the phenomenology of the fullerine and fullerite configurations (at least in the continuum limit) and this will be the kind of systems we have in mind for the bulk of this work.

3.1 The Dipole Field

We consider the *spherical dipole system*, a novel variation of Haldane's spherical monopole system obtained by replacing the single monopole of the Haldane sphere with *two* monopoles with charges $+b$ and $-b$, separated by a distance l and aligned along the z-direction. In the limit $l \to 0$ with bl fixed, the resulting magnetic field,

$$\boldsymbol{B} = \frac{|\boldsymbol{\mu}|}{r^3}\left(2\cos\theta\,\widehat{\boldsymbol{r}} + \sin\theta\,\widehat{\boldsymbol{\theta}}\right), \tag{3.1}$$

(see Fig. 3.1) is identical to that produced by a current loop enclosing a flat region with area A_{loop} in the xy-plane. In either case the magnetic moment is aligned in the positive z-direction with $|\boldsymbol{\mu}| = IA_{\text{loop}} = bl$ and associated vector potential

$$\boldsymbol{A} = \frac{1}{r^2}\boldsymbol{\mu}\times\widehat{\boldsymbol{r}} = \frac{|\boldsymbol{\mu}|}{r^2}\sin\theta\,\widehat{\boldsymbol{\phi}}\,. \tag{3.2}$$

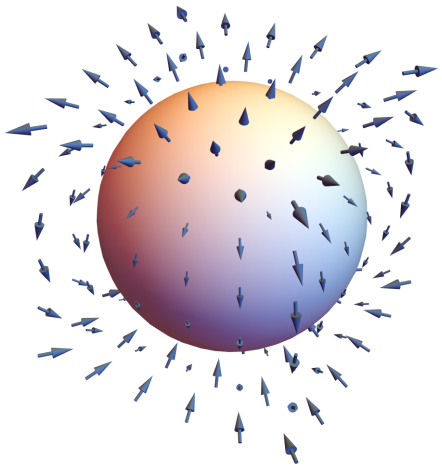

Figure 3.1: The spherical dipole system. The magnetic dipole of strength Q at the center of the sphere produces the magnetic field given by (3.6), illustrated here as a vector field.

For comparison, the vector field associated to the constant magnetic field in the z direction $\boldsymbol{B}_c$ is given by

$$\boldsymbol{A}_c = \frac{B_0}{2} r \sin\theta \widehat{\boldsymbol{\phi}}. \tag{3.3}$$

Evidently, for particles confined to the surface of a sphere of radius $r = R$, the potentials (3.2) and (3.3) are proportional, and will yield very similar results, a point that we will return to at various points in this thesis.

To facilitate comparison with the spherical monopole system, we define the *dipole strength*

$$Q \equiv \frac{e|\boldsymbol{\mu}|}{\hbar R}, \tag{3.4}$$

in terms of which the vector potential and dipole field on the surface of the sphere $r = R$ can be written respectively as

$$\boldsymbol{A} = \frac{\hbar Q}{eR} \sin\theta \, \widehat{\boldsymbol{\phi}}\,, \tag{3.5}$$

$$\boldsymbol{B} = \frac{\hbar Q}{eR^2} \left(2\cos\theta \, \widehat{\boldsymbol{r}} + \sin\theta \, \widehat{\boldsymbol{\theta}} \right) . \tag{3.6}$$

We briefly note that one possibility for producing such inhomogeneous magnetic fields in a laboratory setting is to use the magnetic fields trapped in the core of vortices in

type II superconductors which exhibit such a monotonically decreasing field strength away from the vortex core. Since a typical 200-300 Å core-width vortex traps a 1-2 T magnetic field, reasonably large magnetic fields can be produced. However, boundary conditions are difficult to treat in such setups [34]. An alternative is to confine the electron gas to a curved surface, a sphere of unit radius say, in a constant ambient magnetic field $\boldsymbol{B}_c = B_0\hat{\boldsymbol{z}}$ whose normal component at any point (θ, ϕ) on the sphere is given by $B_0 \cos\theta$ and monotonically decreases from the pole to the equator.

3.2 Spin-0 Particle

Haldane's monopole sphere shares many similarities with the more familiar problem of a particle moving on a plane in a perpendicular magnetic field. In particular, in the planar limit where we take the radius of the sphere $R \to \infty$, the two problems converge. For the dipole system that will be the subject of interest here, this is clearly no longer the case since the magnetic field experienced by the particle is no longer uniform. Since the dipole breaks the $O(3)$ symmetry of the Haldane problem to a $U(1)$ about the dipole axis, in the large radius limit, and sufficiently close to the poles of the sphere, the system reduces to the planar Landau problem but in an *inhomogeneous* magnetic field with azimuthal symmetry.

3.2.1 Oblate spheroidal coordinates

In units of $c = 1$, the Hamiltonian for the system is given by

$$\begin{aligned} H &= \frac{1}{2}(-i\hbar\boldsymbol{\nabla} - e\boldsymbol{A})^2 \\ &= \frac{\hbar^2}{2R^2}\left[-\frac{1}{\sin\theta}\frac{\partial}{\partial\theta}\sin\theta\frac{\partial}{\partial\theta} + \left(\frac{i}{\sin\theta}\frac{\partial}{\partial\phi} - Q\sin\theta\right)^2\right], \end{aligned} \tag{3.7}$$

where we consider a particle of unit mass confined to the surface of the sphere $r = R$, in the vector potential (3.5). Substituting this into the Schrödinger equation and introducing the separable ansatz $\Psi_l^m(\theta, \phi) = e^{im\phi}\psi_l(\theta)$ yields the eigenvalue problem

$$\widetilde{E}_{l,m}\psi_l = -\frac{1}{\sin\theta}\frac{\partial}{\partial\theta}\left(\sin\theta\frac{\partial\psi_l}{\partial\theta}\right) + \frac{\left(m + Q\sin^2\theta\right)^2}{\sin^2\theta}\psi_l\,, \tag{3.8}$$

where we have defined $\widetilde{E}_{l,m} \equiv 2R^2E_{l,m}/\hbar^2$. Before solving the eigenvalue problem, let's build some intuition for what to expect. Using (3.8) the Hamiltonian can be

written as the sum of a kinetic and a potential term

$$H = -\frac{1}{\sin\theta}\frac{\partial}{\partial\theta}\left(\sin\theta\frac{\partial}{\partial\theta}\right) + V(\theta; m, Q), \quad \text{where} \quad V(\theta; m, Q) = \frac{\left(m + Q\sin^2\theta\right)^2}{\sin^2\theta}\,. \tag{3.9}$$

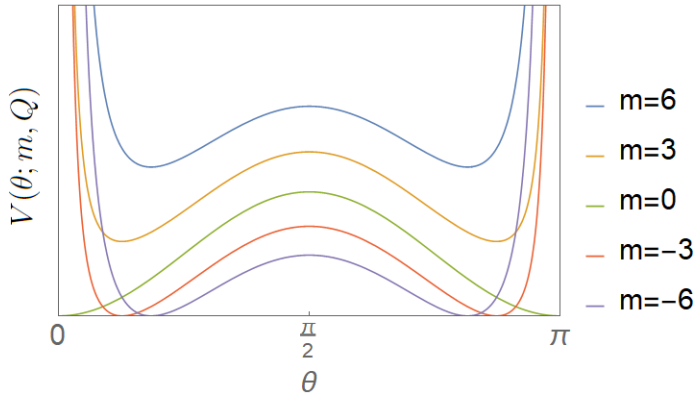

Figure 3.2: The effective potential seen by a spin-0 particle interacting with the dipole field plotted over a polar angle range from the north pole ($\theta = 0$) to the south pole ($\theta = \pi$), for various values of the angular momentum quantum number m and dipole strength $Q = 20$.

Many of the features of the quantum states can be deduced already from the potential. In particular, the potential is positive, symmetric about the equator ($\theta = \pi/2$) and for momenta in the range $-Q \leq m \leq 0$, has real zeros at

$$\theta_\pm = \sin^{-1}\left(\pm\sqrt{-\frac{m}{Q}}\right)\,. \tag{3.10}$$

For momenta in the range $0 < m < Q$, the potential retains the double-well profile but has no real zeros, while for $|m| > Q$ it is a single-well. Physically, this can be understood as follows: since the sign of the cross-term in the potential depends only on the sign of the momentum, only negative momentum states can decrease their energy by coupling to the magnetic field. At fixed Q, as $|m|$ is increased, the minima of such states move away from the poles accompanied by a decrease in the height of the local maximum - see Fig. 3.2. Consequently, we expect that states with larger momenta will localise closer to the equator. Conversely, fixing $|m|$ below its critical value and increasing the strength of the magnetic field (and consequently Q) pushes out the minima of the effective potential to the poles, localising more states near the polar regions.

The Schrödinger equation (3.8) admits a solution in terms of known functions - the analog of spherical harmonics for an oblate spheroid. To see this, let's change variables to $z = \cos\theta$, and write the differential equation in the form

$$\frac{d}{dz}\left[\left(1-z^2\right)\frac{d}{dz}\right]\psi + \left[\lambda_l^m + Q^2 z^2 - \frac{m^2}{(1-z^2)}\right]\psi = 0, \tag{3.11}$$

where

$$\lambda_l^m \equiv \widetilde{E}_{l,m} - 2mQ - Q^2\,. \tag{3.12}$$

This can be recognized as an *angular oblate spheroidal differential equation* [46]. Its solutions are the angular oblate spheroidal wavefunctions,

$$S_l^m(z;Q) = \sum_n d_n^{l,m}(Q) P_n^m(z)\,, \qquad l-|m| = 0,1,2,\ldots \tag{3.13}$$

where $P_n^m(z)$ are the associated Legendre functions, and the coefficient functions $d_n^{l,m}(Q)$ satisfy a three-term recursion relation [46]

$$\alpha_n d_{n+2} + (\beta_n - \lambda_l^m)\, d_n + \gamma_n d_{n-2} = 0\,, \tag{3.14}$$

whose coefficients

$$\begin{aligned}
\alpha_n &= -\frac{(n+2m+1)(n+2m+2)}{(2n+2m+3)(2n+2m+5)}Q^2\,,\\
\beta_n &= (n+m)(n+m+1) - Q^2\frac{2(n+m)(n+m+1)-m^2-1}{(2n+2m+3)(2n+2m-1)}\,,\\
\gamma_n &= \frac{n(1-n)Q^2}{(2n+2m-1)(2n+2m-3)}\,,
\end{aligned} \tag{3.15}$$

are functions of the momentum m and dipole strength Q. The recursion relation itself may be solved by, for example, the method of continued fractions but this will not be necessary for our purposes since many of the properties of the solution can be inferred from its series expansion.

The angular spheroidal wave equation (3.11) has two regular singular points at $z = 1$ and $z = -1$, corresponding to the north and south poles of the sphere respectively. Using the fact that in the interval $z \in [-1,+1]$, the associated Legendre functions can be expressed as derivatives of Legendre polynomials of the first kind, $P_n^m(z) = (1-z^2)^{m/2} d^m P_n(z)/dz^m$, the spheroidal wavefunctions (3.13) can be written as

$$S_l^m(z;Q) = (1-z^2)^{m/2}\sum_n d_n^{l,m}(Q)\frac{d^m P_n(z)}{dz^m}\,, \tag{3.16}$$

In general, solutions that are finite at $z = \pm 1$ will diverge at $z = \mp 1$. However, for a discrete set of eigenvalues λ_l^m, the series will converge to solutions that are finite at both poles. These eigenvalues are fixed by the requirements that the wavefunction remain finite at $z = \pm 1$, and this normalisability condition quantizes the energy spectrum via the relation in (3.12)

$$\widetilde{E}_{l,m} = \lambda_l^m + 2mQ + Q^2 \,. \tag{3.17}$$

The spheroidal eigenvalues are real-valued and satisfy the conjugation relation $\lambda_l^m = \lambda_l^{-m}$ and the equality $\lambda_l^m < \lambda_{l+1}^m$. This ordering means that for a given value of m, the smallest value of the eigenvalue is that for which $l = |m|$. Furthermore, for fixed m, the corresponding set of eigenfunctions with different l values are mutually orthogonal. Consequently, the full wavefunctions are orthonormal with respect to both quantum numbers,

$$\left\langle \Psi_l^m \middle| \Psi_{l'}^{m'} \right\rangle = \delta_{l,l'}\delta_{m,m'} \,. \tag{3.18}$$

There are a number of normalisation schemes for the angular oblate functions. In the Stratton-Morse scheme which will be most convenient for our purposes, S_l^m can be normalised by imposing that, near $z = 1$, it behaves like the associated Legendre functions P_l^m for all values of Q. This in turn requires that the expansion coefficients satisfy

$$\widetilde{\sum_n} \frac{(n+2m)!}{n!} d_n^{l,m}(Q) = \frac{(l+m)!}{(l-m)!} \,. \tag{3.19}$$

The tilde over the summation sign is an instruction to include only even values of n if $(l-m) \in 2\mathbb{Z}$ and only odd values of n if $(l-m) \in 2\mathbb{Z}+1$. With this, the normalisation constants are given by

$$\mathcal{N}^{-1} = \int_{-1}^{1} \Big(S_l^m(Q,z)\Big)^2 dz = \widetilde{\sum_n} \left(d_n^{l,m}(Q)\right)^2 \left(\frac{2}{2n+2m+1}\right)\left(\frac{(n+2m)!}{n!}\right) . \tag{3.20}$$

Drawing this all together, the normalised single-particle eigenstates and energies are given by

$$\Psi_l^m(\theta,\phi;Q) = \mathcal{N} e^{im\phi} (\sin\theta)^m \widetilde{\sum_n} d_n^{l,m}(Q) \frac{d^m P_n(\cos\theta)}{d(\cos\theta)^m}$$

$$m \in \mathbb{Z} \tag{3.21}$$

$$l = |m|, |m|+1, \ldots \tag{3.22}$$

For ease of plotting we define ψ_l^m, the ϕ independent part of the eigenstates, as follows

$$\Psi_l^m(\theta, \phi; Q) \equiv e^{im\phi}\psi_l^m(\theta; Q)\,. \tag{3.23}$$

Note that since the differential equation (3.11) is invariant under $m \to -m$, so too are the $\psi_l^m(\theta; Q)$. It is the full states $\Psi_l^m(\theta, \phi; Q)$ which carry the information about the sign of m in the phase factor $e^{im\phi}$, and differ in energy depending on this sign. By way of a sanity-check of our deductions based on the effective potential seen by the charged particle, we plot in Fig. 3.3 sample wavefunctions confirming the localization of the wavefunctions as a function of the polar distance from the north pole.

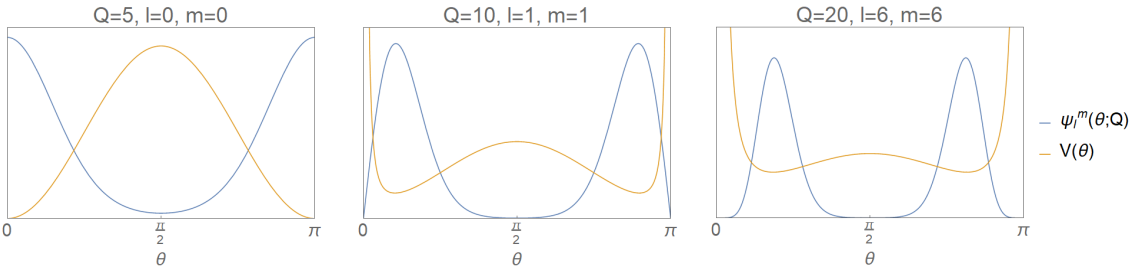

Figure 3.3: Wavefunction $\psi_l^m(\theta; Q)$ and potential $V(\theta)$ for various low energy states. As expected, the wavefunctions are localized at the minima of the effective potential.

3.2.2 The large Q limit

Now let's consider some relevant limits of these solutions. First, note that in the case of a free particle ($Q = 0$) our solutions reduce to the standard spherical harmonics. Analytic results can also be obtained in the limit $Q \ll 1$, and near the north pole ($\theta \to 0$) [30]. However, for the purposes of this thesis, we will focus on the large Q limit, $Q \gg 1$: this corresponds to taking the radius of the sphere R to be small, or dialling up the dipole field strength by increasing $|\boldsymbol{\mu}|$. We begin by considering the case $|m| \ll Q$, where we will see the emergence of a Landau level structure. We will then consider the spectrum for more general $|m|$, for which the Landau level picture will be shown to break down, with some new qualitative features emerging in its place.

In Fig. 3.4 we plot a number of representative states for varying values of Q, to illustrate the behaviour of the system as it approaches the large Q limit. For $Q = 1$ the particle states are relatively delocalised over the entire sphere. As the field strength is increased (Figures 3.4(b)-(d)), the states become progressively more localised around the poles with negligible amplitude in an expanding region surrounding the equator. This localisation is stronger for states with lower values of the combination of quantum numbers $l - m$. Given that in the large Q limit the $|m| \ll Q$ states confine to a region

of approximately uniform magnetic field, we anticipate the energy spectrum to exhibit an approximate Landau level structure there.

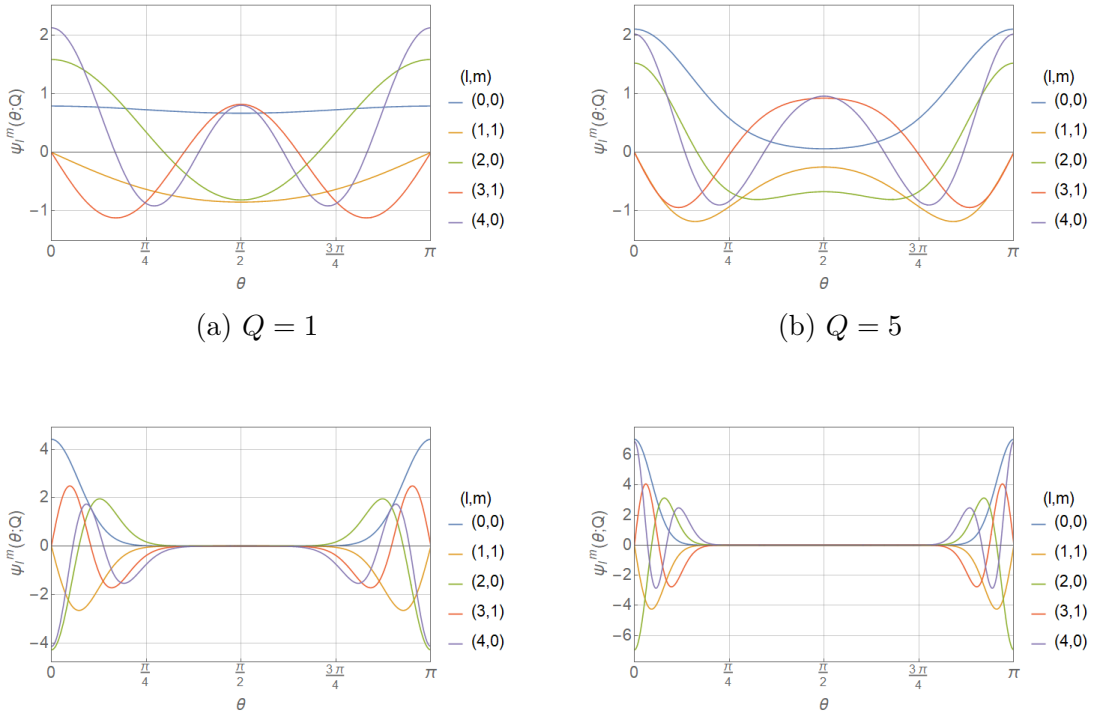

(a) $Q = 1$ (b) $Q = 5$

(c) $Q = 20$ (d) $Q = 50$

Figure 3.4: Eigenstates $\psi_l^m(\theta; Q)$ for various l and m. States become increasingly localised at the poles as the dipole strength Q increases.

To confirm this, note that in the limit $|m| \ll Q$ [47, 48], the spheroidal eigenvalues become

$$\lambda_l^m = 2\big[l + 1 - \mathrm{mod}(l - m, 2)\big]Q + \mathcal{O}(1)\,. \tag{3.24}$$

If m is integer valued, it follows that $\mathrm{mod}(l - m, 2) = \mathrm{mod}(l + m, 2)$. Substituting this into our expression for the energy spectrum (3.17), allows for the spectrum to be expressed as

$$\widetilde{E}_{Q,l,m} = Q^2 + 2\big[l + m + 1 - \mathrm{mod}(l + m, 2)\big]Q + \mathcal{O}(1)\,, \tag{3.25}$$

in the large Q limit. This result exhibits a number of noteworthy features:

- The spectrum only depends on the quantum numbers l and m in the combination $l + m$. The large Q limit spectrum therefore exhibits an (approximate) Landau level structure, where all states of the same $l+m$ are nearly degenerate.

- These (approximate) Landau levels are evenly spaced, with spacing $2Q$.
- Energies of states with pairwise adjacent $l+m$ values become degenerate in the large Q limit.
- The lowest Landau level is comprised of all states with $m \leq 0$ that satisfy $l = |m|$ or $l = |m| + 1$. We expect this Landau level structure to break down for states with $|m| \gtrsim Q$.

In Fig. 3.6, the spectrum is calculated numerically for states of various l and m and plotted as a function of $l - |m|$ for various values of the dipole strength Q. We indeed find the above features of the large Q limit to be supported by this numerical analysis, being already visible in the data at dipole strength $Q = 50$. Most notably, as Q increases, the spectrum converges to the Landau level structure given by the analytic result (3.25), which we plot as black dashed lines in Figures 3.6(g) and (h).

Recall that for a given $Q > 1$, states with smaller $l - |m|$ are more strongly localised around the poles than states with greater $l-|m|$. Intuitively, larger $l-|m|$ states thus experience a more varied magnetic field. We expect this field inhomogeneity to perturb their energies, breaking the Landau level degeneracy. This is observed in Figures 3.6(g) and (h), where we see the Landau level degeneracy breaking as $l-|m|$ increases.

In Fig. 3.6 see states with pairwise adjacent $l+m$ values clearly becoming degenerate in energy as Q is increased. In Fig 3.5 we plot the energy difference between such states, $\tilde{E}_{l,m} - \tilde{E}_{l-1,m}$, as a function of Q. The pairwise convergence is clearly visible, happening faster (for fixed m) for states of lower l.

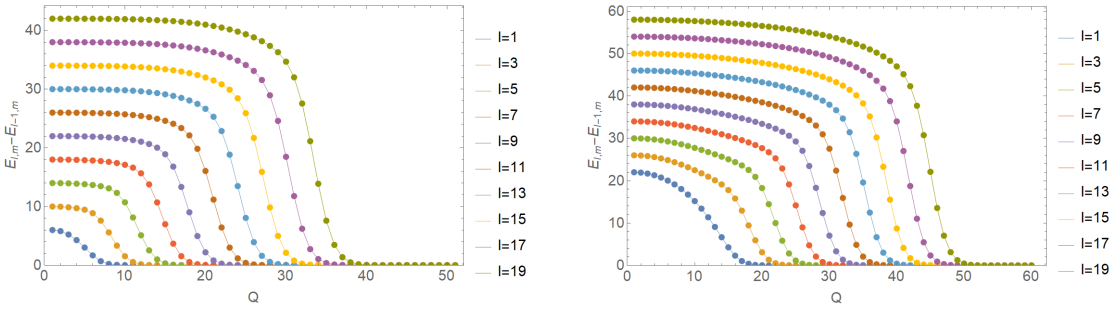

(a) $m = -2$ (b) $m = 10$

Figure 3.5: The energy difference $\tilde{E}_{l,m} - \tilde{E}_{l-1,m}$ as a function of Q, for fixed m and various l. States with adjacent values of $l+m$ become degenerate in the large Q limit.

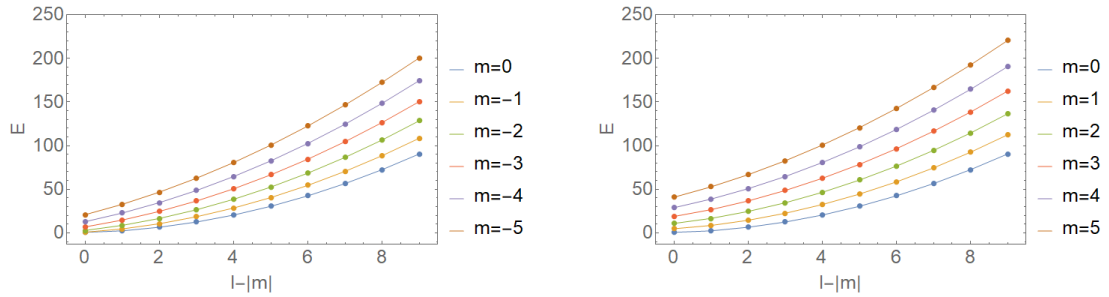

(a) $Q = 1, m \leq 0$

(b) $Q = 1, m \geq 0$

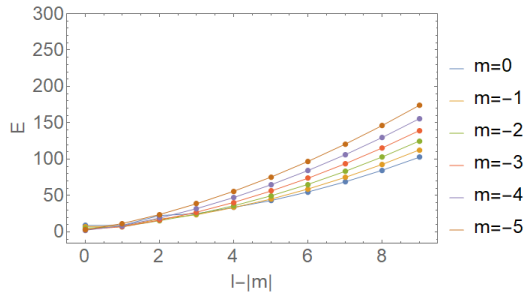

(c) $Q = 5, m \leq 0$

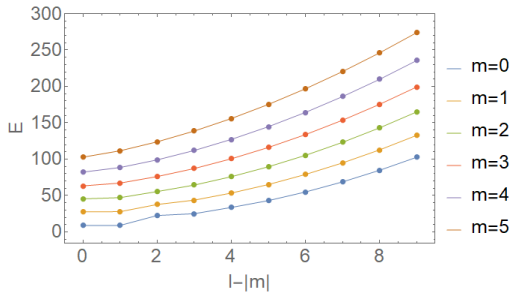

(d) $Q = 5, m \geq 0$

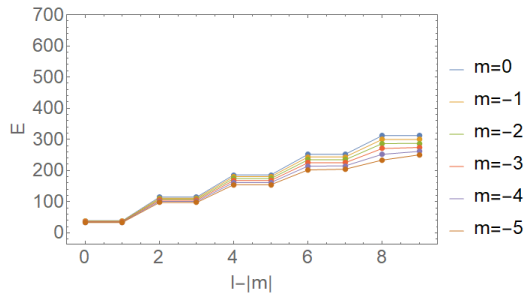

(e) $Q = 20, m \leq 0$

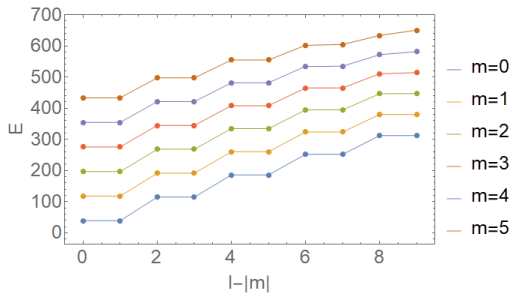

(f) $Q = 20, m \geq 0$

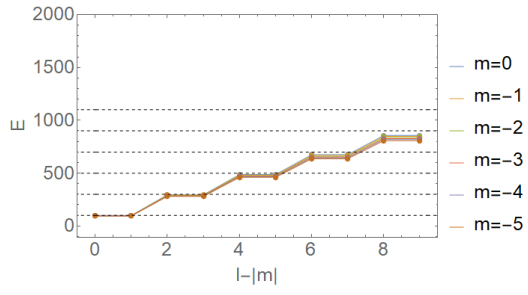

(g) $Q = 50, m \leq 0$

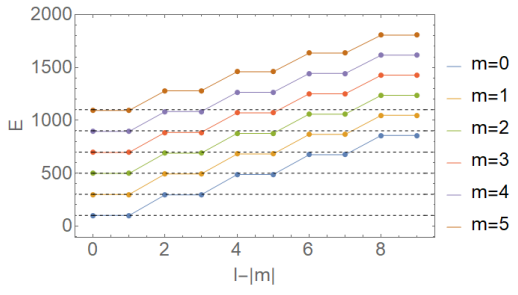

(h) $Q = 50, m \geq 0$

Figure 3.6: Energy spectra as a function of $l - |m|$, for non-positive (left) and non-negative (right) integer values of m. As the dipole strength Q is increased, the spectra converge to the Landau level structure (3.25), plotted as dashed black lines.

We can understand this pairwise degeneracy by considering the corresponding eigenstates. In Figures 3.7 and 3.8 we plot pairs of eigenstates with adjacent values of $l+m$ for various dipole strengths Q. As Q increases, the states, which are originally very different, become increasingly "symmetric" in the following sense: they become identical in the upper-half of the sphere ($0 \leq \theta \leq \pi/2$) and identical, up to a sign difference, in the lower-half of the sphere ($\pi/2 \leq \theta \leq \pi$). Since the probability density is given by $|\psi|^2$, at large Q the particles described by each of the two states become physically indistinguishable, and therefore degenerate in energy. Indeed, we see the corresponding energy difference between the states ΔE going to zero as Q increases and the states manifest the large Q symmetry described above.

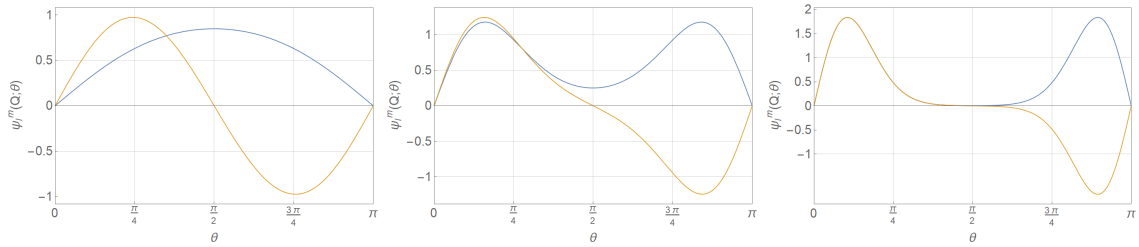

(a) $Q = 1$, $\Delta E = 3.7722$ (b) $Q = 5$, $\Delta E = 0.3656$ (c) $Q = 10$, $\Delta E = 0.0002$

Figure 3.7: Two eigenstates with adjacent values of $l+m$, for various Q. Here we plot the state with $(l,m) = (1,1)$ in blue and $(l,m) = (2,1)$ in yellow. ΔE is the energy difference between the two states, rounded to four decimal places.

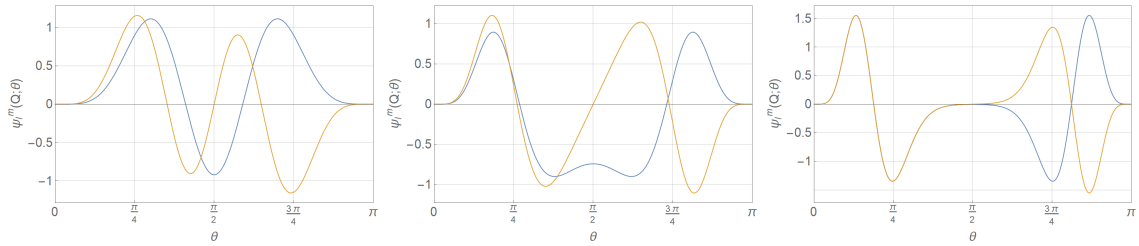

(a) $Q = 1$, $\Delta E = 15.9499$ (b) $Q = 12$, $\Delta E = 4.2375$ (c) $Q = 20$, $\Delta E = 0.0003$

Figure 3.8: As in Fig. 3.7, but we plot the state with $(l,m) = (7,5)$ in blue and $(l,m) = (8,5)$ in yellow.

Now, let's expand the above analysis to include general values of $|m|$. The $m > 0$ case is uninteresting; the structure visible in Fig. 3.6(h) continues in the obvious way for larger m[1]. In Fig. 3.9 we plot the spectrum for $m \leq 0$, fixed $l - |m|$ and various values

[1]While the Landau level structure breaks down for larger m, the relevant point is that for fixed

of Q. For $Q = 20$ and higher, we see the small $|m|$ Landau level structure discussed above. However, as $|m|$ increases, this degeneracy breaks completely. In particular, for $Q = 50$ (see Fig. 3.9(d)) the energies gradually decrease with increasing $|m|$, until they hit a turning point, after which they begin to rapidly increase. The pairwise degeneracy in $l - |m|$ breaks just before this turning point, signaled by the bifurcation of the two coincident energy level curves.

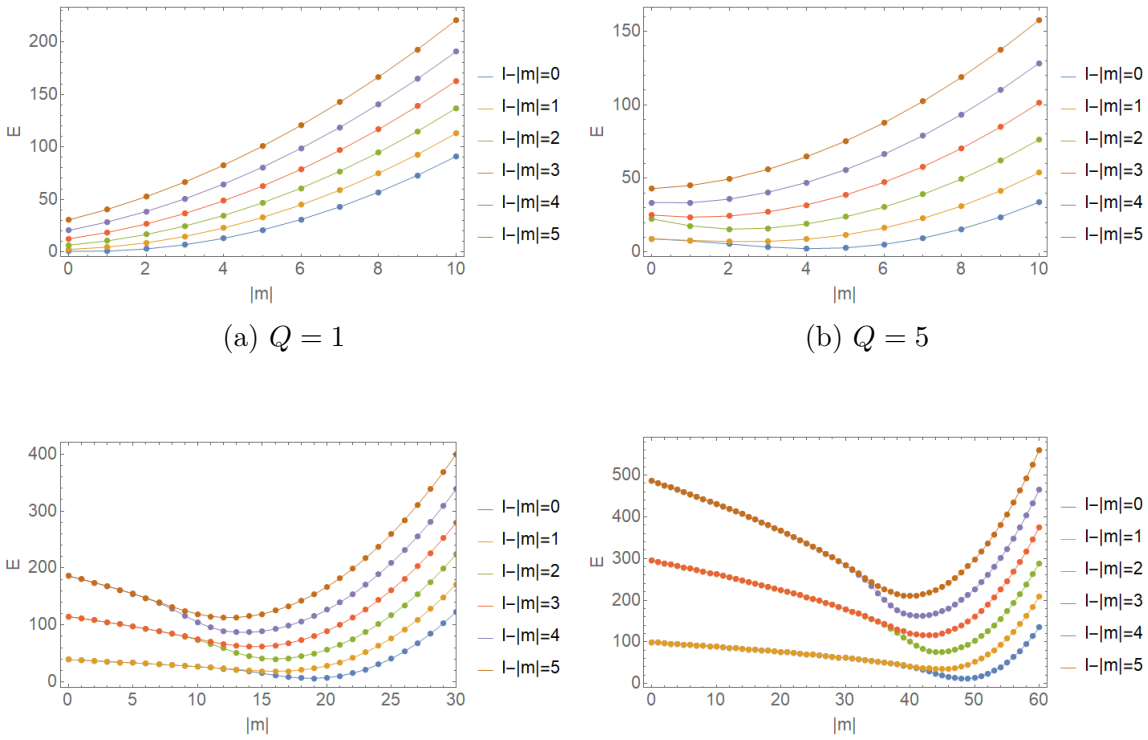

(a) $Q = 1$ (b) $Q = 5$

(c) $Q = 20$ (d) $Q = 50$

Figure 3.9: Energy spectra for $m \leq 0$ and various values of $l - |m|$. In (c) and (d), where the dipole strength Q is larger, we see the approximate Landau level structure for small $|m|$. This structure is broken as $|m|$ increases.

When $|m| > Q$, the spectrum exhibits a quadratic dependence on m. Looking at the Hamiltonian in (3.8) we see that for $|m|$ much larger than Q we can essentially neglect terms proportional to Q in the Hamiltonian, which just leaves the Hamiltonian for a free particle on the sphere. The energy spectrum of this free particle indeed exhibits a quadratic dependence on its quantum number[2]. In this sense, the dipole potential

$l - |m|$, states with larger m have larger energy. This means that the small m Landau level structure is left intact. As we will see, this is no longer the case for $m < 0$.

[2]In particular, the free spectrum is $E \sim l(l+1)$ and is independent of m.

gives a small Q (relative to $|m|$) correction to the free particle spectrum.

One new feature here is a clear ground state for any value of Q, whose energy always lies on the $l = |m|$ branch of the spectrum and satisfies $|m| \approx Q$. This ground state is always localised at the equator.

We can now describe the behaviour of the quantum states in the large Q limit for general quantum numbers, as illustrated in Fig. 3.10(a) for $l = |m|$. The $m = 0$ states are always localised at both poles. As $|m|$ increases, the regions of localisation move away from the poles and inwards towards the equator, while the energy decreases. This is in keeping with our observations at the level of the effective potential that larger $|m|$ means localisation further from the pole, where the (normal component of the) magnetic field is weaker, so we expect lower energy. Eventually at some $|m| = |m_{gs}|$ the two regions of localisation coalesce at the equator, and we obtain the lowest energy state. Increasing $|m|$ further results in a state more sharply localised at the equator, but this localisation comes at a steep energy cost. The high energy states of the system are then those for which the wavefunction is narrowly localised about the equator. States with larger l show the same qualitative behaviour, but with more nodes in the region of localisation, and a correspondingly higher energy (illustrated for $l = |m| + 2$ in Fig. 3.10(b)).

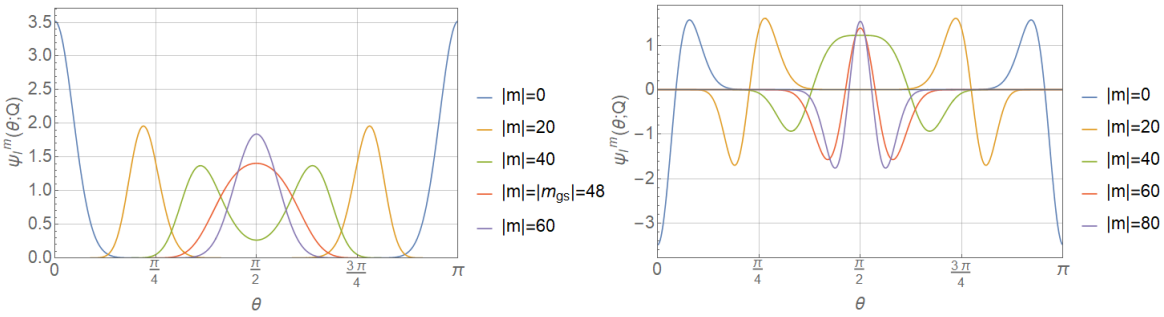

(a) $l = |m|$. (b) $l = |m| + 2$.

Figure 3.10: Eigenstates $\psi_l^m(\theta; Q)$ for fixed dipole strength $Q = 50$ and various $|m|$. As $|m|$ increases from zero, the region of localisation of the states moves from the poles inwards towards the equator.

3.3 Spin-1/2 Particle

Having treated at length the Schrödinger problem, we turn now to the main focus of this chapter, a spin-1/2 Dirac particle on the dipole sphere. As mentioned in Chap-

ter 1, this set up has direct relevance to experimentally testable configurations, for instance the properties of a C_{60} fullerine with a magnetic dipole located at its center, or for that matter in the presence of a uniform, perpendicular magnetic field. Indeed, much theoretical work has been dedicated to the study of such systems [40, 45, 39, 37]. The physics of a free Dirac particle on a sphere was studied in [44], while the problem was considered for some magnetic potentials amenable to supersymmetric methods in [43]. While the problem of Landau level quantization for a Dirac particle on the Haldane sphere has recently been studied in some depth [42], to the best of our knowledge, this is the first calculation carried out in the presence of the physically realisable dipole field.

We will use the framework outlined in Section 2.2.2. In order to study the dipole potential we again choose,

$$\boldsymbol{A} = A(\theta)\hat{\boldsymbol{\phi}} = \frac{|\boldsymbol{\mu}|}{R^2}\sin\theta\hat{\boldsymbol{\phi}}, \tag{3.26}$$

and obtain from (2.99) the eigenvalue equation for the Dirac operator

$$\begin{pmatrix} 0 & -\partial_\theta + \frac{i\partial_\phi}{\sin\theta} - \frac{1}{2}\cot\theta - Q\sin\theta \\ \partial_\theta + \frac{i\partial_\phi}{\sin\theta} + \frac{1}{2}\cot\theta - Q\sin\theta & 0 \end{pmatrix}\Psi = \mathcal{E}\Psi, \tag{3.27}$$

where $\mathcal{E} \equiv \frac{R}{\hbar v}E$ and we have again defined $Q \equiv \frac{e|\boldsymbol{\mu}|}{\hbar R}$. The separable ansatz $\Psi = e^{im\phi}\frac{1}{\sqrt{\sin\theta}}\Phi(\theta)$, puts the eigenvalue problem into the form

$$\begin{pmatrix} 0 & H_+ \\ H_- & 0 \end{pmatrix}\Phi = \mathcal{E}\Phi, \tag{3.28}$$

with

$$H_\pm \equiv \mp\partial_\theta - \frac{m}{\sin\theta} - Q\sin\theta. \tag{3.29}$$

Note that we can decouple the two equations in (3.28) by setting $\mathcal{E} = 0$. There then exist two independent zero-energy solutions given by

$$\Psi = \begin{pmatrix} \tan(\theta/2)^m e^{-Q\cos\theta} \\ 0 \end{pmatrix} e^{im\phi} \quad \text{and} \quad \Psi = \begin{pmatrix} 0 \\ \cot(\theta/2)^m e^{Q\cos\theta} \end{pmatrix} e^{im\phi}. \tag{3.30}$$

In fact, these are the *only* exact analytic solutions. They are only normalizable for $m = 0$.

To proceed to the case of nonzero $\mathcal{E}$, note that we are in the special case in which our potential satisfies the condition of reflection symmetry about the equator of the sphere $A(\theta) = A(\pi - \theta)$. It follows that the operators H_+ and H_- map to each other under the transformation $\theta \to \pi - \theta$. We may then define the two component spinor [38] satisfying

$$H^2 \begin{pmatrix} f_1 \\ f_2 \end{pmatrix} = E^2 \begin{pmatrix} f_1 \\ f_2 \end{pmatrix} . \tag{3.31}$$

It is readily verified that the associated spinor

$$\begin{pmatrix} \psi_1^{\pm} \\ \psi_2^{\pm} \end{pmatrix} \equiv H \begin{pmatrix} f_1 \\ f_2 \end{pmatrix} \pm E \begin{pmatrix} f_1 \\ f_2 \end{pmatrix} \tag{3.32}$$

is an eigenvector of H with eigenvalue $\pm E$. For the Hamiltonian in (3.28), the condition (3.31) yields the decoupled equations

$$H_+ H_- f_1 = \mathcal{E}^2 f_1 \,, \quad H_- H_+ f_2 = \mathcal{E}^2 f_2 \,, \tag{3.33}$$

for the spinor components f_1 and f_2. The fact that the operators H_+H_- and H_-H_+ map into each other by the transformation $\theta \to \pi - \theta$, means that the spinor components are related through

$$f_2(\theta) = f_1(\pi - \theta) \,. \tag{3.34}$$

The prescription (3.32) then yields the following solutions

$$\psi_1^{\pm}(\theta) = \left(-\partial_\theta - \frac{m}{\sin\theta} - Q \sin\theta \right) f_1(\pi - \theta) \pm \mathcal{E} f_1(\theta) \,, \tag{3.35}$$

$$\psi_2^{\pm}(\theta) = \left(\partial_\theta - \frac{m}{\sin\theta} - Q \sin\theta \right) f_1(\theta) \pm \mathcal{E} f_1(\pi - \theta) \,. \tag{3.36}$$

Note that we only need to calculate (3.35); we can obtain (3.36) by applying the transformation $\theta \to \pi - \theta$. Solving the full eigenvalue problem (3.28) therefore requires solving the second order decoupled equation (3.33),

$$-\frac{d^2 f_m}{d\theta^2} + \left((m \csc\theta + Q \sin\theta)^2 + Q\cos\theta - m \cot\theta \csc\theta \right) f_m = \mathcal{E}_m^2 f_m \,. \tag{3.37}$$

Spinor solutions to (3.27) are then given by

$$\Psi_m^{\pm}(\theta, \phi; Q) = \frac{1}{\sqrt{\sin\theta}} \begin{pmatrix} \psi_m^{\pm}(\theta; Q) \\ \psi_m^{\pm}(\pi - \theta; Q) \end{pmatrix} e^{im\phi} \,, \tag{3.38}$$

where

$$\psi_m^{\pm}(\theta; Q) = -\left(\frac{m}{\sin\theta} + Q \sin\theta + \partial_\theta \right) f_m(\pi - \theta) \pm \mathcal{E}_m f_m(\theta) \,, \tag{3.39}$$

f_m is a solution to (3.37) and $\pm\mathcal{E}_m$ is the energy eigenvalue of the spinor $\Psi_m^{\pm}$, now all labelled by the momentum quantum number m.

As a first check, consider the special case $m = 0$ which reduces (3.37) to

$$f_m''(\theta) = \left(Q^2 \sin^2\theta + Q\cos\theta - \mathcal{E}_m^2\right) f_m(\theta)\,, \tag{3.40}$$

denoting $' \equiv d/d\theta$. This simplifies even further in the limit $\mathcal{E}_m \gg Q$, to

$$f_m''(\theta) \approx -\mathcal{E}_m^2 f_m(\theta) \quad \Rightarrow \quad f_m(\theta) = A\sin(\mathcal{E}_m\theta) + B\cos(\mathcal{E}_m\theta)\,. \tag{3.41}$$

This in turn can be substituted into (3.39), yielding

$$\psi_m^{\pm}(\theta) \approx C\cos(\mathcal{E}_m\theta) + D\sin(\mathcal{E}_m\theta)\,, \tag{3.42}$$

where C and D are complex constants depending on $\mathcal{E}_m, A$ and B. In order for (3.42) to satisfy either Neumann or Dirichlet boundary conditions then requires that $\mathcal{E}_m \in \mathbb{Z}$. In other words, $m = 0$ states with energies $\mathcal{E}_m \gg Q$ are oscillatory functions with angular frequency equal to their (quantized) energy values $\mathcal{E}_m$.

Note that in both spin-1/2 systems considered in Chapter 2, the presence of an $SU(2)$ angular momentum algebra allowed for the construction of ladder operators corresponding to those of the spin-0 systems. The appearance of these ladder operators in the Hamiltonian then allowed for an analytic solution to be found, and moreover ensured that the spin-0 eigenstates appeared as the spinor components of these spin-1/2 solutions. For the spherical dipole system on the other hand, there is no $SU(2)$ algebra, and indeed we found no ladder operator structure to the spin-0 eigenstates. For this reason we do not expect the spin-0 eigenstates to appear as the components of the spin-1/2 eigenstates, and indeed we will find that they do not.

For values of $m \neq 0$, we are then forced to resort to numerical methods. In what follows, we will require both spinor components to be normalizable on the sphere as follows:

$$\left\langle \Psi_m^{\pm} \middle| \Psi_m^{\pm} \right\rangle = R^2 \int_{S^2} d\theta d\phi \sin\theta \left| \frac{1}{\sqrt{\sin\theta}} \psi_m^{\pm}(\theta) \right|^2 = 2\pi \int_0^{\pi} d\theta |\psi_m^{\pm}(\theta)|^2 = 1. \tag{3.43}$$

Numerically enforcing this condition quantizes the allowed energy eigenvalues $\mathcal{E}_m$. This then introduces the dependence of our solutions on a new quantum number n, which labels the successive allowed energies for a given value of m.

3.3.1 Half-odd m

We'll start with the case where the momentum quantum number $m \in \mathbb{Z} + \frac{1}{2}$ and show that in the large Q limit when $|m| \ll Q$, we again see the emergence of an approximate Landau level structure just like in the spin-0 system. For more general $|m|$, this structure again breaks, revealing some other interesting qualitative spectral features.

The eigenstates plotted in Fig. 3.11 exhibit the same qualitative behaviour as in the spin-0 case: as Q is increased they become progressively more localised around the poles with negligible amplitude in an expanding region surrounding the equator. Our earlier argument for the existence of Landau levels still holds and will be verified below.

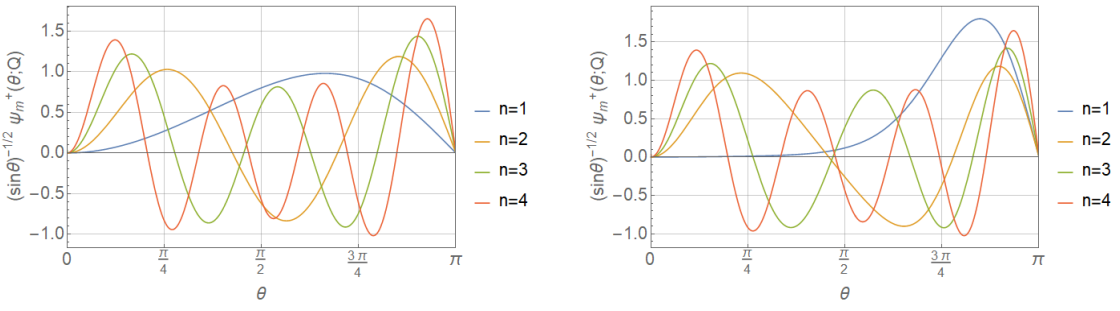

(a) $Q = 1$ (b) $Q = 5$

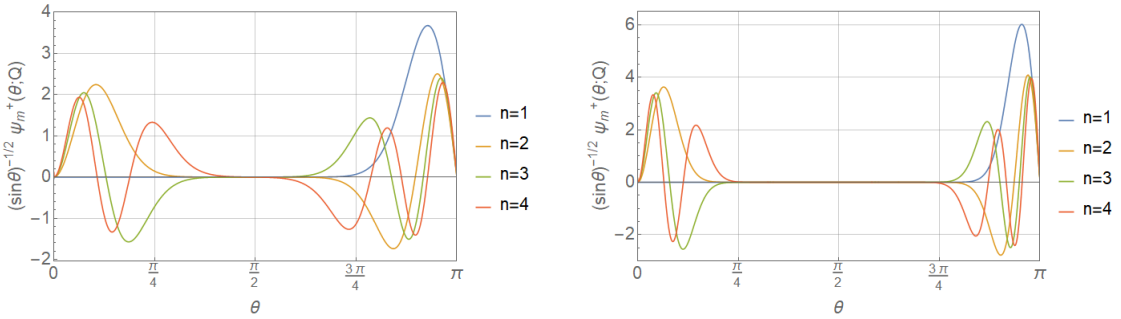

(c) $Q = 20$ (d) $Q = 50$

Figure 3.11: An illustrative set of positive energy wavefunctions $\frac{1}{\sqrt{\sin\theta}}\psi_m^+(\theta;Q)$ for $m = 3/2$ and increasing magnetic field strength Q. The quantum number n labels successive allowed energies for a given value of m. In each case, we plot the first spinor component, recalling that the second component is obtained by reflecting the wavefunction about the equator.

In Figures 3.14 and 3.15 we compute the positive and negative energy spectra for various values of m and Q. For $m > 0$, we note that as the dipole strength is increased to $Q = 50$, a series of systematic (approximate) degeneracies become visible in the spectrum (see Figures 3.14(h) and 3.15(h)): states which share an $m+n$ value have degenerate energies. This is easy to see for the first few "levels" marked in dashed black lines in these Figures. While our numerical methods become unstable for $Q \gg 50$, we conjecture that in the $Q \to \infty$ limit, this degeneracy becomes exact for all levels.

For $m < 0$, a different degeneracy emerges in the large Q limit. In this case, all states with the same n value become degenerate, regardless of m (see Figures 3.14(g) and 3.15(g)). This is again clear for the lower levels, after which the degeneracy breaks down at larger n ($n \gtrsim 5$). Our analysis again suggests that this degeneracy becomes exact for all levels in the $Q \to \infty$ limit. Finally, we note that the $m < 0$ and $m > 0$ levels coincide.

Thus we see the emergence of a Landau level structure in the large Q limit, consistent with our expectation from the spin-0 study in Section 3.2. Note that for the positive (negative) spectrum, the spacing between the levels increases with increasing (decreasing) energy. We also note that for small n, some level crossing occurs among the various $m \leq 0$ states as Q is increased. We show this for $n = 1$ in Fig. 3.12.

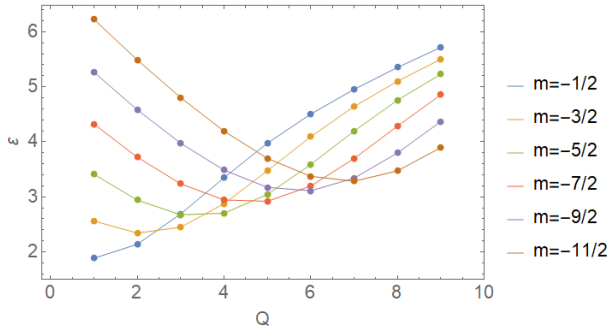

Figure 3.12: Level crossing of $n = 1$ states as Q is increased.

We now expand the above analysis to more general values of $|m|$. As in the spin-0 system, the general $m > 0$ case does not exhibit any interesting features. In Fig. 3.13 we plot the spectrum for $m < 0$ for various values of Q. The qualitative behaviour of the spectra is entirely analogous to that of the spin-0 case, except for two new features.

Firstly, recall that in the large Q limit of the spin-0 case, branches of the spectrum with adjacent $l - |m|$ values were degenerate for small $|m|$, until splitting occurs be-

yond some critical value of $|m|$ (see Fig. 3.9(c) and (d)). Plotting the *absolute value* of all the energies in the spin-1/2 spectra would produce a similar result. However, each of the pair of degenerate branches of the spin-1/2 spectrum takes a different sign, effectively lifting the pairwise degeneracy present in the spin-0 system. This is because one of either ψ_m^+ or ψ_m^- in (3.39) always vanishes and is thus not a true solution. The alternating manner in which this occurs gives rise to the spectrum in Fig. 3.9, which is not symmetric about $\mathcal{E} = 0$ as one might expect.

Secondly, the large Q limit now exhibits an (approximately) zero energy, highly degenerate "lowest Landau level," visible in Fig. 3.13(d). For sufficiently large values of the momentum quantum number (in this case, $|m| \approx 45$) the degeneracy breaks as the energies move away from zero and close the gap to the negative energy band below. However, the system does have a large number of (approximately) degenerate states with energies very close to zero. This "lowest Landau level" persists well past the value of $|m|$ at which the Landau level structure of the rest of the spectrum breaks down.

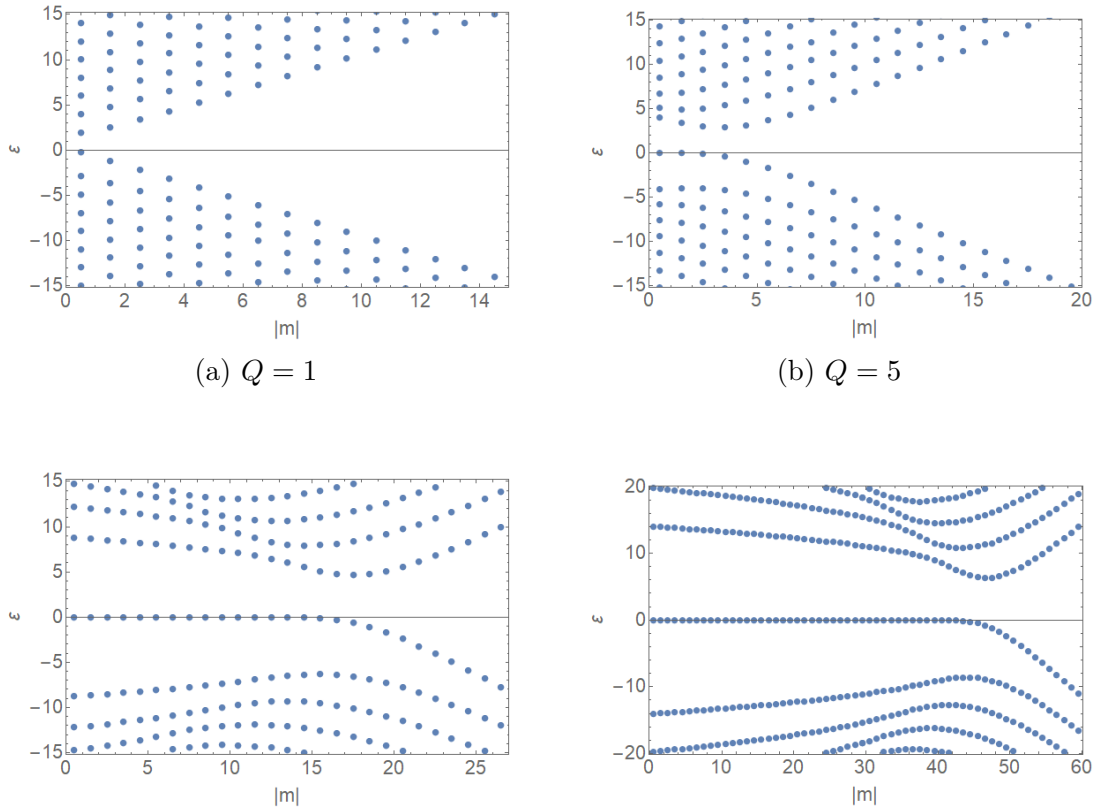

(a) $Q = 1$ (b) $Q = 5$

(c) $Q = 20$ (d) $Q = 50$

Figure 3.13: Energy spectra for $m < 0$, plotted for various dipole strengths Q. As Q is increased, a Landau level structure emerges at small m, including a zero energy "lowest Landau level".

3.3.2 Integer m

Finally, let's consider the case where $m \in \mathbb{Z}$, and compute the positive (Fig. 3.16) and negative (Fig. 3.17) spectra for various values of the momentum and dipole strength. Note that for fixed Q the spectrum for $m = 0$ takes on twice as many values within the same energy interval as the spectra for $m < 0$ and $m > 0$. The spectra for both $m < 0$ and $m > 0$ behave qualitatively as before, and our prior observations still hold. However, they relate to the $m = 0$ spectra in a qualitatively new way. In the large Q limit:

- The positive spectra are computed numerically and plotted in Fig. 3.16. Notice that the $m < 0$ energies merge into each other and into the $m = 0$ energies with even n. The $m > 0$ energies on the other hand are coincident with each other

and with the $m = 0$ energies with odd n. This is why we have chosen to plot the $m \neq 0$ spectra only for every second[3] n value.

- Similarly, the negative spectra, plotted in Fig. 3.17, show that $m < 0$ states merge into each other and with $m = 0$ states corresponding to odd n while positive momentum states are coincident with each other and with $m = 0$ states corresponding to even n.

The new feature of the overall spectrum in the large Q limit as compared to the half-odd m case is that the $m > 0$ and $m < 0$ levels no longer coincide, they now alternate, resulting in twice as many Landau levels as before[4]. Finally, we also note that at small n, the spectrum again exhibits level crossing among the various $m \leq 0$ states as Q is increased.

[3]Note that this means that the quantum number n which labels successive allowed energies only applies to the $m = 0$ energies here.

[4]When $Q \to \infty$ we expect there to be infinitely many Landau levels, so technically the statement should be that the *density* of levels doubles.

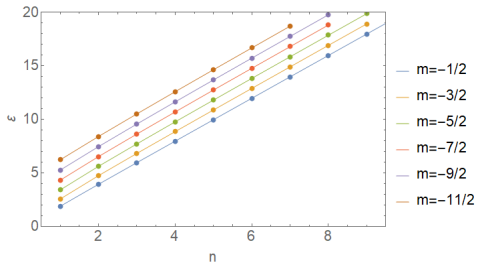

(a) $Q = 1,\ m < 0$

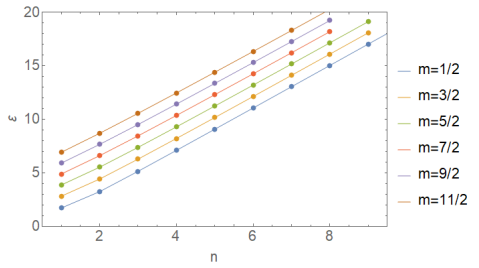

(b) $Q = 1,\ m > 0$

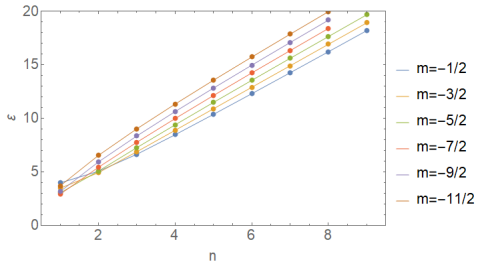

(c) $Q = 5,\ m < 0$

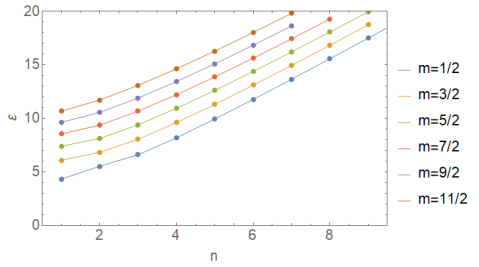

(d) $Q = 5,\ m > 0$

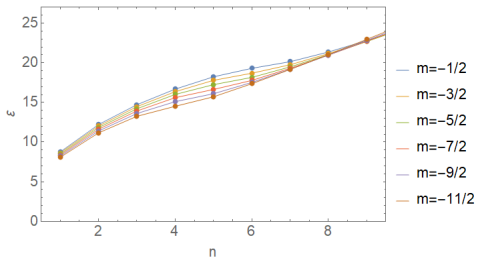

(e) $Q = 20,\ m < 0$

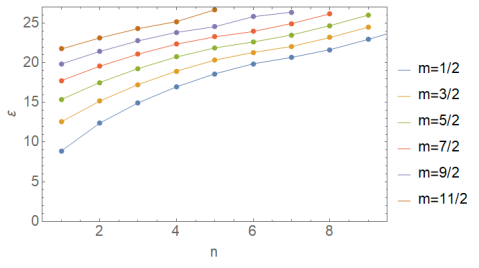

(f) $Q = 20,\ m > 0$

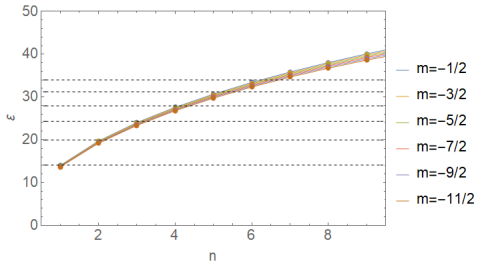

(g) $Q = 50,\ m < 0$

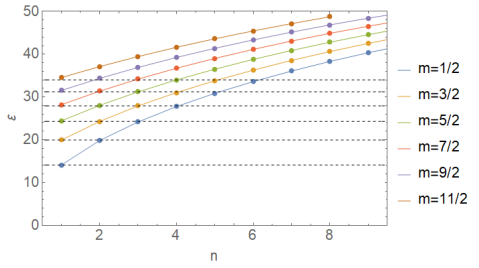

(h) $Q = 50,\ m > 0$

Figure 3.14: Positive energy spectra for m half-odd. For negative m (left), states with equal values of n become degenerate as Q is increased. For positive m (right), states with equal values of $m+n$ become degenerate as Q is increased. The resulting Landau levels are plotted as black dashed lines in (g) and (h).

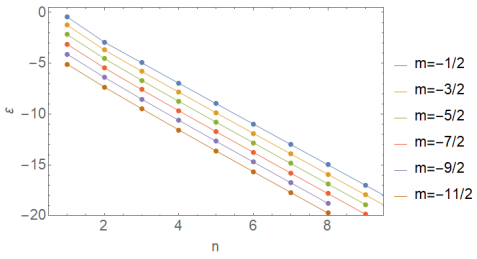

(a) $Q = 1,\ m < 0$

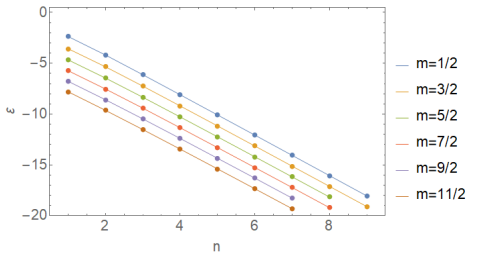

(b) $Q = 1,\ m > 0$

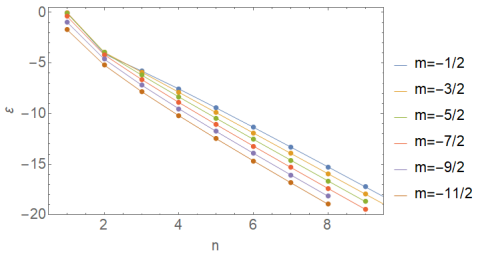

(c) $Q = 5,\ m < 0$

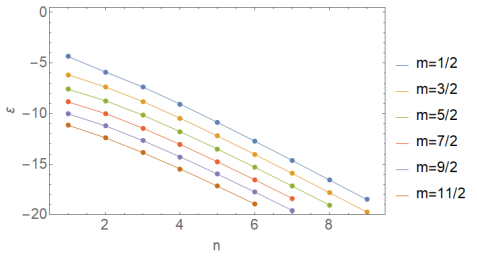

(d) $Q = 5,\ m > 0$

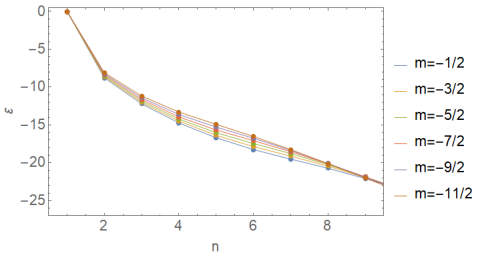

(e) $Q = 20,\ m < 0$

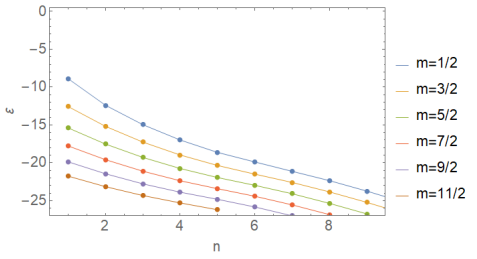

(f) $Q = 20,\ m > 0$

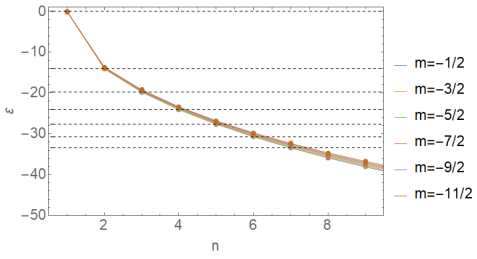

(g) $Q = 50,\ m < 0$

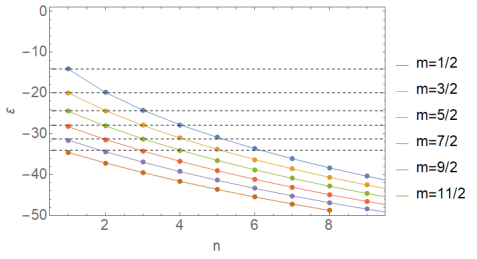

(h) $Q = 50,\ m > 0$

Figure 3.15: Negative energy spectra for m half-odd. For negative m (left), states with equal values of n become degenerate as Q is increased. For positive m (right), states with equal values of $m+n$ become degenerate as Q is increased. The resulting Landau levels are plotted as black dashed lines in (g) and (h).

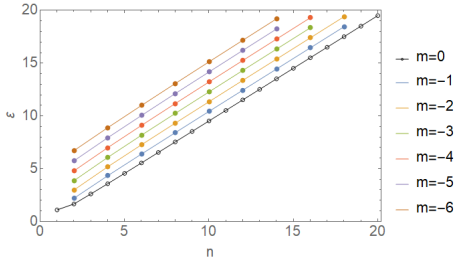

(a) $Q = 1,\ m \leq 0$

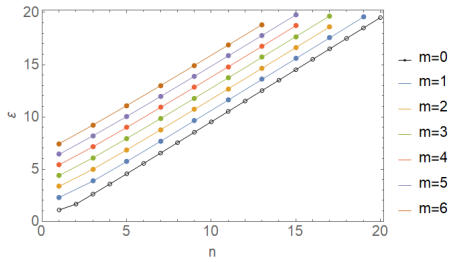

(b) $Q = 1,\ m \geq 0$

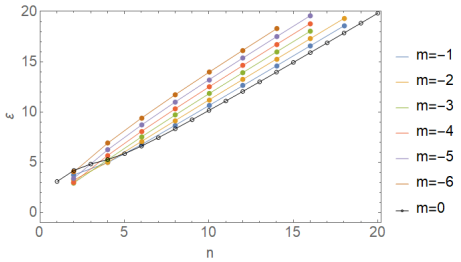

(c) $Q = 5,\ m \leq 0$

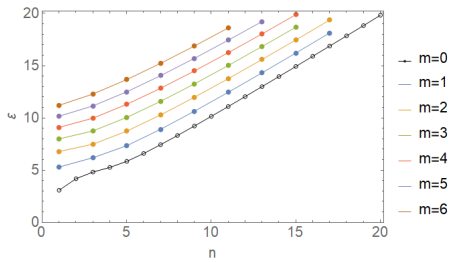

(d) $Q = 5,\ m \geq 0$

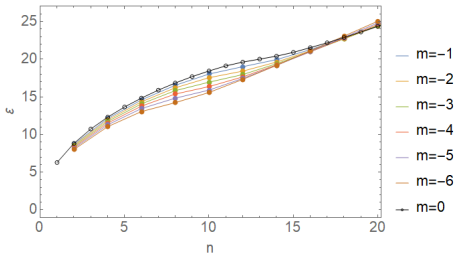

(e) $Q = 20,\ m \leq 0$

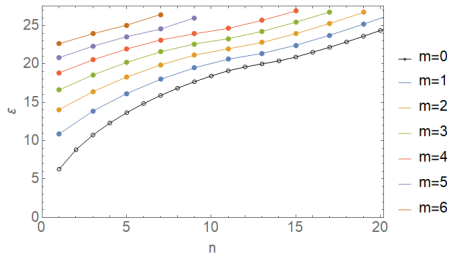

(f) $Q = 20,\ m \geq 0$

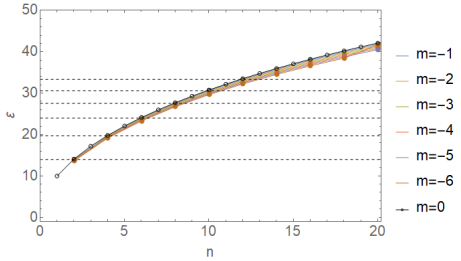

(g) $Q = 50,\ m \leq 0$

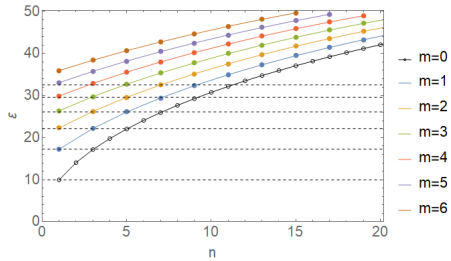

(h) $Q = 50,\ m \geq 0$

Figure 3.16: Positive energy spectra for integer m. For $m \leq 0$ (left), states with equal values of n become degenerate in energy as Q is increased. For $m \geq 0$ (right), states with equal values of $m+n$ become degenerate in energy as Q is increased. The resulting Landau levels are plotted as black dashed lines in (g) and (h).

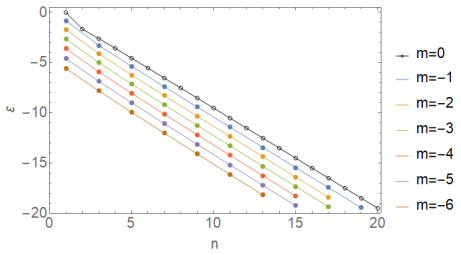

(a) $Q = 1,\ m \leq 0$

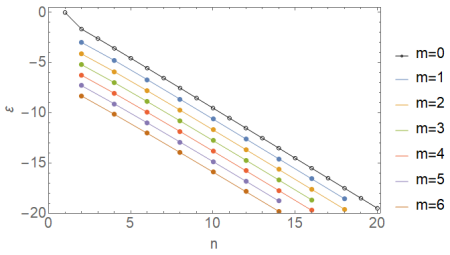

(b) $Q = 1,\ m \geq 0$

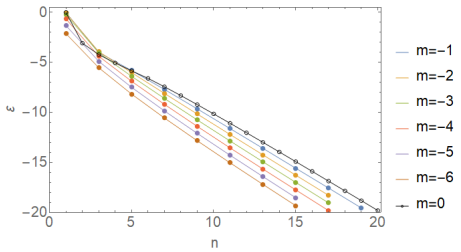

(c) $Q = 5,\ m \leq 0$

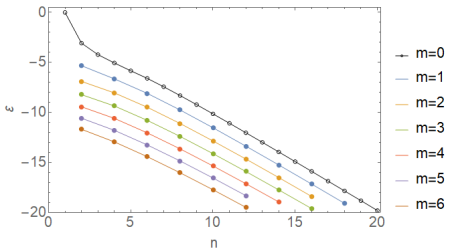

(d) $Q = 5,\ m \geq 0$

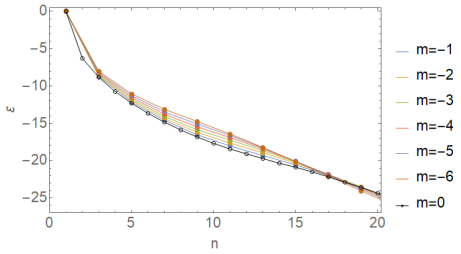

(e) $Q = 20,\ m \leq 0$

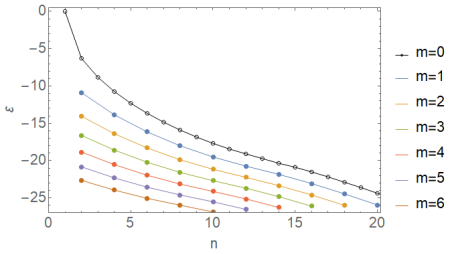

(f) $Q = 20,\ m \geq 0$

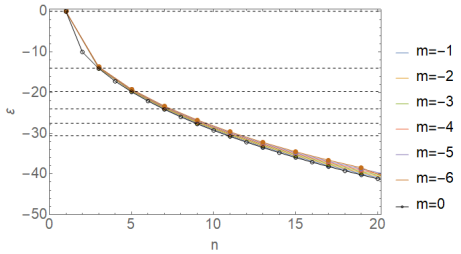

(g) $Q = 50,\ m \leq 0$

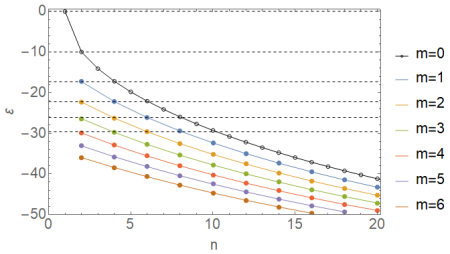

(h) $Q = 50,\ m \geq 0$

Figure 3.17: Negative energy spectra for integer m. For $m \leq 0$ (left), states with equal values of n become degenerate in energy as Q is increased. For $m \geq 0$ (right), states with equal values of $m+n$ become degenerate in energy as Q is increased. The resulting Landau levels are plotted as black dashed lines in (g) and (h).

Chapter 4

Conclusion to Part I

In this part of the thesis, we have reviewed the solutions to the eigenvalue problems of spin-0 and spin-1/2 particles both on planar and spherical surfaces, in the presence of perpendicular and constant magnetic fields. This was accomplished using primarily algebraic methods utilising various sets of raising and lowering operators.

We then generalised these results to the case of the *spherical dipole system*. In the spin-0 case we found the Hilbert to be made up of the angular oblate spheroidal wavefunctions, labelled by integer quantum numbers m and l. Unlike the Haldane sphere, Gauss' law renders the problem topologically trivial. Nevertheless, it exhibits a rich spectral structure, which is of particular interest in the strong-field limit $Q \gg 1$, in which it may be summarised as follows:

- In the $|m| \ll Q$ regime, energy levels display an approximate, evenly spaced Landau level structure and states are localised about the poles. Additionally, states ψ_l^m with pairwise adjacent $l - |m|$ values have equal probability density $|\psi_l^m|^2$ and degenerate energy.
- In the $|m| \gg Q$ regime, energy levels display a quadratic dependence on $|m|$ and states are localised sharply about the equator.
- In the intermediate regime, the localisation of the wavefunctions drifts from the poles to the equator as $|m|$ increases. The spectrum has interesting structure only for $m < 0$, where we find the system's lowest energy states, which satisfy $l = |m| \approx Q$, are localised weakly about the equator.

We then computed the corresponding Hilbert space for the spin-1/2 case, which may be summarised as follows:

- The two spinor component wavefunctions are related by reflection about the equator, and exhibit the same qualitative behaviour in the large Q limit as the spin-0 wavefunctions.

- The same is true for the spectrum in the large Q limit, with the exceptions that the Landau levels are no longer evenly spaced; the pairwise degeneracy in $l - |m|$ is now broken (with each degenerate branch taking opposite sign); and, we now see the existence of an approximately zero-energy lowest Landau level which persists past the $|m| \ll Q$ regime into the regime $|m| < Q$.

We now contextualize these results and speculate on some applications to condensed matter and gravitational physics.

Graphene

Modulo finite-size effects, graphene - a quasi-planar sheet of carbon atoms arranged in a hexagonal lattice and that exhibits some of the most remarkable known electronic and tensile properties - shares its electronic spectrum with the Dirac equation in (2+1)-dimensions. In particular, single electron dynamics in a graphene sample is captured by massless QED_2 on $\mathbb{R}^{2,1}$. This remains true for local (geometric) deformations of the graphene sheet. However, to form a spherical ball of graphene - a fullerine molecule like C_{60} - Euler's theorem requires the addition of pentagonal defects into the hexagonal graphene lattice; 12 pentagons in the case of C_{60}. The effect of these defects can be encoded in the continuum field theory through the introduction of a fictitious magnetic monopole with fractional magnetic charge [37]. The spectrum is obtained by solving the eigenvalue problem, $i\gamma^\mu \left(\partial_\mu + \Omega_\mu - iW_\mu\right)\Psi_n = E_n\Psi_n$, with spin connection $\Omega_\mu = \frac{1}{8}\omega_\mu^{\alpha\beta}[\gamma_\alpha, \gamma_\beta]$ and $(W_\theta, W_\phi) = (0, g\cos\theta)$ is the gauge connection for a Dirac monopole. Inserting the fullerene into a constant external magnetic field has the effect of modifying the Dirac equation to $i\gamma^\mu \left(\partial_\mu + \Omega_\mu - iW_\mu - iA_\mu\right)\Psi_n = E_n\Psi_n$, where, if the sphere is taken to have radius R, the only nonzero component of the gauge field is $A_\phi = \frac{1}{2}B_0 R\sin\theta$. While the physics of this system is different from the dipole case - a spherical fullerene in a constant external field versus a fullerene enclosing a current loop in the latter - mathematically, for a fixed size sphere, they are identical. In this case also an exact solution can be found in terms of oblate spheroidal functions [41].

The effect of this external constant magnetic field is two-fold; in the large Q limit ($Q_{\text{const.}} \gg 1$) the spectrum is dominated by a Landau regime, while in the weak field limit ($Q_{\text{const.}} \ll 1$) we observe splitting as the degeneracy of the Landau level structure is broken while. At the crossover point between these two regimes, the spectrum exhibits a series of overlapping bands. Again, this is consistent with our

findings in the dipole case. This is unsurprising since, for a fixed size of the sphere, both gauge potentials are functionally the same. In the constant-field case, since $Q_{\text{const.}} = eB_0^2R^2/2$, the large Q regime can be accessed by either turning up the strength of the magnetic field or increasing the size of the sphere (since the particle 'sees' more of the magnetic field). In our dipole case however, since $Q_{\text{dipole}} = e|\boldsymbol{\mu}|/R$, increasing the size of the sphere *decreases* the effective dipole strength. Consequently, increasing the cluster size from[1] C_{60} to C_{240} in a fixed external B_0 increases Q_{const} and drives the system toward more defined Landau quantization, even as the continuum approximation improves. On the other hand, increasing the size of a spherical fullerene housing a current loop should have the opposite effect; the accompanied decrease in Q_{dipole} leads to enhanced splitting in the spectrum as the approximate Landau level degeneracy is broken (see, for example Fig. 3.6). The 0.7nm diameter of the C_{60} fullerene sets a natural scale for this problem and, given the recent leaps in nano-technology, it seems to us that fabrication of such a system of a fullerine enclosing a current loop is almost within reach. It would offer an exciting possibility to test some of these ideas.

Black Holes

More speculatively, we now remark on the potential application of our results to gravitational physics. A resurgence of interest in wormholes in the context of two-dimensional gravity has led to some interesting developments in 4-dimensional magnetically charged black holes (4.1), and their relation to traversable wormholes in four dimensions [35, 36]. It is anticipated that the spectral problem for the Schrödinger (or Dirac) operator for a charged particle confined to a sphere punctured by a dipole magnetic field has some bearing on the physics of massless charged fermions moving in a magnetically charged black hole background [35, 36],

$$\begin{aligned} ds^2 &= -\left(1 - \frac{2MG_N}{r} + \frac{r_e}{r^2}\right) dt^2 + \left(1 - \frac{2MG_N}{r} + \frac{r_e}{r^2}\right)^{-1} dr^2 + r^2 d\Omega_{S^2}^2 \\ A &= \frac{q}{2}\cos\theta\, d\phi\,, \quad r_e^2 = \frac{\pi q^2 G_N}{g^2}\,. \end{aligned} \tag{4.1}$$

Key to stabilising such wormholes is the Landau degeneracy that accompanies the dynamics of massless charged fermions in the presence of a magnetic field on the sphere. The energy in each level receives contributions from orbital motion as well as

[1] For topological reasons, this is also accompanied by an increase in the strength of the monopole field. However, this is small relative to the parametrically dialled external field.

a magnetic dipole contribution which, for a fermion in the lowest Landau level, exactly cancel as a consequence of the cancellation of the two-dimensional gravitational anomaly. The result is a large set of states - corresponding to the large q degeneracy of the lowest Landau level - with zero energy on the sphere giving rise to an equally large set of massless two-dimensional chiral fermions in the (r, t)-directions. It is precisely the Casimir energy of these compact fermions that stabilizes the wormhole.

Specifically, on the background (4.1) and in global coordinates, the representation $\gamma^1 = i\sigma_x \otimes \mathbb{I}, \gamma^2 = \sigma_y \otimes \mathbb{I}, \gamma^3 = \sigma_z \otimes \sigma_x$ and $\gamma^4 = \sigma_z \otimes \sigma_y$ for the γ-matrices, together with the ansatz $\chi_{\alpha\beta} = \psi_\alpha \otimes \eta_\beta$ for the 4-dimensional spinor in terms of the two-dimensional spinors η on the S^2 and ψ in the remaining two directions, factorizes the 4-dimensional Dirac equation into a free massless Dirac equation for ψ and a Dirac equation on the 2-sphere with magnetic field $(\not{\nabla} - i\not{A})\eta = 0$. The relevant geometry for the two mouths of the wormhole are a *pair* of oppositely charged magnetic black holes which produces a *dipole* vector potential of the kind that is the subject of this article. The authors of [36] show that at distances comparable to the distance between the sources, the fermion wavefunctions localize on the field lines. This is sufficient for their purposes. However, when the distances is much larger than between the magnetic sources, our analysis above should be more appropriate. In particular, as we have shown, this would have implications for the lifting of the Landau degeneracy as well as the localization of the fermion wavefunctions, both of which, in turn, have consequences for the wormhole construction.

Part II

Quantum Chaos and Disordered Systems

Chapter 5

Introduction to Part II

The second part of this thesis will be concerned with the physics of quantum chaos and disordered systems. Chaos was originally conceived of as a feature of classical dynamical systems, namely those whose time evolution in phase space exhibits sensitive dependence on their initial conditions, diverging exponentially in time for any initial displacement. Extending this concept to the quantum realm, where the uncertainty principle ensures that there is no well-defined notion of a phase-space trajectory, poses a deep and difficult challenge. In this case, chaos must be conceptualised and studied from a very different perspective. As we shall see, the key turns out to lie in spectral statistics, in particular the spectral statistics of random matrices[1].

The field of random matrix theory (RMT) has seen a long list of successful and fascinating applications in physics and beyond, including describing the statistical distributions of zeros of the Riemann Zeta function [64], the spacing between parked cars [65], bus system schedules [66], and the energy spectra of atomic nuclei [69]. The earliest and admittedly most influential of these applications was the latter, first studied by Wigner in 1951. The ideas of universality developed by him, and subsequently Dyson, in this context have served as the conceptual basis for the application of RMT to physical systems ever since. One such application, most relevant for us, was the definition of quantum chaos in the 1980s in terms of the famous Bohigas-Giannoni-Schmit conjecture [111], which elegantly states that quantum chaotic systems are precisely those whose spectral correlations are described by RMT.

The diagnostics of chaos developed in the context of RMT have a long history of successful application to quantum mechanical systems described by Schrodinger's

[1] An alternative conception of quantum chaos in terms of out-of-time-ordered correlators (OTOCs), has more recently come to prominence, although its precise relation to the definition in terms of spectral statistics is a subject of ongoing research - see Section 7.5.

equation. More recently, they have found application in the study of quantum systems formulated within the more sophisticated framework of quantum field theory. One such diagnostic, which has come to increasing prominence in this new context [91], is the spectral form factor (SFF), which probes pairwise spectral correlations at various energy separations. Though it may be (and most commonly is) calculated numerically using diagonalisation techniques, this approach does not yield insight into the physical mechanisms underlying those of its features which indicate the presence (or absence) of chaos. The SFF does however have an alternative, field theoretic definition in terms of the path integral[2]. For systems which are sufficiently amenable to analytic methods, the rich gamut of techniques and concepts from quantum field theory may then be applied and explored.

We consider one such system, which has played a central role in the recent resurgence of interest in quantum chaos: the Sachde-Ye-Kitaev (SYK) model. The model describes the physics of fermions in (0+1)-dimensions which interact in a random, or disordered, way. The model sits at the fascinating interface between condensed matter and gravitational/holographic physics, due to the fact that it describes both non-Fermi liquids [140] and low-dimensional black holes [137]. The presence of disorder in the model not only allows for the convenient application of concepts and techniques from RMT [91], but is crucial in giving rise to a number of remarkable properties. As we shall see, beyond just being amenable to a variety of analytic techniques, the model is in fact exactly solvable in a particular (strong coupling) limit. In this limit, subject to some assumptions, analytic progress may be made calculating the SFF, shedding light on various questions in holographic duality [91, 184] and chaotic-integrable transitions in quantum systems [179, 169].

The quadratic version of the model, the SYK_2 model, despite its relative simplicity, presents an analytically tractable context in which to explore the physical mechanisms underlying the characteristic features of the SFF, in a way which requires fewer simplifying assumptions and is valid for all values of the coupling strength. In Part II of this thesis, after discussing all of the requisite ideas, models and techniques mentioned above, we present a detailed study of the SFF for a novel variant of the SYK_2 model, the gauged complex SYK_2 model.

[2]This is notwithstanding the fact that it has no clear interpretation as a physical observable.

Chapter 6

Random Matrix Theory

This chapter will provide a summary of the history and key results of RMT and their relation to the study of quantum chaos. This will serve as necessary background to our exposition of the spectral form factor (SFF) and its characteristic features in Chapter 7.

6.1 Introduction to RMT

We begin by considering Wigner's seminal 1951 study [69] of nuclear physics[1]. At the time of this research, experimental nuclear physicists had collected an abundance of data on the excitation spectra of different nuclei, which required theoretical explanation. While the data for some low energy states could be theoretically explained[2], a description of the individual, high energy interacting states was rendered impossible by the complicated nature of the many body nucleus [62]. But it was out of this complicated nature that, in the spirit of thermodynamics, Wigner discerned the possibility of a *statistical* description: concerned not with the details of any particular realisation, but with the *average properties* of the states. His bold proposal was to consider ensembles of Hamiltonians which share only the basic symmetries of the physical system under consideration, and to compute its spectral statistics via averages over this ensemble[3]. The remarkable success of this approach is illustrated in Fig. 6.1.

[1] RMT was first introduced in 1928 [68] in the context of mathematical statistics, but attracted little interest until Wigner's 1951 paper.

[2] In terms of a model where nucleons move freely in a potential well.

[3] Note that such an approach differs fundamentally from the usual way in which statistical concepts are applied in physics: while in standard statistical mechanics one deals with ensembles of physical systems governed by the *same* Hamiltonian but differing in initial conditions, Wigner's approach required considering ensembles of *different* Hamiltonians (with some common symmetry property).

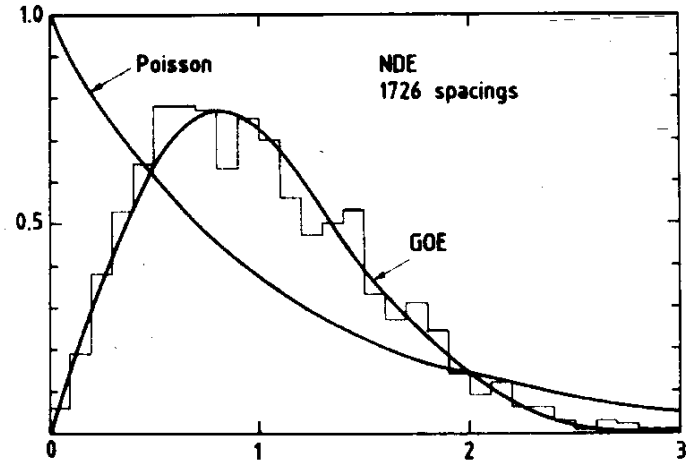

Figure 6.1: Nearest-neighbour spacing distribution of nuclear energy levels, versus the RMT prediction (labelled GOE). The result for a Poisson distribution is also shown. Image taken from [112].

The mathematical foundations of RMT were later established in a series of 1962 papers by Dyson [72, 74], who motivated as well as expanded on Wigner's philosophy:

> *"What is here required is a new kind of statistical mechanics, in which we renounce exact knowledge not of the state of the system but of the system itself. We picture a complicated nucleus as a "black box" in which a large number of particles are interacting according to unknown laws. The problem then is to define in a mathematically precise way an ensemble of systems in which all possible laws of interaction are equally possible." [72]*

The application of RMT to physical quantum systems thus rests on the proposition that the coarse statistical properties of the spectra depend not on the detailed form of the interaction described by the Hamiltonian, but only on its symmetries. This proposition is implemented by replacing the Hamiltonian by a *random matrix*: a matrix whose elements are randomly drawn from some distribution, up to some symmetry constraints which are determined by the symmetries of the physical system. The particular choice of distribution then defines an RMT *ensemble*.

As we shall continue to see in this chapter, such a radical simplification turns out to yield miraculously accurate results in the study of physical reality. The only price to be paid is that, as a statistical theory, RMT cannot ever reproduce a given data set;

it can only yield distributions and correlations for data points.

6.2 Wigner-Dyson Statistics

Before returning to the question of physical applications, we first introduce the formal aspects of RMT. For a more detailed review we refer the reader to the reviews [59, 60, 61] and the classic text by Mehta [62].

6.2.1 The Gaussian ensembles

We begin by introducing the canonical class of RMT ensembles: the *Gaussian ensembles*. These can be derived by seeking an ensemble of random matrices, where the matrix M occurs with probability $P(M)$ and its entries M_{ij} occur with probability $P_{ij}(M_{ij})$, satisfying two conditions:

> 1) *Uncorrelated Matrix Elements:* Up to the symmetry requirements we impose, the matrix elements are independent random variables: $P(M) = \prod_{i,j} P_{ij}(M_{ij})$.
>
> 2) *Rotational Invariance:* Matrices that are related by permissible similarity transformations U occur in the ensemble with equal probability: $P(UMU^{-1}) = P(M)$.

The particular choice of symmetry requirements define the three Gaussian ensembles: the Gaussian Orthogonal Ensemble (GOE) contains real symmetric matrices, the Gaussian Unitary Ensemble (GUE) contains Hermitian matrices and the Gaussian Symplectic Ensemble (GSE) contains quarternionic matrices. As their names suggest, the permissible symmetry transformations are taken to be orthogonal for the GOE, unitary for the GUE and symplectic for the GSE[4].

It turns out that both of the above conditions are *uniquely* satisfied for all three ensembles by the following (unnormalised) distribution

$$P(M) = \exp\left(-\alpha \operatorname{Tr} M^2\right), \tag{6.1}$$

where M is an $N \times N$ matrix and α is a constant which fixes the units of energy. See Appendix C for an explicit derivation of this result in the simplest case, that of the

[4]We additionally require that the measures of each distribution, dM_{ij}, must also be invariant under the relevant similarity transformation; a fact we will assume and not prove here.

2×2 GOE.

The distribution (6.1) clearly satisfies rotational invariance $P(M') = P(UMU^{-1})$ by cyclicity of the trace. To see that the elements of M are uncorrelated in the GOE[5], note that $\operatorname{Tr} M^2 = \sum_i (M^2)_{ii} = \sum_{i,j} M_{ij} M_{ji} = \sum_{i,j} M_{ij}^2$ since M is symmetric, so clearly the probability distribution factorises as $P(M) = \prod_{i,j} P_{ij}(M_{ij})$, where

$$P_{ij}(M_{ij}) = \exp\left(-\alpha \operatorname{Tr} M_{ij}^2\right). \tag{6.2}$$

6.2.2 Eigenvalue distribution

In order to analyse the spectra of random matrices belonging to the three Gaussian ensembles, we would like to be able to rewrite their probability distributions in terms of matrix elements M_{ij} (6.1), as probability distributions in terms of matrix eigenvalues E_i. In the 2×2 GOE case, the eigenvalues of M are

$$E_\pm = \tfrac{1}{2}(M_{11} + M_{22}) \pm \tfrac{1}{2}\sqrt{(M_{11} - M_{22})^2 + 4M_{12}^2}. \tag{6.3}$$

Diagonalising M with the orthogonal matrix

$$\begin{pmatrix} \cos\theta & -\sin\theta \\ \sin\theta & \cos\theta \end{pmatrix}, \tag{6.4}$$

we obtain

$$\begin{aligned} M_{11} &= E_+ \cos^2\theta + E_- \sin^2\theta, \\ M_{22} &= E_+ \sin^2\theta + E_- \cos^2\theta, \\ M_{12} &= (E_+ - E_-)\cos\theta \sin\theta. \end{aligned} \tag{6.5}$$

Crucially, the Jacobian of these transformations is $(E_+ - E_-)$, which has no θ dependence. It follows that the probability distribution, written in terms of eigenvalues, is given by

$$P(E_+, E_-) = (E_+ - E_-) e^{-\alpha(E_+^2 + E_-^2)}, \tag{6.6}$$

where we have neglected the constant obtained by performing the trivial θ integral, which is irrelevant up to the overall normalisation which we have yet to determine. In the GUE and GSE cases we obtain a similar result, differing only by the power

[5] Similar arguments hold for the GUE and GSE.

of the Jacobian factor. Generalising to the $N \times N$ case, the full result for all three Gaussian ensembles is given by

$$P(E_1, \cdots, E_n) = \prod_{i<j} |E_i - E_j|^\beta e^{-\alpha \sum_i^N E_i^2}, \tag{6.7}$$

where $\beta = 1, 2, 4$ for the GOE, GUE, GSE respectively. These are the celebrated *Wigner-Dyson distributions*. They are characterised by the conflicting features of *confinement* and *repulsion*[6], the interplay of which is the physical mechanism at the heart of many results in RMT. The decaying exponential confines the eigenvalues by ensuring that they have diminishing probability of being too far apart. The Jacobian factor ensures that no two eigenvalues are likely to be found too close together (with zero probability of equality), a phenomenon well known in quantum mechanics as *level repulsion*. This Jacobian is given by the β'th power of the *Vandermond determinant*

$$\Delta(\{E\}) \equiv \prod_{i<j} (E_i - E_j). \tag{6.8}$$

Crucially, this Vandermond determinant correlates the eigenvalues; every eigenvalue feels the presence of every other, and the probability distribution no longer factorises.

The case where eigenvalues are completely uncorrelated is described by the *Poisson ensemble*, where eigenvalues are Poisson distributed. We will often compare the GUE ensembles to the Poisson ensemble to illustrate the effects of the Wigner-Dyson correlations. In Fig. 6.2 we compare sample eigenvalue spectra for the three Gaussian ensembles, the Poisson ensemble and the uniform distribution. Note how the level repulsion gets stronger as we increase β from the GOE case to the GSE case, as we would expect from (6.7). In the Poisson ensemble, the clustering of eigenvalues (forbidden by level repulsion) is evident.

[6]Perhaps most intuitively exemplified by the tendency, well described by RMT in [65], of drivers to "park their cars near to each other and at the same time keep a distance sufficient for manoeuvring."

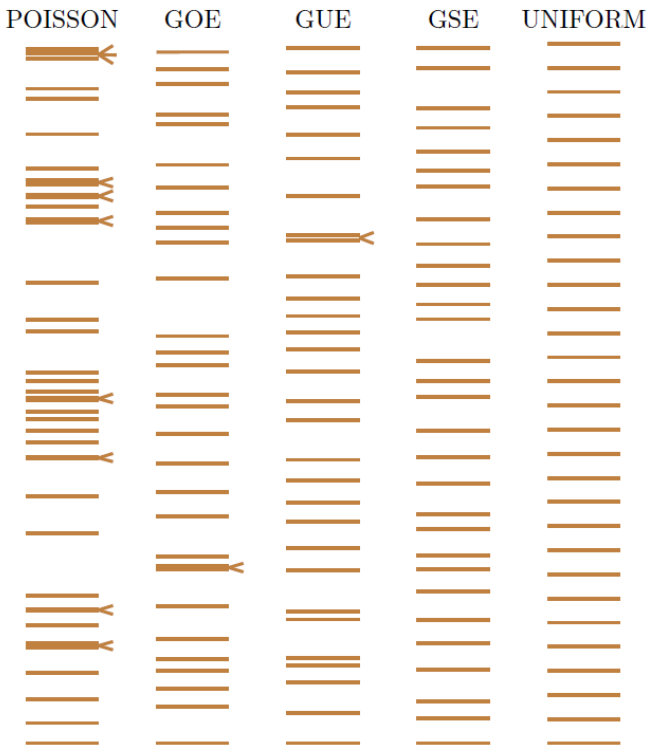

Figure 6.2: A single realisation of the spectrum sampled from the various ensembles, each plotted on the scale where the local average spectral density is constant. Arrowheads mark the occurrences of pairs of levels which are very close together. Image taken from [109].

6.2.3 Time reversal symmetry

We have already mentioned that the RMT ensemble chosen to model the statistics of a given physical system must be determined by the symmetries of that system, but we have not specified which physical symmetries matter, or how they correspond to the three Guassian ensembles introduced thus far.

It turns out that there is only one physical symmetry which matters: each of the Gaussian ensembles precisely correspond to systems with various behaviour under *time reversal symmetry* [72]. The GOE corresponds to systems with time reversal symmetry and either rotational symmetry or integer spin. The GSE corresponds to systems with a spin-dependent Hamiltonian that preserves time reversal symmetry and describes particles with half-integer spin. The GUE does not assume any definite relationship between the Hamiltonian and its Hermitian conjugate, and thus

describes systems with broken time-reversal symmetry[7]. We here see Wigner and Dyson's philosophy of RMT at play: systems with complicated interactions can be classified and then described by a suitable RMT ensemble according only to their symmetry properties under time reversal[8].

An important detail is that in the application of RMT to physical systems, the Hamiltonian must always be reduced with respect to all of its symmetries such that it becomes block–diagonal, each block being characterized by a fixed set of quantum numbers. It is these blocks, and not the full Hamiltonian, that then each display Wigner-Dyson statistics and are modelled by RMT.

6.2.4 Nearest-neighbour spacing distribution

The *nearest-neighbour spacing distribution* $P(s)$ is an important spectral statistic, which gives the probability that two adjacent energy levels are a spacing s apart. It can be calculated explicitly for the 2×2 GOE case, using (6.6), as follows

$$\begin{aligned} P(s) &= \int dE_+ dE_- \delta(s - |E_+ - E_-|)(E_+ - E_-) e^{-\alpha(E_+^2 + E_-^2)} \\ &= \int dE_+ s \left[e^{-\alpha(E_+^2 + (E_+ - s)^2)} + e^{-\alpha(E_+^2 + (E_+ + s)^2)} \right] \\ &= 2se^{-\alpha s^2} \int dE_+ e^{-2\alpha E_+^2} \cosh(2\alpha E_+ s) \\ &= \sqrt{\frac{2\pi}{\alpha}} s e^{-\alpha s^2/2}. \end{aligned} \tag{6.9}$$

Implementing the normalisation $\int ds P(s) = 1$ and fixing the units of energy α such that the mean spacing is unity, $\int ds P(s) s = 1$, then yields the famous *Wigner surmise* [70] for the GOE

$$P(s) = \frac{s\pi}{2} e^{-\pi s^2/4}. \tag{6.10}$$

Similar results hold for the GUE and GSE; they all share the expected characteristics of level repulsion as well as exponential fall-off for large spacing, and are plotted in Fig. 6.3. Note again how the level repulsion increases as β increases from GOE

[7] These facts are easily proved, see for instance [63].

[8] We briefly mention for completeness that Dyson's three symmetry classes outlined here can be naturally extended to ten classes, based on a general mathematical classification scheme for symmetric spaces, if one introduces particle-hole symmetry in addition to time-reversal symmetry [116].

through to GSE. In the case of completely uncorrelated eigenvalues, we would obtain the Poisson distribution $P(s) = e^{-s}$ which attains its maximum at $s = 0$. This explains the clustering in the Poisson spectrum in Fig. 6.2. Miraculously, for larger N the distributions differ only slightly from the $N = 2$ case [61].

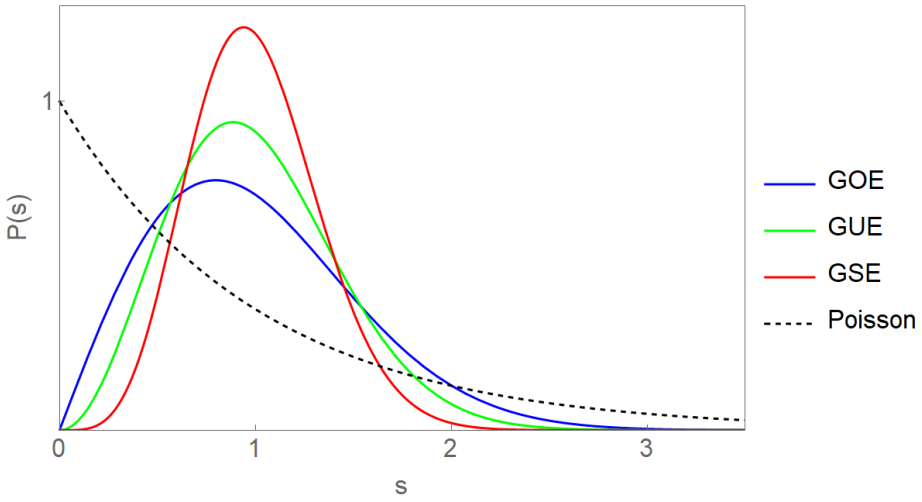

Figure 6.3: Nearest-neighbour spacing distributions for the Gaussian ensembles and the Poisson ensemble.

6.2.5 Universality

Recall that (6.1), $P(M) = e^{-\alpha \operatorname{Tr} M^2}$, is the unique distribution satisfying the two conditions of rotational invariance and uncorrelated matrix elements. That all M dependence appears through the trace of (some power of) M is clearly sufficient to ensure rotational invariance $P(M) = P(U^{-1}MU)$. In fact, it is also necessary: the condition of rotational invariance constrains $P(M)$ to take the form [80]

$$P(M) = f(\operatorname{Tr} M, \operatorname{Tr} M^2, ..., \operatorname{Tr} M^N), \tag{6.11}$$

for $N \times N$ matrices M. It turns out, however, that different matrix elements become correlated when f depends on any power higher than M^2. One can then consider probability distributions for the class of rotationally invariant ensembles,

$$P(M) = e^{-\alpha \operatorname{Tr} V(M)}, \tag{6.12}$$

where $V(M)$ is a polynomial of order less than or equal to N, which we will refer to as the *potential*. Quadratic potentials correspond to the Gaussian ensembles, which satisfy the additional condition of uncorrelated matrix elements. Higher order potentials correspond to rotationally invariant ensembles with *correlated* matrix elements.

One may then ask the question, how do the statistics of these more general ensembles compare to their Gaussian counterparts?

We first consider their eigenvalue distributions. Recall that when changing variables from the probability distribution over matrix elements to one over eigenvalues in (6.6), we were able to perform the trivial integral over the extra variable θ which parameterise the symmetry transformations, to obtain a distribution which depends only on the eigenvalues E_i. While this integral over extra variables cannot be evaluated analytically for general RMTs[9], thankfully it can always be evaluated for distributions (6.12) satisfying the condition of rotational invariance[10], for which one obtains the eigenvalue distribution

$$P(E_1, ..., E_N) = \prod_{i<j} |E_i - E_j|^\beta e^{-\alpha \sum_i^N V(E_i)}. \tag{6.13}$$

The variable $\beta = 1, 2, 4$ again describes the case for real symmetric, Hermitian or quarternionic matrices respectively. The Vandermonde determinant appearing here is exactly the same as in the Guassian distributions, while the potential V appearing in the exponential is not, it is model specific[11]. One may then ask which other statistical features of general rotationally invariant RMTs (6.12) are well described by the corresponding Gaussian model, and which features are unique to the Gaussian case. We will refer to features of the former kind as *universal*, and the latter as *non-universal*.

We will soon see that while the average spectral density (the one-point correlation function) is strongly model dependent and thus non-universal, remarkably, higher-point correlation functions are universal. This fact will have central significance for the applicability of RMT to modelling physical systems.

6.3 Spectral Correlation Functions

For a given realisation of any RMT ensemble, the spectral density is given by

$$n(E) = \frac{1}{N} \sum_{i=1}^{N} \delta(E - E_i), \tag{6.14}$$

[9]For non-rotationally invariant RMTs with uncorrelated matrix elements, finding the joint probability densities of the eigenvalues remains an open problem.

[10]This is due to the lemma (6.11), first proved by Weyl.

[11]Note that (6.13) contains (6.7) as a special case when the potential V is quadratic.

a normalised sum of delta functions at the locations of each of the N eigenvalues E_i. The integral $\int_a^b n(E)dE$ then gives the fraction of eigenvalues between $E = a$ and $E = b$. By averaging this function over the ensemble, we obtain the average eigenvalue density distribution, or *average spectral density*

$$\begin{aligned} P(E) &\equiv \int dE_1 \dots dE_N P(E_1, E_2, \cdots, E_n) n(E) \\ &= \int dE_2 \dots dE_N P(E, E_2, \cdots, E_n), \end{aligned} \tag{6.15}$$

where in the second line we have used the fact that the Wigner-Dyson distributions (6.7) are symmetric under any swapping of arguments (they do not care how we label the eigenvalues). Notice how the integral does not factorise because the Vandermonde determinant correlates the different eigenvalues. The average spectral density $P(E)$ then tells us the likelihood for a matrix randomly drawn from the ensemble to have an energy eigenvalue equal to E.

We may generalise the above expression to obtain the *n-point correlation functions* of the ensemble, defined as

$$R(E_1, E_2, ..., E_n) \equiv \frac{N!}{(N-n)!} \int dE_{n+1} ... dE_N P(E_1, E_2, ..., E_N). \tag{6.16}$$

These correlation functions tell us the likelihood of a matrix randomly drawn from the ensemble having n energy eigenvalues at precisely the energies $E_1, ..., E_n$. As such they characterise the statistical properties of the spectrum, and computing them is a central task of RMT.

6.3.1 The method of orthogonal polynomials

The first reliable general method for computing such correlation functions was discovered in 1960 by Mehta [62], and lead to huge advances in the field of RMT. It goes by the name of the method of *orthogonal polynomials*, and can be successfully applied not just to the Gaussian ensembles, but to all rotationally invariant ensembles.

We will now use it to compute the non-trivial integral (6.15). We will restrict our attention to the simplest case, $\beta = 2$, corresponding to unitarily invariant ensembles. Note that we consider the general potential $V(E)$ which contains the GUE as a special case, to which we will specialise later. Fixing $\alpha = N$, our distribution (6.13) becomes

$$P(E_1, \cdots, E_N) = \Delta^2(\{E\}) e^{-N \sum_i V(E_i)}, \tag{6.17}$$

where we note that the Vandermonde determinant can be written as

$$\Delta(\{E\}) = \prod_{i<j}(E_i - E_j) = \begin{vmatrix} 1 & 1 & \cdots & 1 \\ E_1 & E_2 & \cdots & E_N \\ E_1^2 & E_2^2 & \cdots & E_N^2 \\ \vdots & \vdots & \ddots & \vdots \\ E_1^{N-1} & E_2^{N-1} & \cdots & E_N^{N-1} \end{vmatrix}. \tag{6.18}$$

Defining the polynomials

$$p_n(E) = a_n E^n + \text{ terms of lower order in } E, \tag{6.19}$$

we may rewrite this as [61]

$$\Delta(\{E\}) = \frac{1}{a_0 a_1 \cdots a_{N-1}} \underbrace{\begin{vmatrix} 1 & 1 & \cdots & 1 \\ p_0(E_1) & p_0(E_2) & \cdots & p_0(E_N) \\ p_1(E_1) & p_1(E_2) & \cdots & p_1(E_N) \\ \vdots & \vdots & \ddots & \vdots \\ p_{N-1}(E_1) & p_{N-1}(E_2) & \cdots & p_{N-1}(E_N) \end{vmatrix}}_{\equiv \det\{p_i(E_j)\}}, \tag{6.20}$$

Note that the polynomials p_n are undetermined up to the requirement that they are of order n with leading coefficient a_n; the terms of lower order have no effect on the value of the Vandermonde determinant. We will later exploit this freedom to great effect. It follows from the fact that $(\det M)^2 = \det M^T M$ that the square of (6.20) can be written

$$\Delta^2(\{E\}) = \frac{1}{(a_0 a_1 \cdots a_{N-1})^2} \det\left\{\sum_{k=0}^{N-1} p_k(E_i) p_k(E_j)\right\}. \tag{6.21}$$

Using the following property of the determinant

$$\prod_{k=0}^{N-1} c_k \det\{M_{ij}\} = \det\{\sqrt{c_i c_j} M_{ij}\}, \qquad i,j = 0,1,\cdots,N-1, \tag{6.22}$$

we can now write the distribution (6.17) as

$$P(E_1,...,E_N) = \frac{1}{(a_0 a_1 \cdots a_{N-1})^2} \det\left\{\sum_{k=0}^{N-1} \psi_k(E_i)\psi_k(E_j)\right\}, \tag{6.23}$$

where we have defined

$$\psi_n(E) \equiv e^{-NV(E)/2} p_n(E). \tag{6.24}$$

We now define one of the central objects of study in RMT, the *kernel*, given by

$$\begin{aligned} K(x,y) &\equiv \sum_{k=0}^{N-1} \psi_k(x)\psi_k(y) \\ &= e^{-\frac{N}{2}(V(x)+V(y))} \sum_{k=0}^{N-1} p_k(x)p_k(y). \end{aligned} \tag{6.25}$$

The kernel depends on the model specific potential $V(E)$, as well as the polynomials (6.19), which at this point are still completely undetermined. Our distribution (6.17) then becomes

$$P(E_1, ..., E_N) = \frac{1}{(a_0 a_1 \cdots a_{N-1})^2} \det\left\{K(E_i, E_j)\right\}, \tag{6.26}$$

allowing us to rewrite the average spectral density (6.15) as a multiple integral over the determinant of the kernel,

$$P(E) = \frac{1}{(a_0 a_1 \cdots a_{N-1})^2} \int dE_2 \cdots dE_N \det\left\{K(E_i, E_j)\right\}. \tag{6.27}$$

This is a highly non-trivial integral to perform in general, but it turns out that a special choice of the polynomials p_n simplifies the task. Namely, we choose p_n to be orthonormal with respect to the weight $e^{-V(E)}$ (equivalently, $\psi_n(E)$ to be orthonormal with respect to the flat measure)

$$\int dE e^{-NV(E)} p_n(E) p_m(E) = \int dE \psi_n(E)\psi_m(E) = \delta_{nm}. \tag{6.28}$$

With this choice, the kernel satisfies the property

$$\begin{aligned} \int dy K(x,y)K(y,z) &= \sum_{k,l=0}^{N-1} \psi_k(x)\psi_l(z) \underbrace{\int dy \psi_k(y)\psi_l(y)}_{=\,\delta_{kl}} \\ &= K(x,z), \end{aligned} \tag{6.29}$$

This property will allow us to reduce the integral (6.27) over $N-1$ variables to an integral over $N-2$ variables, and so on recursively. To see this, let us first consider

the $N = 2$ case, where

$$\begin{aligned} P(x) &\sim \int dy \begin{vmatrix} K(x,x) & K(x,y) \\ K(y,x) & K(y,y) \end{vmatrix} \\ &= \int dy \left[K(x,x)K(y,y) - K(x,y)K(y,x) \right] \\ &= (N-1)K(x,x), \end{aligned} \tag{6.30}$$

where we have used the fact that

$$\int dy K(y,y) = \sum_{k=0}^{N-1} \underbrace{\int dE \psi_k(y)\psi_k(y)}_{=1} = N. \tag{6.31}$$

Extending this result to the $N \times N$ case [61], one may similarly obtain

$$\int dE_N \det\{K(E_i,E_j)\}_{1\leq i,j\leq N} = \det\{K(E_i,E_j)\}_{1\leq i,j\leq N-1}. \tag{6.32}$$

An analogous, more general result holds for any function of two variables satisfying the property (6.29), and goes by the name of the Dyson-Gaudin integration lemma [95]. Iterating this result $N-k$ times, we obtain

$$\int dE_{k+1}...dE_N \det\{K(E_i,E_j)\}_{1\leq i,j\leq N} = (N-k)! \det\{K(E_i,E_j)\}_{1\leq i,j\leq k}. \tag{6.33}$$

Choosing $k = 1$, the left hand side is equal to the average spectral density (6.27), so we obtain the simple expression

$$P(E) = \frac{1}{Z_N} \frac{(N-1)!}{(a_0 a_1 \cdots a_{N-1})^2} K(E,E), \tag{6.34}$$

where we have introduced the normalisation $\frac{1}{Z_N}$, which we now fix by imposing the normalisation condition

$$\begin{aligned} 1 = \int dE P(E) = \frac{1}{Z_N} \frac{(N-1)!}{(a_0 a_1 \cdots a_{N-1})^2} \int dE K(E,E) = \frac{1}{Z_N} \frac{N!}{(a_0 a_1 \cdots a_{N-1})^2} \\ \Rightarrow Z_N = \frac{(a_0 a_1 \cdots a_{N-1})^2}{N!}, \end{aligned} \tag{6.35}$$

using (6.31). Substituting back into (6.34), we obtain our final expression for the average spectral density of any RMT with unitary rotational invariance,

$$P(E) = \frac{1}{N} K(E,E). \tag{6.36}$$

The method of orthogonal polynomials outlined here solves the problem not just for the average spectral density, but for *any* higher-point correlation function of the theory. Indeed, using (6.33) and the normalisation (6.35), we obtain from (6.16) that the n-point functions of the theory are given by a simple determinant of the kernel

$$R(E_1, E_2, ..., E_n) = \det\{K(E_i, E_j)\}_{1\leq i,j\leq n}. \tag{6.37}$$

This expression illustrates why the kernel is so central to the study of RMT. We have just shown that the one-point function, proportional to the average spectral density, is given by

$$R(E) = NP(E) = K(E, E). \tag{6.38}$$

The two-point function, or *pair correlator*, is given by

$$R(E_1, E_2) = K(E_1, E_1)K(E_2, E_2) - K(E_1, E_2)^2, \tag{6.39}$$

where we have used that the kernel is symmetric in its arguments. We will now evaluate these two expressions explicitly in the Gaussian case.

6.3.2 The Gaussian case

Specialising to the GUE where $V(E) = \frac{1}{2}E^2$, we need to find the corresponding orthogonal polynomials 6.19. These turn out to be slightly modified versions of the Hermite polynomials. We will now define them explicitly and sketch the calculation following [97], using our results for the kernel (6.25) and the explicit forms of the average spectral density (6.38) and the pair correlator (6.39).

The Hermite polynomials are defined as

$$H_k(x) = (-1)^k e^{x^2} \frac{d^k}{dx^k}\left(e^{-x^2}\right), \tag{6.40}$$

and are orthogonal with respect to the weight e^{-x^2},

$$\int dx H_n(x) H_m(x) e^{-x^2} = \sqrt{\pi} 2^n n! \delta_{nm}. \tag{6.41}$$

We will work with polynomials of the slightly different form

$$h_k(x) = (-1)^k e^{Nx^2/2} \frac{d^k}{dx^k}\left(e^{-Nx^2/2}\right), \tag{6.42}$$

which are orthogonal with respect to the weight $e^{-Nx^2/2}$. This orthogonality becomes orthonormality when we normalise them as

$$\tilde{h}_k(x) = \left(k! N^k \sqrt{\tfrac{2\pi}{N}}\right)^{-1/2} h_k(x). \tag{6.43}$$

The unnormalised polynomials satisfy the difference relation

$$h_{k+1}(x) = Nx h_k(x) - Nk h_{k-1}(x). \tag{6.44}$$

while their derivatives satisfy

$$\frac{d}{dx} h_k(x) = Nk h_{k-1}(x). \tag{6.45}$$

A crucial ingredient in our derivation will be the Christoffel-Darboux formula [96], which prescribes how a finite series of orthogonal polynomials can be rewritten in terms of only the last two polynomials in the series. Specialised to our polynomials, it takes the form

$$\sum_{k=0}^{n-1} \tilde{h}_k(x)\tilde{h}_k(y) = \sqrt{\frac{n}{N}} \frac{\tilde{h}_{n-1}(y)\tilde{h}_n(x) - \tilde{h}_{n-1}(x)\tilde{h}_n(y)}{x-y}. \tag{6.46}$$

We may then immediately write an expression for the GUE kernel (6.25) in terms of our unnormalised orthogonal polynomials

$$\begin{aligned} K(x,y) &= e^{-\frac{N}{2}(V(x)+V(y))} \sum_{k=0}^{n-1} \tilde{h}_k(x)\tilde{h}_k(y) \\ &= \sqrt{\frac{N}{2\pi}} \frac{e^{-\frac{N}{4}(x^2+y^2)}}{N! N^{N-1}} \frac{h_{N-1}(y)h_N(x) - h_{N-1}(x)h_N(y)}{x-y}. \end{aligned} \tag{6.47}$$

To obtain the result for $x = y$, we add and subtract the term $h_{n-1}(y)h_n(y)$ from the numerator, take the limit $x \to y$, and use (6.45) to obtain

$$K(x,x) = \sqrt{\frac{N}{2\pi}} \frac{e^{-Nx^2/2}}{N! N^{N-1}} \left[h_N^2(x) - h_{N-1}(x)h_{N+1}(x)\right]. \tag{6.48}$$

Since all n-point eigenvalue correlations functions are written in terms of the kernels (6.47) and (6.48), we have just shown the following remarkable fact: almost all RMT quantities of interest depend only on a few Hermite polynomials $h_{N+\mathcal{O}(1)}$.

We would like to extract approximate expressions for (6.47) and (6.48) in the large N limit, from which we can obtain the large N average spectral density and pair correlators (6.38) and (6.39) respectively. To this end, consider the Gaussian identity

$$e^{-Nx^2/2} = \sqrt{\frac{N}{2\pi}} \int_{-\infty}^{\infty} d\alpha e^{-N\alpha^2/2 + ix\alpha N}. \tag{6.49}$$

Substituting into the definition of our polynomials (6.42), we obtain the *integral representation*

$$h_k(x) = (-iN)^k \sqrt{\frac{N}{2\pi}} e^{Nx^2/2} \int_{-\infty}^{\infty} d\alpha e^{-N\alpha^2/2 + ix\alpha N}. \tag{6.50}$$

We may then write

$$h_{N+n}(x) = (-iN)^{N+n} \sqrt{\frac{N}{2\pi}} \left[I_{N+n}(x) + (-1)^{N+n} I_{N+n}(-x) \right], \tag{6.51}$$

where

$$I_{N+n}(x) = \int_0^{\infty} d\alpha \alpha^n e^{Nf(\alpha)}, \qquad f(\alpha) = \ln \alpha - \tfrac{1}{2}(\alpha - ix)^2. \tag{6.52}$$

Clearly we have arrived at an expression for our polynomials which is amenable to analysis at large N by means of saddle point approximation methods[12] on the integrals $I_{N+n}(\pm x)$. Performing the saddle point analysis[13] up to quadratic fluctuations, one obtains the following expression, valid for $|x| < 2$ and $n \ll N$,

$$h_{N+n}(x) \approx N^{N+n} \sqrt{\frac{2}{\sin\phi}} e^{\frac{N}{2}\cos 2\phi} \cos\chi, \tag{6.53}$$

where

$$\chi = \left(n + \tfrac{1}{2}\right)\phi - \tfrac{\pi}{4} + N\left(\phi - \tfrac{1}{2}\sin 2\phi\right), \qquad x = 2\cos\phi, \qquad 0 < \phi < \pi. \tag{6.54}$$

6.3.3 The average spectral density

We may now use the expression (6.53) to determine the average spectral density for the GUE in the large N limit. First note that

$$\begin{aligned} h_N^2(x) - h_{N-1}(x)h_{N+1}(x) &= N^{2N} \frac{2}{\sin\phi} e^{N\cos 2\phi} \underbrace{\left[\cos^2\chi - \cos(\chi+\phi)\cos(\chi-\phi)\right]}_{\sin^2\phi} \\ &= 2N^{2N} e^{N\cos^2\phi - N} \sin\phi, \end{aligned} \tag{6.55}$$

[12] Such an asymptotic analysis of orthogonal polynomials goes by the name of Plancherel-Rotach asymptotics [81].

[13] We refer the reader to [97] for the details.

so that, substituting into (6.48), we obtain

$$P(x) = \frac{1}{N}K(x,x) = \frac{1}{N}\sqrt{\frac{N}{2\pi}}\frac{2N^N}{(N-1)!}e^{-N}\sin\phi = \frac{1}{\pi}\sin\phi, \tag{6.56}$$

where in the final equality we have used Stirling's approximation $(N-1)! \approx \sqrt{\frac{2\pi}{N}}N^N e^{-N}$ valid for $N \gg 1$. Finally, recalling that $x = 2\cos\phi$, we obtain a final expression for the average spectral density of the GUE,

$$P_\infty(E) \equiv \frac{1}{2\pi}\sqrt{4-E^2}. \tag{6.57}$$

This famous result was first derived by Wigner in 1957 [70] and is often refered to as the *Wigner semicircle distribution*. It describes a semi-ellipse of width 2, centered at the origin. In this infinite N limit the distribution has hard edges; there is zero probability of finding an eigenvalue with magnitude greater than 2. For finite N, the corresponding distribution is given by (6.48). When N is large it still takes a semicircular shape, but now with soft edges, so that there is always a nonzero probability of sampling eigenvalues which exceed the edge points (see Fig. 6.4).

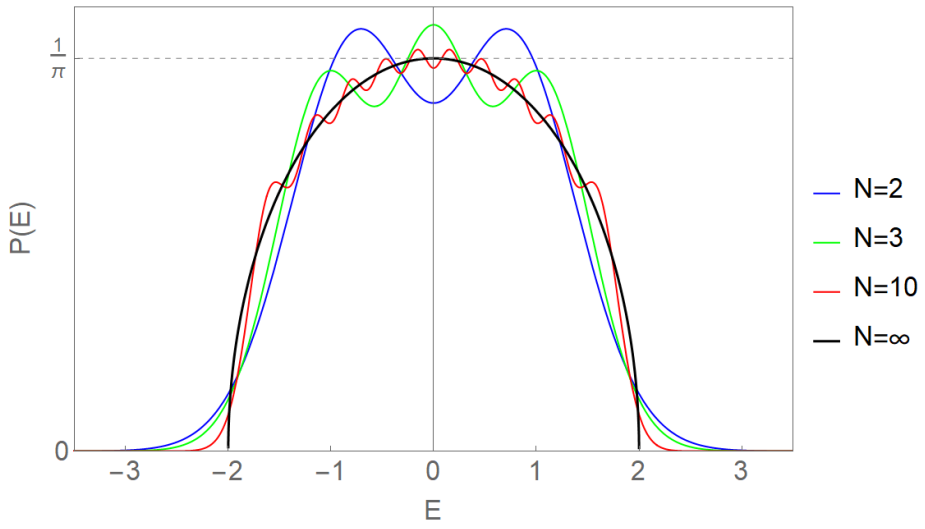

Figure 6.4: Average spectral density for various finite N (6.48) and in the limit $N \to \infty$ (6.57).

The average spectral density is not universal

Let us now address the question of whether or not the average spectral density is universal, in other words, whether the Wigner semicircle distribution we derived for

the GUE also describes non-Gaussian ensembles with unitary rotational invariance. To this end, our calculation may be extended [82] to a non-Gaussian potential given by an even polynomial of degree $2p$

$$V(E) = \sum_{k=1}^{p} \frac{c_k}{2k} E^{2k}, \tag{6.58}$$

where the c_k are constants. In this case, one obtains the average spectral density [94]

$$P(E) = \frac{1}{\pi} \xi(E) \sqrt{a^2 - E^2}, \tag{6.59}$$

where ξ is an even polynomial of degree $2p-2$

$$\xi(E) = \frac{1}{2} \sum_{k=1}^{p} c_k \sum_{n=0}^{k-1} \binom{2n}{n} \frac{a^{2n}}{4^n} E^{2k-2n-2}, \tag{6.60}$$

and a is the endpoint of the spectrum, given by the algebraic equation

$$\frac{1}{2} \sum_{k=1}^{p} c_k \binom{2k}{k} \frac{a^{2k}}{4^k} = 1. \tag{6.61}$$

In Fig. 6.5 we plot the average spectral densities for some quartic and sextic potentials. Evidently, the semicircle distribution obtained in the Gaussian case is not universal among RMTs with unitary rotational invariance. It turns out [60] that it is the condition of uncorrelated matrix elements which is the essential ingredient in obtaining the semicircle distribution, which is precisely the condition sacrificed by considering ensembles with more general, non-Gaussian potentials $V(E)$.

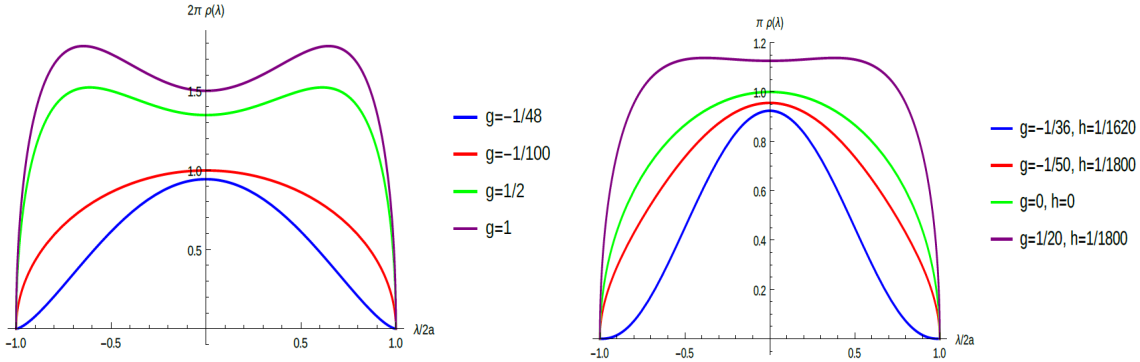

(a) Quartic potential, with $h = 0$.

(b) Sextic potential.

Figure 6.5: Average spectral densities for the potentials $V(E) = \frac{1}{2}E^2 + \frac{g}{N}E^4 + \frac{h}{N^2}E^6$, clearly illustrating that the semicircle is non-universal. Images taken from [100].

6.3.4 The pair correlator

A similar derivation of the pair correlator (6.39) involving $K(x, y)$ (6.47) is slightly more involved[14]. Substituting in the saddle point result (6.53), one eventually obtains

$$\lim_{N\to\infty} \frac{K(E, E')}{K(E, E)} = \frac{\sin \varepsilon}{\varepsilon}, \quad \text{where} \quad \varepsilon = N\pi(E - E')P_\infty\left(\tfrac{E+E'}{2}\right). \tag{6.62}$$

This result is known as the *sine kernel*. From (6.39), we obtain the pair correlator

$$R(E, E') = P_\infty(E)P_\infty(E')\left(1 - \frac{\sin^2 \varepsilon}{\varepsilon^2}\right), \quad \text{where} \quad \varepsilon = N\pi(E - E')P_\infty\left(\tfrac{E+E'}{2}\right). \tag{6.63}$$

One crucial point is that in the derivation of the sine kernel it was assumed that $E - E' = \mathcal{O}(1/N)$. This condition holds when the eigenvalues are away from the spectral edge at $E = \pm 2$ and are located in the *bulk* of the spectrum. Our result (6.62) then holds under the conditions that the separation between the eigenvalues is small and their average is not near spectral edge[15].

The pair correlator is universal

Having seen that the average spectral density is not universal, we may now ask whether the same is true for the pair correlator. Let us then consider the latter for more general, non-Gaussian potentials $V(E)$.

Motivated by the asymptotic form of the orthogonal polynomials (6.53), one may make the ansatz [94] that when $V(E)$ is an arbitrary even polynomial, the asymptotic form of the orthogonal polynomials ψ_n for $n = N + \mathcal{O}(1)$ will be given by

$$\begin{aligned}\psi_n(E) &= p_n(E)e^{-NV(E)/2} \\ &= \frac{1}{\sqrt{f(E)}} \cos\left[N\alpha(E) - (N - n)\beta(E) + \gamma(E)\right].\end{aligned} \tag{6.64}$$

The unknown functions f, α, β, γ may then be fixed by imposing the orthonormality and recurrence relations for orthogonal polynomials. In the large N limit one then obtains the same sine kernel expression (6.62), provided that the correlation functions are measured on the correct scale set by the average spectral density. This process of scaling the spectrum such that the local average spectral density becomes constant is

[14] We refer the reader to see [97] for more details.

[15] A corresponding result valid in the vicinity of the spectral edge, called the *Airy kernel* [85], may be obtained using similar methods to those outlined above.

known as *unfolding*, and all further statements about the universality of RMT fluctuations are made with reference to the unfolded spectrum.

The calculation can be further generalised to arbitrary potentials $V(E)$ using the supersymmetric method[16] [83], where one again obtains the same sine kernel expression for the large N pair correlator, this time for all three cases of orthogonal, unitary and symplectic rotational symmetry ($\beta = 1, 2, 4$ in (6.13)).

Thus we see that, unlike the average spectral density, the pair correlator *is* universal in the large N limit, as are *all* of the higher-point correlation functions.

These facts bring us to a general feature of the applications of RMT to physics: the distinction between average quantities and their fluctuations. In the Gaussian ensembles, we have seen that the average spectral density is bounded (as a consequence of the cutoff imposed by the Gaussian weight factors) and has the shape of a semicircle in the large N limit. For most physical systems, such a spectrum is completely unrealistic, so Gaussian RMT is not useful for modelling these and other average properties. However, we have just seen that the large N *statistical fluctuations* of observables about their average values, as encoded in the higher-point correlation functions, may become independent of the form of the global spectrum and of the particular choice of potential $V(E)$, and thus attain universal validity. It is this fact which has allowed for the wide range of successful applications of RMT in its Gaussian form to physical systems, which we will now discuss.

6.4 RMT and Quantum Chaos

Having reviewed the formalism and key results of RMT, we now give an overview of one of its primary applications in quantum physics: as a diagnostic of *quantum chaos*. Unlike in its initial application to nuclear physics, where RMT was conceived as a statistical approach to systems with many degrees of freedom, in the context of quantum chaos RMT applies also to systems with few degrees of freedom. For excellent reviews of the topic we refer the reader to the classic texts [106, 108, 107]. We begin by elucidating the concept of quantum chaos via the problem of quantum billiards.

[16] See Section 6.4 for more on the supersymmetric method.

6.4.1 Quantum billiards

Classically, a billiard system is comprised of a free particle which obeys classical rules of reflection, moving in some two-dimensional region with a boundary. For a system with a circular boundary, nearby trajectories of the particle in phase space remain near to each other for all times. This behaviour characterises classically *integrable* systems: systems which possess a maximal set of conserved quantities and are therefore analytically solvable. However, upon changing the shape of the boundary, the system can become *chaotic*[17]: trajectories which start arbitrarily close in phase space diverge exponentially over time. This characteristic behaviour can for our purposes be taken as the definition of classical chaos: *exponentially sensitive dependence on initial conditions*. We note that fully chaotic dynamics also have the property of *ergodicity*: over long periods of time, everywhere in the accessible phase space is visited with equal likelihood.

For the corresponding *quantum* billiard system, eigenfunctions are given by solutions of the free-particle Schrödinger equation with Dirichlet boundary conditions, and one obtains a discrete spectrum of energy levels. The problems with formulating a proper definition of quantum chaos in this context have their origin in the concept of the trajectory, which completely loses its significance in quantum mechanics, due to the Heisenberg uncertainty principle. However, all is not lost: one may study the quantum problem for billiard systems which are classically integrable and for those which are classically chaotic, and see what characteristics distinguish the two cases. It is in this sense that the term 'quantum chaos' was originally introduced: it refers to the study of the *quantum mechanical* behaviour of *classically* chaotic systems.

In 1979, numerical results for the spectrum of the circular quantum billiard were obtained and subjected to statistical analysis [110]. The spectrum was shown to exhibit level clustering and degeneracies, ruling out the possibility of level repulsion. The results for the nearest-neighbour spacing distribution, shown in Fig. 6.6, showed good agreement with the Poisson distribution (see Fig. 6.3). This turns out to be a generic feature of the quantum spectra of classically integrable systems: the spectrum exhibits level clustering and Poisson distributed nearest-neighbour level spacings, illustrating that different energy levels are uncorrelated[18].

[17] We will not spend much time discussing the fascinating and well-developed field of classical chaos, and refer the reader instead to the many good resources available on the topic, including [104, 108, 105].

[18] This unproven but generally accepted result goes by the name of the Berry-Tabor conjecture [113].

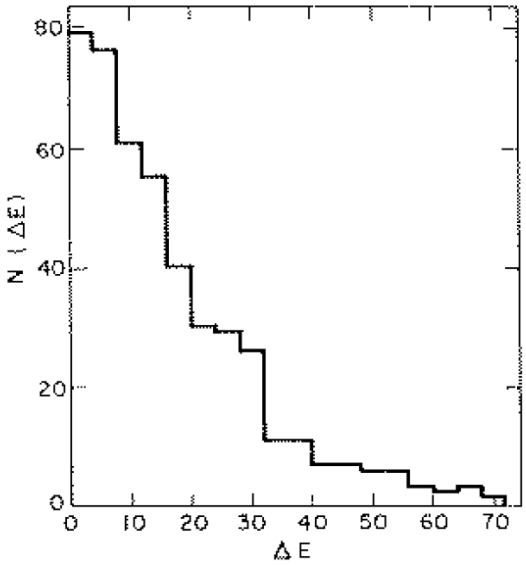

Figure 6.6: Nearest-neighbour spacing distribution for odd parity energy levels for the circular billiard. Image taken from [110].

In the case of classically chaotic billiards, the quantum spectra have been studied for many different systems[19]. We will mention only the most historically significant: the Sinai billiard.

6.4.2 The BGS conjecture

The Sinai billiard consists of a square outer boundary and an inserted concentric circle which forms a circular inner boundary, leaving a domain in between the two to which the particle is confined. In a groundbreaking 1984 paper [112], Bohigas, Giannoni and Schmit produced a large set of spectral data for the Sinai billiard, to which they applied Wigner's methods of statistical analysis previously developed in the context of nuclear physics. They obtained the nearest-neighbour spacing distribution[20], and found very good agreement with the nearest-neighbour spacing distribution for the GOE (6.10), see Fig. 6.7a. On the basis of these results, the authors formulated the famous *BGS conjecture*, which applies far more broadly than the simple billiards system which motivated it. This conjecture, alongside the invention of the powerful supersymmetric method at almost the same time, triggered a period of explosive

[19]See part V, section C of [60] for an overview.

[20]They also calculated another statistical quantity, the *spectral rigidity*, about which we will have more to say shortly.

growth in the field of RMT [60]. Initially formulated only for time-reversal invariant systems and the GOE distribution, we state the conjecture here in its stronger and better known form [133],

> *The BGS Conjecture:*
> The level correlations of quantum systems whose corresponding classical systems are chaotic, are given by RMT.[21]

The BGS conjecture has never been proven. However, much analytic understanding has been obtained through various approaches[22], most notably *periodic orbit theory*, which utilises semiclassical approximation based on the Feynman path integral to express the spectral statistics of chaotic systems in terms of infinite sums over classical periodic trajectories. The conjecture has however been confirmed for numerous systems, and there exists overwhelming evidence that for fully chaotic systems, the conjecture applies[23]. There also exists numerical evidence that the converse of the BGS conjecture is true: if the system is not completely chaotic, the spectral correlations are not given by the RMT Wigner-Dyson ensembles [118].

We note that most real systems are neither completely chaotic nor integrable, but have a mixed classical phase space [107]. In such systems the nearest neighbour spacing distribution is somewhere in between the Poisson and Wigner-Dyson cases. The status of the BGS conjecture for such cases is less clear [60].

Crucially, quantum billiards are not purely theoretical constructs. They can be realized experimentally: by vibrating quartz blocks, microwave cavities and vibrating discs. The level spacing distributions of data sets obtained from these physical systems are shown in Fig. 6.7. Remarkably, these are not true quantum mechanical systems, illustrating that the BGS conjecture remains valid in a much more general context.

Fig. 6.7 gives just a taste of the large variety of very different physical systems in which Wigner-Dyson statistics are observed, corroborating Wigner and Dyson's insight that in the description of complicated systems, the details of interaction do not matter. Indeed, the BGS conjecture was made in the same spirit, but with the further insight that the "complicated" systems referred to are precisely those which are classically

[21] As always, we refer to correlations of the unfolded spectrum.

[22] See part V, section I of [60] for further details.

[23] This is subject to the condition that the system be governed by a single time scale - for systems such as a chain of pairwise weakly coupled, fully chaotic billiards which have more than one intrinsic time scale, RMT does not apply.

chaotic[24].

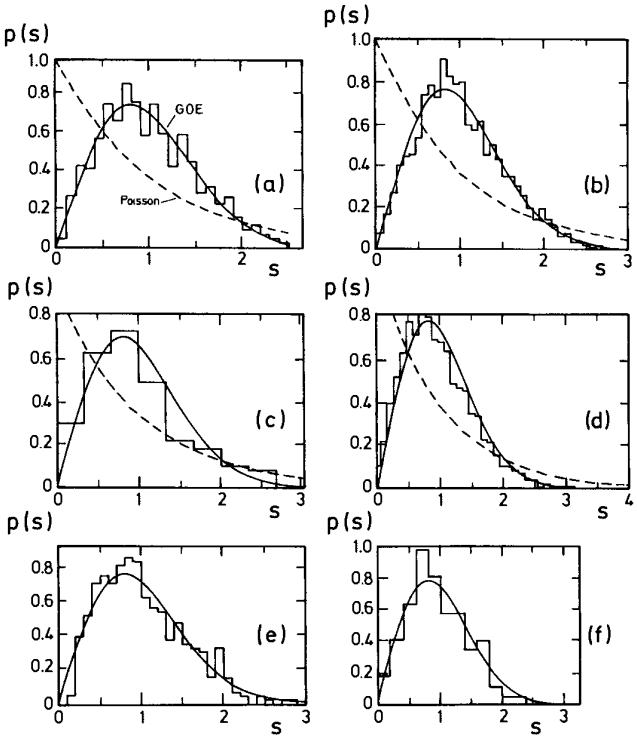

Figure 6.7: Nearest-neighbour spacing distributions for a) the Sinai billiard [111], b) a hydrogen atom in a strong magnetic field[25][120], c) an NO_2 molecule [121], d) the vibration spectrum of a quartz block shaped like a three-dimensional Sinai billiard [122], e) the microwave spectrum of a 3 dimensional chaotic cavity [123], f) the vibration spectrum of an elastic disc shaped like a quarter stadium [124]. Image taken from [107].

Finally, we note that we have defined quantum chaos as referring to the quantum mechanical behaviour of classically chaotic systems. The BGS conjecture then characterises this behaviour. However, we have seen that such behaviour also appears in quantum systems without a clear classical analogue, such as mesoscopic systems and atomic nuclei. For this reason it is usually assumed that the BGS conjecture as

[24]Note that the non-integrability of Wigner's nuclei is due to the existence of a large number of degrees of freedom, while the non-integrability of the billiards, with only two degrees of freedom, is due to boundary conditions.

[25]Alongside billiard systems, the hydrogen atom in a strong magnetic field played a central role in the conceptual development of quantum chaos as another analytically tractable system (also with only two degrees of freedom), for which early experimental data was available.

stated above in fact *defines* fully chaotic quantum systems. This is the sense in which we will talk about systems which don't have a classical analogue as being quantum chaotic [134].

6.4.3 RMT and disordered systems

The development of quantum chaos has been closely linked to applications of RMT in the field of disordered systems, to which we briefly turn our attention. Such applications originally arose in *localisation theory*, the study of the properties of electrons in disordered materials birthed by Anderson's discovery of strong localisation in 1958 [75]. In such problems, the effect of disorder is usually simulated by introducing randomness into the physical model. For example, in the study of metallic resistance, since the exact distribution of the impurities off of which the conducting electrons scatter is not known, the impurity potential is modelled as an ensemble of impurity potentials. Observables are then calculated as averages over this ensemble. It is frequently assumed that the impurity potential is a Gaussian random process, so the ensemble has a Gaussian distribution. This results in a Gaussian distributed ensemble of single–particle Hamiltonians with some symmetry properties.

Despite these obvious similarities to RMT, the field of disordered systems proceeded independently from RMT and its applications until the discovery in 1983 of the *supersymmetric method*[26] by Efetov and collaborators [78, 79]. Applied to the problem of level statistics in small disordered metal particles[27], described by a 0-dimensional σ model, the supersymmetric method yielded surprising results: the resulting correlation function had exactly the form of the RMT result. The solution of this model was thus the first analytic confirmation of RMT.

Before the development of the supersymmetric method, the field–theoretical approach to localisation made use of the *replica trick*[28], introduced by Edwards and Anderson a decade earlier [76] in the study of spin glasses. While this method can deal with interacting systems and has broad applicability, it only works for perturbative calcu-

[26] While the supersymmetry in the context of this method does still involve the usual symmetry between bosonic and fermionic integration variables, the invariance properties of a relativistic field theory are absent - the fermionic variables are simply used as bookkeeping devices, lacking physical meaning.

[27] The application of RMT in the theory of small metallic particles goes back to 1965 [77]. RMT continues to be a key tool in the field of mesoscopic physics - a subdiscipline of condensed matter physics dealing with materials of an intermediate size. Here, in addition to spatial disorder, another source of randomness arises from wave reflection at the sample boundaries which in the classical limit would lead to chaotic motion. Such "quantum dots" can be viewed as quantum billiards.

[28] See Section 7.4.3

lations[29]. The supersymmetric method is in a sense complementary; it can model the non-perturbative features of non-interacting systems. Both methods have found wide application in RMT and are commonly used today in the treatment of randomness in physical systems.

Having given a thorough overview of the field of RMT, as well as its applications to the study of quantum chaos, we are suitably prepared to introduce a spectral statistical quantity which will facilitate the study of disordered quantum systems from a field theoretic perspective: the spectral form factor.

[29]We will have more to say about the replica trick in Chapter 7.

Chapter 7

The Spectral Form Factor

Having built up the necessary tools in the previous chapter, we now present an overview of what will serve as the key diagnostic of chaos for the remainder of this thesis, the spectral form factor (SFF). Our exposition here follows [90, 91, 184], and we encourage the reader to see [89] for a good review of the SFF and its applications to quantum chaos.

7.1 Spectral Rigidity

In our exposition of RMT in Chapter 6, the nearest-neighbour spacing distribution occupied center stage as the diagnostic used in the analysis of the chaos properties of experimental or numerical spectra. It contains information about all n-point correlation functions of *nearby* energy levels. There are other statistical quantities which contain, at the expense of information about higher order correlations, information about correlations between *pairs* of *well-separated* energy levels. Such quantities allow us to extract the universal character of long-range pair correlations typical of RMTs, which we may then use as diagnostic of chaos in the analysis of quantum systems. We introduce two such quantities here; the *number variance* and *spectral rigidity*.

The number variance $\Sigma^2(L)$ is defined as the variance of the number of levels $N(L)$ inside an energy interval of the unfolded spectrum containing L eigenvalues on average: $\Sigma^2(L) \equiv \langle N^2(L)\rangle - \langle N(L)\rangle^2$. For Poisson distributed spectra typical of integrable systems, the complete lack of correlations between energy levels gives rise to a linear number variance with unit slope $\Sigma^2(L) = L$ [90]. For Wigner-Dyson distributed spectra, on the other hand, level repulsion gives rise to a slow, logarithmically increasing number variance, provided that the spectral interval we consider satisfies $L \gg 1$ (thus taking into account correlations between well-separated eigenvalues). In

the GUE case, this universal behaviour is given by

$$\Sigma^2(L) = \frac{1}{\pi^2}(\log 2\pi L + \gamma + 1), \tag{7.1}$$

where $\gamma = 0.5772...$ is Euler's constant. This behaviour, of very small fluctuation around its average of the number of levels found in an interval of given length, is termed *spectral rigidity*. It signifies long-range pair correlations between levels, which we thus identify as another universal property of RMTs.

Somewhat confusingly, the spectral rigidity is not just a qualitative descriptor of the above phenomenon, but a statistical quantity itself, usually denoted $\Delta_3(L)$. While we will largely use the term in the former sense, we note that $\Delta_3(L)$ is defined [62], for a fixed interval L, as the least-squares deviation of the cumulative density of energy levels (a staircase function), from the best straight line fitting it. It can be thought of as a smoothed version of the number variance [107], and like the former it is linear in L for Poisson distributed spectra and logarithmic in L for Wigner-Dyson spectra.

As we shall see, the spectral rigidity of the spectrum can also be discerned from the characteristic behaviour of another statistical quantity, closely related to the pair correlator; the *spectral form factor* (SFF).

7.2 The SFF

The SFF, which we will call $g(T)$, was originally introduced in [88]. It is simply defined as the Fourier transform of the pair correlator (6.63),

$$g(T) = \int dE dE' R(E, E') e^{i(E-E')T}. \tag{7.2}$$

The Fourier transform takes us from the energy domain into a conjugate "time" domain. The SFF probes correlations between energy levels, where the time T determines the scale of the energy differences being probed: at very late times only individual energy levels are probed, while at earlier times the SFF is sensitive to correlations between levels that are much farther apart than the average level spacing. Like the spectral rigidity, the SFF thus contains information about the pair correlations between well-separated eigenvalues that the nearest-neighbour energy spacing distribution does not, but, as is clear from the definition, it contains no information about multi-point correlation functions.

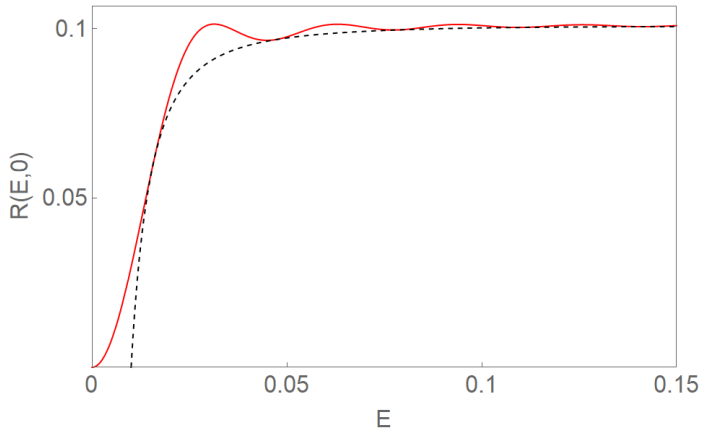

Figure 7.1: The pair correlator (7.3), where we have left out the delta function term, for $E' = 0$ and $N = 100$ (red) and its minimal envelope (dashed).

Recall that the large N GUE pair correlator (6.63), valid for $E - E' \ll 1$ and E, E' away from the edges of the spectrum, is given by

$$R(E, E') = P_\infty(E)P_\infty(E')\left(1 - \frac{\sin^2 \varepsilon}{\varepsilon^2}\right) + \frac{1}{N\pi}P_\infty(E)\delta(E - E') \tag{7.3}$$

where

$$\varepsilon = N\pi(E - E')P_\infty\left(\tfrac{E+E'}{2}\right), \tag{7.4}$$

and the large N average spectral density of the GUE is given by the Wigner semicircle distribution $P_\infty(E)$ (6.57). We have also now included a delta function term which accounts for the case where the two eigenvalues are coincident.

We plot the pair correlator (7.3) in Fig. 7.1, alongside its *minimal envelope* function obtained by setting $\sin^2 \varepsilon$ to unity. From considering this minimal envelope, it is clear that there is slightly higher probability for the second eigenvalue to be further away from, rather than closer to, the first. Since this change in probability decays only as a power, it is long-range, and when balanced against the confining effects of the random matrix potential $V(E)$, it gives rise to a rigid eigenvalue structure [91]. Thus the long-range, power-law repulsive anti-correlation between pairs of eigenvalues present in the pair correlator is another manifestation of the same spectral rigidity discussed above. As we shall see, this feature of the pair-correlation function manifests in Fourier space as a robust, prominent feature of the SFF for RMTs.

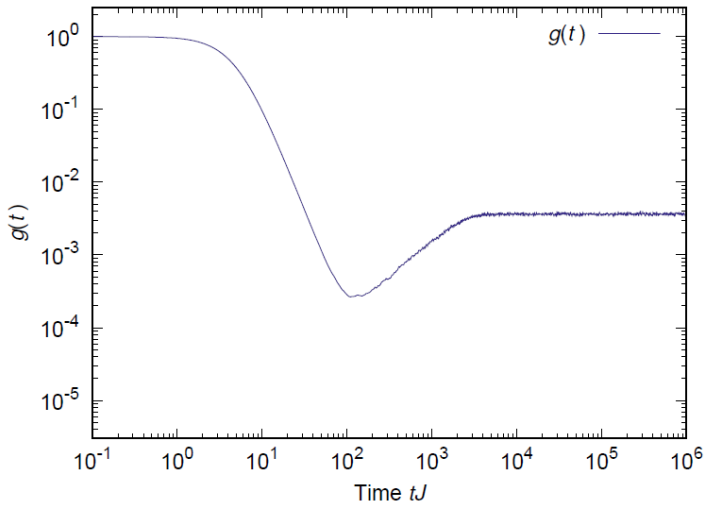

Figure 7.2: The SFF for the GUE with $N = 4096$, averaged over 1200 samples. Taken from [91].

7.3 Characteristic Features of the SFF

We begin by plotting the SFF for the GUE in Fig. 7.2, normalised so that $g(0) = 1$. The figure displays the key characteristic features of the SFF for an RMT. At $T = 0$, the SFF starts at unity and decays quickly, through a region called the *slope*. The slope ends when it reaches a minimum, the *dip*, at a time called the *dip time*. This is followed by a region of roughly linear increase called the *ramp*, which plateaus into a constant region, the *plateau*. Note that the SFF must be plotted on a log-log scale to make these features simultaneously visible.

Before we begin discussing each of these features in more detail, notice that the slope region of the SFF in Fig. 7.2 is smooth, while the ramp and plateau exhibit small, rapid fluctuations. Had we plotted the SFF for a single realisation of the ensemble, or performed the ensemble average over infinite realisations, the slope would look virtually identical. Such statistical quantities are called *self-averaging*: the ensemble average and the most probable value within the ensemble coincide, assuming infinite system size, or in our case, large N.

The fluctuations in the ramp and plateau in Fig. 7.2 are a result of the fact that only finitely many realisations have been numerically averaged over to obtain the plot; performing the true infinite ensemble average would yield a smooth curve. On the other hand, the SFF calculated for a single realisation of the ensemble would

exhibit much larger fluctuations in these regions, and we would obtain a curve which look very different from the ensemble averaged result[1]: the ramp and plateau are *not* self-averaging [99].

7.3.1 The slope

The slope can be explained by the first, factorised term in the pair correlator (7.3). Indeed, for most purposes the pair correlator can be approximated by the (order one) product of the individual Wigner semicircle distributions $P_\infty(E)$, neglecting the (order $1/N^2$) oscillating term which correlates the two. In this sense the slope comes from the *disconnected* part of the SFF,

$$\begin{aligned} g_d(T) &\equiv \int dE dE' P_\infty(E) P_\infty(E') e^{i(E-E')T} \\ &= \left| \int dE P_\infty(E) e^{iET} \right|^2 . \end{aligned} \tag{7.5}$$

We may evaluate this expression using the Wigner semicircle distribution (6.57) to obtain

$$g_d(T) = \left(\frac{J_1(2T)}{T} \right)^2 \sim \frac{1}{T^3}, \tag{7.6}$$

where J_1 is the first Bessel function. At large T, the Bessel function goes like $T^{-1/2}$, which gives the late time decay of the slope just before the dip time. Another perspective on this result is that the Fourier transform for large time argument depends on the region of the function which varies most rapidly, which in the case of the semicircle distribution is the spectral edge, which vanishes like a square root, whose Fourier transform is $T^{-3/2}$. Squaring this, we obtain the result (7.6).

We have already seen that unlike the higher-point correlation functions, the average spectral density of an RMT is not universal. It follows that the shape of the SFF slope, which is determined by this density, is also *not* universal. Different choices of random matrix potentials $V(M)$ will give rise to different spectral density edges, which will give rise to slopes different to the $1/T^3$ slope calculated here for the Guassian theory.

7.3.2 The ramp

To see the ramp analytically from the full SFF expression, one has to take the full pair correlator into account, including the subleading oscillating term. As a first

[1] See Fig. 8.6 for an example of this difference in the case of the SYK model.

approximation, we take the average spectral density $P_\infty(E)$ to be equal to a constant C (this amounts to the assumption that the eigenvalue spacing is everywhere uniform), so that the pair correlator (7.3) becomes a function only of the energy difference $x = E - E'$, with

$$R(x) \;=\; C^2\left(1 - \frac{\sin^2(N\pi Cx)}{(N\pi Cx)^2}\right) + \frac{C}{N\pi}\delta(x). \tag{7.7}$$

The SFF (7.2) is then given by [90]

$$g(T) \;\sim\; \int dx R(x) e^{ixT} \sim \begin{cases} T/2\pi N^2, & T < 2\pi NC, \\ C/\pi N, & T \geq 2\pi NC. \end{cases} \tag{7.8}$$

The early time, linear T behavior gives the ramp; the late time, constant region gives the plateau. The time at which the two intersect is known as the *plateau time*[2] or the *Heisenberg time*, T_H, given here by $T_H = 2\pi NC$.

We used a crude approximation to the spectral density to obtain this result. It nonetheless forms the basis of a more accurate and enlightening derivation of the ramp, as follows. Consider dividing up the area under the Wigner semicircular curve $P_\infty(E)$ into rectangular slices of equal width, allowing us to approximate this area to our desired precision á la Riemann sums [90]. The SFF is then given by the sum of the Fourier transforms of the pair correlators corresponding to each slice[3].

The functional form (7.8) of each of these contributions is evidently unaffected by the height C of that particular slice; only the plateau height $C/\pi N$ and plateau time $2\pi NC$ are affected. The sum of all of these contributions, each a linear ramp with a plateau, is also a linear ramp with a plateau. However, due to the different plateau times, the transition between the two regions may no longer appear sharp[4].

Since nothing about this derivation depended on the original semicircular shape of the distribution $P_\infty(E)$; the argument holds for any spectral density. We thus see that, unlike the slope, the ramp *is* universal. But what does this universal linear ramp tell us about the underlying level statistics? It turns out that if we replace the oscillating $\sin^2$ factor in (7.3) by its average value of one half, we still recover the

[2] In general, the plateau time is determined by the scale of nearest neighbour eigenvalue spacings.

[3] We make the approximation [90] of using the range of inegration $(-\infty, \infty)$ each time.

[4] The size of this effect depends on the system being studied. Indeed, the SFF for the GOE, GSE and GUE differ slightly in this regard: in the GUE the ramp and plateau intersect at a sharp corner (the sharpness is not visible in Fig. 7.2 due to the finite number of samples averaged over); in the GOE the transition between the two is smooth, and in the GSE they intersect at a kink.

ramp in (7.8): the SFF is then given by the Fourier transform of the $-1/E^2$ minimal envelope discussed earlier, which is linear in T. Since this power-law anti-correlation of the minimal envelope characterises spectral rigidity, this is then the sense in which spectral rigidity leads to the linear ramp[5]. Again we see that the ramp must be universal, as the consequence of the universal feature of spectral rigidity.

7.3.3 The dip time

We have seen that the slope comes from the edge behaviour of the spectral density, while the ramp comes from correlations in the bulk of the spectrum. The dip time is just the crossover between regimes where the bulk dynamics come to dominate those of the edge; it does not signal any new physical phenomenon [91]. We may estimate the dip time T_{dip} using (7.6) and (7.8) as satisfying $1/T_{\text{dip}}^3 = T_{\text{dip}}/2\pi N^2$, which gives $T_{\text{dip}} \sim \sqrt{N}$.

Comparing this to the plateau time $T_H \sim N$, we find $T_H/T_{\text{dip}} \sim \sqrt{N}$. Since the ramp is present for times $T_{\text{dip}} < T < T_H$, this then shows that the ramp survives, and indeed grows longer, in the large N limit [91].

7.3.4 The Thouless time

We now define an inherent timescale, valid for RMTs in general, called the *Thouless time* [152]. It is best understood as being the time domain analogue of the *Thouless energy*[6], a characteristic energy scale below (above) which the energy level correlations are universal (non-universal). In other words, it measures how many energy levels apart one can go before the characteristic correlations of RMT are lost [90]. The Thouless time is then the inverse of this energy. In the oft repeated statement in the literature that generic chaotic quantum systems are believed to exhibit RMT behavior at *late times*, the phrase *late times* means *times later than the Thouless time*.

In the context of the SFF, the Thouless time then refers to the time at which spectral rigidity, the characteristic RMT behaviour, appears. But this is just the time

[5]The effect of including the $\sin^2$ factor is to give the sharp kink where the ramp intersects the plateau: $\sin^2$ can be written as a constant plus a cosine, which oscillates at a specific frequency, showing up as this sharp feature in Fourier space. This kink however gets smoothed out since the argument of the $\sin^2$ is modulated by the non-constant spectral density, so the ramp is again the sum of many ramps each with different plateau times [103].

[6]The term has its origins in the study of disordered metals [131], in which it is given by the inverse of the characteristic time for an electron to diffuse through the metallic sample [130] and feel the presence of the boundary [132].

at which the ramp begins[7] - which is why the Thouless time is also known as the *ramp time*[8]. Looking at a plot of the SFF, one might naively then think that the Thouless time is just equal to the dip time. However, the ramp begins before the dip, where it is obscured by the slope until the dip time, where the two intersect. To find the Thouless time, one needs to look "beneath" the slope, and some method is then required to isolate the ramp from the slope.

For the GUE, one can simply calculate the connected and disconnected pieces of the SFF separately; the disconnected part contains the slope while the connected part contains the ramp. However, the task is less simple for more general models. For the SYK_4 model[9] for example, this technique fails due to the fact that the connected piece contains its own slope [91]. Various ways of dealing with this have been proposed involving variations of the SFF [92]. The "Gaussian-filtered SFF" [90] eliminates the slope by softening the hard edge of the spectral density from which it arises, allowing for the ramp to be visible at earlier times. The "connected unfolded SFF" [152] is the SFF computed using the unfolded spectrum and removing the disconnected piece.

7.3.5 The plateau

We have already seen the late time plateau show up in our calculation of the ramp (7.8) and the subsequent arguments. We simply add that the plateau characterises the discreteness of the spectrum. This claim is best motivated via a field theoretic view of the SFF, so we defer this to the discussion in Section (7.4.4).

7.4 The SFF for Quantum Theories

We have identified the linear ramp as a feature of the SFF that is universal, characterising the spectral rigidity of an RMT ensemble. Taking spectral rigidity as an expected feature of the spectrum of any quantum chaotic system (which the BGS conjecture tells us ought to have level correlations described by RMT), we may then use the linear ramp of the SFF as a diagnostic of quantum chaos.

[7] Note that the arguments given above imply that spectral density fluctuations from sample to sample do not affect the ramp structure, so it is a robust diagnostic of the Thouless time even without unfolding the spectrum [90], in contrast to other diagnostics such as the number variance.

[8] In Chapter 9, we will use this phrase to refer to the timescale at which another type of ramp, not linear but *exponential* in T, begins. As we shall discuss, such an exponential ramp is conjectured to be a characteristic of the SFF for *integrable* disordered systems [179]. In that case, it does not have the interpretation as a Thouless time, as the system in question is not chaotic and therefore does not exhibit RMT universality.

[9] See Chapter 8.

7.4.1 Definition

In order to apply this diagnostic, we need a method to calculate the SFF for a quantum theory. One may ask whether it can be computed by relating it to some observable in the theory. To this end, recall that the partition function for a quantum theory, which encodes all thermodynamic information about the theory, is given by

$$Z(\beta) = \operatorname{Tr} e^{-\beta H}, \tag{7.9}$$

where H is the Hamiltonian of the theory and β is the inverse temperature. Consider now the following object, obtained by analytically continuing $\beta \to iT$,

$$|Z(iT)|^2 = |\operatorname{Tr} e^{-iTH}|^2 = \left|\sum_k e^{-iTE_k}\right|^2 = \sum_{k,l} e^{i(E_k - E_l)T}. \tag{7.10}$$

We may average this quantity over a suitably defined ensemble of Hamiltonians, to obtain

$$\overline{|Z(iT)|^2} = \overline{\sum_{k,l} e^{i(E_k - E_l)T}} \tag{7.11}$$

$$= \overline{\int dE dE' n(E) n(E') e^{i(E-E')T}}$$

$$= \int dE dE' \overline{n(E)n(E')} e^{i(E-E')T}, \tag{7.12}$$

where in the second equality we have replaced each of the two sums over eigenvalues by an integral over the spectral density $n(E)$ (6.14). However, the ensemble average of the product of densities is nothing but the familiar pair correlator $\overline{n(E)n(E')} = R(E, E')$, which gives the probability of finding an eigenvalue at both E and E'. Comparing to the definition of the SFF (7.2), we have thus shown that

$$g(T) = \overline{|Z(iT)|^2}. \tag{7.13}$$

This gives us a prescription for calculating the SFF for a quantum theory. Note that the SFF calculated in this way doesn't have a direct physical interpretation, making it an unusual "observable". It serves purely as a tool with which to diagnose statistical features of the energy spectrum. In a quantum theory it is possible to consider a finite temperature generalisation[10] of the SFF where β is nonzero

$$g(\beta; T) = \overline{|Z(\beta + iT)|^2} = \sum_{k,l} e^{-\beta(E_k + E_l)} e^{i(E_k - E_l)T}. \tag{7.14}$$

[10]Note however that the SFF depends on level statistics of the spectrum and thus, strictly speaking, has no notion of temperature [169].

Written in this form, it is clear that the inverse temperature plays the role of a cut-off [92], exponentially suppressing those contributions to the SFF for which $\beta(E_k + E_l)$ is large. We will consider some examples of this when reviewing the SFF for the SYK model, but will mostly stick to the $\beta = 0$ case.

Practically speaking, the SFF (7.13) may be computed for a given quantum theory by diagonalising the Hamiltonian (using numerical methods, as this is seldom possible analytically for the chaotic cases of interest) for a large number of Hamiltonians from the relevant ensemble, and simply calculating the ensemble average of the object $\sum_{k,l} e^{i(E_k - E_l)T}$ as per (7.11). However, the path integral approach to a quantum theory offers other, more sophisticated methods of calculating the object $Z(\beta)$, which may then be extended to its analytically continued counterpart which appears in the SFF (7.13).

7.4.2 Disorder averages

Recall that taking the ensemble average of $|Z(iT)|^2$ in (7.11) was crucial in making the connection with the SFF, via the pair correlator in (7.12). Since we are now considering quantum theories and not RMTs, instead of averaging over ensembles of matrices, we must now average over ensembles of *Hamiltonians*. How will such ensembles be defined?

For the purposes of this thesis, our ensemble averages will always be averages over *disorder*. In particular, we will consider quantum theories with *disordered couplings*, namely, couplings constants in the Hamiltonian of the theory which are randomly drawn from some probability distribution. Such theories are not described by a particular Hamiltonian, but by the ensemble of Hamiltonians described by that distribution. Making a particular choice for the various disordered couplings gives us a particular realisation of the theory. In order to calculate n-point correlation functions, we need to perform a *disorder average* over the ensemble. Additionally, we must perform the usual averaging using the path integral, corresponding in real (imaginary) time to a sum over quantum (thermal) fluctuations . In general, we denote the former averaging by $\overline{\cdot}$ and the latter, where necessary, by $\langle \ \cdot \ \rangle$. The order in which we carry out these two types of averages is important, and correspond to two different types of disorder: *quenched* and *annealed*.

For a general disordered QFT in imaginary time, one may think of the disorder average as a sum over *disorder fluctuations*, which take place on some timescale. If this timescale is longer than the timescale which characterises the thermal fluctuations, then the fields thermally equilibrate *first*, for a fixed realisation of disorder.

This corresponds to evaluating the thermal path integral first, to obtain the partition function, from which the correlation functions can then be computed as functions of the random couplings. The disorder average is then taken as the final step in the calculation. When treated in this way, the disorder is said to be *quenched*.

If, on the other hand, the timescales of the thermal and disorder fluctuations are comparable, one may think of the dynamical field variables and the disorder couplings fluctuating and thermalizing together. This amounts to taking the disorder average of the thermal path integral *first*, and then evaluating the resulting path integral to obtain the disorder-averaged partition function, from which the correlation functions can be computed. In this case, the disorder is said to be *annealed*.

As an example, for quenched disorder, the free energy is $\overline{\log Z}$, for annealed disorder it is $\log \overline{Z}$. Annealed quantities are more straightforward to calculate using standard techniques, while quenched quantities are much more difficult. It was this difficulty that necessitated the development of advanced methods for performing quenched averages; the replica trick and the supersymmetric method (see Section 6.4.3).

7.4.3 Replicas

We have already seen that the slope comes from the disconnected part of the SFF (7.5), which for a quantum theory is given by[11]

$$g_d(T) = \left|\overline{Z(iT)}\right|^2, \tag{7.15}$$

which is simply the modulus squared of the disorder-averaged partition function after we have performed the analytic continuation $\beta \to iT$. To obtain the full SFF for a quantum theory, we must take the disorder average of the *square* of the (analytically continued) partition function. In practice, this requires us to introduce two copies of the theory called *replicas*, one for each of the two copies of the partition function inside the disorder average. Each replica has its own distinct set of fields, usually distinguished by replica indices $\alpha = 1, 2$. The random couplings in the two are taken to be the *same*. Taking the disorder average of the product of these two partition functions then yields what can be thought of as a new theory, with an action that *couples* fields with different replica indices. The path integral for this theory must then be evaluated to obtain the full SFF. The best method for this is precisely the introduction of the collective field variables mentioned earlier, with the exception that these fields are now two-index objects (matrices) in replica space[12], $G_{\alpha\beta}$ and $\Sigma_{\alpha\beta}$.

[11] The connected part of the SFF is of course given by $g_c(T) = g(T) - g_d(T)$.

[12] We will discuss this method further when we use it in Chapter 9.

Clearly the full SFF is then a much trickier object to compute than its disconnected component $g_d(T)$.

Having discussed replicas, we may finally state in simple terms the essence of the replica trick, which may be written as

$$\overline{\log Z} = \lim_{M \to 0} \frac{\overline{Z^M} - 1}{M}. \tag{7.16}$$

This equation is easily justified by Taylor expanding the right hand side. It states that calculating the quenched average of the free energy is equivalent to calculating the disorder average of the product of M partition functions, each of which involves a distinct replica, then taking the number of replicas to infinity. Note that by contrast, in the annealed calculation of the SFF outlined above, we only require two replicas as opposed to infinitely many.

7.4.4 Time Averaging

More generally, one may ask if it is possible to meaningfully calculate the SFF for a non-disordered quantum theory. Is there any other kind of averaging we can perform? One alternative, for a suitably large Hilbert space, is to perform a time average instead of an ensemble average. By time averaging over a parametrically small window we may smooth out the fluctuations in the parts of the SFF which are not self-averaging (the ramp and plateau), which will then restore the universal characteristic RMT behaviour of the SFF in the case of a chaotic theory. In this sense it is still meaningful to discuss features of the full SFF (not just its self-averaging features) even in an ordinary quantum theory without disorder [102].

Time averaging is also useful as a simple way to quantify the late time behavior of an observable: the late time behaviour washes out the early time behaviour in the average, provided the average is performed over a sufficiently long time. For quantum theories, we can then easily understand the presence of the late time plateau by considering the long-time-averaged SFF [91]

$$\lim_{t \to \infty} \frac{1}{t} \int_0^t dT |Z(iT)|^2 = \lim_{t \to \infty} \frac{1}{t} \int_0^t dT \sum_{k,l} e^{i(E_k - E_l)T} = \sum_k N_k^2, \tag{7.17}$$

where N_k is the degeneracy of the energy level E_k. Here we have used the fact that after time averaging, the fluctuating phases $e^{i(E_k - E_l)T}$ cancel out all terms except those for which $E_k = E_l$. Assuming a chaotic system with level repulsion, we have that $N_k = 1$ for all k. The sum (7.17) then simply counts the number of energy levels

of the system, which is equal to L, the size of the Hilbert space. This then approximates the constant value which we expect the SFF to take at late times: the plateau. It turns out that the long-time average would have vanished if we had replaced the discrete sum in (7.17) by an integral over a smooth density [91]. It is in this sense that the existence of the SFF plateau is a result of the discreteness of the spectrum[13].

On the other hand, for $T = 0$, simply looking at (7.11) shows that the SFF takes the initial value[14] $\sum_{k,l} 1 = L^2$. However, the SFF for a quantum theory is often normalised such that $g(0) = 1$, which necessitates working with the normalised object $Z(\beta+iT)/Z(\beta)$ instead of $Z(\beta+iT)$. For nonzero β, there is then a difference between the annealed and quenched treatment of the SFF, since

$$\overline{\left(\frac{|Z(\beta+iT)|^2}{Z(\beta)^2}\right)} \neq \frac{\overline{|Z(\beta+iT)|^2}}{\overline{Z(\beta)^2}}. \tag{7.18}$$

In the case of the SYK model, $Z(0)$ is a constant which is independent of the random couplings. For $\beta = 0$ then, the normalisation is unaffected by the disorder average and one can define the SFF unambiguously.

7.5 The out-of-time-order correlator (OTOC)

Our treatment of quantum chaos thus far has focused entirely on spectral statistics[15]. We now shift gears and present an alternative means of characterizing quantum chaos: the so-called out-of-time-order correlators (OTOCs). While entirely distinct from RMT, we briefly review the topic here for completeness and later reference.

Initially discussed in the 1960s in the context of few-body chaos [125], OTOCs were recently rediscovered in the general many-body context [128] for the purposes of understanding the quantum chaotic nature of black holes [126, 127]. The use of OTOCs as a diagnostic of chaos is motivated by the classical definition of chaos: sensitive dependence on initial conditions. For two points in phase space separated initially by an amount $\delta x(0)$, in a chaotic system this separation will initially diverge

[13] This has been a major reason for the surge in research interest in the SFF in recent years: as a probe of the quantum nature (discrete energy spectrum) of black holes [98].

[14] While for a chaotic theory with Wigner-Dyson statistics we have seen that these two regimes are separated by the characteristic slope, dip and ramp structure (sometimes referred to as the *correlation hole*), for a theory with Poisson statistics we simply expect these regimes to be connected by a monotonically decreasing function [103].

[15] Note that there are spectral statistical quantities that are used as diagnostics of quantum chaos which we have not considered in this thesis, such as the average adjacent gap ratio [84].

exponentially, at a rate $\delta x(t) = \delta x(0) e^{\lambda_L t}$, where λ_L is the *Lyapunov exponent*. Using the standard definition of the Poisson bracket, this gives

$$e^{\lambda_L t} = \frac{\partial x(t)}{\partial x(0)} = \{x(t), p(0)\}. \tag{7.19}$$

While we have already discussed how the notion of a trajectory is lost in the fully quantum regime of a system, let us consider the semiclassical regime, in which the standard generalization to quantum systems consists of replacing the Poisson bracket by a commutator (up to a factor of $\hbar$). As the commutator is generally an operator, we can take a thermal expectation value, but this always vanishes in the thermal state as a result of phase cancellations [101]. Considering instead the square of the commutator [125], we obtain the nonvanishing result

$$\langle [x(t), p(0)]^2 \rangle \sim \hbar^2 e^{2\lambda_L t}. \tag{7.20}$$

This quantity consists of sums of out-of-time-order four-point functions, which must then exhibit exponential growth if the system is to be defined as chaotic. Generalising this to a diagnostic of chaos for general quantum theories, we simply consider two generic operators in the theory, W and V, and look for the characteristic behaviour

$$\langle W(t)V(0)W(t)V(0) \rangle \sim e^{\lambda_L t}. \tag{7.21}$$

A positive value of this *quantum Lyapunov exponent* λ_L is then taken to be a signature of strong many-body chaos. The timescale at which the exponential behavior becomes dominant is known as the *scrambling time*, and signals the appearance of quantum effects of chaos. The so-called Maldacena-Shenker-Stanford (MSS) bound [144] $\lambda_L \leq \frac{2\pi}{\beta}$ gives the maximum value that the quantum Lyapunov exponent can take, allowing for the identification of a class of maximally chaotic systems which saturate this bound. Such systems include black holes, and the SYK model, about which we will have more to say in Chapter 8.

While it is currently thought that both spectral statistics and the behavior of the OTOC serve as central diagnostics of chaos, the precise nature of their relation is not yet understood[16]. Spectral statistics take a statistical approach and offer a description which is valid at late times, when RMT universality sets in, while OTOCs take a field theoretic approach, and are valid at short times where the semiclassical motivation for their use (see Section 7.5) applies. The two diagnostics offer different descriptions of the onset of chaos: the scrambling time is not the same as the Thouless time [90].

[16] In fact, at present it is conceivable that some systems could be chaotic according to one and not the other [92].

The notion of maximal chaos, characterised in terms of the Lyapunov exponent of the OTOC, has no characterisation from the perspective of spectral statistics. Some connections between the two have however been made: it has been conjectured that systems with larger (smaller) Lyapunov exponents should exhibit universal RMT behavior at earlier (later) times [92], and it has been argued that the SFF can be obtained from the OTOC by an averaging procedure [93, 173]. Indeed, the SFF in its field theoretic formulation discussed above may present the best opportunity for making contact with the OTOC characterisation of quantum chaos.

Having given an in-depth overview of the SFF in this chapter, with a particular focus on its applicability to the study of quantum systems from a field theoretic perspective, we now turn our attention fully towards quantum field theory. In particular, we study a model which has generated huge interest from the perspective of quantum chaos in recent years, and which presents an ideal context in which to explore the interesting physics underlying the characteristic features of the SFF: the SYK model.

Chapter 8

The SYK Model

The Sachdev-Ye-Kitaev (SYK) model [136, 137, 138] details the properties of a family of (0+1)-dimensional quantum mechanics of N Majorana fermions with all-to-all, random q-fermi interactions (we will sometimes refer to these as SYK_q models). In recent years, it has become a reference model for the study of many-body quantum chaos, and provides an interesting context in which to consider the various ideas and diagnostics introduced in the previous chapter.

8.1 The Model

The SYK_q model contains N Majorana fermions with a q-body interaction, where q is even. The Hamiltonian is given by[1]

$$H = (i)^{q/2} \sum_{1 \leq i_1 < i_2 < \ldots < i_q \leq N} J_{i_1 i_2 \ldots i_q} \chi_{i_1} \chi_{i_2} \cdots \chi_{i_q}, \tag{8.1}$$

where χ are the Majorana fermions which obey the anticommutation relations

$$\{\chi_i(\tau), \chi_j(\tau')\} = \delta_{ij} \delta(\tau - \tau'). \tag{8.2}$$

[1]The prefactor of $(i)^{q/2}$ is there to enforce hermiticity. Notice that the fermions have length dimension $[\chi] = L^0$, which means that the coupling constants $J_{i_1 i_2 \ldots i_q}$ have dimensions of inverse length $[j_{i_1 i_2 \ldots i_q}] = L^{-1}$ for any q, making H a relevant operator in the renormalisation group sense. This will allow us to speak of the strong-coupling ($J \gg 1$) limit and the low-energy/infrared limit of the theory interchangeably.

Each $J_{i_1 i_2 \ldots i_q}$ is taken to be a real variable drawn from a random Gaussian distribution, satisfying for the q=4 case,

$$P(J_{ijkl}) = \sqrt{\frac{N^3}{12\pi J^2}} \exp\left(-\frac{N^3 J_{ijkl}^2}{12 J^2}\right), \tag{8.3}$$

$$\overline{J_{ijkl}} = 0, \tag{8.4}$$

$$\overline{J_{ijkl} J_{i'l'k'l'}} = \frac{3! J^2}{N^3} \delta_{ii'} \delta_{jj'} \delta_{kk'} \delta_{ll'}. \tag{8.5}$$

The overall scale of the Hamiltonian is set by the constant J, which has units of energy. It follows from the fermionic anticommutation relations that $J_{i_1 i_2 \ldots i_q}$ is completely antisymmetric in its indices.

The standard SYK_4 model [136] model has some well-documented and remarkable properties [138]:

- It manifests an *emergent conformal symmetry* at low energies and large N.
- It is *solvable* in this limit. At zero temperature and large N, the solution to the Schwinger-Dyson equation for the thermal fermionic two-point function is

$$\langle \chi_i(\tau) \chi_j(0) \rangle = \left(\frac{1}{4\pi J^2}\right)^{1/4} \frac{\mathrm{sgn}(\tau)}{|\tau|^{1/2}} \delta_{ij}\,, \tag{8.6}$$

  in the infrared and for $\tau \gg 1/J$.
- It is *maximally chaotic*, in the sense that the quantum Lyapunov exponent, extracted from the out-of-time-ordered thermal fermion 4-point function, saturates the MSS bound $\lambda_L \leq 2\pi/\beta$ at inverse temperature β.

The SYK model is a rare example of a quantum mechanical system which is strongly interacting, but nonetheless solvable at large N, where one can sum over all the Feynman diagrams and obtain a closed form expression for the correlation functions. This makes it of interest from a wide variety of perspectives. In the field of condensed matter, in which the model originally appeared as the SY model [136], it is important in the study of strange metals/non-Fermi liquids [140]. Through the idea of *holographic duality*, the SYK model acquires significance in the study black holes and two-dimensional Anti-de Sitter space (AdS_2) [142, 141]. We will however primarily be interested in the model from the perspective of the theory of quantum chaos, in which it has played a singular role in recent years.

The SYK model is an example of a quantum theory with disordered couplings described in Section 7.4.2. It is described by the ensemble of Hamiltonians described by the Gaussian distribution (8.3) of couplings J_{ijkl}. Since the couplings in the SYK model are time-independent, the disorder would ordinarily have to be treated as quenched. However, in the large N limit, it has been shown that one obtains the same results treating the disorder as quenched or annealed[2] [146]. This convenient fact allows for two complementary approaches to be taken when studying the large N SYK model.

The first approach it to treat the disorder as annealed and take the disorder average of the path integral first. The disorder-averaged action thus obtained may be simplified by the introduction of *collective field variables*, commonly denoted by G and Σ. The path integral over the original fermionic χ variables can then be evaluated, leaving an *exact* rewrite of the theory, now described by an action written in terms of the collective G and Σ fields only[3]. The key point is that this action turns out to be *semiclassical*, with a coefficient proportional to N. In this way, the large N limit appears naturally, and the theory becomes amenable to saddle point methods in this limit. Correlation functions may be computed by studying the saddle point and small fluctuations around it, and diagrammatic perturbation theory can be completely avoided. We will use this approach in Chapter 9.

In the second, complimentary approach, the disorder is treated as quenched. Standard Feynman perturbation methods are applied to the path integral for the Hamiltonian (2.34), to calculate the correlation functions of the fermionic fields χ in terms of the random couplings. At strong coupling, the large N solvability of the theory then manifests in the following way: after taking the disorder average of each Feynman diagram, the sum over the subset of diagrams which contribute at leading order in N can be performed exactly, yielding closed form expressions for the correlation functions. This is the approach we will take in this chapter.

8.1.1 Feynman diagrams

For $q = 0$, the SYK model is simply the theory of free fermions in $0 + 1$ dimensions. This is an exactly conformal quantum mechanics of $2^{N/2}$ zero-energy states and a

[2]Treating quenched disorder as annealed is however generally unreliable at low temperature. In this case, breakdown of the annealed approximation may signal the onset of a spin glass phase [146].

[3]These fields turn out to be *bilocal* in time, with the field $\Sigma(t, t')$ as the Lagrange multiplier imposing the definition $G(t, t') = \frac{1}{N}\sum_{i=1}^{N} \chi_i(t)\chi_i(t')$. More on this in Chapter 9.

global $SO(N)$ flavour symmetry, with two-point function in frequency space given by

$$G_{ij}^{(0)}(\omega) = -\frac{1}{i\omega}\delta_{ij}. \tag{8.7}$$

When calculating Feynman diagrams for the $q > 0$ theory (see Fig. 8.1), everything proceeds in the standard fashion, with the usual Wick contractions between fields given by the free propagator (8.7) and denoted by black lines. However, every 4-point vertex comes with a factor of J_{ijkl}, and these must be averaged over the distribution (8.3). This disorder averaging happens pairwise (since diagrams involving an odd number of vertices give a vanishing contribution), and is denoted graphically by a dashed line connecting two vertices. As per (8.5), such a disorder contraction yields a factor proportional to J^2/N^3 if the two disordered couplings have matching indices, and vanishes otherwise.

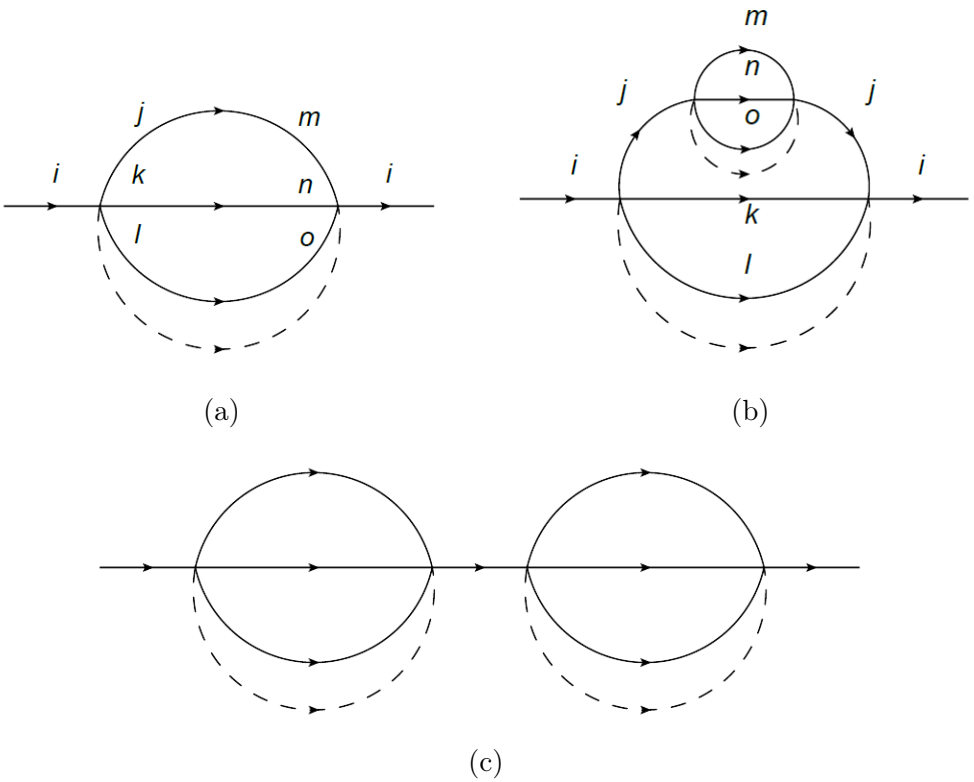

Figure 8.1: The set of Feynman diagrams which contribute in the large N limit. Black lines denote free propagators and dashed lines denote disorder contractions.

Let us now check which diagrams contribute at leading order in N. Consider the only diagram at second order in the couplings, the so-called *melonic diagram*, in

Fig. 8.1a. The disorder contraction causes the contribution of this diagram to vanish unless $j = m$, $k = n$ and $l = o$, in which case each of the sums over these three internal indices yield a factor of N. The total contribution of the diagram is then proportional to $N^3(J^2/N^3) = J^2$. Therefore, any diagram built out of these melonic diagrams, such as the diagrams in figures 8.1b and 8.1c, survive in the large N limit.

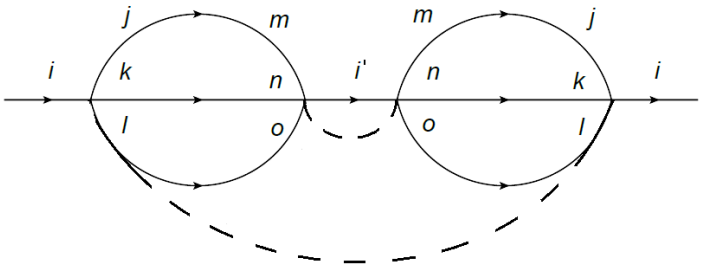

(a)

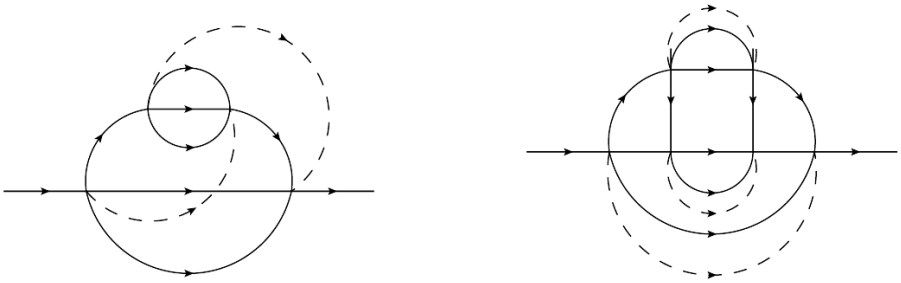

(b) (c)

Figure 8.2: Some examples of Feynman diagrams which contribute at subleading order in N, and can be ignored in the large N limit.

On the other hand, consider the diagram in Fig. 8.2a, where the indices have already been fixed such that the disorder contractions don't vanish. Since the indices internal to each melon don't match, three of the seven sums over free indices just fix $j = m$, $k = n$ and $l = o$. The remaining four sums yield a factor of N each, so the diagram contributes at order $N^4 \left(J^2/N^3\right)^2 = J^4/N^2$. It can thus be neglected in the large N limit.

It turns out that only diagrams built out of melonic diagrams, as in Fig. 8.1, survive in the large N limit. All other diagrams, such as those depicted in Fig. 8.2, are subleading in N and can be neglected. To calculate the full large N two-point function, we must then sum all of the leading order diagrams, which is best achieved using standard Feynman diagrammatic methods.

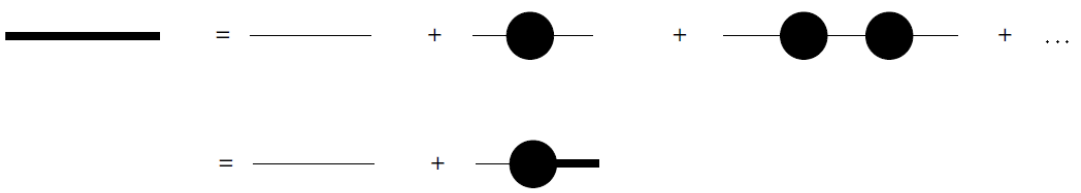

(a) Definition of the full two-point function (thick line).

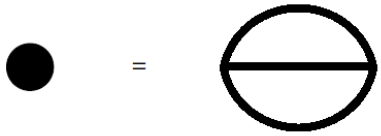

(b) Definition of the self energy (blob).

Figure 8.3: Diagrammatic representation of the large N Schwinger-Dyson equations for the $q = 4$ SYK model. These are used to sum the leading order diagrams shown in Fig. 8.1. Blobs represent the self energy, Σ, thick lines represent the full two-point function G and thin lines represent the free two-point functions $G^{(0)}$.

In Fig. 8.3 we show the $q = 4$ diagrammatic Schwinger-Dyson equations, which sum all leading order diagrams in the large N limit. Defining the variables $\Sigma(\tau, \tau')$ for the self energy and $G(\tau, \tau')$ for the full two-point function, the diagrammatic equation in Fig. 8.3a may be written as

$$G(\tau_1, \tau_2) = G^{(0)}(\tau_1, \tau_2) + \int d\tau d\tau' G^{(0)}(\tau_1, \tau)\Sigma(\tau, \tau')G(\tau', \tau_2). \tag{8.8}$$

The corresponding equation in frequency space is

$$G(\omega) = G^{(0)}(\omega) + G^{(0)}(\omega)\Sigma(\omega)G(\omega), \tag{8.9}$$

which, using the expression for the free two-point function (8.7), can be rewritten as

$$\frac{1}{G(\omega)} = -i\omega - \Sigma(\omega). \tag{8.10}$$

The diagrammatic equation in Fig. 8.3b can likewise be written as

$$\Sigma(\tau, \tau') = J^2 G(\tau, \tau')^3. \tag{8.11}$$

These equations may be easily generalised to arbitrary q, in which case we obtain the large N Schwinger-Dyson equations

$$\frac{1}{G(\omega)} = -i\omega - \Sigma(\omega), \tag{8.12}$$

$$\Sigma(\tau, \tau') = J^2 G(\tau, \tau')^{q-1}. \tag{8.13}$$

Solving them will yield the full two-point function G and self energy Σ of the theory for any q. However, this is easier said than done, and no analytic solution exists for the general case[4]. In the weak coupling $J \ll 1$ limit we may neglect the self energy term in 8.12 and of course recover propagator for the free theory 8.7; this is the trivial limit of the theory. In the opposite, strong coupling $J \gg 1$ limit, we observe something remarkable. While most quantum theories become unsolvable at strong coupling (where standard perturbation theory generally breaks down), the SYK theory exhibits an emergent conformal symmetry, and becomes solvable.

8.1.2 Emergent Conformal Symmetry and Solvability

To see this, we take the $J \gg 1$ limit, and neglect the left hand side of (8.8) to obtain

$$G^{(0)}(\tau_1, \tau_2) = -\int d\tau G^{(0)}(\tau_1, \tau) \int d\tau' \Sigma(\tau, \tau') G(\tau', \tau_2). \tag{8.14}$$

This can only be true if

$$\int d\tau' \Sigma(\tau, \tau') G(\tau', \tau'') = -\delta(\tau - \tau''), \tag{8.15}$$

which, using (8.13), can be written

$$J^2 \int d\tau' G(\tau, \tau')^{q-1} G(\tau', \tau'') = -\delta(\tau - \tau''). \tag{8.16}$$

Thus, to find the full two-point function in the strong coupling limit, we simply need to find a function $G(\tau, \tau')$ which satisfies this equation. But before trying to solve it explicitly, we can learn something crucial by considering its bahaviour under the reparametrisation $\tau \to f(\tau)$. Such a reparametrisation is simply a diffeomorphism, and in one dimension, the diffeomorphism group is isomorphic to the conformal group, $\mathrm{Diff}(\mathbb{R}) \cong \mathrm{Conf}(\mathbb{R})$. Assuming that our fermion fields transform as primary operators of conformal dimension Δ, the two-point function then transforms as

$$G(\tau, \tau') \to |f'(\tau) f'(\tau')|^{\Delta} G(f(\tau), f(\tau')). \tag{8.17}$$

[4]We will see in Chapter 9 that the $q = 2$ case is the exception.

We now show that the strong coupling Schwinger-Dyson equation (8.16) is invariant under such a conformal transformation, provided that our fermions have conformal dimension

$$\Delta = \frac{1}{q}. \tag{8.18}$$

Setting $\sigma = f(\tau)$, the left hand side of (8.16) transforms into

$$\begin{aligned}
& J^2 \int d\tau' |f'(\tau) f'(\tau')|^{\Delta(q-1)} |f'(\tau') f'(\tau'')|^{\Delta} G(\sigma, \sigma')^{q-1} G(\sigma', \sigma'') \\
= \; & |f'(\tau)|^{\Delta(q-1)} |f'(\tau'')|^{\Delta} \underbrace{J^2 \int d\tau' |f'(\tau')|^{\Delta q} G(\sigma, \sigma')^{q-1} G(\sigma', \sigma'')}_{= J^2 \int d\sigma' G(\sigma,\sigma') G(\sigma',\sigma'')^{q-1} = -\delta(\sigma - \sigma'') \text{ by (8.16)}} \\
= \; & -\left| \frac{f'(\tau'')}{f'(\tau)} \right|^{\Delta} |f'(\tau)| \delta(\sigma - \sigma'') \\
= \; & -\left| \frac{f'(\tau'')}{f'(\tau)} \right|^{\Delta} \delta(\tau - \tau'') \\
= \; & -\delta(\tau - \tau''),
\end{aligned} \tag{8.19}$$

where in the third equality we have used the transformation property of the delta function

$$\delta(f(\tau) - f(\tau')) = \frac{1}{|f'(\tau)|} \delta(\tau - \tau'). \tag{8.20}$$

We have thus shown that the large N, strongly coupled theory is indeed invariant under conformal transformations provided that the two-point function transforms as prescribed in (8.17) and our fermion fields are primary operators of conformal dimension $\Delta = 1/q$.

We may now seek an explicit solution for the full two-point function G. Motivated by the emergent conformal symmetry, we make the ansatz for a conformal two-point function [138]

$$G_c(\tau) = A \frac{\mathrm{sgn}(\tau)}{|\tau|^{2\Delta}}, \tag{8.21}$$

which may be substituted into (8.16) to find (see Appendix D for the details)

$$A = \left[\frac{1}{\pi J^2} \left(\frac{1}{2} - \Delta \right) \tan(\pi \Delta) \right]^{\Delta}. \tag{8.22}$$

For $q = 4$, this solution reduces to the result (8.6).

Having solved the Schwinger-Dyson equation at strong coupling, let us examine the solution (8.22). It turns out that this two-point function is only invariant under $SL(2)$ transformations, where $SL(2)$ is a subgroup of the conformal group which acts as

$$\tau \mapsto \frac{a\tau + b}{c\tau + d}, \quad \text{where} \quad ad - bc = 1. \tag{8.23}$$

The symmetry under the full conformal group exhibited by the Schwinger-Dyson equation (8.16) is thus *spontaneously broken* by the full two-point function (8.22). The Goldstone modes associated with this symmetry breaking play a key role in the chaos properties of the model.

8.1.3 The Schwarzian Theory

In the strong coupling limit, the four-point function can be constructed out of the full conformal two-point functions (8.21) derived above[5] in the following way. At large N, it reduces to a sum of *ladder diagrams*, in which two "side rails", connecting to the four external lines, are joined by any number of "rungs" comprising pairs of internal lines. The sum over all such diagrams can be performed using standard techniques. Namely, defining a kernel, K, that corresponds to adding a rung to a ladder, the sum of all ladders is proportional to the geometric series $\frac{1}{1-K}F_0$, where F_0 is the diagram with no rungs. Inverting the kernel to evaluate this expression then leads to an expression for the four-point function in terms of a sum over intermediate states [138].

However, the geometric series above contains a singular contribution, corresponding to the case when the ladder kernel $K = 1$ (so the geometric series diverges). This contribution comes from the aforementioned Goldstone modes associated with the spontaneous symmetry breaking of the full conformal group down to the $SL(2)$ subgroup. To remove this unphysical singularity, one must study the *near-conformal limit*, in which the emergent conformal symmetry of the action for the theory in the strong coupling limit is *explicitly* broken by an additional term which is nonzero when evaluated on the reparametrisations[6] $\tau \mapsto f(\tau)$. This term is the *Schwarzian action*

$$S \propto -\frac{N}{\beta J}\int d\tau \, \{f, \tau\} \tag{8.24}$$

[5] Using holographic duality, the six-point function may also be calculated [166], which then together with the four-point function determines all higher-point correlation functions [183].

[6] This explicit breaking of the symmetry at the level of the action, in addition to the spontaneous symmetry breaking mentioned above, means that the Goldsone bosons are technically pseudo-Goldstone bosons, or "soft modes", as they now acquire nonzero action.

where $\{f, \tau\}$ is the Schwarzian derivative of $f(\tau)$ given by

$$\{f, \tau\} \equiv \frac{f'''}{f'} - \frac{3}{2}\left(\frac{f''}{f'}\right)^2 . \tag{8.25}$$

This $SL(2)$ invariant action then defines the so-called *Schwarzian theory* of reparametrisations [159, 160], which provides the low-energy description of the SYK model[7]. For large $N > \beta J$, the coefficient of the action (8.24) is large and so the Schwarzian theory is weakly coupled, dominated by small fluctuations about the saddle point configuration of f. On the other hand, when $\beta J > N$, the action describes a strongly coupled theory dominated by wildly fluctuating field configurations. One would not expect the partition function for such a theory to be analytically tractable, however, it turns out to be one-loop exact [159]. We will return to this point when discussing the SFF for the SYK model.

8.2 Chaos Properties

The SYK model is, famously, quantum chaotic[8]. We will briefly overview the results which support this claim, for the case $q = 4$. We will consider both the OTOC and spectral statistics as diagnostics of chaos, deferring a discussion of the SYK SFF to Chapter 7.

8.2.1 The OTOC

As the OTOC is a sum of four-point functions, it may be calculated using the results for the four-point function obtained above. It turns out that it is precisely the contribution of the Goldstone modes in the near-conformal limit, described by the Schwarzian theory, that gives rise to exponential growth of the OTOC characteristic of quantum chaos [138]. Moreover, the calculation yields a quantum Lyapunov exponent which saturates the MSS bound, $\lambda_L = \frac{2\pi}{\beta}$. This means that the SYK_4 model is *maximally* chaotic.

8.2.2 Spectral statistics

It has been shown that the spectrum of the SYK model exhibits RMT features [91, 150, 155], confirming the OTOC result that the theory is indeed quantum chaotic.

[7] It also describes some variations of the SYK model, such as the supersymmetric SYK model [161], at low energies.

[8] Again, the $q = 2$ case is the exception in this regard.

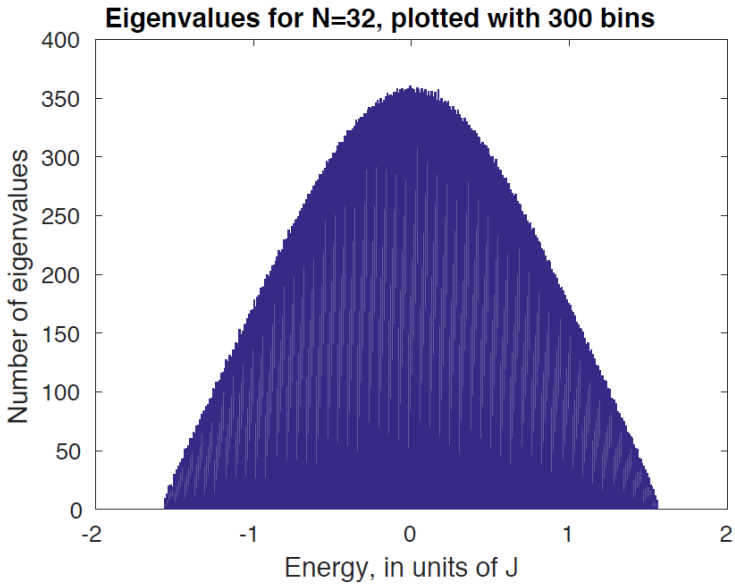

Figure 8.4: Spectral density for SYK_4 with $N = 32$ fermions. Taken from [138].

Firstly, we note that the particular RMT universality class that the SYK_4 model belongs to (according to its properties under time-reversal symmetry, see Section 6.2.3) depends on the type of allowed representations of the Clifford algebra of the Majorana fermions, which in turn depends on N through the quantity N mod 8 [150]. For N mod $8 = 2, 6$ the ensemble is GUE, N mod $8 = 0$ the ensemble is GOE and for N mod $8 = 4$ the ensemble is GSE[9].

The nearest-neighbour level spacing distribution for the model, shown in Fig. 8.5, has been shown to be consistent with RMT predictions [155]. The spectral density for a *particular* realisation of disorder[10] is shown in Fig. 8.4; it is clearly not described by the Wigner semicircle distribution. Since the spectral density is not universal, that the spectral density is not well described by RMT is not relevant to the chaos properties of the system. However, the spectral edge is well described by the Wigner semicircle, since it goes like a square root, a fact which will be relevant for the SYK SFF, to which we now turn our attention.

[9] See Appendix A of [91] and Appendix A of [150] for more details.

[10] While the result has not been averaged over the ensemble, since this is a self-averaging quantity we expect it to be consistent with the ensemble averaged result.

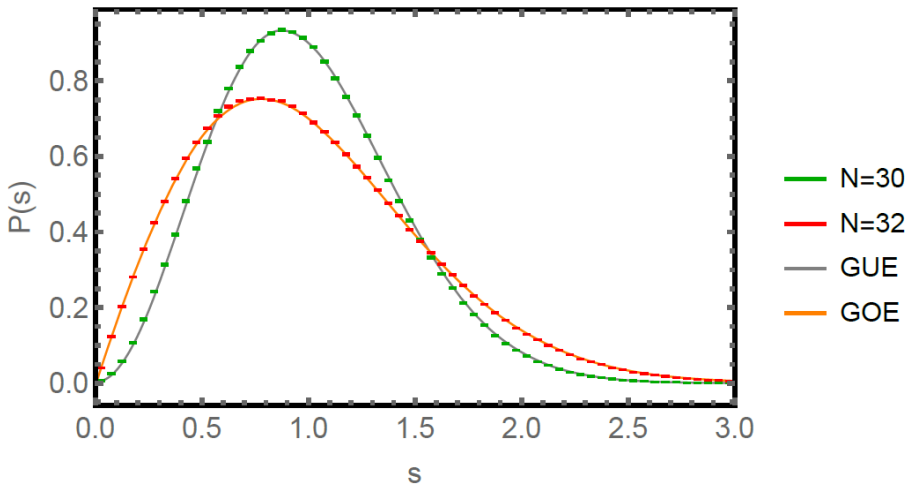

Figure 8.5: Unfolded nearest-neighbour level spacing distribution for SYK vs. RMT. The SYK results are obtained via exact numerical diagonalisation for $L = 12870$. Here s is measured in units of the mean spacing. Image taken from [91].

8.2.3 The SFF

In recent years, motivated primarily by the aforementioned applications to holographic duality, much work has been done calculating the SFF for various SYK like models[11]. Here we review the SFF results for the SYK_4 case studied in [90, 91, 147, 148, 149], where numerical results have been obtained for quenched disorder: the finite N Hamiltonian is exactly diagonalised for some realisation of disorder, with the ensemble average being performed afterwards. On the other hand, the analytical results have been obtained by treating the disorder as annealed, which makes for simpler calculations. As mentioned before, these approaches are complimentary since in the large N limit the quenched and annealed averages coincide.

[11] Particular examples for which the computation has been done include the double scaled SYK [176], sparse SYK [174] and supersymmetric SYK models [180, 181]. More generally, we note that the SFF has been calculated for QFTs such as holographic 2d CFTs [102], various Ising models [135, 175] and the Chern-Simons matrix model [221].

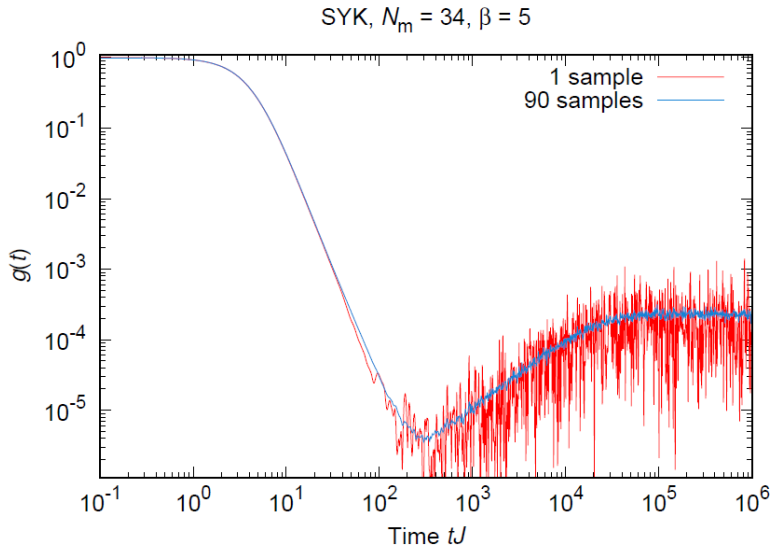

Figure 8.6: The SFF for the SYK_4 model, for $N = 34$ and $\beta = 5$. Image taken from [91].

In Fig. 8.6 we plot the SFF for the SYK_4 model. The similarities to the Gaussian RMT case are immediately apparent (see Fig. 7.2). We now turn to a comparison of the SFF features for the respective theories.

The slope: spectral edges and Schwarzian modes

Both the SYK and RMT slopes exhibit the same $1/T^3$ power-law decay at *large times*, where the SFF is described by the Fourier transform of the *edge* of the average spectral density. For the SYK model, the low-energy edge of the spectrum is described by the Schwarzian theory, and the one-loop exact result for this theory then yields a spectral edge which goes as a square root [103], just like the RMT Wigner semicircle. The difference between the RMT and SYK spectral densities in the *bulk* (where the RMT spectrum is semicircular but the SYK spectrum is not, see Fig. 8.4) manifests as different initial decays in the respective slopes at *early times*[12]. Comparing the two curves in Fig. 8.6 we also see that, like in the RMT case, the SYK slope is self-averaging while the ramp and plateau are not.

We may get another view of the SYK slope by recalling that in the field theory description, it is described by the disconnected part of the SFF, which is simply the modulus squared of the analytically continued partition function $Z(\beta + iT)$. In the

[12]The difference is not obvious when comparing figures 8.6 and 7.2.

collective field description of the theory, we have seen that the path integral expression for this partition function is semiclassical, and the saddle point contribution may be evaluated explicitly in the large N, conformal limit. For large values of $\beta+iT$ however, we need to consider fluctuations about this saddle point [91]. These are precisely the Goldstone modes described at low energies by the Schwarzian theory. As mentioned, the partition function of this theory is one-loop exact and may be calculated explicitly. The contribution from the Goldstone fluctuations can then be combined with the collective field saddle point contribution to give the partition function of the SYK model in the conformal limit. From this, one obtains the disconnected part of the large N, finite temperature SFF [91]

$$g_d(\beta, T) = \frac{\beta^3}{(\beta^2+T^2)^{3/2}} \exp\left\{-\frac{cNT^2}{\beta(\beta^2+T^2)}\right\}, \tag{8.26}$$

where c is the specific heat. Note that the time dependence of the exponent becomes negligible at late times $T > \sqrt{N}$ in which case we indeed have the power law decay $\sim 1/T^3$.

The ramp: non-diagonal saddles and symmetry breaking

The most important feature of the SYK SFF from the quantum chaos perspective is its linear ramp, clearly visible in Fig. 8.6. This large N ramp[13], however, cannot be explained by the contributions from or fluctuations around the same saddles which give rise to the slope as described above[14]. However, its presence is entirely expected given that we know the model to be chaotic from the OTOC result and we therefore expect its spectrum to exhibit RMT statistics. The challenge is then to explain the ramp using the large N collective field variables[15] $G_{\alpha\beta}$ and $\Sigma_{\alpha\beta}$.

The answer turns out to lie in the consideration of *non-diagonal* saddles. Recall that $G_{\alpha\beta}$ and $\Sigma_{\alpha\beta}$ are matrices in replica space, and may thus take values which are diagonal (where the only nonzero components have replica indices $\alpha = \beta$), or non-diagonal (where nonzero components with $\alpha \neq \beta$ correlate the respective replicas together).

[13] It is found numerically in [91] that as N is increased the plateau time grows faster than the dip time does, resulting in a more and more prominent ramp. This implies that the ramp is still a feature of the large N theory, just like in the RMT case.

[14] The plateau also cannot be explained in terms of fluctuations about the large N semiclassical path integral for the collective field description of the theory. In fact, it is described by doubly-nonperturbative effects of order $1/e^{e^N}$ [91, 184]. It can however be treated analytically by certain effective field theories [129], but we will not discuss this here.

[15] In the context of holography, these variables correspond to bulk gravity variables for a black hole. Finding an explanation of the ramp in terms of them is then motivated by the black hole information problem [184].

Quenched quantities computed for the large N SYK model using the replica trick generally assume that saddle point solutions are diagonal[16]. However, the arguments supporting this assumption are all only relevant to the infinite replica case, and are not conclusive for the two-replica case needed for the calculation of the SFF. While taking only diagonal solutions into account is sufficient for the two-replica calculation of the SYK slope outlined above, we will need to go further in order to explain the ramp.

Indeed, non-diagonal saddle point solutions for $G_{\alpha\beta}$ and $\Sigma_{\alpha\beta}$, whose existence has been motivated in [184], play the essential role in giving rise to the linear ramp. They give subdominant contributions at early times, so our explanation of the slope in terms of the diagonal saddles and the fluctuations about them remains valid. However, at late times, the non-diagonal saddles become dominant. Note that this late time contribution is non-perturbative, in the sense that it cannot be recovered by doing perturbation theory on (considering fluctuations about) the original diagonal saddles.

To see how these give rise to the linear ramp, we must consider the effect that they have on the symmetries of the theory. Since diagonal solutions do not correlate different replicas, each replica has an independent $U(1)$ time translation symmetry, giving the two-replica theory the symmetry group $U(1) \times U(1)$. On the other hand, non-diagonal saddle points correlate the two replicas, so that these time translations can no longer be applied independently. The symmetry of the theory is then spontaneously broken from $U(1) \times U(1)$ to the diagonal $U(1)$, giving rise to a Goldstone zero mode. This zero mode is degenerate with respect to the residual $U(1)$ symmetry, whose action then generates a degenerate saddle point manifold. This manifold has compact volume proportional to T, the periodicity of the real time circle. Crucially[17], the zero mode has vanishing action, so integrating over it in the path integral just gives a factor proportional to T: this is the linear ramp[18].

We will see a similar mechanism at play in our calculation of the SFF for the gauged complex SYK_2 model in Chapter 9, and will return to discuss the differences and similarities between these two cases in Chapter 10.

[16] This assumption is justified by exact diagonalization numerics [138, 91, 150], and by a physical qualitative argument [182, 186]. The existence of particular replica-non-diagonal saddle points in the quenched free energy path integral signals the onset of spin glass phase, but it has been argued that the SYK model has no such phase [190].

[17] See Appendix B of [184].

[18] This explanation applies to the SFF with $\beta = 0$; the explanation for the nonzero β case is more involved.

8.3 The SYK model and Holography

We conclude our review of the SYK by briefly mentioning the significance of some of the above results from the perspective of holography[19]. The Schwarzian theory, which describes the low-energy behaviour of the model, also describes a two-dimensional theory of gravity known as Jackiw-Teitelboim (JT) gravity, which arises in the near-horizon limit of an AdS_2 extremal black hole with dilaton [156, 157, 158]. Additionally, the SYK OTOC is characteristic of a maximally chaotic quantum system, a property shared by black holes [162]. These connections have motivated huge interest in the SYK model [215] as a low-dimensional toy model of many complex black hole phenomena, such as the black hole information paradox [126], traversable wormholes [163] and information scrambling [127]. However, JT gravity cannot be considered as a complete gravity dual of the SYK model as it incorporates only the low-energy features described by the Schwarzian action.

[19]The original SY model was first discussed from the perspective of holography in [142].

Chapter 9

SFF for the Gauged Complex SYK_2 Model

In this chapter we introduce a novel variant of the SYK model and calculate its SFF. While much of the discussion in the previous chapter focused on the standard $q = 4$ model, we begin by motivating why the simplest $q = 2$ case is worthy of study.

9.1 The SYK_2 Model

The SYK_2 model, with a disordered 2-fermi interaction term, is equivalent to a theory of free fermions with a random mass matrix. As we shall see, using the standard SYK approach to formulate the theory in terms of the collective field variables, the Schwinger-Dyson equations may be combined into a single quadratic equation. This may then be solved for the large N two-point correlation function for *arbitrary* coupling strength. This is in contrast to the $q > 2$ cases of the model, in which one can only find an analytic expression for the large N two-point function in the strong-coupling, conformal limit (see Section 8.1.2).

This great simplification makes the SYK_2 model particularly amenable to analytic study, where it has been shown to have the following basic features: firstly, it is an integrable model, as the OTOC does not exhibit the exponential growth characteristic of quantum chaos [165]. Secondly, it has an average spectral density given by the Wigner semicircle law in the large N limit [165, 91], just like the Gaussian RMT ensembles. However, despite these seemingly trivial features, the model has proven to be a worthwhile object of study.

In particular, the model may be used to study and better understand its $q > 2$ coun-

terparts. For example, in its collective field variable formulation, explicit subleading replica-diagonal saddle points of the model can be found. These may then be used as trial functions in an iterative procedure to generate the subleading saddles of the SYK_4 model, which cannot otherwise be found explicitly [91, 186].

The model is also interesting in its own right. For example, it has been proven to satisfy the Eigenstate Thermalization Hypothesis (ETH)[1] [223, 224] in the multiparticle sector [167]. Proving that a theory satisfies the ETH is generically very difficult due to the presence of non-linear interactions, and in this case the simple, quadratic nature of the SYK_2 model is its virtue - the model presents an analytically tractable context in which to test claims which are difficult to prove for theories with more complicated, higher-order interactions[2].

In this spirit, the SFF for the model [179, 177] and its *charged* counterpart [168], the complex SYK_2, have have been computed and studied from the perspective of spectral statistics and quantum chaos. There, despite the fact that the theory is integrable, the SFF is found to have non-trivial structure which does not reflect purely Poisson spectral statistics. Rather, the SFF is shown to exhibit the slope, dip and ramp structure characteristic of quantum chaos and Wigner-Dyson statistics. However, instead of the linear ramp which is characteristic of the latter, an *exponential* ramp is found. This combination of integrable and chaotic spectral signatures is conjectured to follow from the fact that in a many-body model such as SYK_2 there are single- and multi-particle sectors; while eigenvalues in the single-particle sector repel strongly due to the usual RMT level repulsion, eigenvalues in the multi-particle sector with very different particle numbers will repel only weakly [91].

In [179] the authors show that the two-replica action, relevant for the calculation of the SFF, possesses an unusual, large unitary symmetry, which gives rise to the exponential ramp. They conjecture that this exponential ramp should be a feature of *all* non-interacting, disordered systems, and attribute this behaviour of the SFF to the presence of a high-dimensional manifold of saddle points resulting from the symmetry group. The generalisation of the SYK_2 model which we consider in this chapter will provide another setting in which to test these claims, and we will discuss them further in Chapter 10.

[1] The main idea of the ETH is that individual energy eigenstates behave in many ways like a statistical ensemble, see [226].

[2] In the context of black hole thermalization, the model has also been studied in [101, 171, 172].

Chaotic-Integrable transition

We note that the transition between the integrable SYK$_2$ model and the chaotic SYK$_4$ model has been studied using the so-called *mass-deformed* SYK model [153, 92], whose Hamiltonian is written as the sum of the Hamiltonians of the two models. By adjusting the relative coupling strengths for the quadratic and quartic interactions (which are both disordered), one may observe the transition between chaotic and integrable behaviour at the level of both the OTOC and spectral statistics, although they do not agree on the precise value of the couplings at which the transition takes place.

More generally, any interaction which isn't quadratic is expected to break the integrability of the SYK$_2$ model. The resulting chaotic-integrable transition in the presence of a (non-SYK$_4$) four-fermi term has been studied analytically at the level of the SFF in [169, 170, 179][3], where the non-integrable interaction is treated as a perturbation about the SYK$_2$ solution. We will have more to say about this in Chapter 10.

Having motivated the SYK$_2$ model as worthy of study in its own right, we now proceed to introduce a novel variation of the model, which we will study in this chapter.

9.2 The Gauged Complex SYK$_2$ Model

Before introducing our model, we introduce the charged, or complex, SYK$_q$ model [141, 191, 192] in which the N Majorana fermions χ are replaced by N spin-0 complex fermions ψ and $\psi^\dagger$, which satisfy the anticommutation relations $\{\psi_a, \psi_b\} = 0$ and $\{\psi_a, \psi_b^\dagger\} = \delta_{ab}$. This model shares many properties with its more well-understood real counterpart, but differs in that it possesses a global $U(1)$ symmetry. For the $q = 4$ case, it is described by the action

$$I_{\text{CSYK}} = \int d\tau \left[\sum_{a=1}^{N} \psi_a^\dagger \left(\frac{d}{d\tau} - \mu \right) \psi_a - \sum_{a,b,c,d=1}^{N} J_{ab;cd}\, \psi_a^\dagger \psi_b^\dagger \psi_c \psi_d \right] . \tag{9.1}$$

Here, μ is a chemical potential that tunes the $U(1)$ charge $Q = \sum_{a=1}^{N} \langle \psi_a^\dagger \psi_a \rangle$ and the $J_{ab;cd}$ are now complex, independent, random couplings drawn from a Gaussian distribution with zero mean. They satisfy the symmetry properties

$$\begin{aligned} J_{ab;cd} &= -J_{ba;cd} = -J_{ab;dc} = J^*_{cd;ab} \,, \\ \overline{|J_{ab;cd}|^2} &= J^2 \,. \end{aligned}$$

[3] This transition has also been studied numerically from the perspective of spectral statistics in [178].

The novel model which we consider in this chapter, the *gauged* complex SYK$_2$ model, is obtained by gauging the global $U(1)$ symmetry by coupling the complex fermions to a one-dimensional, external[4] $U(1)$ gauge field, $A(t)$. There is no Maxwell kinetic term in (0+1)-dimensions, making the gauge field non-dynamical[5]. The Lagrangian of this *gauged complex SYK$_2$ model* is then given by

$$L = \sum_{j=1}^{N} \psi_j^\dagger (\partial_\tau - iA)\psi_j + \sum_{ij} \psi_i^\dagger m_{ij} \psi_j, \tag{9.2}$$

where the fermions satisfy $\left\{\psi_i^\dagger, \psi_j\right\} = \delta_{ij}$, and $U(1)$ gauge transformations act on the fields as

$$\begin{aligned} \psi &\rightarrow e^{i\omega(\tau)}\psi \\ A &\rightarrow A + \partial_\tau \omega. \end{aligned} \tag{9.3}$$

In order to maintain the antiperiodicity of the gauge transformed fermion fields, the phase must satisfy

$$\omega(\beta) - \omega(0) = 2\pi k, \quad k \in \mathbb{Z}. \tag{9.4}$$

Transformations for which $k \neq 0$ are called *large gauge transformations*. This gauge freedom means that we need only consider constant gauge field configurations since, for any $A(\tau)$, we may always make the gauge transformation[6]

$$\omega(\tau) = \frac{a}{\beta}\tau - \int_0^\tau d\tau' A(\tau'), \tag{9.5}$$

where $a = \int_0^\beta d\tau A(\tau)$, to get to the constant configuration

$$A(\tau) \rightarrow \frac{a}{\beta}. \tag{9.6}$$

[4]It is *external* in that we do not integrate over it in the path integral. In (0+1)-dimensions, doing so would just restrict the theory to its zero charge sector (or in the presence of a Chern-Simons term $-i\kappa A$ in the Lagrangian (9.2), to the sector of states with charge κ).

[5]Being an odd-dimensional spacetime, a Chern-Simons term can be added, which in this (0+1)-dimensional case is simply linear in the gauge field $A(t)$. The result is a form of topological quantum mechanics [193, 194, 195] originally studied in the context of finite temperature Chern-Simons theory [196] with the aim of understanding puzzles arising from perturbative treatments of 2+1-dimensional Chern-Simons theories. However, we verified that the addition of such a Chern-Simons term to our model would simply cancel out of our SFF (and OTOC) calculations, having no effect on the chaos properties of the model.

[6]Note that this is not a large gauge transformation since $\omega(\beta) = \omega(0)$.

In the following, for convenience, we will often simply refer to a as the gauge field[7]. Note that, because $A(\tau)$ is treated as external, it will not be integrated over in the path integral. One could thus redefine the fermion fields as

$$\psi'(\tau) = \psi(\tau)e^{-i\int_0^\tau d\tau' A(\tau')}, \tag{9.7}$$

which eliminates $A(\tau)$ from our action (9.2). Where the original fields ψ satisfy the usual antiperiodicity condition, the new fields ψ' satisfy

$$\psi'(\beta) = e^{-ia}\psi'(0). \tag{9.8}$$

Thus we see that the introduction of the external gauge field is equivalent to introducing a *twisted boundary condition* for the fermions[8]. Under this interpretation, invariance under large gauge transformations amounts to the fact that the phase appearing in the boundary condition only depends on $a \mathrm{mod} 2\pi$.

The disordered coupling in this model is given by the *random mass matrix* m_{ij}. It satisfies the symmetry property

$$m_{ij}^* = m_{ji}, \tag{9.9}$$

which ensure Hermiticity of the Hamiltonian. Its components are drawn from a Gaussian distribution with zero mean,

$$P(m_{ij}) = \begin{cases} e^{-\frac{N}{2m^2}|m_{ij}|^2} & i \neq j, \\ e^{-\frac{N}{2m^2}m_{ii}^2} & i = j, \end{cases} \tag{9.10}$$

and variance,

$$\overline{m_{ij}m_{ji}} = \overline{m_{ii}^2} = \frac{m^2}{N}\,. \tag{9.11}$$

Here we have defined

$$\begin{aligned} \overline{F} &\equiv \int F \prod_{i\neq j} P(m_{ij}) Dm_{ij} \prod_i P(m_{ii}) Dm_{ii}, \\ Dm_{ij} &\equiv \left(\frac{N}{\pi m^2}\right)^{1/4} dm_{ij}, \quad Dm_{ii} \equiv \left(\frac{N}{2\pi m^2}\right)^{1/2} dm_{ii}, \end{aligned} \tag{9.12}$$

[7]Note that large gauge transformations (9.4) act on a as $a \to a + 2\pi k,\ k \in \mathbb{Z}$.

[8]See [229] for a discussion of D dimensional QFTs with twisted boundary conditions in the (compactified) time direction. See also [230].

and use an overline to denote the disorder averaging throughout. Note that we have included the normalisation of the Gaussian distributions in the measures Dm_{ij}.

We need to specify whether we will treat the disorder as annealed or quenched. Recall that for the former, the disorder averaging is performed first to obtain a new disorder-averaged action; for the latter, correlation functions involving the disordered couplings m_{ij} are computed and disorder averages are taken afterwards. In this chapter we will utilise both approaches, indeed, at large N we expect these results to coincide [146].

Why gauge the SYK$_2$ model?

We briefly recount our initial motivations for considering the model introduced above. Knowing that the SYK model is solvable, possesses a low-energy emergent conformal symmetry and is maximally chaotic, one might very reasonably presume that it furnishes the CFT dual to an AdS$_2$/CFT$_1$ correspondence [213]-[216]. However, this hope was convincingly dashed in [212] where it was pointed out that the SYK model *cannot* have a conventional weakly-coupled, low-curvature gravity dual for two crucial reasons:

1. The large N Majorana fermions $\chi_a(t)$ of the SYK model are dual to N degenerate bulk fermions $\Psi_a(t, x)$ whose one-loop contribution to the bulk partition function is comparable to the classical saddle, consequently invalidating the saddle point approximation.

2. The model does not exhibit the large N factorization expected of theories with a conventional gravitational dual.

Interpreting these observations is tricky. In [212] it was suggested that perhaps the correct statement is that the singlet sector of the SYK model is dual to a two-dimensional higher spin theory[9]. Crucially for us, another viewpoint was put forward: that the ills of an SYK/AdS duality might be cured by gauging a large subgroup of the $SO(N)$ global flavour symmetry, to construct a *gauged* SYK/AdS correspondence [212]. It was this observation that gave the initial motivation for studying a gauged SYK model.

Instead of gauging the non-abelian $SO(N)$ flavour symmetry of the model, we decided to begin by looking for a simpler, abelian symmetry to gauge. Considering the

[9]To support this assertion, it was shown there that the gravitational dynamics near an AdS$_2$ throat can be re-written in terms of an effective quantum hydrodynamical action that precisely matches with the Schwarzian action describing the low energy, large N solution of the SYK model - see Sections 8.1.3 and 8.3.

complex, not Majorana, variant of the model provided just such an option: the global $U(1)$ colour group associated with the charges of the complex fermions. While this is of course a different undertaking to that suggested in [212], we nonetheless hoped to learn something about the effects that gauging the model might have on the chaos properties of the (complex) SYK model.

As we have mentioned, in the $q = 2$ case, while the SYK model doesn't have a holographic dual or conformal limit, it may be solved exactly at arbitrary coupling. Gauging it then serves as a natural starting point for the investigation of the gauged SYK$_q$ model for $q > 2$. In particular, the SYK$_2$ model is not chaotic, so a natural first question to investigate is whether the inclusion of the gauge field spoils its solvability properties and/or introduces chaotic regions in its parameter space. Additionally, from the perspective of the SFF, we would like to see whether the gauge field has any interesting effects on the slope, and whether it has an effect on the exponential ramp which is conjectured to be a feature of all non-interacting, disordered systems [179]. We expect that the analytic techniques needed to answer our original questions could be more easily understood and developed in the $q = 2$ context, before being deployed to study the $q > 2$ models and the gauging of non-abelian symmetries.

9.2.1 Euclidean time two-point function

In this section we compute the disorder-averaged two-point function in Euclidean time. We will do this by treating the disorder as *quenched*. We begin by computing the two-point function $G^0(\tau)$ for the free theory, with the random mass matrix turned off; $m_{ij} = 0$ for all i, j. Working in constant gauge $A(\tau) = a/\beta$, the free propagator $G^0(\tau)$ must satisfy

$$\left(\frac{d}{d\tau} - i\frac{a}{\beta}\right) G^0(\tau - \tau') = \delta(\tau - \tau'), \tag{9.13}$$

which is solved using the Fourier series

$$G^0(\tau) = \frac{1}{\beta}\sum_{n=-\infty}^{\infty} G^0(\omega_n) e^{i\omega_n \tau}, \qquad \omega_n = \frac{(2n-1)\pi}{\beta}, \tag{9.14}$$

where the Matsubara frequencies ω_n are fixed by the fermionic boundary condition $G^0(\tau) = -G^0(\tau + \beta)$. We obtain

$$G^0(\omega_n) = \frac{\beta}{i(2n-1)\pi - ia}, \tag{9.15}$$

from which we obtain [196]

$$\begin{aligned} G^0(\tau-\tau') &= \sum_{n=-\infty}^{\infty} \frac{e^{i\omega_n(\tau-\tau')}}{i\pi(2n-1)-ia} \\ &= \frac{i}{2}\left[\sin\left(\frac{a}{\beta}|\tau-\tau'|\right) - \tan\left(\frac{a}{2}\right)\cos\left(\frac{a}{\beta}|\tau-\tau'|\right)\right] \\ &\quad + \frac{1}{2}\epsilon_\beta(\tau-\tau')\left[\cos\left(\frac{a}{\beta}|\tau-\tau'|\right) + \tan\left(\frac{a}{2}\right)\sin\left(\frac{a}{\beta}|\tau-\tau'|\right)\right], \end{aligned} \tag{9.16}$$

where

$$\epsilon_\beta(\tau) = \begin{cases} 1, & 0<\tau<\beta \\ -1, & -\beta<\tau<0 \\ 0 & \tau = n\beta. \end{cases} \tag{9.17}$$

Note that in the limit $a \to 0$, (9.16) reduces to

$$G^0(\tau-\tau') = \frac{1}{2}\epsilon_\beta(\tau-\tau'), \tag{9.18}$$

which is the appropriate generalisation to the thermal circle of the usual propagator $G^0(\tau) = \frac{1}{2}\mathrm{sgn}(\tau)$ for the operator ∂_τ for non-compact time [138].

We may rewrite (9.16) as

$$G^0(\tau) = \begin{cases} \frac{1}{2}\left(-1 - i\tan\left(\frac{a}{2}\right)\right)e^{i\frac{a}{\beta}\tau} & -\beta<\tau<0 \\ -\frac{i}{2}\tan\left(\frac{a}{2}\right) & \tau = 0 \\ \frac{1}{2}\left(1 - i\tan\left(\frac{a}{2}\right)\right)e^{i\frac{a}{\beta}\tau} & 0<\tau<\beta \\ \frac{i}{2}\tan\left(\frac{a}{2}\right) & \tau = \beta. \end{cases} \tag{9.19}$$

The two-point function of the free theory is then given by

$$\langle\psi_i^\dagger(\tau_1)\psi_j(\tau_2)\rangle \equiv G^0_{ij}(\tau_1-\tau_2) = \delta_{ij}G^0(\tau_1-\tau_2). \tag{9.20}$$

The full, disorder-averaged two-point function is given by the sum of all Feynman diagrams consisting of integrals of the propagators (9.20) with some collection of m_{ij} terms inserted as vertices:

$$\begin{aligned} &\overline{\langle\psi_i^\dagger(\tau)\psi_j(0)\rangle} \equiv \overline{G_{ij}(\tau)} \\ &= \sum_{l=0}^{\infty}\int_0^\beta d\tau_1\cdots\int_0^\beta d\tau_{2l}\; G^0_{ii}(\tau-\tau_1)G^0_{k_1k_1}(\tau_1-\tau_2)\cdots G^0_{k_{2l-1}k_{2l-1}}(\tau_{2l-1}-\tau_{2l})G^0_{jj}(\tau_{2l})\times \\ &\quad \left(\sum_{k_a=1}^{N}\overline{m_{ik_1}m_{k_1k_2}\cdots m_{k_{2l-1}j}}\right), \end{aligned} \tag{9.21}$$

Note that because the two-point function G^0_{ij} is proportional to δ_{ij}, the indices of the mass insertions order into a sequence as above. The mass averaging can be carried out for arbitrary collections of mass insertions. We can do the integrals separately for the diagonal couplings, and pairwise separately for the non-diagonal ones, to obtain [222]

$$\begin{aligned}\overline{m^s_{ij}m^r_{ji}} &= r\frac{m^{2r}}{N^r}\Gamma(r)\delta_{s,r}, \quad i\neq j,\\ \overline{m^{2r}_{ii}} &= 2^r\frac{m^{2r}}{N^r}\frac{\Gamma(r+\frac{1}{2})}{\sqrt{\pi}},\\ \overline{m^{2r+1}_{ii}} &= 0,\end{aligned} \tag{9.22}$$

where r and s are positive integers. In order for the quantity involving the mass averages in (9.21) to be nonzero, the number of m_{ij} terms must match the number of m_{ji} terms for all i, j. The leading large N contribution comes from the so-called *rainbow diagrams* [165], illustrated in Fig. (9.1). To sum all such diagrams, one may solve the recursive equation illustrated in Fig. (9.2), to obtain

$$\sum_{k_i=1}^{N}\overline{m_{ik_1}m_{k_1k_2}\cdots m_{k_{2l-1}j}} = \frac{1}{l+1}\begin{pmatrix}2l\\ l\end{pmatrix}m^{2l}\delta_{ij}+\mathcal{O}(\frac{1}{N}). \tag{9.23}$$

The convolution of n free two-point functions (9.20), required in the calculation of the full two-point function (9.21), can be written as

$$\begin{aligned}&\int_0^\beta d\tau_1\int_0^\beta d\tau_2\cdots\int_0^\beta d\tau_n G^0_{k_1k_1}(t_1-\tau_1)G^0_{k_2k_2}(\tau_1-\tau_2)\cdots G^0_{k_nk_n}(\tau_n-t_2)\\ =\;& e^{i\frac{a}{\beta}(t_1-t_2)}\sum_{p=0}^{n}\frac{(t_1-t_2)^{n-p}\beta^p(-1)^p}{2^{p+1}p!(n-p)!}\frac{\partial^p}{\partial x^p}\left(\tanh x+\mathrm{sgn}(t_1-t_2)\right)\Big|_{x\to\tanh^{-1}(-i\tan\left(\frac{a}{2}\right))}.\end{aligned} \tag{9.24}$$

Remarkably, this result may be combined with the mass averaging (9.23) to give a closed form expression for the large N, fully dressed two-point correlation function (9.21). By taking the large N limit and making use of an integral representation of the hypergeometric function, we obtain

$$\begin{aligned}\overline{G_{i_1j_2}(\tau)} &= \delta_{j_2i_1}e^{\frac{ia}{\beta}\tau}\frac{1}{\pi}\int_{-1}^{1}dy\sqrt{1-y^2}e^{-2my\tau}\left(\tanh\left(-i\frac{a}{2}+my\beta\right)+\mathrm{sgn}(\tau)\right)\\ &= \delta_{j_2i_1}\mathrm{sgn}(\tau)e^{i\frac{a}{\beta}\tau}\frac{2}{\pi}\int_{-1}^{1}dy\sqrt{1-y^2}\frac{e^{-2my\tau}}{1+e^{-2\mathrm{sgn}(\tau)my\beta}e^{i\mathrm{sgn}(\tau)a}}\\ &= \delta_{j_2i_1}\mathrm{sgn}(\tau)\frac{2}{\pi}\int_{-1}^{1}dy\sqrt{1-y^2}\frac{e^{-\left(2my+i\frac{a}{\beta}\right)\tau}}{1+e^{-\mathrm{sgn}(\tau)\left(2my+i\frac{a}{\beta}\right)\beta}}.\end{aligned} \tag{9.25}$$

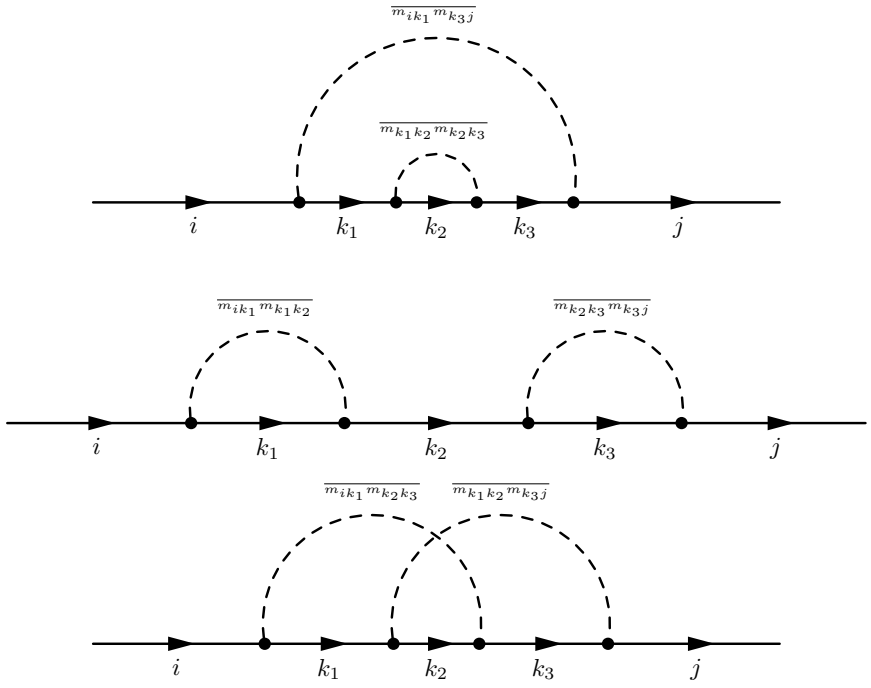

Figure 9.1: The diagrams relevant for four mass insertions. The fermion propagators are indicated by solid lines and are directed from $\psi^\dagger$ to ψ. The dashed lines are related to the mass-averaging, which require the masses to be paired up to give a nonzero result. The top two diagrams are rainbow diagrams for which the dashed lines do not intersect. Diagrams such as this represent the leading large N contribution since the smallest number of flavor indices are contracted.

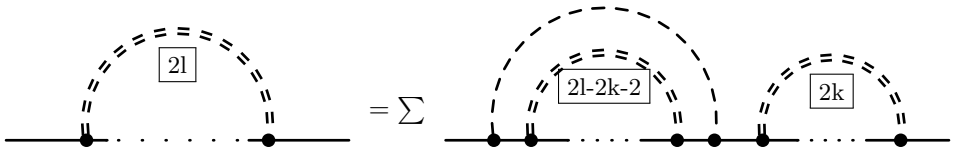

Figure 9.2: The number of rainbow diagrams for $2l$ mass insertions can be determined by a recursive relation, displayed here in diagrammatic form. The double dashed lines sum over all rainbow diagrams involving the number of insertions in the square box.

Taking $0 < \tau < \beta$ and rescaling the $2my \to y$, we obtain

$$\overline{G_{i_1 j_2}(\tau)} = \delta_{j_2 i_1} e^{i\frac{a}{\beta}\tau} \int_{-2m}^{2m} dy \frac{\sqrt{4m^2 - y^2}}{2\pi m^2} \frac{e^{-y\tau}}{1 + e^{-y\beta} e^{ia}}, \tag{9.26}$$

which is invariant under large gauge transformations as required[10]. This is our result for the disorder-averaged, Euclidean time two-point function.

In Appendix E we use this result to outline the calculation of the OTOC for our model. It is found that all dependence on the gauge field a cancels out of the calculation and we simply obtain the same OTOC result as for the underlying SYK$_2$ model, which does not exhibit the exponential growth characteristic of quantum chaotic models [182, 165]. We conclude, unsurprisingly, that our model is not chaotic. Recalling however that the SFF for an integrable but disordered non-interacting system may still have interesting features, we now proceed with a calculation of SFF in the large N limit.

9.3 The SFF

Recall that the $\beta = 0$ SFF can be computed by analytically continuing the partition function $Z = Z(\beta)$ to $Z(iT)$, and the SFF is subsequently defined as

$$g(T) \equiv \frac{\overline{Z(iT) Z^*(iT)}}{\overline{Z(0)}^2}. \tag{9.27}$$

The disconnected and connected components are defined respectively by

$$g_d(T) = \frac{\overline{Z(iT)}\ \overline{Z^*(iT)}}{\overline{Z(0)}^2}, \tag{9.28}$$

$$g_c(T) = g(T) - g_d(T). \tag{9.29}$$

To calculate $Z(iT)$, we simply Wick rotate from Euclidean time to real time, under which $\tau \to it$, $A(\tau) \to -iA(t)$ and integration now runs from 0 to T. Working in the constant gauge $A(\tau) = a/\beta$ which in real time becomes $A(t) = a/T$, the resulting real-time action is given by

$$\tilde{I} = iS = -\int_0^T dt \left[\sum_{i=1}^N \psi_i^\dagger \left(\frac{d}{dt} - i\frac{a}{T} \right) \psi_i + i \sum_{i,j=1}^N m_{ij} \psi_i^\dagger \psi_j \right]. \tag{9.30}$$

[10]Note that the overall phase accounts for the transformation of the fermion fields under the gauge transformation.

As is usual in the path integral computation of the SFF, we consider the physics of fermions in *periodic* real time, with period T and with the fermions satisfying anti-periodic boundary conditions.

9.3.1 Derivation of the two-replica SFF

For convenience, we define the real and imaginary parts of the complex random mass matrix as follows

$$m_{ij} = m_{R,ij} + i m_{I,ij}. \tag{9.31}$$

It follows from the constraint $m^*_{ij} = m_{ji}$ that

$$m_{I,ii} = 0, \quad m_{R,ij} = m_{R,ji}, \quad m_{I,ij} = -m_{I,ji}. \tag{9.32}$$

Introducing the replica index $\alpha = 1, 2$, the two-replica path integral relevant for the calculation of the SFF[11] may then be written as

$$\begin{aligned}
& Z(iT)Z(iT)^* \\
= & \int \left[\prod_{\alpha=1}^{2}\prod_{i_\alpha=1}^{N} \mathcal{D}\psi^\dagger_{i_\alpha}\mathcal{D}\psi_{i_\alpha}\right] e^{I_1+I_2} \exp\left\{i\frac{a}{T}\int dt\,\left(\psi^\dagger_{i_1}\psi_{i_1} - \psi^\dagger_{i_2}\psi_{i_2}\right)\right\} \\
& \prod_i \exp\left\{-i\int dt\; m_{R,ii}(\psi^\dagger_{i_1}\psi_{i_1} - \psi^\dagger_{i_2}\psi_{i_2})\right\} \\
& \prod_{i<j} \exp\left\{-i\int dt\; m_{R,ij}(\psi^\dagger_{i_1}\psi_{j_1} + \psi^\dagger_{j_1}\psi_{i_1} - \psi^\dagger_{j_2}\psi_{i_2} - \psi^\dagger_{i_2}\psi_{j_2})\right\} \\
& \prod_{i<j} \exp\left\{\int dt\; m_{I,ij}(\psi^\dagger_{i_1}\psi_{j_1} - \psi^\dagger_{j_1}\psi_{i_1} + \psi^\dagger_{j_2}\psi_{i_2} - \psi^\dagger_{i_2}\psi_{j_2})\right\},
\end{aligned} \tag{9.33}$$

where we have defined

$$I_\alpha = -\int_0^T dt \sum_{i=1}^{N} \psi^\dagger_{i_\alpha}\frac{d}{dt}\psi_{i_\alpha}. \tag{9.34}$$

We now perform the disorder average (9.12) directly on this two-replica path integral using the probability distributions (9.10), corresponding to an annealed treatment of

[11] See Section 7.4.3.

the disorder.

$$
\begin{aligned}
&\overline{Z(iT)Z(iT)^*} \\
=\ & \int \left[\prod_{\alpha=1}^{2}\prod_{i_\alpha=1}^{N}\mathcal{D}\psi^\dagger_{i_\alpha}\mathcal{D}\psi_{i_\alpha}\right] e^{I_1+I_2}\exp\left\{i\frac{a}{T}\int dt\left(\psi^\dagger_{i_1}\psi_{i_1}-\psi^\dagger_{i_2}\psi_{i_2}\right)\right\} \\
& \left(\prod_i\int Dm_{R,ii}\exp\left\{-i\int dt\ m_{R,ii}(\psi^\dagger_{i_1}\psi_{i_1}-\psi^\dagger_{i_2}\psi_{i_2})\right\}e^{-\frac{N}{2m^2}m^2_{R,ii}}\right) \\
& \left(\prod_{i<j}\int Dm_{R,ij}\exp\left\{-i\int dt\ m_{R,ij}(\psi^\dagger_{i_1}\psi_{j_1}+\psi^\dagger_{j_1}\psi_{i_1}-\psi^\dagger_{j_2}\psi_{i_2}-\psi^\dagger_{i_2}\psi_{j_2})\right\}e^{-\frac{N}{m^2}m^2_{R,ij}}\right) \\
& \left(\prod_{i<j}\int Dm_{I,ij}\exp\left\{\int dt\ m_{I,ij}(\psi^\dagger_{i_1}\psi_{j_1}-\psi^\dagger_{j_1}\psi_{i_1}+\psi^\dagger_{j_2}\psi_{i_2}-\psi^\dagger_{i_2}\psi_{j_2})\right\}e^{-\frac{N}{m^2}m^2_{I,ij}}\right) \\
=\ & \int \left[\prod_{\alpha=1}^{2}\prod_{i_\alpha=1}^{N}\mathcal{D}\psi^\dagger_{i_\alpha}\mathcal{D}\psi_{i_\alpha}\right] e^{I_1+I_2}\exp\left\{i\frac{a}{T}\int dt\left(\psi^\dagger_{i_1}\psi_{i_1}-\psi^\dagger_{i_2}\psi_{i_2}\right)\right\} \\
& \exp\left\{-\frac{m^2}{2N}\int dtdt'\sum_i(\psi^\dagger_{i_1}\psi_{i_1}(t)-\psi^\dagger_{i_2}\psi_{i_2}(t))(\psi^\dagger_{i_1}\psi_{i_1}(t')-\psi^\dagger_{i_2}\psi_{i_2}(t'))\right. \\
& -\frac{m^2}{4N}\int dtdt'\sum_{i<j}(\psi^\dagger_{i_1}\psi_{j_1}(t)+\psi^\dagger_{j_1}\psi_{i_1}(t)-\psi^\dagger_{i_2}\psi_{j_2}(t)-\psi^\dagger_{j_2}\psi_{i_2}(t)) \\
& \qquad\qquad (\psi^\dagger_{i_1}\psi_{j_1}(t')+\psi^\dagger_{j_1}\psi_{i_1}(t')-\psi^\dagger_{i_2}\psi_{j_2}(t')-\psi^\dagger_{j_2}\psi_{i_2}(t')) \\
& +\frac{m^2}{4N}\int dtdt'\sum_{i<j}(\psi^\dagger_{i_1}\psi_{j_1}(t)-\psi^\dagger_{j_1}\psi_{i_1}(t)-\psi^\dagger_{i_2}\psi_{j_2}(t)+\psi^\dagger_{j_2}\psi_{i_2}(t)) \\
& \qquad\qquad \left.(\psi^\dagger_{i_1}\psi_{j_1}(t')-\psi^\dagger_{j_1}\psi_{i_1}(t')-\psi^\dagger_{i_2}\psi_{j_2}(t')+\psi^\dagger_{j_2}\psi_{i_2}(t'))\right\},
\end{aligned}
\tag{9.35}
$$

where in the second equality we have simply performed the Gaussian integrals over the components of the random mass matrix. Grouping terms, we may write

$$
\begin{aligned}
&\overline{Z(iT)Z(iT)^*} \\
=\ & \int \left[\prod_{\alpha=1}^{2}\prod_{i_\alpha=1}^{N}\mathcal{D}\psi^\dagger_{i_\alpha}\mathcal{D}\psi_{i_\alpha}\right] e^{I_1+I_2}\exp\left\{-\frac{m^2}{2N}\int dtdt'\sum_{\alpha,\beta}\sum_{i,j}(-1)^{\alpha+\beta}\psi^\dagger_{i_\alpha}\psi_{j_\alpha}(t)\psi^\dagger_{j_\beta}\psi_{i_\beta}(t')\right\} \\
& \exp\left\{i\frac{a}{T}\int dt\left(\psi^\dagger_{i_1}\psi_{i_1}-\psi^\dagger_{i_2}\psi_{i_2}\right)\right\}
\end{aligned}
\tag{9.36}
$$

We now define the collective, bilocal field

$$G_{\alpha\beta}(t',t) = \sum_{i_\alpha=1}^{N} \frac{1}{N}\psi^\dagger_{i_\alpha}(t)\psi_{i_\beta}(t'), \tag{9.37}$$

which we introduce to the partition function via the functional delta function

$$\begin{aligned}
&\delta\left(G_{\alpha\beta}(t',t) - \sum_{i=1}^{N}\frac{1}{N}\psi^\dagger_{i_\alpha}(t)\psi_{i_\beta}(t')\right) \\
&= \prod_{\alpha,\beta}\int \mathcal{D}\Sigma_{\alpha\beta}\exp\left\{-N\Sigma_{\beta\alpha}(t,t')\left(G_{\alpha\beta}(t',t) - \sum_{i=1}^{N}\frac{1}{N}\psi^\dagger_{i_\alpha}(t)\psi_{i_\beta}(t')\right)\right\},
\end{aligned} \tag{9.38}$$

where we have introduced the auxilary field $\Sigma_{\beta\alpha}$ as a Lagrange multiplier[12]. This allows us to rewrite the quartic term in (9.36) as

$$\begin{aligned}
&\exp\left\{-\frac{m^2}{2N}\int dtdt'\sum_{\alpha,\beta}\sum_{i,j}(-1)^{\alpha+\beta}\psi^\dagger_{i_\alpha}\psi_{j_\alpha}(t)\psi^\dagger_{j_\beta}\psi_{i_\beta}(t')\right\} \\
&= \prod_{\alpha,\beta}\int \mathcal{D}\Sigma_{\alpha\beta}\mathcal{D}G_{\alpha\beta}\exp\left\{\int dtdt'\left[(-1)^{\alpha+\beta}\frac{Nm^2}{2}G_{\alpha\beta}(t',t)G_{\beta\alpha}(t,t')\right.\right. \\
&\qquad\left.\left. - N\Sigma_{\beta\alpha}(t,t')\left(G_{\alpha\beta}(t',t) - \sum_{i=1}^{N}\frac{1}{N}\psi^\dagger_{i_\alpha}(t)\psi_{i_\beta}(t')\right)\right]\right\},
\end{aligned} \tag{9.39}$$

so that (9.36) becomes

$$\begin{aligned}
&\int\left[\prod_{\alpha,\beta}\mathcal{D}\Sigma_{\alpha\beta}\mathcal{D}G_{\alpha\beta}\right]\left[\prod_{\alpha}\prod_{i_\alpha=1}^{N}\mathcal{D}\psi^\dagger_{i_\alpha}\mathcal{D}\psi_{i_\alpha}\right] \\
&\exp\left\{\int dtdt'\sum_{\alpha,\beta}\sum_{i}\psi^\dagger_{i_\alpha}(t)\left[-\delta(t-t')\left(\delta_{\alpha\beta}\frac{d}{dt} - i\sigma^z_{\alpha\beta}\frac{a}{T}\right) + \Sigma_{\beta\alpha}(t,t')\right]\psi_{i_\beta}(t')\right. \\
&\left. -N\int dtdt'\sum_{\alpha,\beta}\left[\Sigma_{\beta\alpha}(t',t)G_{\alpha\beta}(t,t') - (-1)^{\alpha+\beta}\frac{m^2}{2}G_{\alpha\beta}(t,t')G_{\beta\alpha}(t',t)\right]\right\},
\end{aligned} \tag{9.40}$$

where σ^z is the usual Pauli z-matrix. Performing the Gaussian integral over the fermions then gives the following expression

$$\overline{Z(iT)Z(iT)^*} \;=\; \prod_{\alpha,\beta}\int \mathcal{D}\Sigma_{\alpha\beta}\mathcal{D}G_{\alpha\beta}e^{NI(G,\Sigma)}\,, \tag{9.41}$$

[12]Note that despite their suggestive names, we do not yet have a physical interpretation of the variables G and Σ.

where

$$I(G,\Sigma) = \log\det\left[-\delta(t-t')\left(\delta_{\alpha\beta}\frac{d}{dt} - i\sigma^z_{\alpha\beta}\frac{a}{T}\right) + \Sigma_{\beta\alpha}(t,t')\right] - \int dtdt' \sum_{\alpha,\beta}\left[\Sigma_{\beta\alpha}(t',t)G_{\alpha\beta}(t,t') - (-1)^{\alpha+\beta}\frac{m^2}{2}G_{\alpha\beta}(t,t')G_{\beta\alpha}(t',t)\right]. \tag{9.42}$$

This is the exact rewrite of the disorder-averaged, two-replica theory in terms of the bilocal, (replica-space) matrix valued, collective field variables $G_{\alpha\beta}$ and $\Sigma_{\alpha\beta}$ mentioned in Section 7.4.3.

9.3.2 The disconnected component of the SFF

We take a brief detour from our SFF calculation to calculate the disorder-averaged partition function (in Euclidean time) for our model, using its collective field formulation derived above. We will then use this to calculate the disconnected component of the SFF. To calculate the partition function, we simply restrict the results (9.41) and (9.42) to a single replica, and return to Euclidean time by analytically continuing $t \to -i\tau$, $a \to ia$ and $m \to im$, to obtain the appropriate path integral

$$\overline{Z(\beta)} = \int \mathcal{D}\Sigma\mathcal{D}G e^{NI}, \tag{9.43}$$

$$I = \log\det\left[-\delta(\tau-\tau')\left(\frac{d}{d\tau} - i\frac{a}{\beta}\right) + \Sigma(\tau,\tau')\right] - \int d\tau d\tau' \left[\Sigma(\tau',\tau)G(\tau,\tau') + \frac{m^2}{2}G(\tau,\tau')G(\tau',\tau)\right]. \tag{9.44}$$

In the large N saddle point approximation, assuming time translation invariance, the Euler Lagrange equations are given by

$$\frac{\delta I}{\delta\Sigma} = 0 \quad \Rightarrow \quad \delta(\tau-\tau'') = \int d\tau' \left[-\delta(\tau-\tau')\left(\frac{d}{d\tau} - i\frac{a}{T}\right) + \Sigma(\tau-\tau')\right] G(\tau'-\tau''), \tag{9.45}$$

$$\frac{\delta I}{\delta G} = 0 \quad \Rightarrow \quad \Sigma(\tau) = -m^2 G(\tau), \tag{9.46}$$

which gives the on-shell action

$$I = \log\det\left[-\delta(\tau-\tau')\left(\frac{d}{d\tau} - i\frac{a}{\beta}\right) + \Sigma(\tau-\tau')\right] + \frac{1}{2m^2}\int d\tau d\tau' \Sigma(\tau'-\tau)\Sigma(\tau-\tau'). \tag{9.47}$$

As an aside, note that if we rewrite (9.45) in frequency space and set $a = 0$, we obtain

$$G(\omega) = \frac{1}{-i\omega - m^2\Sigma(\omega)}. \tag{9.48}$$

Equations (9.46) and (9.48) then agree with the Schwinger-Dyson equations for the SYK$_q$ model (8.12) and (8.13) when[13] $q = 2$. Had we replaced the random mass term with a q-fermi random interaction in the above derivation, we would indeed have recovered those equations exactly. We thus see that the collective field formulation of the SYK model (with annealed disorder), is indeed equivalent to the fermionic variable formulation (with quenched disorder) which we investigated in Section 8.1 using Feynman diagrammatic techniques[14]. Moreover, the collective field variable G which we introduced into the path integral as a convenient change of variables, is precisely the large N, full two-point function which can be calculated using diagrammatic techniques - given in our case by (9.26). Likewise, the Lagrange multiplier field Σ is the self energy corresponding to this propagator.

Returning to our partition function calculation, we begin by considering the free theory where $m = 0$. The operator $\partial_\tau - iA(\tau)$ may be explicitly diagonalised as follows [196]

$$\left(\frac{d}{d\tau} - iA(\tau)\right)\psi_n(\tau) = \Lambda_n\psi_n(\tau) \quad \Rightarrow \quad \psi_n(\tau) = \exp\left\{\int_0^\tau d\tau'(iA(\tau') + \Lambda_n)\right\}. \tag{9.49}$$

Making use of the anti-periodicity of the fermionic field $\psi(0) = -\psi(\beta)$, it follows that

$$\Lambda_n\beta + i\int_0^\beta A(\tau)d\tau \;=\; (2n-1)\pi i \quad \Rightarrow \quad \Lambda_n = -\frac{ia}{\beta} + \frac{(2n-1)\pi i}{\beta}, \tag{9.50}$$

where $n \in \mathbb{Z}$ and $a = \int_0^\beta A(\tau)d\tau$ as before. The free partition is then given by

$$Z_0(\beta) = \left[\det\left(-\partial_\tau + iA(\tau)\right)\right]^N = \prod_{n=-\infty}^{\infty}\left(\frac{ia}{\beta} - \frac{(2n-1)\pi i}{\beta}\right)^N, \tag{9.51}$$

which is formally infinite. We regulate it in the standard way, dividing by the analo-

[13] Under the identification $J \leftrightarrow m$.

[14] We are comparing the complex and Majorana SYK models here, but the Schwinger-Dyson equations are indeed the same for both.

gous expression in the absence of the gauge field, to obtain

$$Z_0(\beta) = \left[\frac{\det\left(-\partial_\tau + iA(\tau)\right)}{\det\left(-\partial_\tau\right)}\right]^N = \prod_{n=-\infty}^{\infty}\left[\frac{-\frac{ia}{\beta}+\frac{(2n-1)\pi i}{\beta}}{\frac{(2n-1)\pi i}{\beta}}\right]^N = \prod_{n=-\infty}^{\infty}\left[1-\frac{a}{(2n-1)\pi}\right]^N$$
$$= \left[\cos\left(\frac{a}{2}\right)\right]^N. \tag{9.52}$$

This means that the free theory with $m = 0$ has a free energy of

$$F_0(\beta) = -\frac{1}{\beta}\log Z_0(\beta) = -\frac{N}{\beta}\log\left[\cos\left(\frac{a}{2}\right)\right]. \tag{9.53}$$

Note that this diverges whenever a is an odd multiple of π.

Generalising to nonzero m, direct evaluation of the functional determinant in (9.47) is best avoided in favour of a different method: formulating a differential equation for the free energy [138, 179] by exploiting the fact that the only dimensionful quantities in the problem are m and β, so all β dependence must be through the quantity $m\beta$. It follows that derivatives acting on the free energy are related as $\beta\dfrac{d}{d\beta} = m\dfrac{d}{dm}$, so that

$$m^2\beta\frac{dI}{d\beta} = -2\frac{dI}{d(m^{-2})} = -\int d\tau d\tau' \Sigma(\tau'-\tau)\Sigma(\tau-\tau'). \tag{9.54}$$

Here we have used that all m dependence of the on-shell action (9.47) is explicit; there is no implicit dependence through the fields, whose variation must vanish due to the equations of motion $\frac{\delta I}{\delta \Sigma} = 0$. The equations of motion (9.45) and (9.46) may be combined and manipulated to obtain

$$\int d\tau d\tau' \Sigma(\tau-\tau')\Sigma(\tau'-\tau) = \left[\beta\frac{d}{d\tau}\Sigma(\tau) - ia\Sigma(\tau)\right]_{\tau\to 0^+}. \tag{9.55}$$

Substituting our result for the real-time propagator (9.26) into (9.46) gives

$$\Sigma(\tau) = m^2 e^{i\frac{a}{\beta}\tau}\int_{-2m}^{2m} dy \frac{\sqrt{4m^2-y^2}}{2\pi m^2}\frac{e^{-y\tau}}{1+e^{-y\beta}e^{ia}}, \tag{9.56}$$

which combined with (9.54) with (9.55) yields the desired differential equation

$$\frac{dI}{d\beta} = \int_{-2m}^{2m} dy \frac{y\sqrt{4m^2-y^2}}{2\pi m^2(1+e^{ia-\beta y})}. \tag{9.57}$$

Integrating with respect to β (swapping the order of integration) yields

$$I = \int_{-2m}^{2m} dy \frac{\sqrt{4m^2 - y^2} \log\left(e^{\beta y} + e^{ia}\right)}{2\pi m^2} + C, \tag{9.58}$$

where C is a constant of integration. The integrand may be expanded as a polynomial in β using

$$\log\left(e^{\beta y} + e^{ia}\right) = \sum_{n=0}^{\infty} y^n \frac{f_n(e^{ia})}{n!(1+e^{ia})^n} \beta^n \tag{9.59}$$

where f_n is a function given for the first few terms by

$$\begin{aligned} f_0(x) &= \log(1+x) \\ f_1(x) &= 1, \\ f_2(x) &= x, \\ f_3(x) &= x^2 - x, \\ f_4(x) &= x^3 - 4x^2 + x, \\ f_5(x) &= x^4 - 11x^3 + 11x^2 - x. \end{aligned}$$

We may then perform the integral (9.58) term by term, to obtain

$$\begin{aligned} I &= -\frac{1}{\sqrt{\pi}} \sum_{n=0}^{\infty} \frac{2^n}{n!} \frac{\Gamma\left(\frac{n+1}{2}\right)}{\Gamma\left(\frac{n}{2}+2\right)} \frac{f_n(e^{ia})}{(1+e^{ia})^n} m^n \beta^n \\ &= \log\cos\left(\frac{a}{2}\right) + \frac{1}{8}\sec^2\left(\frac{a}{2}\right) m^2\beta^2 + \mathcal{O}(m^4\beta^4), \end{aligned} \tag{9.60}$$

where we have fixed the integration constant $C = \log\left(e^{-ia/2}/2\right)$ to ensure that we recover the free result (9.52) in the limit $m \to 0$. The partition function is then given by

$$\overline{Z(\beta)} = \left[\cos\left(\frac{a}{2}\right)\right]^N \exp\left\{\frac{N}{8}\sec^2\left(\frac{a}{2}\right) m^2\beta^2 + \mathcal{O}(m^4\beta^4)\right\}. \tag{9.61}$$

This expression is invariant under large gauge transformations, and like the free result yields a divergent free energy when a is equal to an odd multiple of π. We can understand this by noting that in this case we are effectively shifting all fermionic Matsubara frequencies to bosonic Matsubara frequencies, for which $\omega_n = \frac{2n\pi}{T}$ for integer n. This in turn violates the antiperiodicity requirement on our fields across the thermal circle. We thus take such gauge field configurations to be unphysical, and

exclude them in subsequent analysis of our model.

We may use the result (9.61) to calculate the disconnected component of the SFF (9.28). Accounting for the Wick rotation back to real time amounts to making the replacements $m \to -im$ and $\beta \to T$, so we obtain

$$\begin{aligned} g_d(T) &= \frac{\overline{Z(iT)}\;\overline{Z^*(iT)}}{\overline{Z(0)}^2} \\ &= \exp\left\{-\frac{N}{4}\sec^2\left(\frac{a}{2}\right)m^2T^2 + \mathcal{O}(m^4T^4)\right\}. \end{aligned} \tag{9.62}$$

We will return to discuss this result in Section 9.4.

9.3.3 Saddle point solutions

We now return to calculation of the full SFF. To tackle the two-relica path integral (9.41) and (9.42) we will assume that time-translation invariant configurations of G and Σ dominate [179]. This allows us to take the discrete Fourier transforms

$$G_{\alpha\beta}(t) = \frac{1}{T}\sum_{n\ \text{odd}} G_{\alpha\beta}(\omega_n)e^{-i\omega_n t}, \quad \Sigma_{\alpha\beta}(t) = \frac{1}{T}\sum_{n\ \text{odd}} \Sigma_{\alpha\beta}(\omega_n)e^{-i\omega_n t}, \qquad \omega_n = \frac{n\pi}{T}. \tag{9.63}$$

Note that G and Σ inherit the antiperiodicity around the real-time circle from the original SYK fermions. These Fourier transforms will ensure that variables with different Matsubara frequencies decouple. In terms of these variables the path integral becomes

$$\overline{Z(iT)Z(iT)^*} = \prod_{n\ \text{odd}}\prod_{\alpha,\beta}\left(\int d\Sigma_{\alpha\beta}(\omega_n)dG_{\alpha\beta}(\omega_n)e^{NI_n(G(\omega_n),\Sigma(\omega_n))}\right) \tag{9.64}$$

where now

$$\begin{aligned} I_n(G,\Sigma) &= \mathrm{Tr}\log\left[i\omega_n\delta_{\alpha\beta} + i\frac{a}{T}\sigma^z_{\alpha\beta} + \Sigma_{\alpha\beta}(\omega_n)\right] \\ &\qquad - \Sigma_{\alpha\beta}(\omega_n)G_{\beta\alpha}(\omega_n) + (-1)^{\alpha+\beta}\frac{m^2}{2}G_{\alpha\beta}(\omega_n)G_{\beta\alpha}(\omega_n) \\ &= \mathrm{Tr}\log\left[\left(i\omega_n\sigma^z_{\alpha\gamma} + i\frac{a}{T}\delta_{\alpha\gamma} + \tilde{\Sigma}_{\alpha\gamma}(\omega_n)\right)\sigma^z_{\gamma\beta}\right] \\ &\qquad - (-1)^{\alpha+\beta}\tilde{\Sigma}_{\alpha\beta}(\omega_n)\tilde{G}_{\beta\alpha}(\omega_n) + \frac{m^2}{2}\tilde{G}_{\alpha\beta}(\omega_n)\tilde{G}_{\beta\alpha}(\omega_n). \end{aligned} \tag{9.65}$$

In this expression repeated indices are summed over, the trace is taken over the replica indices, and in the second equality we have defined $\tilde{G} = G\sigma^z$ and $\tilde{\Sigma} = \Sigma\sigma^z$. This may be rewritten as

$$I(G,\Sigma) = \mathrm{Tr}\log\left[\left(i\sigma^z_{\alpha\gamma}\delta^{nn'}\omega_n + i\frac{a}{T}\delta^{nn'}_{\alpha\gamma} + \tilde{\Sigma}^{nn'}_{\alpha\gamma}\right)\sigma^z_{\gamma\beta}\right] - \mathrm{Tr}\left[\left((-1)^{\alpha+\gamma}\tilde{\Sigma}^{np}_{\alpha\gamma} - \frac{m^2}{2}\tilde{G}^{np}_{\alpha\gamma}\right)\tilde{G}^{pn'}_{\gamma\beta}\right], \tag{9.66}$$

with the trace now taken over both replica and (odd n) frequency spaces, with frequency space indices n, n', p. We have defined $\delta^{nn'}_{\alpha\beta} \equiv \delta^{nn'}\delta_{\alpha\beta}$.

The overall factor of N appearing in the action of the path integral (9.64) makes the SFF well suited to a saddle point analysis in the large N limit. From (9.66) we find the $(\tilde{G}, \tilde{\Sigma})$ equations of motion,

$$\frac{\delta I}{\delta\tilde{\Sigma}^{nn'}_{\alpha\beta}} = 0 \quad \Rightarrow \quad \sigma^z_{\alpha\rho}\left[i\sigma^z_{\rho\gamma}\delta^{np}\omega_n + i\frac{a}{T}\delta^{np}_{\rho\gamma} + \tilde{\Sigma}^{np}_{\rho\gamma}\right]\sigma^z_{\gamma\nu}(-1)^{\nu+\beta}\tilde{G}^{pn'}_{\nu\beta} = \delta^{nn'}_{\alpha\beta}, \tag{9.67}$$

$$\frac{\delta I}{\delta\tilde{G}^{nn'}_{\alpha\beta}} = 0 \quad \Rightarrow \quad \tilde{\Sigma}^{nn'}_{\alpha\beta} = (-1)^{\alpha+\beta}m^2\tilde{G}^{nn'}_{\alpha\beta}, \tag{9.68}$$

which can be written as a single equation of motion for $\tilde{\Sigma}$,

$$\left(i\sigma^z\omega + i\frac{a}{T} + \tilde{\Sigma}\right)\tilde{\Sigma} = m^2, \tag{9.69}$$

where we have suppressed the frequency and replica indices[15]. Similarly, we can rewrite the on-shell action (9.66) as

$$I(\tilde{\Sigma}) \;=\; \mathrm{Tr}\log\left[(i\sigma^z\omega + i\frac{a}{T} + \tilde{\Sigma})\sigma^z\right] - \frac{1}{2}\mathrm{Tr}\tilde{\Sigma}^2. \tag{9.70}$$

We briefly pause to consider the symmetry structure of this action. Without the $\sigma^z\omega$ term, the action (9.70) is invariant under general unitary transformations $\tilde{\Sigma} \to U^\dagger\tilde{\Sigma}U$. In the presence of the $\sigma^z\omega$ term, this symmetry is explicitly broken to transformations $\tilde{\Sigma} \to \tilde{U}^\dagger\tilde{\Sigma}\tilde{U}$ for unitaries $\tilde{U}$ satisfying $\tilde{U}\sigma^z\omega\tilde{U}^\dagger = \sigma^z\omega$, where we recall that $\sigma^z\omega$ is actually a matrix in replica and frequency space with matrix elements $(\sigma^z\omega)^{nn'}_{\alpha\beta} = \sigma^z_{\alpha\beta}\delta^{nn'}\omega_n$. The breaking of this symmetry and the associated Goldstone zero modes play a crucial role in giving rise to the exponential ramp exhibited by the SFF in this system, a point which we return to in Section 9.5.

[15]We have also used the fact that these equations only have replica-diagonal solutions.

Solutions to (9.69) are diagonal in both replica and frequency indices, and are given by

$$\tilde{\Sigma}^{nn'}_{\alpha\beta} = \frac{1}{2}\left[-i\left(\xi_\alpha\omega_n + \frac{a}{T}\right) + c^n_\alpha\sqrt{4m^2 - \left(\xi_\alpha\omega_n + \frac{a}{T}\right)^2}\right]\delta^{nn'}_{\alpha\beta}, \tag{9.71}$$

where $\xi_1 = 1,\ \xi_2 = -1$ and the constants $c^n_\alpha = \pm 1$ can be chosen independently for each replica and frequency index. Imposing the condition that for large frequencies our solution must vanish [225, 170] we obtain the following solutions [168]

$$\mathcal{S}^{nn'}_{\alpha\beta} = \begin{cases} \frac{1}{2}\left[-i(\xi_\alpha x_n + b) + c^n_\alpha\sqrt{4 - (\xi_\alpha x_n + b)^2}\right]\delta^{nn'}_{\alpha\beta}, & |\xi_\alpha x_n + b| \le 2, \\ \frac{1}{2}\left[-i(\xi_\alpha x_n + b) + i\mathrm{sgn}(\xi_\alpha x_n + b)\sqrt{(\xi_\alpha x_n + b)^2 - 4}\right]\delta^{nn'}_{\alpha\beta}, & |\xi_\alpha x_n + b| > 2. \end{cases} \tag{9.72}$$

in terms of the dimensionless quantities $\mathcal{S} \equiv \frac{1}{m}\tilde{\Sigma}$, $x_n \equiv \frac{\omega_n}{m} = \frac{n\pi}{mT}$ and $b \equiv \frac{a}{mT}$. The constants c^n_α may be chosen freely for frequencies in the range $|\xi_\alpha x_n + b| \le 2$. For a given b, these solutions take different forms in each of the following four frequency regions, dictated by the values of $|\xi_1 x_n + b|$ and $|\xi_2 x_n + b|$:

$$\begin{aligned} &\text{Region } A: && |x_n \pm b| \le 2, \\ &\text{Region } B: && |x_n + b| \le 2, \quad |x_n - b| > 2, \\ &\text{Region } C: && |x_n - b| \le 2, \quad |x_n + b| > 2, \\ &\text{Region } D: && |x_n \pm b| > 2. \end{aligned} \tag{9.73}$$

9.3.4 On-shell action

We must now evaluate the on-shell action in terms of these various solutions. To this end, we work with a form of on-shell action (9.70) that has been regularized by subtracting off the action for the free theory $\log(i\omega)$, to obtain

$$I(\mathcal{S}) = \mathrm{Tr}\log\left[\left(\sigma^z + \frac{b}{x_n} - \frac{i}{x_n}\mathcal{S}\right)\sigma^z\right] - \frac{1}{2}\mathrm{Tr}\mathcal{S}^2, \tag{9.74}$$

We define $I_J(x) \equiv I(\mathcal{S}^{(J)})$ to be the on-shell action, given by (9.74) evaluated on the solutions (9.72), restricted to the frequency region $J = A, B, C, D$. Depending on the form of the solution $\mathcal{S}$ in the region J, the action $I_J(x)$ may have dependence on the constants c^n_1 and c^n_2. Explicit expressions are given in Appendix F.1.

The total on-shell action, involving all frequencies, is then given by

$$I(\mathcal{S}) = \sum_{x_n\in A} I_A(c_1^n, c_2^n; x_n) + \sum_{x_n\in B} I_B(c_1^n; x_n) + \sum_{x_n\in C} I_C(c_2^n; x_n) + \sum_{x_n\in D} I_D(x_n). \tag{9.75}$$

Note that $I(\mathcal{S})$ depends on the entire set of constants $\{c_\alpha^n\}$, each of which may be chosen freely. Each possible configuration of $\{c_\alpha^n\}$ thus corresponds to a different saddle point. It remains to check which of these saddles contribute to the SFF at large N.

9.3.5 The contributing saddles

To see which saddles contribute, we must analyse fluctuations $\delta\mathcal{S}_{\alpha\beta}^{nn'}$ about the various solutions $\mathcal{S}_{\alpha\beta}^{nn'}$. To this end, consider the variation of the on-shell action (9.74) under $\mathcal{S}\to\mathcal{S}+\delta\mathcal{S}$. We suppress the frequency dependence of x_n. Up to $\mathcal{O}(\delta\mathcal{S}^2)$, we obtain

$$\delta I = \mathrm{Tr}\left[\left(i\sigma^z x + ib + \mathcal{S}^T\right)^{-1}\delta\mathcal{S} - \frac{1}{2}\left(\left(i\sigma^z x + ib + \mathcal{S}\right)^{-1}\delta\mathcal{S}\right)^2\right] \tag{9.76}$$

$$-\frac{1}{2}\mathrm{Tr}\left[\delta\mathcal{S}\mathcal{S} + \mathcal{S}\delta\mathcal{S} + \delta\mathcal{S}^2\right], \tag{9.77}$$

where we have Taylor expanded the log term to second order. Simplifying using the equation of motion (9.69), we obtain

$$\begin{aligned}\delta I &= \mathrm{Tr}\left[\mathcal{S}\delta\mathcal{S} - \frac{1}{2}\left(\mathcal{S}\delta\mathcal{S}\right)^2\right] - \frac{1}{2}\mathrm{Tr}\left[\delta\mathcal{S}\mathcal{S} + \mathcal{S}\delta\mathcal{S} + \delta\mathcal{S}^2\right] \\ &= -\frac{1}{2}\mathrm{Tr}\left[\left(\mathcal{S}\delta\mathcal{S}\right)^2\right] - \frac{1}{2}\mathrm{Tr}\left[\delta\mathcal{S}^2\right],\end{aligned} \tag{9.78}$$

and finally, restoring the replica and frequency space indices, we find

$$\delta I(\mathcal{S}) = -\frac{1}{2}\sum_{\alpha,\beta,n,n'} M_{\alpha\beta}^{nn'}\delta\mathcal{S}_{\alpha\beta}^{nn'}\delta\mathcal{S}_{\beta\alpha}^{n'n}, \tag{9.79}$$

where we have defined the *effective mass matrix*

$$M_{\alpha\beta}^{nn'} \equiv 1 + \mathcal{S}_{\alpha\alpha}^{nn}\mathcal{S}_{\beta\beta}^{n'n'}. \tag{9.80}$$

Note that here $\mathcal{S}_{\alpha\alpha}^{nn}$ denotes a single diagonal component of the matrix $\mathcal{S}$ and not a trace (*i.e.* no summation over repeated indices is implied in the above expression). Note that the effective mass matrices have dependence on the constants c_α^n and $c_\beta^{n'}$

through the solutions $\mathcal{S}^{nn}_{\alpha\alpha}$ and $\mathcal{S}^{n'n'}_{\beta\beta}$, and will thus differ for different saddles.

The saddles which contribute to the SFF at large N are precisely those for which the corresponding effective mass matrix is non-negative, $\mathrm{Re}[M^{nn'}_{\alpha\beta}] \geq 0$. In Appendix F.2 we verify that this condition is met for solutions in all four frequency regions, for any choices of the constants c^n_α and $c^{n'}_\beta$. This ensures that for each frequency, *all* saddles contribute in our saddle point approximation of the SFF.

Furthermore, the real part of the effective mass matrices are all strictly positive, except for frequencies in the ranges $|\xi_\alpha x_n + b| \leq 2$, $|\xi_\beta x_{n'} + b| \leq 2$. In this case, for saddles with $c^n_1 = -c_2^{-n}$, we find that $M^{nn'}_{\alpha\beta} = 0$ when $\alpha \neq \beta$ and $n' = -n$. These vanishing effective mass matrices $M^{n,-n}_{12}, M^{n,-n}_{21} = 0$ signal the presence of zero modes, which dominate the contribution to the fluctuations[16]. We return to discuss their significance in Section 9.5.

Expressed in the above terms, and normalising by dividing by $\overline{Z(0)}^2$ as per (9.27), we then have the following result for the SFF in the saddle point approximation, up to quadratic fluctuations

$$g(T) \;=\; \overline{Z(0)}^{\,-2} \sum_{\{c^n_\alpha\}} \left(e^{NI(\mathcal{S})} \prod_{\alpha,\beta} \prod_{n,n' \text{ odd}} \int \mathcal{D}\delta\mathcal{S}^{nn'}_{\alpha\beta} \exp\left\{ -\frac{N}{2} M^{nn'}_{\alpha\beta} \delta\mathcal{S}^{nn'}_{\alpha\beta} \delta\mathcal{S}^{n'n}_{\beta\alpha} \right\} \right), \tag{9.81}$$

where $I(\mathcal{S})$ is the on-shell action (9.75). To obtain the SFF explicitly in the saddle point approximation, we must perform the Matsubara sums in equation (9.75) as well as the sum over all allowed saddles $\sum_{\{c^n_\alpha\}} e^{NI(\mathcal{S})}$. The former cannot be performed analytically for general values of mT. To proceed, we will then need to consider particular limits of mT.

9.4 The early time SFF

In this section we consider the SFF in the early time, $mT \ll 1$, limit. We begin by treating just the pure saddle point contribution to the SFF, neglecting quadratic fluctuations, which turn out to be subleading in N (we will return to treat these explicitly in Section 9.5). The SFF is then given by

$$g(T) \;=\; \overline{Z(0)}^{\,-2} \sum_{\{c^n_\alpha\}} e^{NI(\mathcal{S})}. \tag{9.82}$$

[16] These are precisely the Goldstone modes arising from the explicit symmetry breaking of the action, discussed earlier.

At early times we assume that $2mT < a$ holds, the frequency region A vanishes (see Table F.2), and we may write the on-shell action (9.75) as follows

$$I(\mathcal{S}) \;=\; \sum_{x_n\in D} I_D(x_n) + \sum_{x_n\in C}\left(I_C(c_1^{-n};\mathrm{sgn}(a)x_n) + I_C(c_2^{n};\mathrm{sgn}(a)x_n)\right). \quad (9.83)$$

Here we have eliminated dependence on the region B by using the symmetry (F.8) $I_B(c;x) = I_C(c;-x)$. Region C contains only frequencies x_n with $|n\pi - a| < 2mT$. Thus all contributions to the Matsubara sums in (9.83) come from region D, unless there is some odd integer n satisfying $|n\pi - a| < 2mT$, in which case there is a single-frequency contribution from region C (since $2mT \ll 1$ there cannot be more than one frequency in this region).

9.4.1 $mT < \frac{\pi-a}{2}$

We start by assuming $mT < \frac{\pi-a}{2}$, in which case there is no contribution from region C. Since I_D does not involve the constants c_α^n, there is just a single saddle in this limit, and using the explicit form (F.7) for $I_D(x)$, we find

$$\begin{aligned} e^{NI(\mathcal{S})} &= \exp\left\{N\sum_{n>0,\mathrm{odd}} I_D(x_n)\right\} \\ &\approx \prod_{n\ \mathrm{odd}}\left(\left[\frac{(n\pi-a)(n\pi+a)}{n^2\pi^2}\right]^N\right)\exp\left\{-Nm^2T^2\sum_{n\ \mathrm{odd}}\frac{(n^2\pi^2+a^2)}{(n\pi-a)^2(n\pi+a)^2}\right\} \\ &= \cos\left(\frac{a}{2}\right)^{2N}\exp\left\{-\frac{Nm^2T^2}{4}\sec^2\left(\frac{a}{2}\right)\right\}, \end{aligned} \quad (9.84)$$

where, in the second equality, we have neglected $\mathcal{O}(m^4T^4)$ terms in the exponent. Implementing the normalisation of dividing by $\overline{Z(0)}^2 = \cos(a/2)^{2N}$ (see (9.61)) we obtain the following expression for the spectral form factor,

$$g(T) = \exp\left\{-\frac{N}{4}\sec^2\left(\frac{a}{2}\right)m^2T^2\right\}. \quad (9.85)$$

This is equal to our result for the disconnected component of the SFF (9.62), calculated using the full two-point function for quenched disorder. As expected, we therefore see that the slope of the full SFF is indeed given by its disconnected component. Note that we also see here an agreement between results calculated using quenched and annealed treatments of disorder respectively. We now explore this result in detail.

First, note that in the limit $a \to 0$ the argument of the exponent reduces to $-Nm^2T^2/4$, in agreement with the Majorana result in [179][17]. We note also that (9.85) is periodic in a with period 2π, ensuring that the early time SFF is indeed gauge-invariant under large gauge transformations. The analytic result up to $\mathcal{O}(m^8T^8)$ is given by[18]

$$g(T) = \exp\left\{N\left(-\frac{1}{4}m^2T^2\sec^2\left(\frac{a}{2}\right)+\frac{1}{48}m^4T^4(\cos a-2)\sec^4\left(\frac{a}{2}\right)\right.\right.$$
$$-\frac{1}{2304}m^6T^6(-26\cos a+\cos 2a+33)\sec^6\left(\frac{a}{2}\right)$$
$$\left.\left.-\frac{m^8T^8(1191\cos a-120\cos(2a)+\cos(3a)-1208)\sec^8\left(\frac{a}{2}\right)}{184320}+\mathcal{O}(m^{10}T^{10})\right)\right\}, \tag{9.86}$$

which is also invariant under large gauge transformations $a \to a + 2k\pi$, $k \in \mathbb{Z}$.

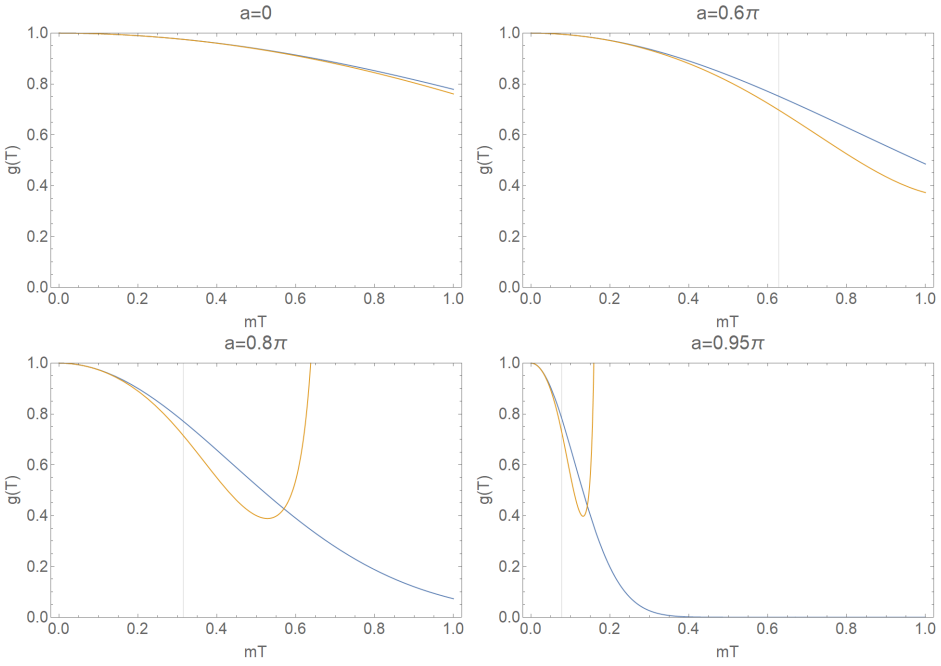

Figure 9.3: The early time SFF (9.86) for various a, to $\mathcal{O}(m^2T^2)$ (blue) and order $\mathcal{O}(m^8T^8)$ (yellow) in the exponent. Grey vertical lines mark $mT = \frac{\pi-a}{2}$, the point beyond which our results are no longer trustworthy. Here we have set $N = 1$.

[17] Our exponent is a factor of 2 larger, arising from the fact that complex fermions have twice as many degrees of freedom as Majorana fermions.

[18] We also verified that this result agrees order by order with (9.62), although the result is only written there to $\mathcal{O}(m^2T^2)$.

In Fig. 9.3 we plot both results in the range $0 < mT < 1$ for various values of a. While the $\mathcal{O}(m^8T^8)$ result can be seen to diverge in this range for larger values of a, note that our result is only valid for $mT < \frac{\pi-a}{2}$ (this is the inequality we have assumed in order to neglect the contribution from the frequency region C), for which we always see the decaying behaviour characteristic of an SFF slope. This decay becomes increasingly rapid as $a \to \pi$, as the exponent of (9.85) blows up to negative infinity[19].

9.4.2 $mT > \frac{\pi-a}{2}$

For the case where a gets sufficiently close to π that we have $mT > \frac{\pi-a}{2}$, we have to include contributions from the region C. To this end, we take $\epsilon \equiv \pi - a$ such that $0 < \epsilon < 2mT \ll 1$ (recall that we are still in the early time limit). We then evaluate the action (9.83) the same as before, except that the $n = 1$ contribution now comes from region C and not region D, so

$$\sum_{\{c_\alpha^n\}} e^{NI(\mathcal{S})} = \sum_{c_1^{-1},c_2^1=\pm 1} \exp\left\{ N \left[I_C(c_1^{-1}; x_1) + I_C(c_2^1; x_1) + 2 \sum_{n>1,\text{odd}} I_D(x_n) \right] \right\}. \quad (9.87)$$

where we have used (F.8). Expanding to $\mathcal{O}(m^2T^2)$, performing the sums and implementing the regularisation and normalisation[20], we obtain

$$g(T) = \frac{1}{4} \exp\left\{ -N\frac{m^2T^2}{\epsilon^2} + 2N \log\left(1 + \frac{1}{e}\frac{m^2T^2}{\epsilon^2} \exp\left\{ \frac{m^2T^2}{\epsilon^2} + \frac{\epsilon^2}{2m^2T^2} \right\} \right) \right\}. \quad (9.88)$$

We verify that the same result is obtained if we had instead set $a = (2k+1)\pi - \epsilon$ for integer k at the start of the calculation and accordingly evaluated the C saddles at $x_n = (2k+1)\pi/mT$. Thus the result is invariant under large gauge transformations $a \to a + 2\pi k$. While we can only obtain an explicit expression for (9.87) for times satisfying $mT \ll 1$, in Appendix F.3 we show that one still obtains a gauge invariant result even when this condition is relaxed[21].

[19] Recall that gauge configurations where a is an odd multiple of π are unphysical.

[20] Since we sum over four saddles here, we implement the additional normalisation of dividing by 4. This can be justified by noting that the contribution from each saddle is equal to 1 at $T = 0$ as per (9.85), and the overall SFF must be normalised such that $g(0) = 1$.

[21] Additionally, we show there that one obtains a gauge-invariant early time SFF even in cases where there is more than one frequency contribution from region C (In such cases we cannot calculate the SFF explicitly as above, since the existence of more than one frequency in region C is inconsistent with the assumption $mT \ll 1$). We thus see that even though the bounds on each Matsubara sum in (9.83) depend on a in a seemingly non-gauge-invariant way, we obtain an overall result which is still gauge-invariant. As we shall see, the same will be true for the late time SFF.

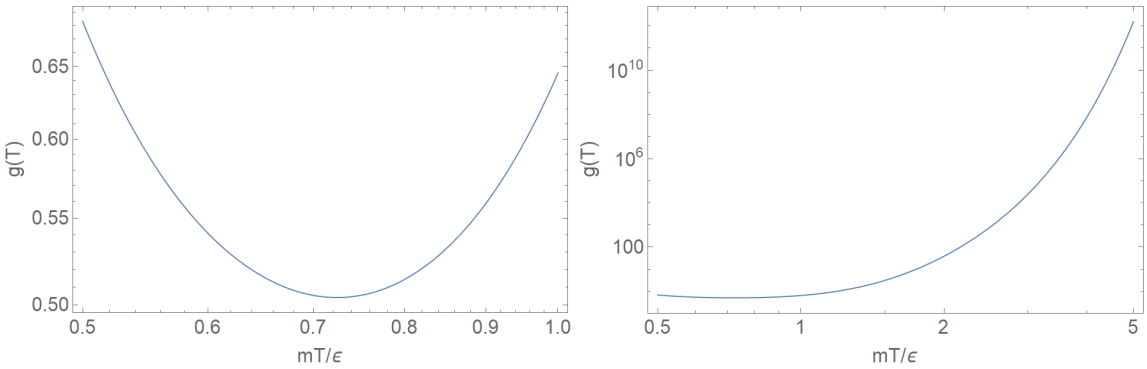

Figure 9.4: Log-log plots of the SFF (9.88) for $a = \pi - \epsilon$ and $0 < \epsilon < 2mT \ll 1$, with $N = 1$.

This result (9.88) is valid for times satisfying $\epsilon < 2mT \ll 1$ (indeed it diverges as $mT \to 0$ for any finite ϵ). We plot this result, which is a function only of the combination mT/ϵ, in Fig. 9.4. In the left hand plot, we zoom in on the region $\epsilon < 2mT < 2\epsilon$, where we see the end of the slope and the beginning of a region of increasing behaviour: this is the characteristic dip of the SFF. The increase after the dip seen here is exponential in N, and likely corresponds to the oscillating behaviour which is known to exist at the start of the SYK$_2$ exponential ramp and which has its origin in pure saddle point contributions to the SFF [179]. Our result cannot be trusted up to the values of mT plotted in the right hand figure.

Note that from the plot we may numerically estimate the dip time as

$$mT_{\text{dip}} \approx 0.73(\pi - a), \tag{9.89}$$

valid for values of the gauge field strength a such that $0 < \pi - a \ll 1$.

9.5 The late time SFF

We now consider the SFF in the late time, $mT \gg 1$, limit. To see interesting results, we will need to include the effect of fluctuations. In particular, as we shall see, the effect of the zero mode fluctuations will be crucial in giving rise to an exponential ramp in the SFF at late times.

At late times we will assume that $2mT > |a|$ holds, so the frequency region A exists (see Table F.2). We then obtain from (9.75) the following expression for the on-shell

action

$$I(\mathcal{S}) = 2\Bigg[\sum_{\substack{n\pi>2mT+|a|\\ n \text{ odd}}}^{\infty} I_D(x_n) + \frac{1}{2}\sum_{\substack{n\pi>2mT-|a|\\ n \text{ odd}}}^{2mT+|a|}\left(I_C(c_1^{-n};\mathrm{sgn}(a)x_n) + I_C(c_2^{n};\mathrm{sgn}(a)x_n)\right) + \frac{1}{2}\sum_{\substack{n\pi>0\\ n \text{ odd}}}^{2mT-|a|}\left(I_A(c_1^{n},c_2^{n};x_n) + I_A(c_2^{-n},c_1^{-n};x_n)\right)\Bigg]. \tag{9.90}$$

Here we have written the bounds of each region (9.73) explicitly in each summation (see the frequency bounds in Table F.2), and we have written the summations over only positive frequencies n (and eliminated dependence on the region B) by using the symmetries (F.8). Note that, unlike for the case $2mT < |a|$ in (9.83), the action now receives contributions from the region A.

We now analyse the fluctuations about the respective saddles. To this end, we rewrite the expression for the SFF as,

$$g(T) = \frac{\int \mathcal{D}\mathcal{S} e^{NI(\mathcal{S})}}{\int \mathcal{D}\mathcal{S} e^{-\frac{N}{2}\mathrm{Tr}\mathcal{S}^2}}, \tag{9.91}$$

where we now normalise by dividing by the free theory [179, 168]

$$\int \mathcal{D}\mathcal{S} e^{-\frac{N}{2}\mathrm{Tr}\mathcal{S}^2} = \prod_{\alpha,\beta,n,n'} \sqrt{\frac{2\pi}{N}}. \tag{9.92}$$

Using the large N saddle point approximation (up to quadratic fluctuations) and summing over all saddles labelled by distinct choices of $\{c_\alpha^n\}$, we can then write the total SFF (9.81) as a sum over saddles $\{c_\alpha^n\}$

$$g(T) \equiv \sum_{\{c_\alpha^n\}} \mathcal{G}(T,\{c_\alpha^n\}), \tag{9.93}$$

where $\mathcal{G}(T,\{c_\alpha^n\})$ is the contribution to the SFF from a *single* saddle,

$$\mathcal{G}(T,\{c_\alpha^n\}) \equiv e^{NI(\mathcal{S})} \prod_{\alpha,\beta,n,n'} F\left[M_{\alpha\beta}^{nn'}\right]. \tag{9.94}$$

Here $F\left[M_{\alpha\beta}^{nn'}\right]$ is the path integral for quadratic fluctuations, with action (9.79) and containing the normalisation (9.92), given by

$$F\left[M_{\alpha\beta}^{nn'}\right] = \sqrt{\frac{N}{2\pi}} \int \mathcal{D}\delta\mathcal{S}_{\alpha\beta}^{nn'} \exp\left\{-\frac{N}{2} M_{\alpha\beta}^{nn'} \delta\mathcal{S}_{\alpha\beta}^{nn'} \delta\mathcal{S}_{\beta\alpha}^{n'n}\right\}. \tag{9.95}$$

Recall that the effective mass matrix $M_{\alpha\beta}^{nn'}$ is dependent on the particular saddle point considered, and therefore may have dependence on the constants $c_\alpha^n, c_\beta^{n'}$. We have already verified that $M_{\alpha\beta}^{nn'} \geq 0$ for all saddles and frequency regions (see Appendix F.2). Let us first consider the massive modes and their fluctuations. For these modes $M_{\alpha\beta}^{nn'} > 0$ and the quadratic fluctuation integral (9.95) is easily carried out in each case to obtain

$$\prod_{\alpha,\beta,n,n'} F\left[M_{\alpha\beta}^{nn'}\right] = \prod_{\alpha,\beta,n,n'} \sqrt{\frac{N}{2\pi}}\sqrt{\frac{2\pi}{NM_{\alpha\beta}^{nn'}}} = \exp\left\{-\frac{1}{2}\sum_{\alpha,\beta,n,n'} \log M_{\alpha\beta}^{nn'}\right\}. \tag{9.96}$$

Note that this contribution is independent of N. While we will not evaluate it explicitly, we argue that it is convergent in Appendix F.4.

We now turn our attention to the zero modes, whose presence is signalled by vanishing effective mass matrices. As discussed, for saddles where $c_1^n = -c_2^{-n}$, the effective mass matrices $M_{\alpha\beta}^{nm}$ vanish for frequencies in the range $|\xi_\alpha x_n + b| \leq 2,\ |\xi_\beta x_m + b| \leq 2$ when $\alpha \neq \beta$ and $n' = -n$. Thus we have

$$M_{12}^{n,-n} = 0 \qquad \text{when} \quad |x_n + b| \leq 2, \tag{9.97}$$

$$M_{21}^{n,-n} = 0 \qquad \text{when} \quad |x_n - b| \leq 2. \tag{9.98}$$

From (9.95), we see that each vanishing mass matrix $M_{\alpha\beta}^{n,-n}$ contributes to the total fluctuation path integral a factor of

$$\int \mathcal{D}\delta\mathcal{S}_{\alpha\beta}^{n,-n}. \tag{9.99}$$

It may appear that this contribution is divergent. However, recall that the zero modes are Goldstone modes that have their origin in the explicit breaking of the symmetry of the equations of motion (9.69) (under general unitary transformations $\tilde{\Sigma} \to U^\dagger \tilde{\Sigma} U$) by the $\sigma^z\omega$ term. The residual symmetry subgroup of unitary transformations which leave this term invariant, transform the zero modes into each other, generating a degenerate saddle point manifold [228]. Crucially, the variations $\delta\mathcal{S}$ associated with zero modes are confined to this manifold, which has a finite volume which is independent of n. We denote this volume by

$$V_{\alpha\beta} \equiv \int \mathcal{D}\delta\mathcal{S}_{\alpha\beta}^{n,-n}. \tag{9.100}$$

Thus see that the contribution from the zero modes in (9.97) to the overall fluctuation path integral $\prod_{\alpha,\beta,n,n'} F\left[M_{\alpha\beta}^{nn'}\right]$ is given by

$$\prod_{\substack{x_n > -2-b \\ n \text{ odd}}}^{2-b} \sqrt{\frac{N}{2\pi}} \int \mathcal{D}\delta\mathcal{S}_{12}^{n,-n} \quad = \quad \prod_{\substack{n\pi > -2mT-a \\ n \text{ odd}}}^{2mT-a} \sqrt{\frac{N}{2\pi}} V_{12} = \left(\sqrt{\frac{N}{2\pi}} V_{12}\right)^{\frac{2mT}{\pi}}. \tag{9.101}$$

Similarly, the contribution from the zero modes in (9.98) is given by

$$\prod_{\substack{x_n>-2+b\\ n\ \text{odd}}}^{2+b}\sqrt{\frac{N}{2\pi}}\int\mathcal{D}\delta\mathcal{S}_{21}^{n,-n} \;=\; \left(\sqrt{\frac{N}{2\pi}}V_{21}\right)^{\frac{2mT}{\pi}}. \tag{9.102}$$

Combining these, and defining the total volume of the degenerate saddle point manifold across all frequencies (normalised by the factor of 2π) as

$$\mathcal{V}\equiv\frac{V_{12}V_{21}}{2\pi}, \tag{9.103}$$

we obtain a total zero mode contribution of

$$(\mathcal{V}N)^{\frac{2mT}{\pi}}. \tag{9.104}$$

Let us now consider the contribution to the SFF from saddle points corresponding to configurations $\{c_\alpha^n\}$ satisfying the conditions $c_1^n=-c_2^{-n}$ for all n; these are precisely the saddle points for which zero modes exist. From (9.94), we have

$$\mathcal{G}(T,\{c_\alpha^n|c_1^n=-c_2^{-n}\})=e^{NI(\mathcal{S})_Z}\prod_{\alpha,\beta,n,n'}F\left[M_{\alpha\beta}^{nn'}\right]. \tag{9.105}$$

where $I(\mathcal{S})_Z$ is the late time on-shell action for these saddle configurations, given by (9.90) evaluated for $c_1^n=-c_2^{-n}$,

$$\begin{aligned}
I(\mathcal{S})_Z &= 2\Bigg[\sum_{\substack{x_n>2+b\\ n\ \text{odd}}}^{\infty}I_D(x_n)+\frac{1}{2}\sum_{\substack{x_n>2-b\\ n\ \text{odd}}}^{2+b}\left(I_C(-c_2^n;x_n)+I_C(c_2^n;x_n)\right)\\
&\qquad+\frac{1}{2}\sum_{\substack{x_n>0\\ n\ \text{odd}}}^{2-b}\left(I_A(c_1^n,c_2^n;x_n)+I_A(-c_1^n,-c_2^n;x_n)\right)\Bigg]\\
&= 2\left[\sum_{\substack{x_n>2+b\\ n\ \text{odd}}}^{\infty}I_D(x_n)+\sum_{\substack{x_n>2-b\\ n\ \text{odd}}}^{2+b}\text{Re}\left[I_C(1;x_n)\right]+\sum_{\substack{x_n>0\\ n\ \text{odd}}}^{2-b}\text{Re}\left[I_A(1,1;x_n)\right]\right],
\end{aligned} \tag{9.106}$$

where we have used (F.9) and taken $b>0$ for convenience. For $mT\gg1$, the variable $x_n=\frac{n\pi}{mT}$ may be treated as a continuous variable x, and we may replace sums over n with integrals over x, allowing us to rewrite this on-shell action as

$$\begin{aligned}
I(\mathcal{S})_Z &= \frac{mT}{\pi}\left(\int_{2+b}^{\infty}dxI_D(x)+\int_{2-b}^{2+b}dx\,\text{Re}\left[I_C(1;x)\right]+\int_0^{2-b}dx\,\text{Re}\left[I_A(1,1;x)\right]\right)\\
&= 0,
\end{aligned} \tag{9.107}$$

where calculating the sum of these integrals using the explicit forms in Appendix F.1, one finds an exactly vanishing result. It follows that the saddle point contribution to the SFF from these configurations is given by

$$e^{NI(\mathcal{S})_Z} = 1. \tag{9.108}$$

The contribution of the zero mode saddles (9.105) is thus given by[22]

$$\mathcal{G}(T, \{c_\alpha^n | c_1^n = -c_2^{-n}\}) = (\mathcal{V}N)^{\frac{2mT}{\pi}} \exp\left\{ -\frac{1}{2} {\sum_{\alpha,\beta,n,n'}}' \log M_{\alpha\beta}^{nn'} \right\}. \tag{9.109}$$

The second factor here is the contribution of the massive modes (where the summation ${\sum}'_{\alpha,\beta,n,n'}$ excludes the zero modes), which is independent of N. All N dependence of this result is contained in the first factor, which is the contribution of the zero modes (9.104). This is precisely the exponential ramp typical of non-interacting disordered systems, first discussed in [179].

We expect the contribution from the massive modes to become important at times $mT \gg N$, where the soft modes combine with the zero mode fluctuations to produce the late time plateau characteristic of the SFF [179]. In addition, we expect that the coefficient of the exponent in the N dependent ramp may receive corrections from higher order fluctuations than the quadratic ones we have considered here [168]. Note also that we have neglected saddle point solutions which break time translation invariance, which may slightly alter the results obtained.

9.6 The ramp time

In this section we calculate the ramp time, mT_{ramp}, which we define as the timescale at which the exponential ramp begins. Note that because we are dealing with an integrable system, which does not exhibit RMT universality and therefore has no Thouless time, the ramp time cannot in our case be taken to be synonymous with the Thouless time[23]. Nonetheless, it will prove a useful definition to facilitate discussion of our results in Chapter 10.

[22] See Appendix F.5 for a discussion of why these give the dominant contribution to the late time SFF.

[23] See Section 7.3.4.

Recall that the zero modes which we have identified in (9.97) and (9.98) receive contributions from the following regions respectively

$$|x_n + b| \leq 2 \quad \Longleftrightarrow \quad |n\pi + a| \leq 2mT, \tag{9.110}$$
$$|x_n - b| \leq 2 \quad \Longleftrightarrow \quad |n\pi - a| \leq 2mT. \tag{9.111}$$

In the case of a vanishing gauge field, $a = 0$, these coincide into the single region $|n\pi| \leq 2mT$. Recalling that n must be an odd integer, we see that for times $mT < \pi/2$ there is no such n. Thus, as noted in the context of the Majorana SYK$_2$ model in [179], the ungauged model has a ramp time of $mT_{\text{ramp}} = \pi/2$.

However, this changes in the presence of a nonzero external gauge field[24], $0 < a < 2\pi$. In this case, there are zero mode contributions for $|\pi - a| \leq 2mT$, which gives a ramp time of

$$mT_{\text{ramp}} = |\pi - a|/2. \tag{9.112}$$

Recalling that the gauge configuration $a = \pi$ is unphysical, we see that the ramp time can never be zero. However, by tuning a, it may be made arbitrarily small[25]. We will return to discuss the significance of this in Chapter 10.

9.6.1 The early time SFF revisited

Having examined the effect of zero modes at late times in the previous section, we now consider them at early times. In particular, we reconcile the case $mT_{\text{ramp}} \ll 1$ with our results for the $mT \ll 1$ SFF in Section 9.4. For concreteness, we set $a = \pi - \epsilon$ where $\epsilon \ll 1$, giving a ramp time of $mT_{\text{ramp}} = \epsilon/2$. Then for $mT < mT_{\text{ramp}}$ (note that this implies $mT \ll 1$), the zero mode contribution vanishes and we again obtain the early time slope (9.85).

On the other hand, when $mT \geq mT_{\text{ramp}}$, saddle configurations with $c_1^n = c_2^{-n}$ (for all n) give rise to zero modes with contributions from the frequencies x_1 and x_{-1}, which give an exponential ramp (9.104). The corresponding on-shell action evaluated for

[24] We need only consider the case $0 < a < 2\pi$ due to the invariance of all of our results under large gauge transformations.

[25] Note that while the ramp time depends on a, the ramp itself, $(\mathcal{V}N)^{2mT/\pi}$, has no explicit dependence on the gauge field.

these configurations is given in (9.87) as

$$\begin{aligned} I(\mathcal{S})_Z &= I_C(-c_2^1; x_p) + I_C(c_2^1; x_1) + 2\sum_{\substack{n>1\\ n \text{ odd}}} I_D(x_n) \\ &= 2\,\mathrm{Re}\,[I_C(1; x_1)] + 2\sum_{\substack{n>1\\ n \text{ odd}}} I_D(x_n), \end{aligned} \tag{9.113}$$

where we have used (F.9). Unlike for the late time case considered in (9.107), the action $I(\mathcal{S})_Z$ does not vanish at early times, $mT \ll 1$. The total contribution (9.105) to the SFF from such a saddle is then given by

$$\begin{aligned} \mathcal{G}(T, \{c_\alpha^n | c_1^n = -c_2^{-n}\}) &= e^{NI(\mathcal{S})_Z} (\mathcal{V}N)^{\frac{2mT}{\pi}} \exp\left\{ -\frac{1}{2}{\sum_{\alpha,\beta,n,n'}}' \log M_{\alpha\beta}^{nn'} \right\} \\ &= \exp\left\{ NI(\mathcal{S})_Z + \frac{2mT}{\pi}\log(N\mathcal{V}) - \frac{1}{2}{\sum_{\alpha,\beta,n,n'}}' \log M_{\alpha\beta}^{nn'} \right\} \end{aligned} \tag{9.114}$$

where the summation $\sum'_{\alpha,\beta,n,n'}$ excludes the zero modes, which give a $\mathcal{O}(N^0)$ contribution to the exponent and may be neglected. It may then be verified that the subleading $\mathcal{O}(\log N)$ term resulting from the early time ramp gives a negligible contribution at large N for $mT \ll 1$. We therefore expect our previous analysis of the early time results in Section (9.4), where we neglected fluctuation contributions, to hold.

Chapter 10

Conclusion to Part II

We have concluded the second part of this thesis with a calculation of the SFF for the complex SYK_2 model in the presence of an external gauge field, in the large N limit. While the gauge field is not integrated over in the path integral, and is therefore equivalent to a twisting of the fermionic boundary conditions, it nonetheless features prominently in our results in the form of the quantity[1] $a = \int_0^T dt A(t)$. All results are verified to be invariant under large gauge transformations $a \to a + 2\pi k$ for integer k, so in the following we restrict a to take values $0 \leq a < 2\pi$, with the case $a = \pi$ excluded as unphysical.

We obtained distinct expressions in the saddle point approximation for the two time regimes $|a| > 2mT$ and $|a| < 2mT$ in terms of Matsubara sums. At early times, $mT \ll 1$, the purely saddle point result gives the characteristic decaying behaviour of an SFF slope, where the decay rate can be controlled by adjusting a. At times greater than the ramp time $mT_{\text{ramp}} = |\pi - a|/2$, we obtained an N dependent exponential ramp from the zero mode fluctuations about the saddle points, which arise due to an explicitly broken unitary symmetry of the action. We identified the explicit time dependence of this ramp, up to quadratic order in the fluctuations. This ramp dominates the SFF at late times, $mT \gg 1$, but gives a subleading contribution to the purely saddle point result at early times.

In this chapter we discuss and make some speculative comments on these results, as well as discuss some natural follow-ups to this work.

[1] We often refer to this quantity a simply as the gauge field.

Chemical potential vs external guage field

The complex SYK_2 model with chemical potential has been considered in [168], largely using different methods to the path integral approach utilised here and in [179]. Their model is equivalent to ours under the replacement of the chemical potential μ by the gauge field $iA(\tau)$. What distinguishes our model is that in periodic *real time* with period T, relevant for the calculation of the SFF, the constant gauge configuration[2] is $A(t) = a/T$. Since T is the time argument of the SFF, the external gauge field in our model therefore introduces additional "time" dependence into the SFF calculation, which cannot be introduced through a constant chemical potential. Indeed, our SFF results are not equivalent to those of [168] under the simple continuation $\mu \to ia/T$. Under this replacement, their result for the SFF slope[3],

$$g(T) = \exp\left\{-\frac{NT^2}{2}\cos(\mu T)\right\} \to \exp\left\{-\frac{NT^2}{2}\cosh(a)\right\}, \tag{10.1}$$

has different qualitative behaviour and, unlike all of our results, is not invariant under large gauge transformations.

The SFF for intermediate times

In the intermediate time regime, for which neither $mT \ll 1$ nor $mT \gg 1$, we expect the SFF to be described by a combination of the purely saddle point contributions from the on-shell actions (9.90) and (9.83) (although the Matsubara sums cannot be evaluated explicitly in this case[4]), and the zero mode fluctuations about them. We expect these various contributions to combine into the dip. For certain values of the gauge field strength we actually have analytic access to this dip region in the purely saddle point approximation[5], and have given an estimation of the dip time (9.89) $mT_{\text{dip}} \approx 0.73(\pi - a)$, valid for a such that $0 < \pi - a \ll 1$. However, if we simply ignore this range of validity and set $a = 0$, we obtain a dip time (for $m = 1$) for the SYK_2 model of

$$T_{\text{dip}} \approx 0.73\pi. \tag{10.2}$$

[2]Recall that in Euclidean time, the constant gauge configuration is $A(\tau) = a/\beta$.

[3]Here we have normalised their result and taken the limit $T \ll 0$ and $m = 1$.

[4]However, in [179] some methods are used to directly manipulate the (G, Σ) path integral to obtain an expression for saddle point contributions to the SFF for times beyond the $mT \ll 1$ approximation.

[5]It is not unexpected that the dip can still be seen even without including the fluctuations which give rise to the ramp. In [179], for example, the saddle point result for the slope ends in oscillating behaviour bounded from below by an increasing envelope, from which the dip time can already be discerned, and is barely affected by the inclusion of the ramp.

Using equations (17) and (33) of [179] for the SFF[6], we obtain a corresponding dip time of

$$T_{\text{dip}} \approx 0.76\pi. \tag{10.3}$$

Using equation (5b) of [168] for the SFF, with the chemical potential switched off, we obtain a corresponding dip time of

$$T_{\text{dip}} \approx 0.8\pi. \tag{10.4}$$

It thus appears that our result for the $0 < \pi - a \ll 1$ dip time remains valid for values of a outside of these bounds. It would be interesting to investigate the reasons for this, which we leave to future work.

The exponential ramp

In our model, we indeed found the presence of a late time exponential ramp, in line with the conjecture in [179] that such a ramp should be a feature of all non-interacting, disordered systems. The explicit expression which we find for the ramp (9.104), up to quadratic order in fluctuations, has no explicit dependence on the gauge field a. This is not surprising, as naively taking the limit $T \to \infty$ in the action (9.30) kills off the gauge field term and leaves the action of the complex SYK_2, which is known to have an exponential ramp [168]. However, we obtain a *ramp time* which *does* depend on the gauge field: $mT_{\text{ramp}} = |\pi - a|/2$. Our ramp time coincides with that of [179] for $a = 0$, but may be made arbitrarily small as a approaches π.

If our system were chaotic and our ramp were linear, this ramp time would have a significant interpretation: it would be none other than the Thouless time, the timescale which signals the onset of RMT universality in a quantum chaotic system (see Section 7.3.4). The significance of the timescale at which the exponential ramp begins in a non-chaotic system is less clear. However, the fact that tuning the gauge field may be used to alter this timescale in the way described above, poses the interesting question: would the introduction of an external gauge field in the SYK_4 model allow for the *Thouless time* to be tuned in a similar way? We discuss this possibility further below.

First, we review the different mechanisms underlying the linear and exponential ramps in the Majorana SYK_4 model and the (Majorana and complex) SYK_2 models, respectively. For the Majorana SYK_4 model, the contributions of the replica-diagonal

[6]Note that we are here comparing the dip times of the complex and Majorana SYK_2 models. This is justified since we expect these results to differ only by a power of 2 (accounting for the difference between the number of degrees of freedom in the models) which does not affect the dip time.

saddles to the full SFF just give the disconnected SFF [184], which describes the slope. The ramp can only be seen by including the late time contributions of the replica-non-diagonal saddles[7], which spontaneously break time translation symmetry. In the SYK_2 cases considered here and in [179, 168], we see that the ramp has different origins: considering only replica-diagonal solutions still leads to symmetry breaking and an exponential ramp, which is not present in the disconnected SFF. The replica-non-diagonal solutions thus appear to play less of a role in the $q = 2$ models.

Specifically, in the Majorana SYK_2 case studied in [179], the $SU(2)$ conjugation symmetry of the two-replica action is *spontaneously* broken by the form of the diagonal saddle point solutions above a critical frequency. The associated Goldstone zero modes give rise to an exponential ramp. In the complex SYK_2 case studied here and in [168], the the two-replica action contains a term which *explicitly* breaks the unitary conjugation symmetry that it would otherwise possess. A subset of the associated Goldstone soft modes are indeed zero modes (with vanishing action) and these give rise to an exponential ramp.

The gauged, mass-deformed SYK model

A natural follow-up to our work would be to study the gauged SYK_2 model when perturbed by an SYK_4 interaction term. In this case, with the gauge field turned off, we obtain a complex version of the mass-deformed SYK model studied in [152, 92], which exhibits a chaotic-integrable transition[8].

In [179], a qualitative explanation is given for this transition at the level of the SFF, where it manifests as the transition from an exponential to a linear ramp. In particular, it is argued that the introduction of $q > 2$ SYK_q interactions breaks the unitary symmetry of the SYK_2 action to a relative time translation which acts independently on each replica. This symmetry breaking changes the structure of the degenerate zero mode vacuum manifold from $(\mathcal{V})^{\frac{2mT}{\pi}}$ (as in (9.104)) down to a real-time circle with volume proportional to T, resulting in a linear-in-T ramp[9].

If we were to similarly perturb our model with an SYK_4 interaction, we would expect the mechanism described above to result in a transition from an exponential ramp to a linear ramp. Since in our model, increasing the gauge field ensures that zero modes are present at earlier times, this presents the possibility that the change in vacuum manifold induced by the SYK_4 term would result in a linear ramp which also begins

[7] See the discussion in Section 8.2.3.
[8] See Section 9.1.
[9] See the discussion for the SYK_4 model in Section 8.2.3.

at earlier times. Consequently, the *Thouless time* in the chaotic phase of the gauged, mass-deformed SYK model could be tuned by a in a way similar to in our model[10].

In the event that this is correct, we may speculate further. We have shown that for the SYK_2 model, the introduction of an external gauge field leaves the OTOC unaffected. If this statement were to hold also for the mass-deformed SYK model, this would have implications for the relation between the OTOC and the SFF as diagnostics of chaos (see the discussion in Section 7.5). In particular, the gauged, mass-deformed SYK model would have a parameter a which affects (universal features of) the SFF, while leaving the OTOC invariant. It is already known [92] that an RMT analysis and an OTOC analysis are not affected in the same way by parameters of the mass-deformed theory: the OTOC picks up on the chaotic-integrable transition for smaller values of the SYK_2 coupling than the RMT analysis. It would be interesting to see how our gauge field parameter a fits into this picture.

The above discussion suggests that, for the SYK_q models and their variants, the presence of an external gauge field may introduce a parameter of key importance to the quantum chaotic properties of the system. We leave more concrete investigations of these speculations to future work.

Other non-integrable perturbations

Notwithstanding the qualitative discussion from [179] referenced above, an explicit analytic treatment of the SFF for the SYK_2 model perturbed by a fully random SYK_4 interaction term (the mass-deformed SYK model) is still outstanding. It is therefore likely that the prospective calculations discussed above would have to be performed numerically. However, analytic inroads have already been made for calculating the SFF for the complex SYK_2 model when perturbed by quartic, non-SYK_4 interactions.

Namely, the SFF for the SYK_2 model perturbed by a *non-random* 4-fermi interaction term [169] and by a random 4-fermi SYK_2^2 interaction (the square of an SYK_2 term)

[10] On the other hand, in [189] it is shown that the Lyapunov exponent of the complex SYK_q model in the $q \to \infty$ limit is strongly suppressed by a nonzero chemical potential. Given the structural similarity (discussed above) between a gauge field and a chemical potential in $(0+1)$-dimensions, it might be the case that a gauge field has this same effect of pushing the mass-deformed complex SYK model into an integrable phase for all values of the SYK_4 coupling, in which case we would not see a linear ramp in its SFF at all. However, the large q results from [189] may not be relevant to the $q = 2, 4$ cases. Indeed, in [164], the complex SYK_4 model with nonzero chemical potential is studied numerically at the level of the free energy, and a nontrivial chaotic-integrable phase diagram is found as a function of temperature and chemical potential, which might be more releant to our situation of interest.

[170] have been studied. In both cases the solution for the SYK_2 SFF serves as the conceptual and analytical solution about which the full solutions are constructed as perturbations. It is found that the quartic interactions induce a mass for the SYK_2 soft modes, which would otherwise give rise to the exponential ramp[11]. The exponential ramp is then suppressed, which is a necessary prerequisite for the emergence of RMT statistics.

Another natural follow-up to our work, more suited to analytical analysis, would then be to repeat our calculation for the gauged SYK_2 model perturbed by non-SYK four-fermi interaction such as those considered in [169, 170], and to see what effect the gauge field has on the chaotic-integrable transition.

A gauged AdS/SYK correspondence

Finally, we circle back to our initial motivation outlined in Section 9.2, and point out that a gauged SYK model may have a role to play in the formulation of a more conventional weakly-coupled, small curvature gravity dual. In particular, having developed intuition and tools for the investigation of the chaos properties of the model with a local *abelian* (colour) symmetry, it would be interesting to apply these to the model with a local *non-abelian* (flavour) symmetry. Such a study brings us closer to the suggestion in [212] that gauging a large subgroup of the $SO(N)$ flavour symmetry might be key to fixing the issues with the construction of an AdS/SYK correspondence.

In this part of the thesis, by considering a variation of the well understood complex SYK_2 model consisting of the introduction of an external gauge field (or equivalently the twisting of the fermionic boundary conditions), we have found results which both confirm existing expectations as to the behaviour of the SFF for non-interacting disordered systems, and also exhibit new and novel behaviour. The latter give rise to a number of promising questions for future research into the rich and active field of quantum chaos and disordered systems.

[11] While the model in [169] is chaotic, the model in [170] has chaotic and integrable regimes. In the integrable regime no mass is induced for the soft modes and the exponential ramp survives.

Part III

Appendices

Appendix A

Parity and discrepancy with the literature

In Section 2.1.2 we followed [52] in using $\Pi_i = -i\hbar\partial_i - eA_i$. To compare to similar results in the literature we need to use the more standard $\hat{\Pi}_i = -i\hbar\partial_i + eA_i$. Physically, changing between the two corresponds to flipping the direction of the magnetic field through the plane, $B \to -B$.

Flipping B is equivalent to leaving B invariant but flipping the plane with the parity transformation [51] $x_2 \to -x_2$ (we can think of this as rotating the plane through the third dimension about the x_1-axis). The gauge field transforms as $A_2 \to -A_2$, so the vector potential in symmetric gauge transforms as $B/2(-x_2, x_1) \to B/2(x_2, -x_1)$, confirming that the net effect of parity is to change the sign of B. In complex coordinates, our parity transformation is given by $(z, \bar{z}) \to (\bar{z}, z)$, or in complex polar coordinates $(r, \phi) \to (r, -\phi)$.

Transforming our solutions under parity for the spin-0 case is straightforward. The raising and lowering operators of ψ_n^m transform as[1]

$$a^\dagger \to \tilde{a}^\dagger = -l\Big(\bar{\partial} - \frac{1}{2l^2}z\Big)\,, \qquad a \to \tilde{a} = l\Big(\partial + \frac{1}{2l^2}\bar{z}\Big)\,, \quad \text{with} \quad [\tilde{a}, \tilde{a}^\dagger] = 1\,. \tag{A.1}$$

The Hamiltonian becomes

$$H_0 \to \tilde{H}_0 = \tilde{a}^\dagger\tilde{a} + \frac{1}{2} \tag{A.2}$$

with eigenstates given by

$$\tilde{\psi}_n^m(r, \phi) = \psi_n^m(r, -\phi)\,. \tag{A.3}$$

[1] Note that $\tilde{a}^\dagger = b^\dagger$ and $\tilde{a} = b$, so parity swaps our a and b operators.

They have the same energy as before, and the transformed operators $\tilde{a}, \tilde{a}^\dagger$ act on them analogously to (2.29). The only difference is that the factor $e^{im\phi}$ in the states is replaced by $e^{-im\phi}$. Since parity sends

$$J_0 = -i\partial_\phi \to \tilde{J}_0 = -J_0\,, \tag{A.4}$$

orbital angular momentum is left invariant[2].

We move now to the spin-1/2 system. The transformed Hamiltonian is

$$\tilde{H} = v\begin{pmatrix} 0 & \tilde{\Pi}_1 - i\tilde{\Pi}_2 \\ \tilde{\Pi}_1 + i\tilde{\Pi}_2 & 0 \end{pmatrix} = \frac{\sqrt{2}v\hbar}{il}\begin{pmatrix} 0 & \tilde{a} \\ -\tilde{a}^\dagger & 0 \end{pmatrix}. \tag{A.5}$$

Comparing to (2.34), we see that to get from H to $\tilde{H}$ we need both implement the parity coordinate transformation and take the transpose. Thus we deduce that parity acts not only on our physical coordinates but on the spinor space of our 2-component solutions via some unitary operator P, such that operators transform as

$$H \to P\tilde{H}P^\dagger\,, \tag{A.6}$$

where

$$\tilde{H} \equiv H(z \to \bar{z}, \bar{z} \to z)\,. \tag{A.7}$$

We deduce that

$$P = \begin{pmatrix} 0 & 1 \\ 1 & 0 \end{pmatrix} = \sigma_1\,, \tag{A.8}$$

which satisfies $P^2 = 1$ as required by a parity operator, and it is easily verified that conjugation by P is equivalent to taking the transpose. Eigenstates and eigenvalues will then be given by

$$P\tilde{\Psi}^m_n(z,\bar{z}) = \begin{pmatrix} \tilde{\psi}^{m+1}_{n-1}(z,\bar{z}) \\ i\tilde{\psi}^m_n(z,\bar{z}) \end{pmatrix} \tag{A.9}$$

$$\begin{aligned} E_n &= v\sqrt{2\hbar eBn} \\ n &= 1, 2, 3, ... \\ m &= -n, -n+1, ... \end{aligned} \tag{A.10}$$

since

$$\tilde{H}\tilde{\Psi}^m_n = PHP^\dagger P\Psi^m_n = PH\Psi^m_n = PE_n\Psi^m_n = E_n\tilde{\Psi}^m_n\,. \tag{A.11}$$

[2]If we had define our angular momentum operator relative to our original coordinates, i.e. setting $\tilde{J}_0 = J_0$, it would follow that flipping the magnetic field reverses the angular momentum of our states (changes the sign), as we would classically predict: $\tilde{J}_0\tilde{\psi}^m_n = -\hbar m\tilde{\psi}^m_n$.

Thus the energy spectrum for our flipped B system is the same as before. By an analogous calculation we see that the total angular momentum of these states is also the same as before,

$$\tilde{J}\tilde{\Psi}_n^m = (m + 1/2)\tilde{\Psi}_n^m \,, \tag{A.12}$$

where

$$\tilde{J} = P\tilde{J}P^\dagger = i\hbar\partial_\phi + \frac{\hbar}{2}\sigma_1\sigma_3\sigma_1 = i\hbar\partial_\phi - \frac{\hbar}{2}\sigma_3 = -J \,, \tag{A.13}$$

which can easily be shown to satisfy $[\tilde{J}, \tilde{H}] = 0$ as it should.

Having cast our solutions for the standard B field configuration considered in the literature in (A.9), we see that they differ from the solution given in the literature [20, 49, 50], where the angular momentum m of both components of the solution are equal:

$$\Psi_m^n \sim \begin{pmatrix} \hat{\psi}_{n-1}^m \\ i\hat{\psi}_n^m \end{pmatrix} \tag{A.14}$$

Such solutions are eigenstates of orbital angular momentum $J_0 = i\hbar\partial_\phi$, which contradicts the fact that J_0 does not commute with the Hamiltonian. They are also not eigenstates of total angular momentum $J = i\hbar\partial_\phi + \hbar\sigma_3/2$, which we would expect them to be as this is the conserved quantity following from the rotational symmetry of the problem. It seems to me that the authors have not taken into account the fact that the operators $a(a^\dagger)$ which appear in the Hamiltonian do not only raise (lower) energy n, but also lower (raise) angular momentum m.

Appendix B

Spherical harmonics

We follow [32] and derive the spherical harmonics $Y_{Q,l,m}$. These are eigenstates of the Hamiltonian (2.51)

$$\begin{aligned} |\mathbf{\Lambda}|^2 Y_{Q,l,m} &= (L^2 - Q^2) Y_{Q,l,m} \\ &= \big[l(l+1) - Q^2\big] Y_{Q,l,m}, \end{aligned} \tag{B.1}$$

where we have chosen the standard form $l(l+1)$ for the eigenvalue of L^2. The energy eigenvalues are therefore given by

$$E = \frac{\omega_B}{2Q}\big[l(l+1) - Q^2\big] \tag{B.2}$$

Defining m to be the eigenvalue of L_z, it follows from the explicit form of L_z (2.60) that

$$Y_{Q,l,m}(\theta, \phi) = e^{im\phi} P_{Q,l,m}(\theta) \tag{B.3}$$

Using (2.53) it then follows that

$$\left[-\frac{1}{\sin\theta}\frac{\partial}{\partial\theta}\sin\theta\frac{\partial}{\partial\theta} + \frac{1}{\sin^2\theta}(Q\cos\theta - m)^2 \right] P_{Q,l,m} = \big[l(l+1) - Q^2\big] P_{Q,l,m}. \tag{B.4}$$

Making the substitution $x = \cos\theta$, this becomes

$$\left[2x\frac{\partial}{\partial x} - (1-x^2)\frac{\partial^2}{\partial x^2} + \frac{(m - Qx)^2}{1-x^2} \right] P_{Q,l,m} = \big[l(l+1) - Q^2\big] P_{Q,l,m}. \tag{B.5}$$

To eliminate the $(1-x^2)$ in the denominator we make the substitution

$$P_{Q,l,m} = (1+x)^{\frac{b+a}{2}}(1-x)^{\frac{b-a}{2}} R_{Q,l,m}, \tag{B.6}$$

which yields

$$\left[(1-x^2)\frac{\partial^2}{\partial x^2}+[2a-2(b+1)x]\frac{\partial}{\partial x}-\frac{C}{1-x^2}\right]P_{Q,l,m}=\big[Q^2-l(l+1)\big]P_{Q,l,m}, \quad \text{(B.7)}$$

where

$$C=(Q^2-b^2-b)x^2+2(ab-mQ)x+(m^2-a^2+b). \quad \text{(B.8)}$$

Making the choice $a=Q, b=m$ gives $C=(m^2+m-Q^2)$ which kills the $(1-x^2)$ in the denominator as intended. We are left with the following second order differential equation

$$(1-x^2)R''+[2Q-2(m-1)x]R'-[m^2+m-2Q^2+l(l+1)]R=0 \quad \text{(B.9)}$$

which we recognise as having the form of the hypergeometric equation

$$(1-x^2)y''+(\beta-\alpha-(\alpha+\beta+2)x)y'+n(n+\alpha+\beta+1)y=0 \quad \text{(B.10)}$$

with solutions given by the Jacobi polynomials

$$P_n^{\alpha,\beta}(x)=\frac{(-1)^n}{2^n n!}(1-x)^{-\alpha}(1+x)^{-\beta}\frac{d^n}{dx^n}\big[(1-x)^{n+\alpha}(1+x)^{n+\beta}\big] \quad \text{(B.11)}$$

$$=\frac{1}{2^n}\sum_{s=0}^{n}\binom{n+\alpha}{s}\binom{n+\beta}{n-s}(x-1)^{n-s}(x+1)^s. \quad \text{(B.12)}$$

Matching coefficients, we find $\alpha=m-Q$, $\beta=m+Q$ and $n=l-m$. We have now found the explicit form of the monopole harmonics

$$Y_{Q,l,m}(\theta,\phi)=\mathcal{N}_{Qlm}2^{-m}(1-x)^{\frac{m-Q}{2}}(1+x)^{\frac{m+Q}{2}}P_{l-m}^{m-Q,m+Q}(x)e^{im\phi} \qquad \text{where} \quad x=\cos\theta \quad \text{(B.13)}$$

where

$$\mathcal{N}_{Qlm}=\sqrt{\frac{(2l+1)}{4\pi}\frac{(l-m)!}{(l-Q)!}\frac{(l+m)!}{(l+Q)!}} \quad \text{(B.14)}$$

is a normalisation constant.

Appendix C

Derivation of the $N = 2$ GOE probability distribution

We derive the GOE probability distribution (for which the calculations are analogous to the GUE and GSE cases, but computationally simpler) in the smallest number of dimensions: we work with 2×2 real symmetric matrices. The probability densities we will find, following the treatment in [106], hold true for the general $N \times N$ case.

To this end, consider the real symmetric matrix

$$M = \begin{pmatrix} M_{11} & M_{12} \\ M_{12} & M_{22} \end{pmatrix}. \tag{C.1}$$

We seek a probability density $P(M)$ which must satisfy the normalisation condition

$$\int_{-\infty}^{\infty} dM_{11} dM_{12} dM_{22} P(M) = 1. \tag{C.2}$$

The condition of uncorrelated matrix elements ensures that we can decompose $P(M) = P_{11}(M_{11})P_{12}(M_{12})P_{22}(M_{22})$, while rotational invariance requires that

$$P(M) = P(M'), \quad M' = OMO^{-1}, \tag{C.3}$$

where the orthogonal matrices O satisfy $O^{-1} = O^T$. We also requires that the measure $\prod_{i,j} dM_{ij}$ be rotationally invariant, a fact we will assume and not prove here. Working with an infinitesimal orthogonal transformation

$$O = \begin{pmatrix} 1 & -\theta \\ \theta & 1 \end{pmatrix}, \tag{C.4}$$

where θ is infinitesimal, we have that

$$M' = OMO^{-1} = M + \theta\delta M, \quad \text{where} \quad \delta M = \begin{pmatrix} -2M_{12} & M_{11} - M_{22} \\ M_{11} - M_{22} & 2M_{12} \end{pmatrix}. \tag{C.5}$$

It follows that

$$\begin{aligned} P(M') &= \prod_{i,j} P(M'_{ij}) \\ &= \prod_{i,j} \left[P(M_{ij}) + \theta\delta M_{ij} \frac{dP_{ij}}{dM_{ij}} \right] \\ &= \prod_{i,j} P(M_{ij}) \left[1 + \theta\delta M_{ij} \frac{1}{P_{ij}} \frac{dP_{ij}}{dM_{ij}} \right] \\ &= P(M) \left[1 + \theta \left(\delta M_{11} \frac{d\log P_{11}}{dM_{11}} + \delta M_{12} \frac{d\log P_{12}}{dM_{12}} + \delta M_{22} \frac{d\log P_{22}}{dM_{22}} \right) \right]. \end{aligned} \tag{C.6}$$

The condition of rotational invariance demands that the term in brackets vanishes, so

$$(M_{11} - M_{22}) \frac{d\log P_{12}}{dM_{12}} = 2M_{12} \frac{d\log P_{11}}{dM_{11}} - 2M_{12} \frac{d\log P_{22}}{dM_{22}} \tag{C.7}$$

$$\Rightarrow \frac{1}{M_{12}} \frac{d\log P_{12}}{dM_{12}} = -4\alpha = \frac{2}{M_{11} - M_{22}} \left(\frac{d\log P_{11}}{dM_{11}} - \frac{d\log P_{22}}{dM_{22}} \right), \tag{C.8}$$

where since the two sides in the equation above depend on different sets of variables, they must both be equal to some constant which we have judiciously chosen as -4α. It follows that

$$P_{12}(M_{12}) = A_{12} e^{-2\alpha M_{12}^2}, \tag{C.9}$$

and

$$\begin{aligned} \frac{d\log P_{11}}{dM_{11}} + 2\alpha M_{11} = \beta = \frac{d\log P_{22}}{dM_{22}} + 2\alpha M_{22}, \\ \Rightarrow P_{ii}(M_{ii}) = A_{ii} e^{-\alpha M_{ii}^2 + \beta M_{ii}}, \quad i = 1, 2, \end{aligned} \tag{C.10}$$

where the A_{ii} are integration constants. Putting these results together, we have obtained

$$P(M) = \gamma e^{-\alpha(M_{11}^2 + 2M_{12}^2 + M_{22}^2) + \beta(M_{11} + M_{22})}, \tag{C.11}$$

where γ is a constant determined by the normalisation condition (C.2), α fixes the units of energy and β can be made to vanish by choosing the zero of energy. Noting

that the term multiplying α is simply the trace of M^2, we have arrived at the final answer for the GOE ensemble

$$P(M) = e^{-\alpha \operatorname{Tr} M^2}, \tag{C.12}$$

up to normalisation. An identical result would have been obtained by an analogous calculation for the GUE or GSE cases.

Appendix D

Conformal two-point function of the SYK_4 model

Substituting the ansatz (8.21)

$$G_c(\tau) = A\frac{\mathrm{sgn}(\tau)}{|\tau|^{2\Delta}}, \tag{D.1}$$

into the strong-coupling Schwinger-Dyson equation (8.16)

$$J^2 \int d\tau' G(\tau,\tau')^{q-1} G(\tau',\tau'') = -\delta(\tau-\tau''). \tag{D.2}$$

yields[1]

$$J^2 A^q \int d\tau' \frac{\mathrm{sgn}(\tau-\tau')\mathrm{sgn}(\tau'-\tau'')}{|\tau-\tau'|^{2\Delta}|\tau'-\tau''|^{2\Delta(q-1)}} = -\delta(\tau-\tau''). \tag{D.3}$$

Now, using the Fourier transform [138]

$$\frac{\mathrm{sgn}(\tau)}{|\tau|^{2\Delta}} = \frac{C[2\Delta]}{2\pi}\int_{-\infty}^{\infty} d\omega e^{-i\omega\tau}|\omega|^{2\Delta-1}\mathrm{sgn}(\omega), \tag{D.4}$$

where

$$C[2\Delta] = i2^{1-2\Delta}\sqrt{\pi}\frac{\Gamma(1-\Delta)}{\Gamma(\frac{1}{2}+\Delta)}, \tag{D.5}$$

[1] Note that $\mathrm{sgn}(\tau'-\tau'')^{q-1} = \mathrm{sgn}(\tau'-\tau'')$ for q even.

the left hand side of (D.3) becomes

$$\begin{aligned}
&\frac{J^2A^q}{(2\pi)^2}C[2\Delta]C[2\Delta(q-1)]\int d\tau'\int_{-\infty}^{\infty}d\omega e^{-i\omega(\tau-\tau')}|\omega|^{2\Delta-1}\mathrm{sgn}(\omega)\int_{-\infty}^{\infty}d\omega' e^{-i\omega'(\tau'-\tau'')}|\omega'|^{2\Delta(q-1)-1}\mathrm{sgn}(\omega')\\
&=\frac{J^2A^q}{(2\pi)^2}C[2\Delta]C[2\Delta(q-1)]\int_{-\infty}^{\infty}d\omega e^{-i\omega\tau}|\omega|^{2\Delta-1}\mathrm{sgn}(\omega)\int_{-\infty}^{\infty}d\omega' e^{i\omega'\tau''}|\omega'|^{2\Delta(q-1)-1}\mathrm{sgn}(\omega')\underbrace{\int d\tau' e^{i(\omega-\omega')}}_{=2\pi\delta(\omega-\omega')}\\
&=\frac{J^2A^q}{2\pi}C[2\Delta]C[2\Delta(q-1)]\int_{-\infty}^{\infty}d\omega e^{-i\omega(\tau-\tau'')}\underbrace{|\omega|^{2\Delta q-2}}_{=1\ \text{since}\ \Delta q=1}\\
&=J^2A^qC[2\Delta]C[2\Delta(q-1)]\delta(\tau-\tau''). \qquad \text{(D.6)}
\end{aligned}$$

Equating this to the right hand side of (D.3) yields

$$\begin{aligned}
J^2A^q&=-\frac{1}{C[2\Delta]C[2\Delta(q-1)]}\\
&=\frac{\Gamma(\frac{1}{2}+\Delta)\Gamma(\frac{1}{2}+\Delta(q-1))}{2^{1-2\Delta}\sqrt{\pi}\Gamma(1-\Delta)2^{1-2\Delta(q-1)}\sqrt{\pi}\Gamma(1-\Delta(q-1))}\\
&=\frac{1}{\pi}\frac{\Gamma(\frac{1}{2}+\Delta)\Gamma(\frac{3}{2}-\Delta)}{\Gamma(1-\Delta)\Gamma(\Delta)} \qquad \text{(D.7)}\\
&=\frac{1}{\pi}\left(\frac{1}{2}-\Delta\right)\tan\pi\Delta, \qquad \text{(D.8)}
\end{aligned}$$

where in the last equality we have used a Gamma function identity. This fixes the coefficient A, confirming our ansatz and yielding the following solution for the conformal two-point function

$$G_c(\tau)=A\frac{\mathrm{sgn}(\tau)}{|\tau|^{2\Delta}},\qquad A=\left[\frac{1}{\pi J^2}\left(\frac{1}{2}-\Delta\right)\tan\pi\Delta\right]^{\Delta}. \qquad \text{(D.9)}$$

Appendix E

The OTOC for the gauged complex SYK_2 model

Recall from Section 7.5 that the out-of-time-ordered correlator may be used as a diagnostic of quantum chaos; for chaotic systems it is expected to exhibit exponential growth at early times, with the rate of exponential growth characterised by the spectrum of Lyaponov exponents. The closely-related double commutator correlation function [144]

$$C(t) = \theta(t)\langle\sqrt{\rho}\left\{\psi^\dagger(t)_i, \psi(0)_j\right\}^\dagger\sqrt{\rho}\left\{\psi^\dagger(t)_i, \psi(0)_j\right\}\rangle, \tag{E.1}$$

may also be used for this purpose, where the splitting of the thermal density matrix $\rho = \rho(\beta)$ into the two factors of $\sqrt{\rho}$ regulates some divergences and places the insertions on opposite sides of the thermal circle [227]. In this section we present our calculation from [222] of this quantity for the gauged complex SYK_2 model. We will first need to calculate the real-time two-point function, picking up from where we left off in Section 9.2.1.

Equation (9.26) can be written as

$$\overline{G_{i_1 j_2}(\tau)} \;=\; \delta_{j_2 i_1}\frac{2}{\pi\beta}\int_{-1}^{1} dy\sqrt{1-y^2}\sum_{n=-\infty}^{\infty}\frac{e^{i(2n-1)\frac{\pi}{\beta}\tau}}{\frac{(2n-1)\pi i}{\beta}+(2my+i\frac{a}{\beta})} \tag{E.2}$$

after making use of an identity in [196]. By making the identification $\omega_n = \frac{\pi}{\beta}(2n-1)$ one can then read off an expression for the Fourier modes in the discrete Fourier transform of the propagator,

$$\overline{G_{j_2 i_1}(\omega_n)} \;=\; \frac{2}{\pi}\delta_{j_2 i_1}\int_{-1}^{1} dy\sqrt{1-y^2}\frac{-1}{i\omega_n-(2my+i\frac{a}{\beta})}. \tag{E.3}$$

Note that while the above expression for an individual mode is not invariant under the large gauge transformation $a \to a + 2\pi k$, the set of *all* modes is.

Given $\overline{G}_{j_2 j_1}(\omega_n)$, the real-time retarded Green's function is usually obtained by analytically continuing $i\omega_n \to \omega + i\epsilon$. In addition, however, we need to Wick rotate the gauge field $a \to -ia$ as we are transforming from real to imaginary time. To disambiguate between the real- and imaginary time expressions we also replace $\beta \to T$. This step is essential for preserving the gauge invariance of our expressions. Then, taking the Fourier transform and carrying out the integral over y, we obtain

$$\begin{aligned} \overline{G_{j_2 i_1}(t)} &= \frac{2}{\pi}\delta_{j_2,i_1}\int\frac{d\omega}{2\pi}\int_{-1}^{1}dy\sqrt{1-y^2}\frac{-1}{\omega+i\epsilon-(2my+\frac{a}{T})}e^{-i\omega t} \\ &= ie^{-i\frac{a}{T}t}\frac{J_1(2mt)}{mt}\theta(t)\,, \end{aligned} \tag{E.4}$$

where J_1 is a Bessel function of the first kind. This agrees with the corresponding expression in [101] up to an additional phase factor in t, which does not affect the late time decay of the expression $\frac{J_1(2mt)}{mt} \sim t^{-\frac{3}{2}}$. Without simultaneously Wick rotating the gauge field, we would instead obtain an overall (decaying) exponential factor which breaks the gauge invariance. We first performing the integral over y in (E.4), followed by the analytic continuation and Wick rotation we obtain

$$\bar{G}_{j_2 i_1}(\omega) = -\delta_{j_2 i_1}\left(\omega - \frac{a}{T}\right)\frac{1-\sqrt{1-\frac{4m^2}{(\omega-\frac{a}{T}+i\epsilon)^2}}}{2m^2} \tag{E.5}$$

The square root factor introduces a branch cut that is shifted just off the real axis. For positive time we close the contour in the lower complex plane and get a non-vanishing result since the branch cut is contained in the contour. The contour may be deformed to one that hugs the branch cut, yielding (E.4). The combination $\frac{J_1(2mt)}{mt}$ decays as $t^{-\frac{3}{2}}$ at late times.

To compute $C(t)$ (in the quenched averaging prescription) we need to perform the standard summation over all Feynman diagrams. As emphasised in Section 9.2.1, this involves the sum of convolutions of the undressed two-point function, which follows from the Wick contractions. The structure of the Wick contractions for $C(t)$ has a special feature due to the anti-commutators. Specifically, as a result of the fermionic statistics, contractions involving an anti-commutator of fields vanish unless the fields in the anti-commutator are contracted with each other. At tree level this implies factorisation of (E.1) into two retarded propagators, a feature which persists even beyond tree level where perturbative two-body insertions may always be combined into

an anti-commutators of fields. This implies that, for our model, Wick contractions can only occur between fields that are inserted on the same side of the thermal circle, dramatically simplifying (E.1) to

$$\begin{aligned} C(t) &= \theta(t) G_{ij}(t)(G_{ij}(t))^* \\ G_{ij}(t_1 - t_2) &= \sum_{n=0}^{\infty} \int dt_1' dt_2' \cdots dt_n' G^0_{ii}(t_1 - t_1') G^0_{k_1 k_1}(t_1' - t_2') \cdots G^0_{jj}(t_n' - t_2) \times \\ &\quad \sum_{k_i=1}^{N} m_{ik_1} m_{k_1 k_2} \cdots m_{k_{n-1} j} \,, \end{aligned} \tag{E.6}$$

where we have used the fact that $G^0_{ij} \propto \delta_{ij}$. We did not, however, impose any further conditions on G^0_{ij} nor did we need to use the disorder averaging of the mass terms. The result (E.6) only makes use of the fact that we have perturbative two-body interactions and the special form of the Wick contractions for anti-commutators of fields.

The results of Section 9.2.1 can be used directly to simplify the above expression. However, a comment of caution is in order. At first glance the above expression looks like the absolute-value-squared of the dressed two-point function. However, unlike the Wick contractions, the mass averaging need not involve mass insertions from the same side of the thermal circle.

To leading order in $1/N$ then, we can write

$$\bar{C}(t) = \theta(t) \bar{G}_{ij}(t)(\bar{G}_{ij}(t))^* + \frac{\theta(t)}{N} \bar{F}_{ijji}(t) + O(\frac{1}{N^2}) \tag{E.7}$$

so that at leading order in N, the double commutator factorises into the product of dressed two-point functions. The $1/N$ corrections come in two forms. The first are of the kind in (9.23) which will further dress the two-point function. The second come from corrections involving mass averaging on opposite sides of the thermal circle. We will focus on the latter since these give rise to ladder diagrams, the proliferation of which is associated with the spectrum of growth exponents [227].

We may regroup the terms in (E.6) to isolate the masses that are involved in averages on opposite sides of the thermal circle. The sum over mass insertions for masses averaged on the same side of the thermal give rise to dressed two-point functions.

This means that

$$\begin{aligned}\frac{1}{N}F_{ijji}(t) &= \sum_{r=1}^{\infty}\left(\int dt_1 dt_2\cdots dt_n \bar{G}_{ii}(t-t_1)\bar{G}_{k_1k_1}(t_1-t_2)\cdots\bar{G}_{jj}(t_{r-1})\right)\times \\ &\quad \left(\int dt_1' dt_2'\cdots dt_n' \bar{G}_{ii}(t-t_1')\bar{G}_{l_1l_1}(t_1'-t_2')\cdots\bar{G}_{jj}(t_{r-1}')\right)^*\times \\ &\quad \sum_{k_i,l_i=1}^{N}(m_{ik_1}m_{k_1k_2}\cdots m_{k_{r-1}j})(m_{il_1}m_{l_1l_2}\cdots m_{l_{r-1}j})^*\,, \end{aligned} \tag{E.8}$$

where we have isolated the r masses involved in averaging on opposite sides of the thermal circle. Taking the Fourier transform and isolating the leading large N contribution, we find

$$\begin{aligned}\bar{F}_{ijji}(t) &= 2\delta_{ij}\sum_{r=1}^{\infty}\int d\omega_1 d\omega_2 e^{-i(\omega_1-\omega_2)t}\left(\bar{G}(\omega_1)(\bar{G}(\omega_2))^*\right)^{r+1}m^{2r} \\ &= 2\delta_{ij}\int d\omega_1 d\omega_2 e^{-i(\omega_1-\omega_2)t}\frac{m^2\left(\bar{G}(\omega_1)(\bar{G}(\omega_2))^*\right)^2}{1-m^2\bar{G}(\omega_1)(\bar{G}(\omega_2))^*} \\ &= 2\delta_{ij}\int d\omega_1 d\omega_2 e^{-i(\omega_1-\omega_2)t}\left(-\bar{G}(\omega_1)(\bar{G}(\omega_2))^*+\frac{1}{1-m^2\bar{G}(\omega_1)(\bar{G}(\omega_2))^*}\right)\,, \end{aligned}$$

in agreement with the results of [101, 165]. The Green's function in the above expression is the Fourier transform of the real-time Green's function (E.5).

By shifting the integration variables $\omega_j \to \omega_j + \frac{a}{T}$, we obtain an integral of the type considered in [165]. The phase factors from the two-point functions cancel out and thus the gauge field has no effect on the double commutator. As pointed out in [182, 165], the resulting expression does not give rise to exponential growth of the OTOC. We conclude that our model is not chaotic.

Appendix F

Details of the large N SFF calculation

F.1 On-shell actions and frequency regions

Recall that the four frequency regions are dictated by the values of $|\xi_1 x_n + b|$ and $|\xi_2 x_n + b|$:

$$\begin{aligned}
&\text{Region } A: && |x_n \pm b| \leq 2, \\
&\text{Region } B: && |x_n + b| \leq 2, \quad |x_n - b| > 2, \\
&\text{Region } C: && |x_n - b| \leq 2, \quad |x_n + b| > 2, \\
&\text{Region } D: && |x_n \pm b| > 2.
\end{aligned} \tag{F.1}$$

Recalling that $x_n = \frac{n\pi}{mT}$ and $b = \frac{a}{mT}$, these can be written as regions for the corresponding frequency labels n, in the following way

	$2mT < \lvert a\rvert$	$2mT > \lvert a\rvert$
Region A	$\emptyset$	$\lvert n\pi\rvert < 2mT - \lvert a\rvert$
Region B	$\lvert n\pi + a\rvert < 2mT$	$\lvert n\pi + \mathrm{sgn}(a) 2mT\rvert < \lvert a\rvert$
Region C	$\lvert n\pi - a\rvert < 2mT$	$\lvert n\pi - \mathrm{sgn}(a) 2mT\rvert < \lvert a\rvert$
Region D	$\lvert n\pi\rvert < \lvert a\rvert - 2mT$ or $\lvert n\pi\rvert > \lvert a\rvert + 2mT$	$\lvert n\pi\rvert > 2mT + \lvert a\rvert$

(F.2)

We define $I_J(x) \equiv I(\mathcal{S}^{(J)})$ to be the on-shell action, given by (9.74)

$$I(\mathcal{S}) \;=\; \mathrm{Tr}\log\left[\left(\sigma^z + \frac{b}{x} - \frac{i}{x}\mathcal{S}\right)\sigma^z\right] - \frac{1}{2}\mathrm{Tr}\mathcal{S}^2\,, \tag{F.3}$$

evaluated on the solutions (9.72), restricted to the frequency region $J = A, B, C, D$. The explicit expressions, including any dependence on the constants c_1^n and c_2^n, are given by

$$\begin{aligned} I_A(c_1^n, c_2^n; x_n) &= \frac{1}{8}\left(ic_1^n\sqrt{4-(b+x_n)^2}+b+x_n\right)^2 + \frac{1}{8}\left(ic_2^n\sqrt{4-(b-x_n)^2}+b-x_n\right)^2 \\ &\quad + \log\left(\frac{-ic_1^n\sqrt{4-(b+x_n)^2}+b+x_n}{2x_n}\right) + \log\left(\frac{ic_2^n\sqrt{4-(b-x_n)^2}-(b-x_n)}{2x_n}\right), \end{aligned} \tag{F.4}$$

$$\begin{aligned} I_B(c_1^n; x_n) &= \frac{1}{8}\left(\mathrm{sgn}(b-x_n)\sqrt{(b-x_n)^2-4}-b+x_n\right)^2 \\ &\quad + \frac{1}{8}\left(ic_1^n\sqrt{4-(b+x_n)^2}+b+x_n\right)^2 + \log\left(\frac{-ic_1^n\sqrt{4-(b+x_n)^2}+b+x_n}{2x_n}\right) \\ &\quad + \log\left(-\frac{\mathrm{sgn}(b-x_n)\sqrt{(b-x_n)^2-4}+b-x_n}{2x_n}\right), \end{aligned} \tag{F.5}$$

$$\begin{aligned} I_C(c_2^n; x_n) &= \frac{1}{8}\left(-\sqrt{(b+x_n)^2-4}\mathrm{sgn}(b+x_n)+b+x_n\right)^2 \\ &\quad + \frac{1}{8}\left(ic_2^n\sqrt{4-(b-x_n)^2}+b-x_n\right)^2 + \log\left(\frac{ic_2^n\sqrt{4-(b-x_n)^2}-b+x_n}{2x_n}\right) \\ &\quad + \log\left(\frac{\mathrm{sgn}(b+x_n)\sqrt{(b+x_n)^2-4}+b+x_n}{2x_n}\right), \end{aligned} \tag{F.6}$$

$$\begin{aligned} I_D(x_n) &= \frac{1}{8}\left(-\mathrm{sgn}(b+x_n)\sqrt{(b+x_n)^2-4}+b+x_n\right)^2 \\ &\quad + \frac{1}{8}\left(\mathrm{sgn}(b-x_n)\sqrt{(b-x_n)^2-4}-(b-x_n)\right)^2 \\ &\quad + \log\left(\frac{\mathrm{sgn}(b+x_n)\sqrt{(b+x_n)^2-4}+b+x_n}{2x_n}\right) \\ &\quad + \log\left(-\frac{\mathrm{sgn}(b-x_n)\sqrt{(b-x_n)^2-4}+b-x_n}{2x_n}\right). \end{aligned} \tag{F.7}$$

Note the following relations, which will be used in the subsequent calculations. We suppress the n dependence of x_n.

$$\begin{aligned} I_C(c;x) &= I_B(c;-x), && \text{for} \quad x \in C, \\ I_D(x) &= I_D(-x), && \text{for} \quad x \in D, \\ I_A(c_1,c_2;x) &= I_A(c_2,c_1;-x), && \text{for} \quad x \in A, \end{aligned} \tag{F.8}$$

$$\begin{aligned} [I_A(c_1,c_2;x)]^* &= I_A(-c_1,-c_2;x), && \text{for} \quad x\in A,\\ [I_C(c;x)]^* &= I_C(-c;x), && \text{for} \quad x\in C, \end{aligned} \tag{F.9}$$

where all c's take values ± 1. Also, for $x \in A$,

$$\mathrm{Re}\,[I_A(1,1;x)] = \mathrm{Re}\,[I_A(1,-1;x)] = \mathrm{Re}\,[I_A(-1,1;x)] = \mathrm{Re}\,[I_A(-1,-1;x)]\,. \tag{F.10}$$

F.2 Effective mass matrices

Recall that the effective mass matrices are given by

$$M^{nm}_{\alpha\beta} \equiv 1 + \mathcal{S}^{nn}_{\alpha\alpha}\mathcal{S}^{mm}_{\beta\beta}, \tag{F.11}$$

in terms of the saddle point solutions (9.72)

$$\mathcal{S}^{nn'}_{\alpha\beta} = \begin{cases} \frac{1}{2}\left[-i(\xi_\alpha x_n + b) + c^n_\alpha\sqrt{4-(\xi_\alpha x_n+b)^2}\right]\delta^{nn'}_{\alpha\beta}, & |\xi_\alpha x_n + b| \le 2,\\ \frac{1}{2}\left[-i(\xi_\alpha x_n + b) + i\mathrm{sgn}(\xi_\alpha x_n+b)\sqrt{(\xi_\alpha x_n+b)^2-4}\right]\delta^{nn'}_{\alpha\beta}, & |\xi_\alpha x_n + b| > 2. \end{cases} \tag{F.12}$$

We define

$$\mathcal{S}^{nn'}_{\alpha\beta} \equiv \begin{cases} \mathcal{A}(c^n_\alpha;\xi_\alpha x_n+b), & |\xi_\alpha x_n+b|\le 2,\\ \mathcal{B}(\xi_\alpha x_n+b), & |\xi_\alpha x_n+b|>2. \end{cases} \tag{F.13}$$

It follows that for the following frequency regions, mass matrices take the following forms:

$|\xi_\alpha x_n + b| \le 2,\ |\xi_\beta x_m + b| \le 2$:

$$M^{nm}_{\alpha\beta} = 1 + \mathcal{A}(c^n_\alpha;\xi_\alpha x_n+b)\mathcal{A}(c^m_\beta;\xi_\beta x_m+b). \tag{F.14}$$

$|\xi_\alpha x_n + b| \le 2,\ |\xi_\beta x_m + b| > 2$:

$$M^{nm}_{\alpha\beta} = 1 + \mathcal{A}(c^n_\alpha;\xi_\alpha x_n+b)\mathcal{B}(\xi_\beta x_m+b). \tag{F.15}$$

$|\xi_\alpha x_n + b| > 2,\ |\xi_\beta x_m + b| \le 2$:

$$M^{nm}_{\alpha\beta} = 1 + \mathcal{B}(\xi_\alpha x_n+b)\mathcal{A}(c^m_\beta;\xi_\beta x_m+b). \tag{F.16}$$

$|\xi_\alpha x_n + b| > 2,\ |\xi_\beta x_m + b| > 2$:

$$M^{nm}_{\alpha\beta} = 1 + \mathcal{B}(\xi_\alpha x_n+b)\mathcal{B}(\xi_\beta x_m+b). \tag{F.17}$$

These mass matrices satisfy the complex conjugate relation

$$\left[M^{nn'}_{\alpha\beta}(c^n_\alpha, c^{n'}_\beta)\right]^* = M^{nn'}_{\alpha\beta}(-c^n_\alpha, -c^{n'}_\beta), \tag{F.18}$$

The above constitutes an extensive list of all effective mass matrices one may encounter when performing the saddle point approximation for the SFF. Recall that for each frequency, only saddle point solutions whose effective mass matrices have non-negative real parts will contribute in the large N saddle point approximation. We verify that indeed $\mathrm{Re}\left[M^{nm}_{\alpha\beta}\right] \geq 0$ for all choices of c^n_α, c^m_β and for all of the above frequency regions. This ensures that for each frequency, *all* saddles contribute in our saddle point approximation of the SFF (9.81).

The only case where $\mathrm{Re}\left[M^{nm}_{\alpha\beta}\right] = 0$, is in the frequency region $|\xi_\alpha x_n + b| \leq 2,\ |\xi_\beta x_m + b| \leq 2$ when $c^n_\alpha = -c^{n'}_\beta$ and $\xi_\alpha x_n = \xi_\beta x_{n'}$ ($\alpha \neq \beta$ and $n = -n'$)[1], in which case the corresponding effective mass matrices (F.14) vanish: $M^{n,-n}_{12} = M^{n,-n}_{21} = 0$. This signals the presence of zero modes, whose significance is discussed in the main text.

F.3 Gauge-invariance of the early time SFF

Recall that the region C contains frequencies x_n with $|x_n - b| < 2$. Here we show the gauge-invariance of the early time SFF (9.83) in the case where a single frequency contribution, x_p, comes from the region C, with the rest coming from region D. In this case, we obtain an expression similar to (9.87),

$$\overline{Z(iT)Z^*(iT)} = \sum_{c^p_2, c^{-p}_1 = \pm 1} \exp\left\{ I_C(c^{-p}_1; x_p) + I_C(c^p_2; x_p) + 2 \sum_{\substack{n>0,\ \text{odd} \\ n\neq p}} I_D(x_n) \right\}. \tag{F.19}$$

Here we have set $N = 1$ as this has no effect on the argument. We will consider instead the normalised quantity

$$e^{-2I_D(x_p)} \sum_{c^p_2, c^{-p}_1 = \pm 1} e^{I_C(c^{-p}_1; x_p) + I_C(c^p_2; x_p)}, \tag{F.20}$$

obtained by dividing (F.19) by

$$\exp\left\{ 2 \sum_{n>0,\text{odd}} I_D(x_n) \right\} = \exp\left\{ \sum_{n\ \text{odd}} I_D(x_n) \right\}. \tag{F.21}$$

[1] The other case $\alpha = \beta$, $n = n'$ which satisfies $\xi_\alpha x_n = \xi_\beta x_{n'}$ is ruled out by the condition $c^n_\alpha = -c^{n'}_\beta$.

From (F.7) we see that implementing a large gauge transformation $a \to a + 2\pi k$ on this factor can be thought of as shifting the index n (of each frequency x_n) in each term of (F.7) up or down as $n \to n \pm k$. Since the sum is over all integers n, this leaves the sum invariant. Since this factor is therefore gauge invariant, dividinng through by it doesn't affect our argument.

It remains to show the gauge invariance of (F.20) under large gauge transformations $a \to a + 2\pi k$, $k \in \mathbb{Z}$, under which $b \to b + \frac{2\pi k}{mT}$. Note that (F.20) depends only on x_p, where p is the only integer satisfying $|x_p - b| < 2$, since x_p is the only frequency in region C. If we transform $b \to b + \frac{2\pi k}{mT}$, then the only frequency in the new region C will be $x_p + \frac{2\pi k}{mT}$. Thus we need to show that the expression (F.20) is invariant under the *simultaneous* transformations

$$b \to b + \tfrac{2\pi k}{mT}, \quad x_p \to x_p + \tfrac{2\pi k}{mT}. \tag{F.22}$$

Using the identity (F.9) $[I_C(1;x)]^* = I_C(-1;x)$, we can perform the sum over saddles to rewrite (F.20) (suppressing the x_p dependence of I_C) as

$$\begin{aligned} & e^{-2I_D}\left(e^{2I_C(1)} + e^{2I_C(-1)} + 2e^{I_C(1)+I_C(-1)}\right) \\ = \;& e^{-2I_D}\left(2\,\mathrm{Re}\left[e^{2I_C(1)}\right] + 2e^{2\,\mathrm{Re}[I_C(1)]}\right) \\ = \;& e^{-2I_D}e^{-2I_D}\left(\cos\left(\mathrm{Im}\left[2I_C(1)\right]\right) + 1\right) \end{aligned} \tag{F.23}$$

Finally we use fact that in the region C where $|x - b| < 2$, we have $\mathrm{Re}\left[I_C(1;x)\right] = \mathrm{Re}\left[I_D(x)\right]$. In particular, this holds for $x = x_p$, so we rewrite the above as

$$e^{-2i\,\mathrm{Im}[I_D]}\left(\cos\left(\mathrm{Im}\left[2I_C(1)\right]\right) + 1\right). \tag{F.24}$$

This quantity only depends on the imaginary parts of I_D and $I_C^{(1)}$, which are given by

$$\mathrm{Im}[I_D(x)] = \tan^{-1}\left(x - b, \sqrt{4 - (x-b)^2}\right) - \frac{1}{4}(x-b)\sqrt{4-(x-b)^2}\,, \tag{F.25}$$

$$\begin{aligned} \mathrm{Im}[I_C(1;x)] = \;& \frac{4|x-b|\tan^{-1}\left((x-b)|x-b|, \sqrt{4-(x-b)^2}(x-b)\right)}{4|x-b|} \\ & - \frac{(x-b)^2\sqrt{-(x-b+2)(x-b-2)}}{4|x-b|}. \end{aligned} \tag{F.26}$$

Because both of these only depend on x and b in the combination $x - b$, clearly the expression (F.24) is invariant under the simultaneous transformations (F.22). It follows that (F.19) is invariant under large gauge transformations.

Note that while we argued for This in section 9.4, there we only considered times $mT \ll 1$. Our argument here is valid for all early times $2mT < |a|$ such that there is only one frequency contribution from region C.

Let's now consider the case where there are two frequencies, x_p and x_q ($p \neq q$), in region C. The argument above then goes through in the exact same way, but instead of (F.24) we end up with

$$e^{-2i\,\mathrm{Im}[I_D(x_p)+I_D(x_q))]}\cos^2\left(2\,\mathrm{Im}\left[I_C(1;x_p)+I_C(1;x_q)\right]\right). \tag{F.27}$$

Gauge transformations now amount to the simultaneous transformations

$$b \to b + \tfrac{2\pi k}{mT}, \quad x_p \to x_p + \tfrac{2\pi k}{mT}, \quad x_q \to x_q + \tfrac{2\pi k}{mT}, \tag{F.28}$$

under which (F.27) is again invariant due to the $x - b$ dependence in (F.25) and (F.26). Clearly the argument can be extended to any number of frequencies N_C in region C, where in each case we must constrain mT accordingly, *i.e.* such that there are only N_C frequencies n satifying $|n\pi - a| < 2mT$. Recall that the argument is also only valid for early times $2mT < |a|$.

F.4 Convergence of the fluctuation path integral

The quadratic fluctuation path integral is, for massive modes with $M^{nn'}_{\alpha\beta} > 0$, given by

$$\prod_{\alpha,\beta,n,n'} F\left[M^{nn'}_{\alpha\beta}\right] = \exp\left\{-\sum_{\alpha,\beta,n,n'}\frac{1}{2}\log M^{nn'}_{\alpha\beta}\right\}. \tag{F.29}$$

We argue that this fluctuation path integral converges. The effective mass matrices take different forms in each of the various regions which depend on the values of $|\xi_\alpha x_n + b|$ and $|\xi_\beta x_m + b|$ (see Appendix F.2). One of the regions, $|\xi_\alpha x_n + b| \leq 2$, $|\xi_\beta x_m + b| \leq 2$, is finite and so the contribution from the massive modes from this region is clearly finite. In the other, infinite regions, we must entertain the possibility of UV divergences. Consider the region $|\xi_\alpha x_n + b| > 2$, $|\xi_\beta x_m + b| > 2$, where

$$M^{nm}_{\alpha\beta} \;=\; 1 + \mathcal{B}(\xi_\alpha x_n + b)\mathcal{B}(\xi_\beta x_m + b). \tag{F.30}$$

For very large frequencies $x_n, x_m \gg 1$, this effective mass matrix can be approximated by

$$M^{nn'}_{\alpha\beta} \approx 1 - \frac{4}{\xi_\alpha\xi_\beta x_n x_{n'}} \quad \Rightarrow \quad \sum_{\alpha,\beta,n,n'}\log M^{nn'}_{\alpha\beta} \sim \sum_{\alpha,\beta,n,n'}\frac{1}{\xi_\alpha\xi_\beta x_n x_{n'}}. \tag{F.31}$$

The sum is not absolutely convergent, but by imposing any finite frequency cutoff we can ensure that cancellations between either $n' = -n$ or $\alpha \neq \beta$ are sufficient to deal with any UV divergences [179]. The other infinite regions may be treated similarly.

F.5 Pure saddle point contributions to the $mT \gg 1$ SFF

We have demonstrated in the main text that the on-shell action $I(\mathcal{S})$ vanishes at late times for zero mode saddle point configurations $\{c_\alpha^n\}$ with $c_1^n = -c_2^{-n}$ for all n. We will argue here that none of the other saddles give contributions which are exponential in N (if this were the case, they could dominate the ramp which is exponential in $\log N$). First note that all of these other saddles have only massive fluctuations which do not yield any N dependence. We will therefore consider only their pure saddle point contributions.

In the following, we assume $b > 0$, but a similar analysis holds for $b < 0$. At late times the on-shell action is given by (9.90)

$$\begin{aligned} I(\mathcal{S}) \;=\; 2\Bigg[&\sum_{\substack{x_n>2+b \\ n \text{ odd}}}^{\infty} I_D(x_n) + \frac{1}{2}\sum_{\substack{x_n>2-b \\ n \text{ odd}}}^{2+b} \Big(I_C(c_1^{-n};x_n) + I_C(c_2^{n};x_n)\Big) \\ &+\frac{1}{2}\sum_{\substack{x_n>0 \\ n \text{ odd}}}^{2-b} \Big(I_A(c_1^{n},c_2^{n};x_n) + I_A(c_2^{-n},c_1^{-n};x_n)\Big)\Bigg]. \end{aligned} \tag{F.32}$$

Using (F.9) it may be shown that the quantity in the second sum above,

$$I_C(c_1^{-n};x_n) + I_C(c_2^{n};x_n), \tag{F.33}$$

differs only in its imaginary part (and has equal real part) for any choices of $c_2^n, c_1^{-n} = \pm 1$, over the range $2-b < x_n < 2+b$. Similarly, the quantity in the third sum,

$$I_A(c_1^{n},c_2^{n};x_n) + I_A(c_2^{-n},c_1^{-n};x_n), \tag{F.34}$$

differs only in its imaginary part (and has equal real part) for any choices of $c_1^n, c_2^n, c_1^{-n}, c_2^{-n} = \pm 1$, over the range $0 < x_n < 2-b$. Therefore, if we can show that the on-shell action (F.32) vanishes for some choice of the constants $c_1^n, c_2^n, c_1^{-n}, c_2^{-n}$, it follows that for any other possible choices of these constants, the on-shell action

(F.32) either vanishes or is pure imaginary.

To this end, we make the particular choice $c_1^n = c_2^n = 1$ and $c_1^{-n} = c_2^{-n} = -1$, so (F.32) becomes

$$2\left[\sum_{\substack{x_n>2+b\\ n \text{ odd}}}^{\infty} I_D(x_n) + \sum_{\substack{x_n>2-b\\ n \text{ odd}}}^{2+b} \text{Re}\left[I_C(1;x_n)\right] + \sum_{\substack{x_n>0\\ n \text{ odd}}}^{2-b} \text{Re}\left[I_A(1,1;x_n)\right]\right], \tag{F.35}$$

where we have used (F.9). Now for $mT \gg 1$, the variable $x_n = \frac{n\pi}{mT}$ may be treated as a continuous variable x, and we may replace sums over n with integrals over x, allowing us to rewrite the on-shell action above as

$$\begin{aligned} I(\mathcal{S}) &= \frac{mT}{\pi}\left(\int_{2+b}^{\infty} dx I_D(x) + \int_{2-b}^{2+b} dx\, \text{Re}\left[I_C(1;x)\right] + \int_0^{2-b} dx\, \text{Re}\left[I_A(1,1;x)\right]\right) \\ &= 0, \end{aligned} \tag{F.36}$$

where calculating the sum of these integrals using the explicit forms in Appendix F.1, one finds an exactly vanishing result.

It follows that the late time on-shell action (F.32) is pure imaginary for all saddles, *i.e.* for any configuration of constants $\{c_\alpha^n\}$. We write it as $I(\mathcal{S}) = i\frac{mT}{\pi}\mathcal{I}(\mathcal{S})$ where $\mathcal{I}(\mathcal{S})$ is a real number which depends on the particular saddle under consideration. The purely saddle point contribution to the late time SFF from any particular saddle is thus given by

$$e^{NI(\mathcal{S})} = \exp\left\{i\frac{NmT}{\pi}\mathcal{I}(\mathcal{S})\right\}. \tag{F.37}$$

This is clearly a rapidly oscillating complex phase, and not an exponentially increasing function. It therefore cannot dominate the exponential ramp contributions coming from the zero mode configurations.

Note that (F.9) implies that

$$\text{Im}\left[I_C(c_1^{-n};x_n) + I_C(c_2^n;x_n)\right] = -\,\text{Im}\left[I_C(-c_1^{-n};x_n) + I_C(-c_2^n;x_n)\right], \tag{F.38}$$

for $2-b < x_n < 2+b$, and

$$\text{Im}\left[I_A(c_1^n,c_2^n;x_n) + I_A(c_2^{-n},c_1^{-n};x_n)\right] = -\,\text{Im}\left[I_A(-c_1^n,-c_2^n;x_n) + I_A(-c_2^{-n},-c_1^{-n};x_n)\right],$$

for $0 < x_n < 2 - b$. This ensure that for every saddle with a particular value of $\mathrm{Im}[I(\mathcal{S})]$, there is another saddle for which $\mathrm{Im}[I(\mathcal{S})]$ is equal in magnitude but opposite in sign. Consequently the sum over saddles $\sum_{\{c_\alpha^n\}} e^{NI(\mathcal{S})}$, with $I(\mathcal{S})$ given by (F.37), gives a real result for the overall SFF. This is still true when fluctuations are included due to the fact that the effective mass matrices satisfy (F.18).

We also expect the sum over saddles to result in an SFF that is everywhere positive. We speculate that there is some precise cancellation when we sum over the rapidly oscillating complex phases (F.37) that ensures this.

Bibliography

[1] D. Tong *The Quantum Hall Effect: TIFR Infosys Lectures.* (2016) http://www.damtp.cam.ac.uk/user/tong/qhe.html.

[2] S.M. Girvin *The Quantum Hall Effect: Novel Excitations and Broken Symmetries* (1999) arXiv:cond-mat/9907002

[3] K. v Klitzing, G. Dorda and M. Pepper *New Method for High-Accuracy Determination of the Fine-Structure Constant Based on Quantized Hall Resistance* (1980) Phys. Rev. Lett. 45 494.

[4] D.C. Tsui, H.L. Stormer and A.C. Gossard, *Two-Dimensional Magnetotransport in the Extreme Quantum Limit* (1982) Phys. Rev. Lett. 48 1559.

[5] F. Wilczek *Fractional Statistics and Anyon Superconductivity* (1990) World Scientific.

[6] A. Zee *Quantum Hall Fluids* (1995) arXiv:cond-mat/9501022

[7] S. C. Zhang, T. Hansson and S. Kivelson, *Effective-Field-Theory Model for the Fractional Quantum Hall Effect* Phys. Rev. Lett. 62, 82 (1989)

[8] R.P. Slayen, *Quantum States on Spheres in the Presence of Magnetic Fields*, Masters Dissertation, University of Cape Town, (2019)

[9] S.C. Zhang, *The Chern-Simons-Landau-Ginzburg Theory of the Fractional Quantum Hall Effect*, Int. Jour. Mod. Phys. B6 (1992).

[10] T. Senthil, N. Seiberg, E. Witten and C. Wang *A Duality Web in 2+1 Dimensions and Condensed Matter Physics* (2016) ArXiv:1606.01989.

[11] X.-G. Wen, *Vacuum Degeneracy of Chiral Spin State in Compactified Spaces* Phys. Rev. B, 40, 7387 (1989)

[12] A. Kitaev and J. Preskill *Topological Entanglement Entropy* (2006) Phys. Rev. Lett. 96, 110404

[13] X. G. Wen and Q. Niu, *Ground-state degeneracy of the fractional quantum Hall states in the presence of a random potential and on high-genus Riemann surfaces* (1990) Phys. Rev. B **41**, 9377. doi:10.1103/PhysRevB.41.9377

[14] F. Wilczek and A. Zee, *Appearance of Gauge Structure in Simple Dynamical Systems*, Phys. Rev. Lett. **52**, 2111-2114 (1984) doi:10.1103/PhysRevLett.52.2111

[15] X. G. Wen, *Topological orders and edge excitations in FQH states*, Adv. Phys. **44**, no.5, 405-473 (1995) doi:10.1080/00018739500101566 [arXiv:cond-mat/9506066 [cond-mat]].

[16] R.B. Laughlin *The Anomalous Quantum Hall Effect: An Incompressible Quantum Fluid with Fractionally Charged Excitations* (1983) Phys. Rev. Lett. 50, 1395

[17] F. Haldane and E. Rezayi, *Periodic Laughlin-Jastrow wave functions for the fractional quantized Hall effect* Phys. Rev. B **31**, no. 4, 2529 (1985). doi:10.1103/PhysRevB.31.2529

[18] S. Klevtsov, *Random normal matrices, Bergman kernel and projective embeddings*, JHEP 2014 (1) (2014) 1–19.

[19] S. Bellucci and P. Onorato, *Landau levels and edge states in a cylindrical two-dimensional electron gas: A semiclassical approach*, Phys. Rev. B **82**, 205305 (2010). doi :10.1103/PhysRevB.82.205305

[20] T. Can, M. Laskin and P.B. Wiegmann *Geometry of Quantum Hall States: Gravitational Anomaly and Transport Coefficients.* (2015) arXiv:1411.3105v3

[21] J. E. Avron, R. Seiler, P. G. Zograf, *Viscosity of quantum Hall fluids*, Phys. Rev. Lett. 75 (1995) 697–700.

[22] P. Levay, *Berry phases for Landau Hamiltonians on deformed tori*, J. Math. Phys. 36 (6) (1995) 2792–2802.

[23] P. Levay, *Berry's phase, chaos, and the deformations of Riemann surfaces*, Phys. Rev. E 56 (1997) 6173–6176.

[24] P. Dirac (1931) Proc. R. Soc. London A 133, 60

[25] I. Tamm (1931) Z. Phys. 71, 141

[26] S.M. Girvin and T. Jach *Formalism for the quantum Hall effect: Hilbert space of analytic functions* (1984) Phys. Rev. B, 29 5617

[27] T. Dray, *The Relationship Between Monopole Harmonics and Spin Weighted Spherical Harmonics*, J. Math. Phys. **26**, 1030 (1985) doi:10.1063/1.526533

[28] B.I. Halperin *Statistics of Quasiparticles and the Hierarchy of Fractional Quantized Hall States.* Phys. Rev. Lett., 52(18):1583, 1984.

[29] C. Störmer, Arch. Sci. Phys. Nat, **24** (1907)

[30] J. Murugan, J. P. Shock and R. P. Slayen, *Astrophysical Quantum Matter: Spinless charged particles on a magnetic dipole sphere,* Gen. Rel. Grav. **53**, no.3, 29 (2021) [arXiv:1811.03109 [hep-th]].

[31] F. D. M. Haldane, *Fractional quantization of the Hall effect: A Hierarchy of incompressible quantum fluid states,* Phys. Rev. Lett. **51**, 605-608 (1983)

[32] J. Jain, *Composite Fermions*, Cambridge University Press. doi:10.1017/CBO9780511607561

[33] H. Grosse, A. Martin and J. Stubbe, *Splitting of Landau levels in nonconstant magnetic fields*, Phys. Lett. A **181**, 7-12 (1993)

[34] M. Bander, *Fractional Quantum Hall Effect In Nonuniform Magnetic Fields*, UCI-TR-89-26.

[35] J. Maldacena, *Comments on magnetic black holes*, JHEP **04**, 079 (2021) [arXiv:2004.06084 [hep-th]].

[36] J. Maldacena, A. Milekhin and F. Popov, *Traversable wormholes in four dimensions*, [arXiv:1807.04726 [hep-th]].

[37] J. Gonzalez, F. Guinea and M. A. H. Vozmediano, *The Electronic spectrum of fullerenes from the Dirac equation*, Nucl. Phys. B **406**, 771-794 (1993) [arXiv:cond-mat/9208004 [cond-mat]].

[38] A. Jellal, *Anomalous quantum Hall effect on sphere*, Nucl. Phys. B **804**, 361-382 (2008) [arXiv:0709.4126 [hep-th]].

[39] D. Kolesnikov and V. Osipov, *The continuum gauge field-theory model for low-energy electronic states of icosahedral fullerenes*, Eur. Phys. J. B 49, 465–470 (2006). https://doi.org/10.1140/epjb/e2006-00087-y

[40] J. Gonzalez, F. Guinea and M. A. H. Vozmediano, *Continuum approximation to Fullerene molecules*, Phys. Rev. Lett. **69**, no.1, 172 (1992) doi:10.1103/PhysRevLett.69.172

[41] H. Aoki and H. Suezawa, *Landau quantization of electrons on a sphere*, Phys. Rev. A. **46**, no.3, R1163–R1166 (1992)

[42] M. Greiter and R. Thomale, *Landau level quantization of Dirac electrons on the sphere*, Annals Phys. **394**, 33 (2018) [arXiv:1807.05816 [cond-mat.str-el]].

[43] V. Jakubsky, S. Kuru, J. Negro and S. Tristao, *Supersymmetry in spherical molecules and fullerenes under perpendicular magnetic fields*, J. Phys.: Condens. Matter **25** no.15, (2013)

[44] A. A. Abrikosov, Jr., *Dirac operator on the Riemann sphere*, [arXiv:hep-th/0212134 [hep-th]].

[45] K.-I. Imura, Y.Yoshimura, Y. Takanane and T. Fukui *Spherical topological insulator* Phys. Rev. B 86, 235119 (2012).

[46] P.M. Morse and H. Feshbach, *Methods of Theoretical physics*, McGraw-Hill Book Co. Inc., New york NY (1953)

[47] E. Berti, V. Cardoso and M. Casals, *Eigenvalues and eigenfunctions of spin-weighted spheroidal harmonics in four and higher dimensions*, Phys. Rev. D **73**, 024013 (2006) [gr-qc/0511111].

[48] S. Hod, *Eigenvalue spectrum of the spheroidal harmonics: A uniform asymptotic analysis*, Phys. Lett. B **746**, 365 (2015) [arXiv:1506.04148 [gr-qc]].

[49] C. Töke, P.E. Lammert, V.H. Crespi and J.K. Jain, *Fractional quantum Hall effect in graphene*. (2006) PHYSICAL REVIEW B 74, 235417

[50] M. Arciniaga and M.R. Peterson, *Landau level quantization for massless Dirac fermions in the spherical geometry: Graphene fractional quantum Hall effect on the Haldane sphere*. (2016) PHYSICAL REVIEW B 94, 035105

[51] G.V. Dunne, *Aspects of Chern-Simons Theory*. (1999) arXiv:hep-th/9902115v1

[52] G.V. Dunne, *Hilbert Space for Charged Particles in Perpendicular Magnetic Fields*, Annals of Physics 215,233-263 (1991)

[53] T.T. Wu and C.N. Yang, *Dirac Monopole Without Strings: Monopole Harmonics*, Nucl. Phys. B, 365 (1976)

[54] A. Jellal, *Anomalous quantum Hall effect on sphere*, Nuclear Physics B 804 [PM] 361–382 (2008)

[55] A. A. Abrikosov, jr, *Dirac operator on the Riemann sphere* arXiv: hep-th/0212134 (2002)

[56] K.-I. Imura, Y.Yoshimura, Y. Takanane and T. Fukui, *Spherical topological insulator* Phys. Rev. B 86, 235119 (2012).

[57] T. Neupert, S. Rachel, R. Thomale and M. Greiter, *Interacting surface states of three-dimensional topological insulators*, PhysRevLett.115.017001 (2014)

[58] M. Greiter, *Landau Level Quantization on the Sphere*, (2011) Phys. Rev. B 83, 115129 arXiv:1807.0581

[59] P. J. Forrester, N. C. Snaith and J. J. M. Verbaarschot, Developments in random matrix theory, J. Phys. A **36**, R1 (2003) doi:10.1088/0305-4470/36/12/201 [arXiv:cond-mat/0303207 [cond-mat]].

[60] T. Guhr, A. Muller-Groeling and H. A. Weidenmuller, Random matrix theories in quantum physics: Common concepts, Phys. Rept. **299**, 189-425 (1998) doi:10.1016/S0370-1573(97)00088-4 [arXiv:cond-mat/9707301 [cond-mat]].

[61] G. Livan, M. Novaes, and P. Vivo, *Introduction to random matrices theory and practice,* SpringerBriefs in Mathematical Physics, volume 26, Springer, Cham 2018.

[62] M.L. Mehta, *Random matrices and the statistical theory of energy levels,* Academic Press, New York (1967)

[63] V. E. Kravtsov, *Random matrix theory: Wigner-Dyson statistics and beyond: Lecture notes given at SISSA (Trieste, Italy)*, [arXiv:0911.0639 [cond-mat.dis-nn]].

[64] H.L. Montgomery, *The pair correlation of the zeta function,* Proc. Symp. Pure Math. 24 (1973) 181.

[65] A.Y. Abul-Magd, *Modelling gap-size distribution of parked cars using random-matrix theory,* Physica A: Statistical Mechanics and its Applications, Volume 368, Issue 2, 2006, Pages 536-540, ISSN 0378-4371, https://doi.org/10.1016/j.physa.2005.10.059.

[66] J. Baik, A. Borodin, P. Deift and T. Suidan, *A model for the bus system in Cuernavaca (Mexico),* J. Phys. A: Math. Gen. 39 8965 (2006)

[67] P. Deift, *Universality for mathematical and physical systems,* [arXiv:0603038 [math-ph]] (2006)

[68] J. Wishart, *Generalized product moment distribution in samples,* Biometrika 20A (1928) 32.

[69] E.P. Wigner, *On the statistical distribution of the widths and spacings of nuclear resonance levels,* Proc. Cam. Phil. Soc. 47 (1951) 790.

[70] E.P. Wigner, *Statistical properties of real symmetric matrices with many dimensions*, Can. Math. Congr. Proc., University of Toronto Press, Toronto 1957, p. 174.

[71] M. Di Stasio and X. Zotos *Connection between low energy effective Hamiltonians and energy level statistics* Phys. Rev. Lett. 74, 2050 (1995)

[72] F.J. Dyson, *Statistical theory of the energy levels of complex systems, I, II & III* J. Math. Phys. 3 (1962) 140.

[73] F.J. Dyson, *A Brownian motion model for the eigenvalues of a random matrix,* J. Math. Phys. 3 (1962) 1191.

[74] F.J. Dyson, *The threefold way. Algebraic structure of symmetry groups and ensembles in quantum mechanics,* J. Math. Phys. 3 (1962) 1200.

[75] P. W. Anderson, *Absence of Diffusion in Certain Random Lattices,* Phys. Rev. 109, 1492 (1958)

[76] S. F. Edwards and P. W. Anderson, *Theory of spin glasses,* J. Phys. F: Met. Phys. 5 965 (1975) DOI 10.1088/0305-4608/5/5/017

[77] L.P. Gorkov and G.M. Eliasberg, *Minute metallic particles in an electromagnetic field,* Sov. Phys. JETP 21 (1965) 940.

[78] K. B. Efetov, *Supersymmetry and theory of disordered metals,* Adv. in Phys. 32 (1983) 53.

[79] K. B. Efetov, *Supersymmetry in Disorder and Chaos,* Cambridge University Press (1997)

[80] H. Weyl, *Classical Groups*, Princeton Univ. Press, Princeton, (1946)

[81] P. Deift, *Orthogonal Polynomials and Random Matrices: a Riemann-Hilbert approach*, Courant Inst. Lecture Notes (AMS, Rhode Island, 2000).

[82] E. Brezin, C. Itzykson, G. Parisi and J. B. Zuber, *Planar Diagrams*, Commun. Math. Phys. **59**, 35 (1978) doi:10.1007/BF01614153

[83] G. Hackenbroich and H. A. Weidenmuller, *Universality of Random-Matrix Results for Non-Gaussian Ensembles*, Phys. Rev. Lett. **74**, 4118-4121 (1995) doi:10.1103/PhysRevLett.74.4118 [arXiv:cond-mat/9412088 [cond-mat]].

[84] Y. Y. Atas, E. Bogomolny, O. Giraud, and G. Roux, *The distribution of the ratio of consecutive level spacings in random matrix ensembles*, Phys. Rev. Lett. 110, 084101 (2013)

[85] C.A. Tracy and H. Widom, *Level spacing distributions and the Airy kernels*, Commun. Math. Phys. 159, 151-174 (1994).

[86] V. K. B. Kota, Embedded random matrix ensembles in quantum physics, Vol. 884, Springer, (2014).

[87] J.B. French, Elementary aspects of nuclear quantum chaos, in A Gift of Prophecy—Essays in the Celebration of the Life of R.E. Marshak, ed. by E.C.G. Sudarshan (World Scientific, Singapore, 1994), pp. 156–167

[88] L. Leviandier, M. Lombardi, R. Jost, and J.P. Pique, *Fourier Transform: A Tool to Measure Statistical Level Properties in Very Complex Spectra*, Phys. Rev. Lett. 56, 2449 (1986)

[89] J. Liu, *Spectral form factors and late time quantum chaos*, Phys. Rev. D **98**, no.8, 086026 (2018) doi:10.1103/PhysRevD.98.086026 [arXiv:1806.05316 [hep-th]].

[90] H. Gharibyan, M. Hanada, S. H. Shenker and M. Tezuka, *Onset of Random Matrix Behavior in Scrambling Systems*, JHEP **07**, 124 (2018) [erratum: JHEP **02**, 197 (2019)] doi:10.1007/JHEP07(2018)124 [arXiv:1803.08050 [hep-th]].

[91] J. S. Cotler, G. Gur-Ari, M. Hanada, J. Polchinski, P. Saad, S. H. Shenker, D. Stanford, A. Streicher and M. Tezuka, *Black Holes and Random Matrices*, JHEP **05**, 118 (2017) [erratum: JHEP **09**, 002 (2018)] doi:10.1007/JHEP05(2017)118 [arXiv:1611.04650 [hep-th]].

[92] T. Nosaka, D. Rosa and J. Yoon, *The Thouless time for mass-deformed SYK*, JHEP **09**, 041 (2018) doi:10.1007/JHEP09(2018)041 [arXiv:1804.09934 [hep-th]].

[93] J. Cotler, N. Hunter-Jones, J. Liu and B. Yoshida, *Chaos, Complexity, and Random Matrices*, JHEP **11**, 048 (2017) doi:10.1007/JHEP11(2017)048 [arXiv:1706.05400 [hep-th]].

[94] E. Brezin and A. Zee, *Universality of the correlations between eigenvalues of large random matrices,* Nucl. Phys. B **402**, 613-627 (1993) doi:10.1016/0550-3213(93)90121-5

[95] G. Mahoux and M.L. Mehta, *A method of integration over matrix variables: IV,* J. Phys. I France 1, 1093 (1991).

[96] W. Van Assche, *Asymptotics for orthogonal polynomials,* Springer, (2006).

[97] Y. V. Fyodorov, *Introduction to the random matrix theory: Gaussian unitary ensemble and beyond*, Lond. Math. Soc. Lect. Note Ser. **322**, 31-78 (2005) [arXiv:math-ph/0412017 [math-ph]].

[98] K. Papadodimas and S. Raju, *Local Operators in the Eternal Black Hole*, Phys. Rev. Lett. 115 no. 21, (2015) 211601, arXiv:1502.06692 [hep-th].

[99] R. Prange, *The spectral form factor is not self-averaging,* Physical Review Letters 78 (1997) 2280.

[100] A. Gaikwad and R. Sinha, *Spectral Form Factor in Non-Gaussian Random Matrix Theories*, Phys. Rev. D **100**, no.2, 026017 (2019) doi:10.1103/PhysRevD.100.026017 [arXiv:1706.07439 [hep-th]].

[101] B. Michel, J. Polchinski, V. Rosenhaus and S. J. Suh, *Four-point function in the IOP matrix model,* JHEP **05**, 048 (2016) doi:10.1007/JHEP05(2016)048 [arXiv:1602.06422 [hep-th]].

[102] E. Dyer and G. Gur-Ari, *2D CFT Partition Functions at Late Times*, JHEP **08**, 075 (2017) doi:10.1007/JHEP08(2017)075 [arXiv:1611.04592 [hep-th]].

[103] D. Stanford, *Talk given at the Ifsrael Institute for Advanced Studies: Aspects of the SYK Model, 2d Gravity, and Random Matrices 3*, Jan 2019, https://www.youtube.com/watch?v=N5UG4jEKeG8&ab_channel =IsraelInstituteforAdvancedStudies

[104] K.T. Alligood, T. Sauer and J.A. Yorke, *Chaos: an introduction to dynamical systems*, Springer-Verlag. ISBN 978-0-387-94677-1. (1997)

[105] H.G. Schuster, *Deterministic Chaos*, Physik-Verlag, Weinheim, (1988)

[106] F. Haake, *Signatures of Quantum Chaos,* Springer, Berlin, (1991).

[107] H.J. Stöckmann, *Quantum Chaos An Introduction*, Cambridge University Press, (1999), Cambridge, UK.

[108] M. C. Gutzwiller, *Chaos in Classical and Quantum Mechanics*, Springer, NY, (1990)

[109] A Pandey, A Kumar and S. Puri, *Quantum Chaotic Systems and Random Matrix Theory*, arXiv:1905.10596 (2019)

[110] S.W. McDonald and A.N. Kaufman, *Spectrum and Eigenfunctions for a Hamiltonian with Stochastic Trajectories*, Phys. Rev. Lett. 42 (1979) 1189.

[111] O. Bohigas, M. J. Giannoni and C. Schmit, *Characterization of chaotic quantum spectra and universality of level fluctuation laws*, Phys. Rev. Lett. **52**, 1-4 (1984) doi:10.1103/PhysRevLett.52.1

[112] R. U. Haq, A. Pandey, and O. Bohigas, *Fluctuation Properties of Nuclear Energy Levels: Do Theory and Experiment Agree?* Phys. Rev. Lett. 48, 1086 (1982)

[113] M. V. Berry and M. Tabor, *Level Clustering in the Regular Spectrum*, Proceedings of the Royal Society of London. Series A, Mathematical and Physical Sciences Vol. 356, No. 1686 (1977)

[114] M.V. Berry, *Semiclassical theory of spectral rigidity,* Proc. Roy. Soc. A 400 (1985) 229.

[115] D. Wintgen and H. Friedrich, *Classical and quantum-mechanical transition between regularity and irregularity in a Hamiltonian system* Phys. Rev. A 35, 1464(R) (1987)

[116] A. Altland,, C.R. Offer, B.D. Simons, *Quantum Chaos: Lessons from Disordered Metals,* In: Lerner, I.V., Keating, J.P., Khmelnitskii, D.E. (eds) Supersymmetry and Trace Formulae. NATO ASI Series, vol 370. Springer, Boston, MA. (1999)

[117] S. Ryu, A. P. Schnyder, A. Furusaki and A. W. W. Ludwig, *Topological insulators and superconductors: Tenfold way and dimensional hierarchy*, New J. Phys. **12**, 065010 (2010) doi:10.1088/1367-2630/12/6/065010 [arXiv:0912.2157 [cond-mat.mes-hall]].

[118] T. Seligman, J.J.M. Verbaarschot and M.R. Zirnbauer, *Quantum chaos and the transition from chaotic to regular motion*, Phys. Rev. Lett. 53 (1984) 215.

[119] M. R. Zirnbauer, *Riemannian symmetric superspaces and their origin in random-matrix theory* J. Math. Phys. 37,4986 (1996).

[120] A. Hoenig and D. Wintgen, Phys. Rev. A39, 5642 A (1989)

[121] Th. Zimmermann, H. Koppel, L.S. Cederbaum, C. Persch and W. Demtroder, Phys. Rev. Lett. 61, 3 A (1988)

[122] M. Oxborrow and C. Ellegaard, Proceedings of the 3rd Experimental Chaos Conference (Edinburgh 1995)

[123] S. Deus, P.M. Koch and L. Sirko, Phys. Rev. E 52, 1146 A (1995)

[124] 0. Legrand, . Schmit and D. Sornette, Europhys. Lett. 18, 101 A (1992).

[125] A. I. Larkin and Y. N. Ovchinnikov, *Quasiclassical method in the theory of superconductivity,* Sov. Phys. JETP 28, 1200 (1969).

[126] P. Hayden and J. Preskill, *Black holes as mirrors: Quantum information in random subsystems*, JHEP 09 (2007) 120, arXiv:0708.4025 [hep-th].

[127] Y. Sekino and L. Susskind, *Fast Scramblers*, JHEP 0810, 065 (2008) arXiv:0808.2096 [hep-th]

[128] A. Almheiri, D. Marolf, J. Polchinski, D. Stanford and J. Sully, *An Apologia for Firewalls*, JHEP 1309, 018 (2013), arXiv:1304.6483 [hep-th].

[129] A. Altland and J. Sonner, *Late time physics of holographic quantum chaos*, SciPost Phys. **11**, 034 (2021) doi:10.21468/SciPostPhys.11.2.034 [arXiv:2008.02271 [hep-th]].

[130] D. Braun and G. Montambaux, *Spectral correlations from the metal to the mobility edge*, Phys. Rev. B **52**, 13903-13909 (1995) doi:10.1103/PhysRevB.52.13903 [arXiv:cond-mat/9506063 [cond-mat]].

[131] B. Altshuler, I. Zarekeshev, S. Kotochigova, and B. Shklovskii, *Repulsion between energy levels and the metal-insulator transition* , Sov. Phys. JETP [Zh. Eksp. Teor. Fiz. 94, 343] 67, 15 (1988).

[132] J. T. Edwards and D. J. Thouless, *Numerical studies of localization in disordered systems*, J. Phys. C 5, 807 (1972).

[133] S. Muller, S. Heusler, P. Braun, F. Haake and A. Altland, *Semiclassical foundation of universality in quantum chaos*, Phys. Rev. Lett. **93**, 014103 (2004) doi:10.1103/PhysRevLett.93.014103 [arXiv:nlin/0401021 [nlin.CD]].

[134] J. M. G. Gomez, K. Kar, V. K. B. Kota, R. A. Molina, A. Relano and J. Retamosa, *Many-body quantum chaos: Recent developments and applications to nuclei*, Phys. Rept. **499**, 103-226 (2011) doi:10.1016/j.physrep.2010.11.003

[135] P. Kos, M. Ljubotina and T. Prosen, *Many-body quantum chaos: Analytic connection to random matrix theory*, Phys. Rev. X **8**, no.2, 021062 (2018) doi:10.1103/PhysRevX.8.021062 [arXiv:1712.02665 [nlin.CD]].

[136] S. Sachdev and J. Ye, *Gapless spin fluid ground state in a random, quantum Heisenberg magnet*, Phys. Rev. Lett. **70**, 3339 (1993) doi:10.1103/PhysRevLett.70.3339 [arXiv:cond-mat/9212030 [cond-mat]].

[137] A. Kitaev, *A simple model of quantum holography*, http://online.kitp.ucsb.edu/online/entangled15/kitaev/, http://online.kitp.ucsb.edu/online/entangled15/kitaev2/. Talks at KITP, April 7, 2015 and May 27, 2015.

[138] J. Maldacena and D. Stanford, *Remarks on the Sachdev-Ye-Kitaev model*, Phys. Rev. D **94**, no.10, 106002 (2016) doi:10.1103/PhysRevD.94.106002 [arXiv:1604.07818 [hep-th]].

[139] O. Aharony, S. S. Gubser, J. M. Maldacena, H. Ooguri and Y. Oz, *Large N field theories, string theory and gravity*, Phys. Rept. **323**, 183-386 (2000) doi:10.1016/S0370-1573(99)00083-6 [arXiv:hep-th/9905111 [hep-th]].

[140] *Sachdev-Ye-Kitaev models and beyond: Window into non-Fermi liquids*, D. Chowdhury, A. Georges, O. Parcollet, and S. Sachdev Rev. Mod. Phys. 94, 035004 (2022)

[141] S. Sachdev, *Bekenstein-Hawking Entropy and Strange Metals*, Phys. Rev. X **5**, no.4, 041025 (2015) doi:10.1103/PhysRevX.5.041025 [arXiv:1506.05111 [hep-th]].

[142] S. Sachdev, *Holographic metals and the fractionalized Fermi liquid*, Phys. Rev. Lett. **105**, 151602 (2010) doi:10.1103/PhysRevLett.105.151602 [arXiv:1006.3794 [hep-th]].

[143] J. Murugan, D. Stanford and E. Witten, *More on Supersymmetric and 2d Analogs of the SYK Model,* JHEP **08**, 146 (2017) doi:10.1007/JHEP08(2017)146 [arXiv:1706.05362 [hep-th]].

[144] J. Maldacena, S. H. Shenker and D. Stanford, *A bound on chaos*, JHEP **08**, 106 (2016) doi:10.1007/JHEP08(2016)106 [arXiv:1503.01409 [hep-th]].

[145] A. Kitaev and S. J. Suh, *The soft mode in the Sachdev-Ye-Kitaev model and its gravity dual*, JHEP **05**, 183 (2018) doi:10.1007/JHEP05(2018)183 [arXiv:1711.08467 [hep-th]].

[146] C. L. Baldwin and B. Swingle, *Quenched vs Annealed: Glassiness from SK to SYK,* Phys. Rev. X **10**, no.3, 031026 (2020) doi:10.1103/PhysRevX.10.031026 [arXiv:1911.11865 [cond-mat.dis-nn]].

[147] A. del Campo, J. Molina-Vilaplana and J. Sonner, *Scrambling the spectral form factor: unitarity constraints and exact results*, Phys. Rev. D 95, no.12, 126008 (2017) [arXiv:1702.04350 [hep-th]].

[148] J. Sonner and M. Vielma, *Eigenstate thermalization in the Sachdev-Ye-Kitaev model*, JHEP **11**, 149 (2017) doi:10.1007/JHEP11(2017)149 [arXiv:1707.08013 [hep-th]].

[149] G. Gur-Ari, R. Mahajan and A. Vaezi, *Does the SYK model have a spin glass phase?*, JHEP **11**, 070 (2018) doi:10.1007/JHEP11(2018)070 [arXiv:1806.10145 [hep-th]].

[150] A. M. García-García and J. J. M. Verbaarschot, *Spectral and thermodynamic properties of the Sachdev-Ye-Kitaev model*, Phys. Rev. D **94**, no.12, 126010 (2016) doi:10.1103/PhysRevD.94.126010 [arXiv:1610.03816 [hep-th]].

[151] A. M. García-García and J. J. M. Verbaarschot, *Analytical spectral density of the Sachdev-Ye-Kitaev model at finite N*, Phys. Rev. D 96, 066012 (2017)

[152] A. M. García-García, Y. Jia and J. J. M. Verbaarschot, *Universality and Thouless energy in the supersymmetric Sachdev-Ye-Kitaev Model*, Phys. Rev. D **97**, no.10, 106003 (2018) doi:10.1103/PhysRevD.97.106003 [arXiv:1801.01071 [hep-th]].

[153] A. M. García-García, B. Loureiro, A. Romero-Bermúdez and M. Tezuka, *Chaotic-Integrable Transition in the Sachdev-Ye-Kitaev Model*, Phys. Rev. Lett. **120**, no.24, 241603 (2018) doi:10.1103/PhysRevLett.120.241603 [arXiv:1707.02197 [hep-th]].

[154] P. H. Ginsparg, *APPLIED CONFORMAL FIELD THEORY*, [arXiv:hep-th/9108028 [hep-th]].

[155] Y. Z. You, A. W. W. Ludwig and C. Xu, *Sachdev-Ye-Kitaev Model and Thermalization on the Boundary of Many-Body Localized Fermionic Symmetry Protected Topological States*, Phys. Rev. B **95**, no.11, 115150 (2017) doi:10.1103/PhysRevB.95.115150 [arXiv:1602.06964 [cond-mat.str-el]].

[156] R. Jackiw, *Lower Dimensional Gravity*, Nucl.Phys.B252 (1985) 343–356. [4]

[157] C. Teitelboim, *Gravitation and Hamiltonian Structure in Two Space-Time Dimensions*, Phys.Lett.B126 (1983) 41–45.

[158] A. Almheiri and J. Polchinski, *Models of AdS2 Backreaction and Holography*, JHEP11 (2015) 014, arXiv:1402.6334[hep-th].

[159] D. Stanford and E. Witten, *Fermionic Localization of the Schwarzian Theory*, JHEP **10**, 008 (2017) doi:10.1007/JHEP10(2017)008 [arXiv:1703.04612 [hep-th]].

[160] T. G. Mertens, *The Schwarzian theory — origins*, JHEP **05**, 036 (2018) doi:10.1007/JHEP05(2018)036 [arXiv:1801.09605 [hep-th]].

[161] W. Fu, D. Gaiotto, J. Maldacena and S. Sachdev, *Supersymmetric Sachdev-Ye-Kitaev models*, Phys. Rev. D **95**, no.2, 026009 (2017) doi:10.1103/PhysRevD.95.026009 [arXiv:1610.08917 [hep-th]].

[162] S. H. Shenker and D. Stanford, *Black holes and the butterfly effect*, JHEP **03**, 067 (2014) doi:10.1007/JHEP03(2014)067 [arXiv:1306.0622 [hep-th]].

[163] J. Maldacena, D. Stanford and Z. Yang, *Diving into traversable wormholes*, Fortsch. Phys. **65**, no.5, 1700034 (2017) doi:10.1002/prop.201700034 [arXiv:1704.05333 [hep-th]].

[164] N. Sorokhaibam, *Phase transition and chaos in charged SYK model*, . J. High Energ. Phys. 2020, 55 (2020). https://doi.org/10.1007/JHEP07(2020)055

[165] D. J. Gross and V. Rosenhaus, *A Generalization of Sachdev-Ye-Kitaev*, JHEP **02**, 093 (2017) doi:10.1007/JHEP02(2017)093 [arXiv:1610.01569 [hep-th]].

[166] D. J. Gross and V. Rosenhaus, *The Bulk Dual of SYK: Cubic Couplings*, JHEP **05**, 092 (2017) doi:10.1007/JHEP05(2017)092 [arXiv:1702.08016 [hep-th]].

[167] J. M. Magan, *Random free fermions: An analytical example of eigenstate thermalization*, Phys. Rev. Lett. **116**, no.3, 030401 (2016) doi:10.1103/PhysRevLett.116.030401 [arXiv:1508.05339 [quant-ph]].

[168] Y. Liao, A. Vikram and V. Galitski, *Many-body level statistics of single-particle quantum chaos*, Phys. Rev. Lett. **125**, 250601 (2020) doi:10.1103/PhysRevLett.125.250601 [arXiv:2005.08991 [cond-mat.stat-mech]].

[169] Y. Liao and V. Galitski, *Emergence of many-body quantum chaos via spontaneous breaking of unitarity*, Phys. Rev. B **105**, no.14, L140202 (2022) doi:10.1103/PhysRevB.105.L140202 [arXiv:2104.05721 [cond-mat.stat-mech]].

[170] Y. Liao and V. Galitski, *Universal dephasing mechanism of many-body quantum chaos*, Phys. Rev. Research 4, L012037 (2022) [arXiv:2110.02976v2 [cond-mat.stat-mech]].

[171] D. Anninos, T. Anous and F. Denef, *Disordered Quivers and Cold Horizons*, JHEP **12**, 071 (2016) doi:10.1007/JHEP12(2016)071 [arXiv:1603.00453 [hep-th]].

[172] N. Iizuka and J. Polchinski, *A Matrix Model for Black Hole Thermalization*, JHEP **10**, 028 (2008) doi:10.1088/1126-6708/2008/10/028 [arXiv:0801.3657 [hep-th]].

[173] R. de Mello Koch, J. H. Huang, C. T. Ma and H. J. R. Van Zyl, *Spectral Form Factor as an OTOC Averaged over the Heisenberg Group*, Phys. Lett. B **795**, 183-187 (2019) doi:10.1016/j.physletb.2019.06.025 [arXiv:1905.10981 [hep-th]].

[174] E. Cáceres, A. Misobuchi and A. Raz, *Spectral form factor in sparse SYK models*, JHEP **08**, 236 (2022) doi:10.1007/JHEP08(2022)236 [arXiv:2204.07194 [hep-th]].

[175] B. Bertini, P. Kos, and T. Prosen, *Exact Spectral Form Factor in a Minimal Model of Many-Body Quantum Chaos*, Phys. Rev. Lett. 121, 264101 (2018).

[176] M. Khramtsov and E. Lanina, *Spectral form factor in the double-scaled SYK model*, JHEP **03**, 031 (2021) doi:10.1007/JHEP03(2021)031 [arXiv:2011.01906 [hep-th]].

[177] P. H. C. Lau, C. T. Ma, J. Murugan and M. Tezuka, *Randomness and Chaos in Qubit Models*, Phys. Lett. B **795**, 230-235 (2019) doi:10.1016/j.physletb.2019.05.052 [arXiv:1812.04770 [hep-th]].

[178] P. H. C. Lau, C. T. Ma, J. Murugan and M. Tezuka, *Correlated disorder in the SYK_2 model*, J. Phys. A **54**, no.9, 095401 (2021) doi:10.1088/1751-8121/abde77 [arXiv:2003.05401 [hep-th]].

[179] M. Winer, S. K. Jian and B. Swingle, *An exponential ramp in the quadratic Sachdev-Ye-Kitaev model*, Phys. Rev. Lett. **125**, 250602 (2020) doi:10.1103/PhysRevLett.125.250602 [arXiv:2006.15152 [cond-mat.stat-mech]].

[180] T. Li, J. Liu, Y. Xin and Y. Zhou, *Supersymmetric SYK model and random matrix theory*, JHEP **06**, 111 (2017) doi:10.1007/JHEP06(2017)111 [arXiv:1702.01738 [hep-th]].

[181] N. Hunter-Jones and J. Liu, *Chaos and random matrices in supersymmetric SYK*, JHEP **05**, 202 (2018) doi:10.1007/JHEP05(2018)202 [arXiv:1710.08184 [hep-th]].

[182] J. Polchinski and V. Rosenhaus, *The Spectrum in the Sachdev-Ye-Kitaev Model*, JHEP **04**, 001 (2016) doi:10.1007/JHEP04(2016)001 [arXiv:1601.06768 [hep-th]].

[183] D. J. Gross and V. Rosenhaus, *All point correlation functions in SYK*, JHEP **12**, 148 (2017) doi:10.1007/JHEP12(2017)148 [arXiv:1710.08113 [hep-th]].

[184] P. Saad, S. H. Shenker and D. Stanford, *A semiclassical ramp in SYK and in gravity*, [arXiv:1806.06840 [hep-th]].

[185] H. Wang, D. Bagrets, A. L. Chudnovskiy and A. Kamenev, *On the replica structure of Sachdev-Ye-Kitaev model*, JHEP **09**, 057 (2019) doi:10.1007/JHEP09(2019)057 [arXiv:1812.02666 [hep-th]].

[186] I. Aref'eva, M. Khramtsov, M. Tikhanovskaya and I. Volovich, *Replica-non-diagonal solutions in the SYK model,* JHEP **07**, 113 (2019) doi:10.1007/JHEP07(2019)113 [arXiv:1811.04831 [hep-th]].

[187] I. Y. Aref 'eva, I. Volovich and M. A. Khramtsov, *Revealing nonperturbative effects in the SYK model*, Theor. Math. Phys. **201**, no.2, 1585-1605 (2019) doi:10.1134/S0040577919110059 [arXiv:1905.04203 [hep-th]].

[188] V. Rosenhaus, *An introduction to the SYK model*, J. Phys. A **52**, 323001 (2019) doi:10.1088/1751-8121/ab2ce1 [arXiv:1807.03334 [hep-th]].

[189] R. Bhattacharya, S. Chakrabarti, D. P. Jatkar, and A. Kundu, *SYK Model, Chaos and Conserved Charge*, JHEP 11 (2017) 180, [arXiv:1709.07613].

[190] W. Fu and S. Sachdev, Phys. Rev. B **94**, no.3, 035135 (2016) doi:10.1103/PhysRevB.94.035135 [arXiv:1603.05246 [cond-mat.str-el]].

[191] Y. Gu, A. Kitaev, S. Sachdev and G. Tarnopolsky, *Notes on the complex Sachdev-Ye-Kitaev model*, JHEP **02**, 157 (2020) doi:10.1007/JHEP02(2020)157 [arXiv:1910.14099 [hep-th]].

[192] K. Bulycheva, *A note on the SYK model with complex fermions*, JHEP **1712**, 069 (2017) doi:10.1007/JHEP12(2017)069 [arXiv:1706.07411 [hep-th]].

[193] G. V. Dunne, R. Jackiw and C. A. Trugenberger, *Topological (Chern-Simons) Quantum Mechanics*, Phys. Rev. D **41**, 661 (1990) doi:10.1103/PhysRevD.41.661

[194] R. Floreanini, R. Percacci and E. Sezgin, *Infinite dimensional algebras in Chern-Simons quantum mechanics*, Phys. Lett. B **261**, 51-56 (1991) doi:10.1016/0370-2693(91)91323-N [arXiv:hep-th/9111053 [hep-th]].

[195] R. Jackiw and S. Y. Pi, *Reducing the Chern-Simons term by a symmetry*, Phys. Lett. B 423 (1998) 364–368, [hep-th/9712087].

[196] G. V. Dunne, K. M. Lee and C. h. Lu, *On the finite temperature Chern-Simons coefficient*, Phys. Rev. Lett. **78**, 3434-3437 (1997) doi:10.1103/PhysRevLett.78.3434 [arXiv:hep-th/9612194 [hep-th]].

[197] E. Fradkin and A. Lopez, *Fractional Quantum Hall effect and Chern-Simons gauge theories*, Phys. Rev. B **44**, 5246-5261 (1991) doi:10.1103/PhysRevB.44.5246

[198] B. I. Halperin, P. A. Lee, and N. Read, *Theory of the half filled Landau level*, Phys. Rev. B 47 (1993) 7312–7343.

[199] J. K. Jain, *Composite fermion approach for the fractional quantum Hall effect*, Phys. Rev. Lett. 63 (1989) 199–202.

[200] J. K. Jain, *Theory of the fractional quantum Hall effect*, Phys. Rev. B 41 (1990) 7653–7665.

[201] S.-P. Kou, M. Levin, and X.-G. Wen, *Mutual Chern-Simons theory for Z(2) topological order*, Phys. Rev. B 78 (2008) 155134, [arXiv:0803.2300].

[202] D. N. Sheng, Z. C. Gu, K. Sun, and L. Sheng, *Fractional quantum Hall effect in the absence of Landau levels*, Nature Communications 2 (2011) 389, [arXiv:1102.2658].

[203] T. Neupert, L. Santos, C. Chamon, and C. Mudry, *Fractional Quantum Hall States at Zero Magnetic Field*, Phys. Rev. Lett. 106 (2011), no. 23 236804, [arXiv:1012.4723].

[204] N. Regnault and B. A. Bernevig, *Fractional Chern insulator*, Phys. Rev. X 1 (2011) 021014, [arXiv:1105.4867].

[205] Y.-M. Lu and A. Vishwanath, *Classification and properties of symmetry-enriched topological phases: Chern-Simons approach with applications to Z2 spin liquids*, Phys. Rev. B 93 (2016), no. 15 155121, [arXiv:1302.2634].

[206] M. Aganagic, K. Costello, J. McNamara, and C. Vafa, *Topological Chern-Simons/Matter Theories*, arXiv:1706.09977.

[207] E. Witten, *Quantum Field Theory and the Jones Polynomial*, Commun. Math. Phys. 121 (1989) 351–399.

[208] R. Dijkgraaf and E. Witten, *Topological Gauge Theories and Group Cohomology*, Commun. Math. Phys. 129 (1990) 393.

[209] E. Witten, *Chern-Simons gauge theory as a string theory*, Prog. Math. 133 (1995) 637–678, [hep-th/9207094].

[210] M. Marino, *Chern-Simons theory and topological strings*, Rev. Mod. Phys. 77 (2005) M. Marino, Chern-Simons theory and topological strings, Rev. Mod. Phys. 77 (2005) 675–720, [hep-th/0406005].

[211] S. Deser, R. Jackiw, and S. Templeton, *Topologically Massive Gauge Theories*, Annals Phys. 140 (1982) 372–411. [Erratum: Annals Phys. 185, 406 (1988)].

[212] K. Jensen, *Chaos in AdS_2 Holography*, Phys. Rev. Lett. **117**, no.11, 111601 (2016) doi:10.1103/PhysRevLett.117.111601 [arXiv:1605.06098 [hep-th]].

[213] J. Engelsöy, T. G. Mertens and H. Verlinde, *An investigation of AdS_2 backreaction and holography*, JHEP **07**, 139 (2016) doi:10.1007/JHEP07(2016)139 [arXiv:1606.03438 [hep-th]].

[214] A. Almheiri and J. Polchinski, *Models of AdS_2 backreaction and holography*, JHEP **11**, 014 (2015) doi:10.1007/JHEP11(2015)014 [arXiv:1402.6334 [hep-th]].

[215] G. Sárosi, *AdS_2 holography and the SYK model*, PoS **Modave2017**, 001 (2018) doi:10.22323/1.323.0001 [arXiv:1711.08482 [hep-th]].

[216] M. Cvetič and I. Papadimitriou, *AdS_2 holographic dictionary*, JHEP **12**, 008 (2016) [erratum: JHEP **01**, 120 (2017)] doi:10.1007/JHEP12(2016)008 [arXiv:1608.07018 [hep-th]].

[217] M. Cadoni, P. Carta, D. Klemm and S. Mignemi, *AdS(2) gravity as conformally invariant mechanical system*, Phys. Rev. D **63**, 125021 (2001) doi:10.1103/PhysRevD.63.125021 [arXiv:hep-th/0009185 [hep-th]].

[218] S. Deser, R. Jackiw, and S. Templeton, *Three-Dimensional Massive Gauge Theories*, Phys. Rev. Lett. 48 (1982) 975–978.

[219] A. Achucarro and P. K. Townsend, *A Chern-Simons Action for Three-Dimensional anti-De Sitter Supergravity Theories*, Phys. Lett. B 180 (1986) 89.

[220] E. Witten, *(2+1)-Dimensional Gravity as an Exactly Soluble System*, Nucl. Phys. B 311 (1988) 46.

[221] W. L. Vleeshouwers and V. Gritsev, *The spectral form factor in the 't Hooft limit – Intermediacy versus universality*, SciPost Phys. Core **5**, 051 (2022) doi:10.21468/SciPostPhysCore.5.4.051 [arXiv:2201.07841 [cond-mat.str-el]].

[222] J. Murugan, R. P. Slayen and H.J.R. Van Zyl, *A Study of the SYK_2 Model with Twisted Boundary Conditions* (2023), [arXiv:2307.01099]

[223] M. Srednicki, *Chaos and Quantum Thermalization*, Physical Review E. 50 (2): 888–901. (1994)

[224] J. M. Deutsch, *Quantum statistical mechanics in a closed system*, Physical Review A. 43 (4): 2046–2049. (1991).

[225] A. Altland and A. Kamenev, *Wigner-Dyson statistics from the Keldysh sigma-model*, Phys. Rev. Lett. **85**, 5615-5618 doi:10.1103/PhysRevLett.85.5615 [arXiv:cond-mat/0006363 [cond-mat]]. 14 citations counted in INSPIRE as of 22 Feb 2023

[226] J. M. Deutsch, *Eigenstate thermalization hypothesis,* Rept. Prog. Phys. **81**, no.8, 082001 (2018) doi:10.1088/1361-6633/aac9f1

[227] D. Stanford, *Many-body chaos at weak coupling*, JHEP **10**, 009 (2016) doi:10.1007/JHEP10(2016)009 [arXiv:1512.07687 [hep-th]].

[228] A. Kamenev and M. Mezard, *Level correlations in disordered metals: The replica sigma model*, Phys. Rev. B **60**, 3944-3954 (1999) doi:10.1103/PhysRevB.60.3944 [arXiv:cond-mat/9903001 [cond-mat.dis-nn]].

[229] T. Sulejmanpasic, Phys. Rev. Lett. **118**, no.1, 011601 (2017) doi:10.1103/PhysRevLett.118.011601 [arXiv:1610.04009 [hep-th]].

[230] G. V. Dunne, Y. Tanizaki and M. Ünsal, JHEP **08**, 068 (2018) doi:10.1007/JHEP08(2018)068 [arXiv:1803.02430 [hep-th]].

[231] G. Penington, S. H. Shenker, D. Stanford and Z. Yang, *Replica wormholes and the black hole interior*, JHEP **03**, 205 (2022) doi:10.1007/JHEP03(2022)205 [arXiv:1911.11977 [hep-th]].

[232] D. A. Trunin, *Pedagogical introduction to the Sachdev–Ye–Kitaev model and two-dimensional dilaton gravity*, Usp. Fiz. Nauk **191**, no.3, 225-261 (2021) doi:10.3367/UFNe.2020.06.038805 [arXiv:2002.12187 [hep-th]].